

Uptake and subcellular distribution of carbon nanoparticles

INAUGURAL-DISSERTATION

zur Erlangung des Doktorgrades der
Mathematisch-Naturwissenschaftlichen Fakultät der
Heinrich-Heine-Universität Düsseldorf

vorgelegt von:

Christian Wimmenauer

aus Bergisch Gladbach

Düsseldorf, März 2023

aus dem Institut für Experimentelle Physik der kondensierten Materie der
Heinrich-Heine-Universität Düsseldorf

Gedruckt mit der Genehmigung der
Mathematisch-Naturwissenschaftlichen Fakultät der
Heinrich-Heine-Universität Düsseldorf

Berichterstatter:

1. Prof. Dr. Thomas Heinzel
2. Prof. Dr. Cornelia Monzel

Tag der mündlichen Prüfung: 05.06.2023

Abstract

This thesis treats the characterization of carbon nanoparticles regarding their subcellular distribution and cell-specific uptake rate to enable their use in biomedical applications or basic research in the area of life science. Four manuscripts resulting from this work report our main findings.

As discussed in *Paper I*, we found that carbon nanoparticles derived from citric acid and diethylenetriamine in a microwave-assisted bottom-up synthesis accumulate mainly in the lysosomes of the breast cancer cell line MCF-7 after 48 h of exposure. A workflow for object-based colocalization analysis of moving point-like objects was developed and applied to microscopy data acquired via Airy scanning microscopy in super-resolution mode. This workflow, which is based on point pattern analysis, was successfully validated with a positive control and a negative control and allows the assessment of the statistical significance of the results by the comparison with the results from Monte-Carlo simulations under a model assumption. This method overcomes common shortcomings of many traditional colocalization techniques since the analyzed objects do not need to overlap in both channels, and inference on a solid statistical basis is possible.

Paper II investigated the differential uptake of blood cells derived from healthy donors compared to samples from patients with acute myeloid leukemia (AML). A significantly smaller uptake of the same carbon nanoparticles was reported for the $CD33^+$ and $CD34^+$ subsets of samples from AML patients compared to the $CD33^+$ and $CD34^+$ subsets of healthy donors. In good agreement with previous findings with other cells, the nanoparticles showed perinuclear accumulation in the AML cell line HL-60 on confocal microscopy images that may correspond to an immobile pool of lysosomes near the microtubule organizing center.

In *Paper III*, we attempted to modify the cell-specific uptake of the employed carbon nanoparticles via modification with sugar monomers and sugar-decorated oligomers. While we did not observe a cell-type specific uptake, we found that the monomer-functionalized nanoparticles showed a two- to threefold increased uptake rate across all cell types compared to the non-functionalized and oligomer-coupled nanoparticles. Regarding their subcellular localization, no difference between the nanoparticle species was observed since all conditions showed significant accumulation in the lysosomes, as revealed by colocalization experiments.

Finally, *Paper IV* reports the results from tight-binding simulations of multilayer graphene quantum dots. The calculations reveal a redshift with an increasing number of layers, as apparent in the optical absorption spectrum and the decrease of the energy gap. Furthermore, the edge type and the geometry of the multilayer graphene quantum dot play a dominant role not only in the lateral size dependence of the energy spectrum but also in the dependence on the particle's number of layers.

Eidesstattliche Versicherung

Ich versichere an Eides statt, dass die Dissertation von mir selbständig und ohne unzulässige fremde Hilfe unter Beachtung der „Grundsätze zur Sicherung guter wissenschaftlicher Praxis an der Heinrich-Heine-Universität Düsseldorf“ erstellt worden ist.

Ort, Datum

Christian Wimmenauer

Contents

Introduction	1
1 Fundamentals	5
1.1 Carbon nanostructures	5
1.1.1 Graphene	5
1.1.2 Graphene nanoribbons and edges in graphene	8
1.1.3 Graphene quantum dots	10
1.1.4 Carbon nanodots	13
1.2 Biophysical fundamentals	17
1.2.1 Endocytosis	17
1.2.2 Lysosomal transport	20
1.3 Biomedical applications of nanoparticles	22
1.3.1 Fields of biomedical applications of nanoparticles	22
1.3.2 Biomedical applications of carbon nanoparticles	24
1.4 Quantitative analysis of subcellular distributions	29
1.4.1 Colocalization	29
1.4.2 Spatial point pattern analysis	30
2 Experimental methods	35
2.1 Carbon nanoparticles used in this work	35
2.1.1 Microwave-assisted synthesis	35
2.1.2 Modification via EDC and NHS	35
2.1.3 Characterization	36
2.2 Confocal fluorescence microscopy	38
2.2.1 Airyscan microscopy	39
2.3 Flow Cytometry	40
3 Subcellular distribution of carbon nanodots	43
3.1 Paper I	44
4 Differential uptake of carbon nanodots	71
4.1 Paper II	72
4.2 Paper III	83
5 Multilayer graphene quantum dots	91
5.1 Paper IV	92

6 Conclusion and outlook	107
Bibliography	109
Abbreviations	133
Danksagung	135

Introduction

“Although it is a very wild idea, it would be interesting in surgery if you could swallow the surgeon.”

– Richard P. Feynman [1]

Even though significant progress has been made, we are just scratching the surface of understanding the potential of using nanotechnology in medicine. In 1995, the FDA approved the first nanomedical formulation as a drug for tumor chemotherapy [2]. Now, almost 30 years later, mRNA nanomedicine is a field that celebrated recent successes in helping to fight the Covid-19 pandemic and is looking to have a bright future with multiple cancer vaccines in the pipeline that also incorporate nanoparticles in their formulation [3]. Not only is nanotechnology useful when it comes to applications in medicine, but it is also used as a tool in basic research in biology. Applications as fluorescent probes in multicolor imaging [4–6], single particle tracking [7, 8], and intracellular sensing [9], as well as applications as vectors in transfection [10], or as carriers for gene editing constructs [11] are already part of the toolbox of modern biology. Improvements in novel applications such as super-resolution microscopy with nanoprobe [8, 12] and manipulation of cells with magnetic nanoparticles [13] may open up new possibilities for the design of experiments to reveal the inner workings of biological matter.

Since their initial discovery in 2004 as a by-product in the synthesis of carbon nanotubes via arc discharge [14], carbon dots have aroused immense scientific interest. Around the same time, the family of nanographenes or graphene quantum dots, which may be considered a subgroup of carbon dots, rose to prominence [15]. This is exemplified by the fact that the number of scientific publications listed on Google Scholar in the fields that contain the terms "carbon dot" or "graphene quantum dot" grows approximately exponentially with the publication date since the inception of their respective research areas (see Fig. 0.1). Carbon dots and graphene quantum dots have been applied in proof of principle experiments in energy storage and conversion [16], metal ion sensing [17, 18], photocatalysis [19, 20], and as an organic photon source in LEDs [21]. Due to many beneficial characteristics, which include small size and low toxicity in many cases, carbon dots and graphene quantum dots have also been demonstrated to be utilizable in a long list of biomedical applications. These include use cases in intracellular sensing [22–31], drug delivery [32, 33], mRNA delivery [34], super-resolution microscopy [35, 36], and photodynamic therapy [37, 38].

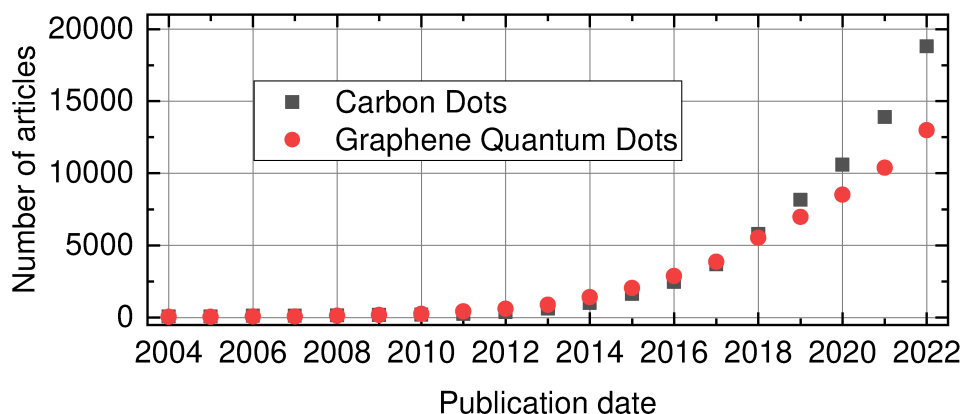


Figure 0.1: Number of search results on Google Scholar for articles plotted against their publication date with the keywords "carbon dots" and "graphene quantum dots".

To effectively apply nanoparticles in biomedicine, preliminary questions regarding their toxicity, intracellular distribution, and differential uptake must be answered. Significant toxicity would hamper applications in biological environments. All cells are compartmentalized, and these compartments fulfill different functions and show varying properties. Knowing the target location of a nanoparticle after uptake is the key to a successful therapeutic or diagnostic application. Finally, the uptake in different cell types may vary, potentially enabling selective delivery of the nanoparticles to specific cells. This work aims to further the understanding of the uptake dynamics and sub-cellular distribution of carbon nanoparticles to lay the ground for future applications in nanomedicine.

Chapter 1 serves the purpose of reviewing the fundamentals relevant to the work presented here. First, in section 1.1, the features of low-dimensional carbon materials, from graphene to carbon nanodots, are introduced. In Section 1.2, the biophysical fundamentals regarding uptake and transport relevant to the publications are presented. In section 1.3, possible biomedical applications of nanoparticles in general are presented, followed by a discussion of possible applications of carbon nanoparticles in particular. Finally, section 1.4 deals with the quantitative analysis of the distribution of fluorescent nanoparticles via colocalization techniques and spatial statistics. In chapter 2, the most important experimental methods are briefly explained. These are namely the preparation and characterization of the nanoparticles (section 2.1) used in the experiments, confocal microscopy (section 2.2), and flow cytometry (section 2.3). Chapter 3 incorporates *Paper I* and presents the results regarding the subcellular distribution of the nanoparticles. The main result of *Paper I* is the development and application of a method to investigate the colocalization of fast-moving vesicles with their fluorescent cargo via spatial statistics. Chapter 4, on the other hand, deals with the modification of the uptake of carbon nanoparticles into different cell types and includes *Paper II* and *Paper III*. While *Paper II* looks at the uptake of the nanoparticles into different types of healthy and malignant primary blood cells, *Paper III* reports the results from experiments in which the uptake of nanoparticles with different modifications is in-

vestigated. These modifications are namely the conjugation of the nanoparticles with sugars and sugar-decorated oligomers. Chapter 5 picks out the electronic and optical properties of multilayer graphene quantum dots that may form as aggregates as its central theme. The results are presented in the form of *Paper IV*. Finally, Chapter 6 summarizes the findings with concluding remarks and provides an outlook on possible future work.

Chapter 1

Fundamentals

1.1 Carbon nanostructures

Carbon is found in many different structural modifications with a wide variety of properties. For instance, carbon in an sp^3 -hybridization may form diamond, which is transparent to visible light and has a hardness of ten on the Mohs scale. On the other hand, graphite, which is formed by stacked layers of sp^2 -hybridized carbon, is opaque and much softer. The comparison of graphite and diamond, even on a macroscopic level, illustrates the variety found in the allotropes of carbon. For nanoscale materials composed of carbon, the possibilities of engineering films, ribbons, or particles with intriguing properties are overwhelming. The following sections will review the properties of low-dimensional carbon materials to finally arrive at the discussion of graphene quantum dots and carbon nanodots.

1.1.1 Graphene

Graphene is an atomically thin layer of sp^2 -hybridized carbon arranged in a two-dimensional honeycomb lattice and can thus be considered as single-layer graphite. In 1947, the band structure of graphene was theoretically explored by Wallace [39]. In 2004 graphene was fully isolated and characterized by Novoselov et al. [40]. Shortly after that, Novoselov et al. showed that charge carriers in graphene behave like a two-dimensional gas of massless Dirac fermions [41], which was predicted by Semenoff [42] as well as DiVincenzo and Mele [43]. The proof of the existence of a two-dimensional gas of massless Dirac fermions in graphene led to the discovery of a myriad of intriguing effects in this material, like the anomalous integer quantum hall effect [44], a charge carrier density dependent cyclotron mass [41] and Klein-Tunneling [45, 46]. In the following paragraph, the derivation of the band structure of graphene will be discussed with special attention to features emerging in proximity to the K and K' points. The presented derivation is strongly based on the review of Neto et al. [47] and Leggett's lecture on this topic [48].

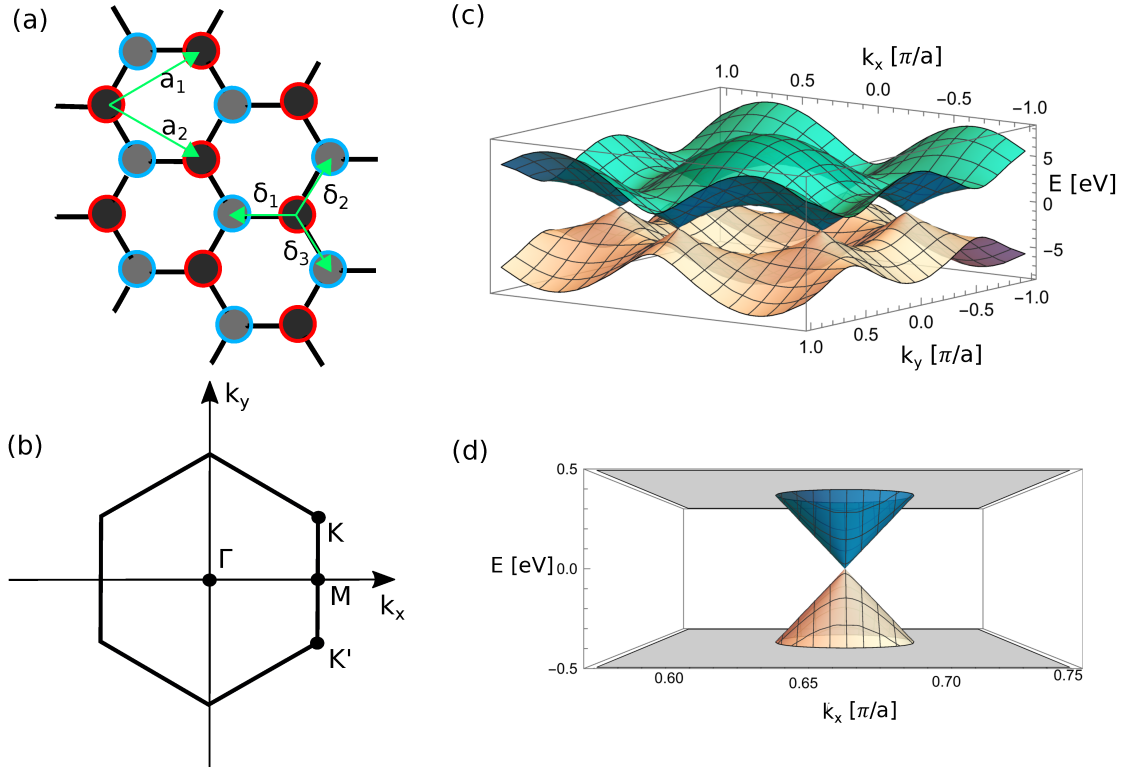


Figure 1.1: (a) Lattice structure of graphene with the lattice vectors \vec{a}_1 and \vec{a}_2 , as well as the nearest neighbor vectors $\vec{\delta}_1$, $\vec{\delta}_2$, $\vec{\delta}_3$. The sublattices A and B are shown with a red and blue outline, respectively. (b) First Brillouin zone of graphene with the characteristic points Γ , M , K , and K' . (c) Band structure of the π and π^* -band of graphene, plotted for $k_x, k_y \in [-\frac{\pi}{a}, \frac{\pi}{a}]$. (d) Band structure for small energy values close to a Dirac point. Note that the bands are reasonably well approximated as conical surfaces.

To arrive at the tight-binding Hamiltonian, first, the geometry has to be defined. The lattice vectors of graphene are given by

$$\vec{a}_1 = \frac{a}{2}(3, \sqrt{3}), \quad \vec{a}_2 = \frac{a}{2}(3, -\sqrt{3}), \quad (1.1)$$

with the carbon-carbon distance $a = 142$ pm. The resulting three nearest neighbor vectors are given by

$$\vec{\delta}_1 = \frac{a}{2}(1, \sqrt{3}), \quad \vec{\delta}_2 = \frac{a}{2}(1, -\sqrt{3}), \quad \vec{\delta}_3 = a(1, 0). \quad (1.2)$$

Both the lattice vectors and the nearest neighbor vectors are displayed in Fig. 1.1 (a). Note that graphene has two unequal sublattices, A and B, with each atom of sublattice A only having nearest neighbors of sublattice B and vice versa. An electron always jumps from one site to a site of the opposite sublattice if only nearest neighbor transport is allowed. Thus, the nearest neighbor tight-binding Hamiltonian for graphene reads [47]

$$\hat{H} = -t \sum_{\langle i,j \rangle, \sigma} (\hat{a}_{i,\sigma}^\dagger \hat{b}_{j,\sigma} + h.c.), \quad (1.3)$$

where $\hat{a}_{i,\sigma}^\dagger$ ($\hat{b}_{i,\sigma}^\dagger$) denotes the creation operator for an electron in site i of sublattice A (B) with spin $\sigma \in \{\uparrow, \downarrow\}$. The operator $\hat{a}_{i,\sigma}$ ($\hat{b}_{i,\sigma}$) is the corresponding annihilation operator. Frequently, $t = 2.7 \text{ eV}$ is chosen as the hopping energy. The expression $\langle i, j \rangle$ denotes that i and j indicate neighboring sites and $h.c.$ is the hermitian conjugate. The representations of the operators \hat{a}^\dagger and $\hat{b}_{i,\sigma}$ on a Fourier basis read

$$\hat{a}_{i,\sigma}^\dagger = \frac{1}{\sqrt{N/2}} \sum_{\vec{k}} e^{i\vec{k}\vec{r}_i} \hat{a}_{\vec{k},\sigma}^\dagger, \quad \hat{b}_{i,\sigma} = \frac{1}{\sqrt{N/2}} \sum_{\vec{k}'} e^{i\vec{k}'(\vec{r}_i + \vec{\delta})} \hat{b}_{\vec{k},\sigma}, \quad (1.4)$$

allowing to transform between real and momentum space. Inserting the representations 1.4 of the annihilation and their respective creation operators in the Hamiltonian (eq. 1.3) yields

$$\hat{H} = -t \sum_{\vec{\delta}, \vec{k}} (e^{-i\vec{k}\vec{\delta}} \hat{a}_{\vec{k},\sigma}^\dagger \hat{b}_{\vec{k},\sigma} + h.c.) \quad (1.5)$$

which can be rewritten as

$$\hat{H} = \sum_{\vec{k}} \vec{\Psi}^\dagger \begin{pmatrix} 0 & \Delta_k \\ \Delta_k^* & 0 \end{pmatrix} \vec{\Psi} \quad (1.6)$$

with $\Psi = (\hat{a}_{\vec{k}}, \hat{b}_{\vec{k}})^T$ and $\Delta_k = \sum_{\vec{\delta}} e^{i\vec{k}\vec{\delta}}$. Solving the eigenvalue problem yields the expression $E_{\pi,\pi^*} = \pm t \sqrt{\Delta_k \Delta_k^*}$ that can be expanded by inserting the nearest neighbor vectors, to the equation

$$E_{\pi,\pi^*}(\vec{k}) = \pm t \sqrt{3 + 2 \cos(\sqrt{3}k_y a) + 4 \cos\left(\frac{\sqrt{3}}{2}k_y a\right) \cos\left(\frac{3}{2}k_x a\right)} \quad (1.7)$$

for the binding π -band and anti-binding π^* -band, shown in Fig. 1.1 (c). Both bands are symmetric around $E = 0$, which is reflected in the electron-hole symmetry.¹ Close to the K - and K' -points (see Fig. 1.1 (b)) at the corners of the Brillouin zone with

$$\vec{K} = \left(\frac{2\pi}{3a}, \frac{2\pi}{3\sqrt{3}a}\right), \quad \vec{K}' = \left(\frac{2\pi}{3a}, -\frac{2\pi}{3\sqrt{3}a}\right) \quad (1.8)$$

the bands from (eq. 1.7) can be linearly approximated (see Fig. 1.1 (d)) with $\vec{\kappa} = \vec{k} - \vec{K}$ for $|\vec{\kappa}| \ll |\vec{K}|$ via the expansion

$$E_{\pi,\pi^*}(\vec{\kappa})|_{|\vec{\kappa}| \ll |\vec{K}|} = \pm v_F |\vec{\kappa}| + \mathcal{O}\left(\frac{\kappa^2}{K^2}\right). \quad (1.9)$$

The Fermi velocity is denoted by $v_F = 3ta/2 \approx 10^6 \text{ m/s}$, that in contrast to the usual case of a parabolic dispersion, does not depend on the mass m . This unusual linear dispersion has the effect that charge carriers behave like massless Dirac fermions close to the K and K' -points with v_F replacing the speed of light. Thus, relativistic effects can be studied in a solid-state system, which would be infeasible to observe on their

¹Please note, that if next nearest neighbor hopping energies $t' \neq 0$ are introduced in the model the electron hole symmetry is broken.

elementary particle counterpart [45]. Close to the K and K' -points the Hamiltonian can be rewritten as the Dirac-Weyl equation [42, 43]

$$\hat{H}(\vec{\kappa}) = -i\hbar v_F \boldsymbol{\sigma} \nabla, \quad (1.10)$$

with the Pauli matrices σ_x and σ_y constituting $\boldsymbol{\sigma} = (\sigma_x, \sigma_y)^T$.

1.1.2 Graphene nanoribbons and edges in graphene

In this subsection, the transition from two-dimensional graphene to electronically one-dimensional nanostructures will be discussed, with an emphasis on the effects emerging from the edge type, since they are of particular interest in the following discussion of graphene quantum dots. There are two pristine edge configurations in graphene, separated by an angle of $\pi/6$, namely, zigzag (Fig. 1.2 (a)) and armchair edges (Fig. 1.2 (b)). Inspecting the geometry of the two sublattices, it becomes apparent that for the zigzag edge, all outermost sites belong to the same sublattice. In the case of the armchair edge, on the other hand, the outermost sites alternate between both sublattices. A nanostructure called graphene nanoribbon (GNR) can be defined with two parallel cuts through the graphene sheet. Charge carriers in a GNR are confined to two dimensions, leaving only one dimension for transport. While GNRs with mixed edges exist, this section will only consider GNRs with a pure edge type. The naming convention for zigzag and armchair GNRs contains the edge type and the number of sites on the axis perpendicular to the axis of translational symmetry, as indicated in Fig. 1.2 (a) and (b), respectively. The band structure of GNRs may be calculated using the tight-binding model for graphene, with a restricted number of atoms in the lateral direction and a translational symmetry only in one dimension. The direction of the translational symmetry determines the edge type. Armchair GNRs display metallic or semiconducting properties depending on their width W , or rather the number of atoms on their lateral axis N_w . The bandgap of armchair GNRs $E_{g,ac}$ approximately scales as given by [49]

$$E_{g,ac} \sim \begin{cases} 0, & N_w = 3m - 1 \\ \frac{\pi}{W + \sqrt{3}/2}, & N_w = 3m \\ \frac{\pi}{W}, & N_w = 3m + 1, \end{cases} \quad (1.11)$$

where $m \in \mathbb{N}$. The bandgap of armchair GNRs against the number of sites on their lateral axis is depicted in Fig. 1.2 (c). The band structure of the metallic armchair-17 and the semiconducting armchair-18 GNR are displayed in Fig. 1.2 (e). Note that the resulting bands can be mapped to parallel one-dimensional cross-sections of the two-dimensional bands of bulk graphene [49]. In contrast, zigzag GNRs display gapless flat bands around $k = \pi$ and thus show metallic behavior independent of the width. Flat bands at $E = 0$ have been explained by localized states at the zigzag edges around $k = \pi$ [50]. Other than in armchair GNRs, the bands of zigzag GNRs cannot be mapped to sections through the band structure of bulk graphene. Consequently, the behavior of nanostructures with a pristine armchair edge is more similar to the behavior of bulk graphene, while the existence of localized states at zigzag edges leads to effects that are not observable in an extended graphene sheet. An example of the band structure of zigzag GNRs is displayed in Fig. 1.2 (d).

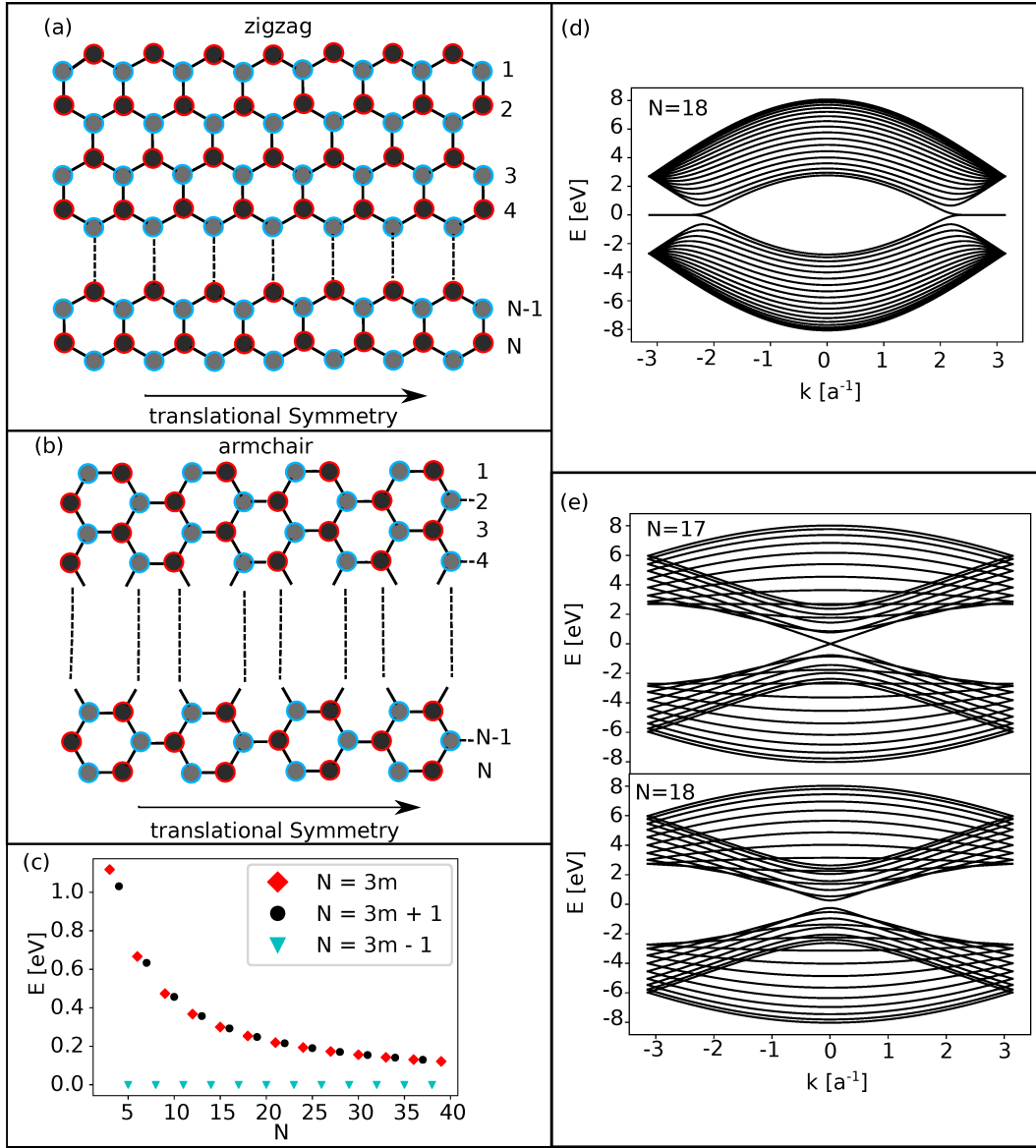


Figure 1.2: General structure of (a) a zigzag graphene nanoribbon (GNR) and (b) an armchair GNR. The direction of translational symmetry as well as the counting scheme for the nomenclature, are indicated. (c) Size dependence of the band gap E of an armchair GNR against the number of atoms on the lateral axis, counted as indicated in (b). (d) Band structure of the $N = 18$ zigzag GNR. (e) Band structure of the metallic $N = 17$ armchair GNR (top) and the semiconducting $N = 18$ armchair GNR (bottom). Figures (c-e) are results of tight-binding calculations with the Python package Kwant [51].

1.1.3 Graphene quantum dots

Graphene quantum dots (GQDs) are electronically zero-dimensional objects defined on a graphene lattice.

Quantum confinement in single-layer GQDs

The energy levels of circular semiconductor quantum dots may be calculated by solving the Schrödinger equation with a potential that is zero inside of a circular region and infinite anywhere else. Suppose the influence of the type edges is neglected altogether. In that case, energy levels of a circular GQD may be calculated analogously, but instead of the Schrödinger equation, the Dirac-Weyl equation needs to be applied. The calculation of the energy spectrum of a circular graphene quantum dot by applying an infinite mass boundary and solving the Dirac-Weyl equation was demonstrated by Schnetz et al. [52] and Recher et al. [53] around the same time. This approach of analytically or numerically solving the Dirac-Weyl equation on a continuous domain will be referred to as the continuum model. While it is possible to confine charge carriers in graphene with a combination of electric and magnetic fields resulting in edgeless GQDs, as experimentally demonstrated by Freitag et al. [54], GQDs with edges are of greater interest for the work related to this thesis. Zarenia et al. [55] introduced zigzag and armchair boundary conditions to the continuum model for triangular and hexagonal GQDs and compared the results to the energy spectra derived from tight-binding simulations. The work of Zarenia et al. shows that while both the tight-binding and the continuum model are in good qualitative agreement, there are non-negligible deviations for small hexagonal GQDs in the continuum model. The nearest neighbor tight-binding Hamiltonian for monolayer GQDs has the same second quantization formulation as in the case of graphene (see eq. 1.3), but only with a finite number of sites and no translational symmetry. Due to the lack of a translational symmetry, the creation and annihilation operators cannot be expressed on a Fourier basis. The Hamiltonian \hat{H} of a GQD with N sites can thus be considered as a finite $N \times N$ matrix. Solving the eigenvalue problem, therefore, leads to discrete energy levels instead of continuous bands, as in the case of bulk graphene and GNRs. Zarenia et al. [55] found that the relationship between the energy gap of a GQD and its size, given by the number of atomic sites at the edge N_s , is described by a power law with the parameters α and γ

$$E_g = \frac{\alpha}{N_s^\gamma}. \quad (1.12)$$

Here, $\gamma = 3.23$ for hexagonal GQDs with zigzag edges and $\gamma = 1$ for triangular GQDs with both edge types and hexagonal GQDs with armchair edges. The counting scheme to yield N_s and the three pristine geometries of GQDs are found in Fig. 1.3. The triangular geometry in GQDs is unique since there is an angle of $\theta = \pi/3$ between all the edges, that does not generate an edge impurity at the corner. In contrast to this, geometries that incorporate at least one angle of $\theta = 2\pi/3$ show an impurity at this corner, and the edge type is incommensurate. This means that at corners with an angle of $\theta = 2\pi/3$, in the case of zigzag edges, the outermost sublattice changes. In the case of armchair edges, the orientation of the dimers changes regarding their

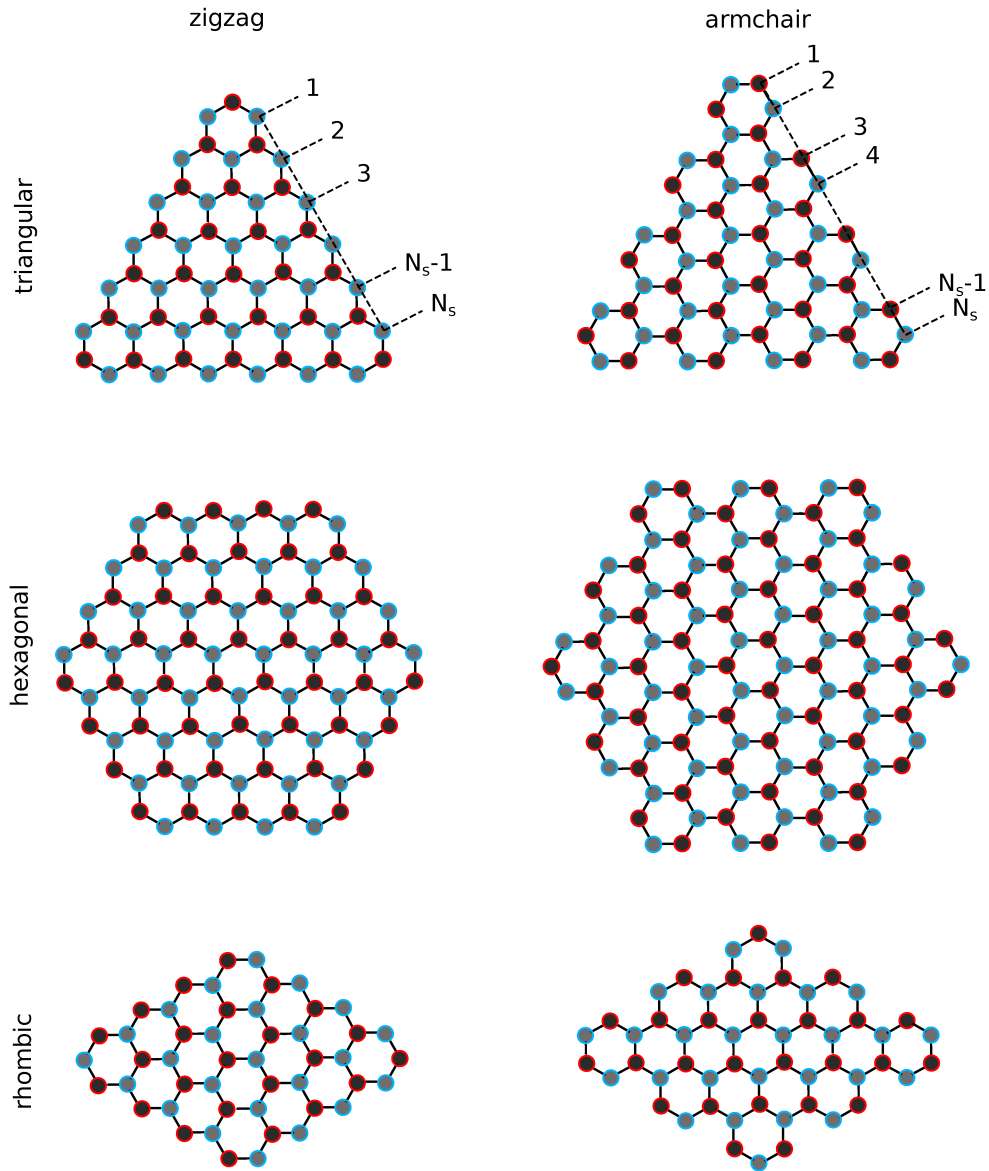


Figure 1.3: Examples of graphene quantum dots (GQDs) with zigzag (left) and armchair (right) edges and triangular (top), hexagonal (middle), and rhombic (bottom) geometries. The counting scheme to find N_S is indicated for the triangular GQDs. The two sublattices, A and B , are colored red and blue, respectively.

sublattice. There are $N_s - 1$ degenerate states at $E = 0$ for zigzag terminated triangular GQDs [56].

The probability densities $|\Psi|^2$ of these triangular zigzag GQDs at $E = 0$ localize at the edges, similarly to the case of zigzag GNRs discussed in section 1.1.2. The optical absorption spectra of GQDs may be determined with Fermi's golden rule, as demonstrated by [57]

$$A(\omega) = \sum_{i,f} |\langle \Psi_f | \hat{P} | \Psi_i \rangle|^2 \delta(\hbar\omega - (E_f - E_i)). \quad (1.13)$$

Here, $\langle \Psi_f |$ ($|\Psi_i\rangle$) is the wave function of the final (initial) state, and \hat{P} is the perturbation by the incident wave that may be linearly approximated. Therefore, the expression $|\langle \Psi_f | \hat{P} | \Psi_i \rangle|^2$ denotes the transition matrix element from the initial state with the energy eigenvalue E_i to the final state with the energy eigenvalue E_f when excited with a photon with the energy $\hbar\omega$. Note that the calculations discussed up to this point were carried out in the single electron picture. Interactions between electrons and between electrons and holes are neither captured by the tight-binding model nor by the continuum model. Corrections due to the formation of excitons from electrons and holes lead to a shift in the absorption spectrum [15, 57].

Multilayer GQDs

Stacking layers of GQDs results in multilayer GQDs. There are many possible configurations for stacking two graphene layers, with AB or Bernal stacking as the most common [58]. Compared to the tight-binding Hamiltonian in monolayer graphene (see eq. 1.3), the Hamiltonian for multilayer graphene has an additional term for interlayer hopping [59]. The tight-binding Hamiltonian with the additional interlayer hopping terms that are greater than 0.2 eV reads

$$\begin{aligned} \hat{H} = & - \sum_{i,j,m} t(\hat{a}_{m,i}^\dagger \hat{b}_{m,j} + h.c.) - \sum_{i,m_1,m_2} \gamma_1(\hat{a}_{m_1,i}^\dagger \hat{a}_{m_2,i} + h.c.) \\ & - \sum_{j,m_1,m_2} \gamma_3(\hat{b}_{m_1,j}^\dagger \hat{b}_{m_2,j} + h.c.). \end{aligned} \quad (1.14)$$

Here, in addition to the terminology used in (eq. 1.3) m_1 and m_2 denote neighboring layers and $\gamma_1 = 0.4$ eV and $\gamma_3 = 0.3$ eV are the interlayer hopping energies. Multilayer GQDs with more than two layers up to the periodic limit are treated in *Paper IV*.

Experimental realizations of GQDs

The theoretical results for the energy spectra of GQDs are in good agreement with the findings from different experimental studies. For example, triangular GQDs with arm-chair edges possess a size-dependent emission wavelength that is in good accordance with theoretical calculations [60]. Often structures with mixed edges and imperfect geometries are encountered [61–63]. For GQDs with mixed edge types, a large share of zigzag edges seems to correlate with a smaller energy gap. Even metallic behavior was observed for predominantly zigzag terminated GQDs with sizes of 7–8 nm [61].

Furthermore, GQDs have been characterized as single photon sources at room temperature by measuring the second-order correlation function $g^{(2)}(\tau)$, which revealed photon anti-bunching at small time scales [64].

1.1.4 Carbon nanodots

Up to this point, only pristine systems were discussed. However, carbon nanoparticles synthesized for biomedical applications may contain considerable amounts of heteroatoms, show mixed edges, and incorporate different hybridizations of carbon. This heterogeneous class of colloidal nanoparticles is called carbon nanodots (CNDs). Carbon nanodots consist of a carbogenic core that may contain mixtures of sp^2 and sp^3 carbon as well as dopant atoms and a surface that may be decorated with functional groups and covalently bound small molecules.² For the sake of this thesis, we will treat GQDs and graphene oxide quantum dots as special cases of the more general group of CNDs, since they fit the definition stated above with the constraint that their carbogenic core predominantly contains graphitic carbon. CNDs may be considered as a hybrid material with properties of nanoscale semiconductors and molecules [67]. The following section will review the synthesis and modification pathways that determine the structure and properties of the CNDs.

Synthesis and Modification

The properties of CNDs depend heavily on their composition, which in turn is determined by the chosen synthesis route. Generally, the synthesis routes of nanostructures can be divided into two categories, namely *top-down* and *bottom-up* approaches. In top-down synthesis routes, nanostructures are cut or carved from the bulk material, as for example, in lithography techniques which are commonly used in semiconductor manufacturing. Top-down methods in CND preparation include arc-discharge assisted breakdown [14], laser ablation [68, 69], and electrooxidation [70, 71]. In bottom-up methods, on the other hand, nanostructures are assembled from smaller precursor molecules. Bottom-up techniques for the synthesis of CNDs include chemical vapor deposition [72, 73] as well as hydrothermal synthesis and solvent-free pyrolysis routes [26, 74]. Since they are of particular interest to the publications resulting from this work, the discussion will focus on solvothermal and pyrolysis methods. While exotic bioderived or waste compounds [75–80] were tested as starting materials in many reports with remarkable results, we will restrict ourselves to the discussion of well defined reactants. A common precursor molecule for bottom-up synthesis is citric acid which is often combined with nitrogen-containing molecules to yield N-doped CNDs [26, 74]. Other precursor molecules that were used as a carbon source instead of citric acid include sugars such as glucose [81, 82] or glucosamine³ [83] and also small aromatic molecules such as phloroglucinol [60, 84]. Doping with other elements like sulfur

²There is some ambiguity when defining the nanoparticle family of carbon nanodots. In some cases, for example, the general family incorporating carbon nanodots and graphene quantum dots is called carbon dots [65], while in other cases, the terms carbon dots and carbon nanodots are used interchangeably [66]. When consulting the literature, please be aware of this ambiguity.

³Also acting as a source of nitrogen.

using, for example, the amino acid cysteine [85,86] or phosphorous using, for example, diammonium phosphate [82], has also been performed by different groups. A variant of the solvothermal and pyrolytic bottom-up approach is the microwave-assisted synthesis of CNDs [87,88], which has some advantages over conventional implementations discussed before [89]. Microwave heating induces rotations in solvent molecules with a dipole moment, leading to an increase in temperature and is, therefore, also termed dielectric heating [90]. The most well known selling point of microwave-assisted synthesis over conventional techniques is the increased reaction rate [91]. Even though microwave chemistry has been an active field for almost 40 years, it is still debatable if the increased reaction rates are only due to dielectric heating or if other microwave-specific effects accelerate the reaction [89]. While convective or conductive heating of the reaction vessel generates a temperature gradient for finite reaction times, microwave heating produces a more homogeneous temperature distribution inside the reaction vessel [92]. Heterogeneous temperature distributions may lead to incomplete reactions resulting in unwanted by-products. This problem is intensified if the reaction vessel is scaled up to larger volumes, further favoring microwave heating over conventional heating techniques. Furthermore, commercially available laboratory microwave ovens allow for increased control over temperature, pressure, and transmitted power to achieve reproducible results.

A myriad of convenient post-synthesis modification pathways has been published that allow for increased control over the CNDs properties [93]. Due to the abundance of amino, hydroxy, or carboxy groups often encountered on the surface of CNDs, these nanoparticles are an excellent target for covalent modification. For example, carboxy groups on the surface of a CND may be used as a target to couple the nanoparticle with amino-terminated molecules, such as polymers with a terminal amino group [94], antibodies [95], or peptides [96]. These coupling reactions are often mediated by the reagents 1-Ethyl-3-(3-dimethylaminopropyl)carbodiimide (EDC) and N-hydroxysuccinimide (NHS) to lower the activation energy stepwise. First, EDC is added to the nanoparticle solution and reacts with the carboxylic group on the surface, leaving a highly reactive moiety. In the second step, NHS and the amino-compound are added to the solution. NHS then binds to the carboxy group on the nanoparticle's surface, replacing EDC in the process. The compound with a terminal amino bond may now covalently bind to the activated amino group, replacing the NHS molecule. The amino group and carboxylic group form an amide bond. This is a standard approach for grafting surfaces with proteins or other amino-terminated polymers [97]. Serap Üçlü from Laura Hartmann's lab also employed this strategy when conjugating the CNDs used in *Paper III* with amino sugars and amino terminated sugar oligomers. Other non-covalent modifications and loading techniques include π -stacking [94,98] and complexation [99]. Non-covalent modification pathways are of high interest for drug delivery applications (discussed in section 1.3) since their dissociation constant may depend on properties of the environment, such as the pH value [100].

Physicochemical Properties

Since the family of CNDs is quite inhomogeneous in structure and composition, it is possible to produce CNDs with a wide range of properties. Depending on the synthesis

route or via post-synthesis treatment CNDs that are hydrophilic [26, 74], hydrophobic [101], or even amphiphilic [102] may be produced. While particles with hydrophobic facets have some use cases in drug delivery [103], hydrophilic interactions with the environment are desirable in most biomedical applications. Currently, there are essentially four competing fluorescence mechanisms that have been identified in CNDs and are present to varying degrees depending on the composition of the nanoparticle [65, 104, 105]. These mechanisms are the quantum confinement effect, the effect of edge/surface states, crosslinking-enhanced emission, and the effects related to small fluorophores bound to the nanoparticle.

Quantum confinement is the dominant effect in CNDs with large sp^2 carbon domains. The extreme case of those CNDs containing only sp^2 carbon in the nanoparticle core are GQDs that were discussed in section 1.1.3. The absorption and emission wavelengths scale with the size of the sp^2 domains, ranging from the subnanometer scale corresponding to polyaromatic hydrocarbons [106] to diameters of almost 50 nm [107], making up the whole nanoparticle core. The relevant transitions are often labelled as $\pi - \pi^*$ transition and $n - \pi^*$ transition, which have been validated by simulations [108] and attributed to absorption peaks found in experiments [74]. The energy of the bonding π and antibonding π^* orbitals is determined by the size of the sp^2 domain, while n denotes the state of the free electron pair in an oxygen or nitrogen atom bound to the sp^2 domain. The presence of the n -state is an effect of doping the CND with heteroatoms. Generally, doping of CNDs is widely considered to have a significant effect on the fluorescence spectrum and the fluorescence quantum yield, especially if the heteroatoms are incorporated into the carbogenic core [67]. In multiple cases, CNDs have been reported to incorporate graphitic structures [109, 110], i.e., multiple stacked layers of sp^2 carbon domains. Stacking multiple layers of sp^2 carbon domains results in a redshift for an increasing number of layers [108, 111].

Edge and surface effects are the second major effect that influences the energy spectra of CNDs. The termination of the sp^2 carbon domains with zigzag or armchair edges modulates the energy spectra of the individual domains that are otherwise determined by quantum confinement, as discussed in sections 1.1.2 and 1.1.3. Furthermore, the decoration of the surface with functional groups also modulates the energy spectra of CNDs. For example, increasing the number of amino groups at the surface of a GQD leads to a reduction of the energy gap and, therefore, a redshift of the GQD's spectrum, as confirmed by Jin et al. [112] via ab initio calculations. The authors of this paper also experimentally observed that the functionalization of GQDs with amino groups leads to a pH dependence of the emission wavelength that can be linked to the protonation and deprotonation of the attached groups. It is reasonable to assume that this behavior also translates to the decoration with amino groups of the sp^2 carbon domains of other CNDs.

Crosslink enhanced emission (CEE) is the third effect that predominately plays a role in CNDs with a carbon core composed of crosslinked polymers, often referred to as polymer dots [113, 114]. The CEE in CNDs derived from the polymer polyethyleneimine (PEI), as described by Zhu et al. [115]. In this article, the authors identify weakly fluorescent amino-based structures as the origin of fluorescence. The fluorescence is

enhanced due to the reduction of vibration and rotation of these fluorescent centers, which the authors elaborated as the CEE.

Small molecular fluorophores that are either covalently bound to the CND or non-covalently associated have been identified as the source of the CND's fluorescence, especially of those that were synthesized with bottom-up approaches and employ citric acid as a precursor, and additional molecules such as urea, diethylenetriamine (DETA) or hydrazine as a nitrogen source by many recent reports [105, 116]. The synthesis of fluorescent citrazinic acid derivatives from citric acid and amines at relatively low temperatures was reported more than a century ago [117, 118]. These fluorophores may also be generated at higher temperatures seen in bottom-up synthesis of the same reactants.⁴ Thus, it is crucial to consider purification techniques post-synthesis to remove potentially unwanted free by-products. Synergistic effects between molecular fluorophores that are likely to be bound instead of free in solution and the nanoparticle core were proposed by Schneider et al. [119]. In some cases, the isolation of the small fluorophore and the carbon dot was possible with considerable effort, which points towards a strong non-covalent association [120]. It was recently demonstrated that small molecular fluorophores and impurities at the surface could be removed via photobleaching, leaving highly photostable CNDs with fluorescence properties dominated by the carbon core [121].

The quantum yield of CNDs varies from single-digit numbers to extraordinarily high numbers of more than 98 %. CNDs often show excitation wavelength-dependent emission peak position and display a non-gaussian emission spectrum [122, 123]. Both the excitation-dependent emission wavelength as well as the asymmetric emission spectrum may either be explained by the heterogeneity of the CNDs in an ensemble, the presence of multiple emission sources inside of one CND or by time-dependent emission spectra [124]. The latter is related to the giant red edge effect (GREE), which was observed in graphene oxide [125] and later in CNDs [123]. When fluorescent particles are excited by incident photons, a dipole moment may be generated. If the particle is immersed in a polar solvent, the solvent molecules will rotate to minimize the energy of the system resulting in a redshift. Usually, the rotation of the dipole molecules happens much faster than the lifetime of the excited state, resulting in a constant Stokes shift. The GREE occurs when solvent relaxation happens on the same time scale as the fluorescence. With these prerequisites, the energetic difference between the state occupied by the electron and the ground state decreases time-dependently, which leads to a time-dependent increase in the emission wavelength on the time scale of the fluorescence process. The GREE is a reasonable explanation in the case of CNDs that share many similarities with graphene oxide in the structural features that may be relevant to their fluorescence behavior. CNDs that are associated with molecular fluorophores, on the other hand, tend to have an excitation wavelength-independent emission peak and high quantum yields [119].

⁴Xiong et al. [116] compiled an overview of potential molecular fluorophores that may be produced as a by-product in the bottom-up synthesis of CNDs from citric acid and different amines.

1.2 Biophysical fundamentals

This section presents the fundamental biophysical mechanisms that drive nanoparticle uptake into and distribution inside the cell and thereby thematically links section 1.1 with sections 1.3 and 1.4.

1.2.1 Endocytosis

Uptake of extracellular material may occur via different routes with different levels of complexity, reaching from simple diffusion to highly specific receptor-mediated entry mechanisms. This overview treats endocytosis as a generic term for pinocytosis, caveolin-, and clathrin-mediated endocytosis, as well as phagocytosis, which are sometimes treated as separate categories. Endocytosis may be specific or non-specific, but it is always a form of active cellular uptake that results in the cargo being encapsulated in a vesicle. The different endocytotic pathways introduced in the following paragraphs are illustrated in Fig. 1.4.

In **clathrin-mediated endocytosis**, a coat of proteins recruited from the cytosol on the inner leaflet of the membrane forms that may help induce a curvature in the membrane, forming an invagination around the cargo [126]. This process is named after the most prominent protein in this coat, clathrin, which assembles in a regular lattice around the pit and later in a cage-like structure around the vesicle [127]. Actin filaments polymerizing around the invagination drive it further inwards, cooperating with the protein coat [128]. The vesicle finally forms with the help of the scission protein dynamin that cuts off the vesicle [129, 130]. After the scission is complete and the endocytotic vesicle migrates away from the cell cortex, the protein coat is stripped away in a process called uncoating. Proteins recovered during uncoating may be recycled to the cytoplasm participating in other endocytotic events. It is to this point unclear if nucleation events that initialize a clathrin-mediated endocytosis event are triggered by a receptor binding event on the extracellular site or if nucleation occurs spontaneously and receptor-bound cargo is recruited to a nucleation site [126].

Caveolin-mediated endocytosis is promoted by caveolins, which are transmembrane proteins, and cavins, which are peripheral membrane proteins. Caveolae, which are lipid rafts enriched with cavins and caveolins, as well as cholesterol and sphingolipids, are the sites where caveolin-mediated endocytosis occurs. The density of caveolae varies considerably between cell types, which leads to different rates of caveolin-mediated endocytosis in different tissues [132, 133]. Caveolae were proposed to fulfill completely different functions, such as sensing of mechanical stress besides endocytosis [134], which might explain the varying availability of caveolae between different cell types. The protein dynamin-2 may bind to the neck of the caveolin-coated pit to induce the scission from the plasma membrane resulting in the formation of an endocytotic vesicle [133]. Both clathrin- and caveolin-mediated endocytosis produce endocytotic vesicles with sizes between 50 nm and 120 nm that may fuse with endosomes and potentially be triggered by receptor binding events [126, 134].

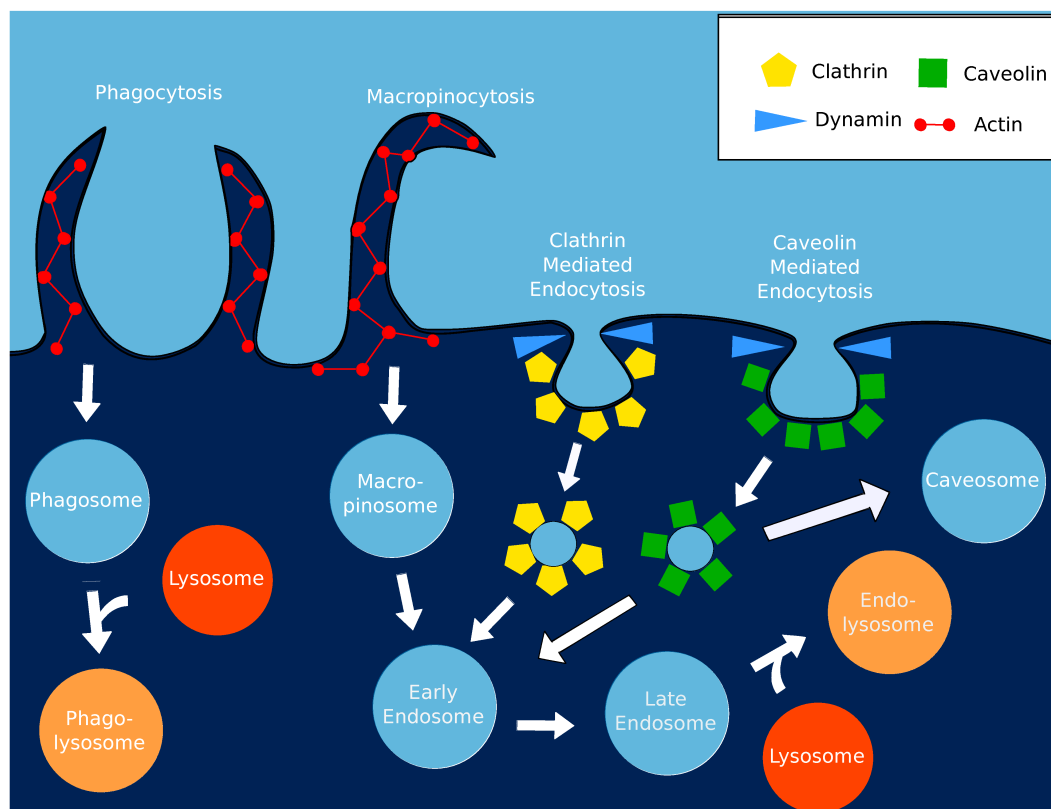


Figure 1.4: Schematic illustration of different endocytosis pathways and the cellular fate of the corresponding vesicles. This figure is based on an illustration from [131] that is distributed under a CC BY 4.0 license by MDPI.

Phagocytosis is a process in which particles larger than 500 nm are actively engulfed in membrane protrusions and internalized. While phagocytosis may be observed in a multitude of different cell types, only a subset of cells display a high frequency of this uptake process and can therefore be described as professional phagocytes, which include monocytes, macrophages, and neutrophils [135]. Recognition of the cargo via a receptor triggers the phagocytotic event. During the formation of the phagosome, the cortical actin forms membrane protrusions around the cargo, and the composition of the membrane changes, altering the local mechanical properties [135, 136].

Macropinocytosis is an endocytotic process where large amounts of extracellular fluid and the solved particles within are incorporated and usually happens in response to the presence of growth factors [137]. Growth factor receptor activation leads to increased actin polymerization on the cell's cortex, which in turn leads to the emergence of "ripples" on the cell surface. While most of these ripples are short-lived, some may develop into protrusions that may fold back on and fuse with the plasma membrane [138, 139]. The size of macropinocytotic vesicles is heterogeneous but is generally considered larger than 200 nm [137, 138].

Some factors have been identified to influence the uptake of small particles, which may be biomacromolecules, viruses, or nanoparticles, into cells via endocytosis (as reviewed

in [140–142]).⁵ The **size** of the cargo particle plays a role in the uptake efficiency, but the exact character of the size dependence has to be treated on a case-by-case basis. For example, Chithrani et al. [143] performed an uptake experiment with spherical gold nanoparticles of diameters between 10 nm and 100 nm. They found a maximum in the number of particles per cell for a diameter of 50 nm. For clathrin-mediated endocytosis, a maximum in cellular uptake for medium-sized particles makes sense since the particle binding to multiple receptors at once and thus inducing a natural curvature that is commensurate with the clathrin lattice on the clathrin-coated pit would reduce the free energy and thus assist the uptake naturally [144]. For other uptake mechanisms, different size dependences are to be expected. The particle **shape** is the second geometric factor besides the size that governs the uptake rate. In the study of Chithrani et al. referenced earlier [143], rod-like gold nanoparticles were also employed, and their uptake was compared with the uptake of the spherical particles. They found that the spherical particles, in this particular case, showed a higher uptake than the rod-like particles. On the other hand, the review of Toy et al. [145] points out that oblate or rod-like functionalized nanoparticles with a sufficiently high ligand density present a larger area for interaction with the cell surface compared to spherical particles and may therefore lead to an increased uptake rate. Different **surface properties** of particles have been identified that impact the uptake rates of particles, namely the effective surface charge [146, 147], the presence of ligands [148, 149], and the affinity of the particle’s surface to assemble a protein corona [150] from the surrounding medium. In general, particles with a positive surface potential experience an attractive interaction with the negatively charged cell membrane [146, 147]. However, particles with a negative surface charge have been, in some cases, shown to also have an increased uptake rate compared to neutral particles since aggregation of the particles may be inhibited by the repulsive electrostatic interaction [151]. A layer of proteins from the medium may assemble around a particle, hiding the core material from the environment, which is named protein corona. The assembly of the protein corona can be modulated by the introduction of spacer molecules or a variation of surface properties that influence the interaction with proteins in the surrounding medium [141, 150]. Lastly, the uptake of particles is modulated by the presence of ligands that may bind to receptors on the cell or grafting with functional groups that modulate the interaction with the cell surface. This is the primary strategy viruses employ to facilitate uptake. For example, influenza viruses bind via the protein hemagglutinin in their viral envelope to the sugar sialic acid, which is present on the surface of the target cell [152]. After binding to the cell surface, the virus is taken up via endocytosis. This strategy is also employed in nanoparticle systems linking antibodies [94, 149, 153], lectins [154] or carbohydrates [148, 155] to nanoparticles to facilitate uptake by the cell. Relatively recent discoveries hint towards another factor that may influence the endocytosis rates of a particle, namely the presence of a second particle species that enables the entry of the first one. This second particle type that gets enabled by the first one is called bystander cargo or bystander nanoparticle [156–158].

⁵ Please note that most of these factors are interrelated and depend on the examined cell type, the medium, and the core material of the particle. Therefore, the following statements are not to be taken as general rules but must be considered on a case-by-case basis.

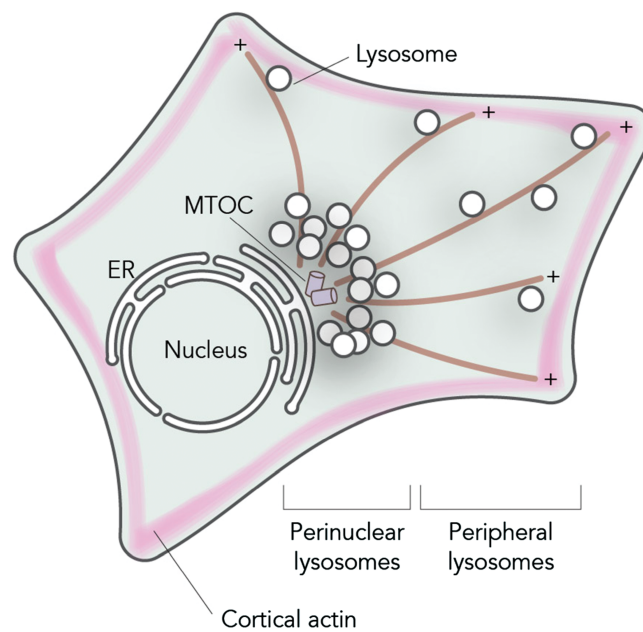


Figure 1.5: Subcellular lysosomal distribution and interplay with the cytoskeleton. An immobile perinuclear pool of lysosomes forms around the microtubule organizing center (MTOC) near the endoplasmic reticulum (ER). The microtubules possess a polarity, in the sense of a preferred direction, as indicated by the (+). The motor proteins kinesin (- to +) and dynein (+ to -) can only actively transport the lysosomes in their specialized direction along the microtubules. Due to the active transport along the cytoskeleton, the peripheral lysosomes are more mobile than the lysosomes in the perinuclear pool. Lysosomes on the cell's cortex are positioned via myosins along the actin cytoskeleton. This figure was reprinted from [159] and is distributed under a CC BY-NC 4.0 license by Wiley.

1.2.2 Lysosomal transport

Lysosomes are vesicles with sizes varying from under 100 nm up to more than 1 μm [160] that, among other functions, play a major role in cargo degradation [161,162], but also signal transduction [163], membrane repair [164,165] and antigen presentation [166]. To fulfill these functions at different locations in the cell, lysosomes are transported along the cytoskeleton via motor proteins [159,167,168]. After endocytosis, the endocytotic vesicles fuse with early endosomes that mature into late endosomes and may then fuse with or further mature into lysosomes, which can be considered the final destination for endocytotic cargo with no otherwise predetermined purpose. Organelles further down the endo-lysosomal pathway become increasingly acidic from around pH 6.5 in early endosomes [169] to pH 4.5–5.0 in lysosomes [162,170,171]. The low pH, in combination with the presence of acidic hydrolases, allows lysosomes to break down proteins and other biomolecules into their constituent building blocks [172]. Regarding their motion, the ensemble of lysosomes can be roughly separated into two pools.

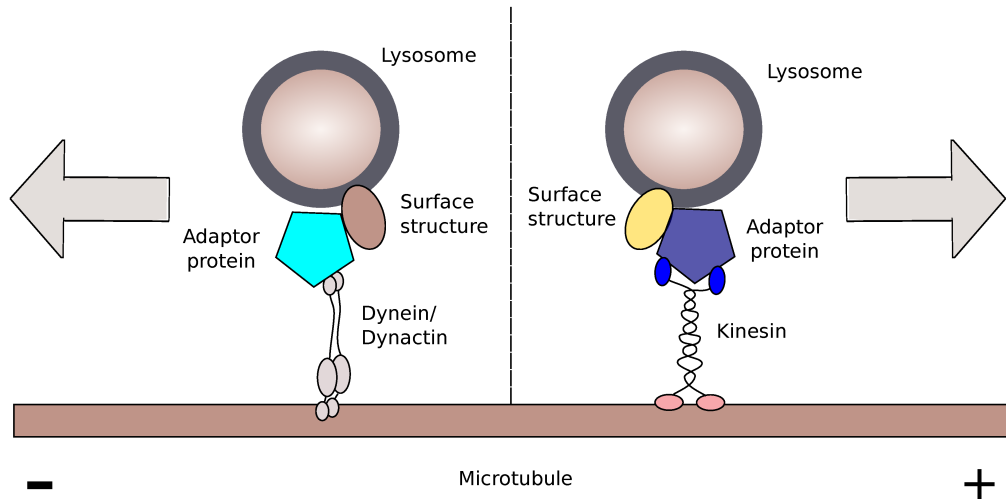


Figure 1.6: Interplay of adaptor proteins with molecular motor proteins and the lysosome. The + and - indicate the polarity of the microtubule, which is relevant for the motor proteins since they are only capable of transport in one specific direction. This figure is based on an illustration from [159] that is distributed under a CC BY-NC 4.0 license by Wiley.

In the perinuclear region around the microtubule organizing center, a pool of immobile lysosomes is formed, while the second pool in the periphery of the cell consists of fast-moving lysosomes [159], as depicted in Fig. 1.5. The positioning of lysosomes in the perinuclear cloud is controlled by contact sites in the endoplasmic reticulum (ER) membrane [173] and lysosomes in this pool may fuse with autophagosomes to form auto-lysosomes or transition back into the pool of mobile lysosomes [159, 174]. Lysosomes in the periphery are actively transported via specialized motor proteins that are recruited from the cytoplasm that bind via scaffolds to the lysosomal membrane, as illustrated in Fig 1.6. Microtubules possess a polarity with the two motor protein families, kinesin and dynein, mediating anterograde and retrograde transport, respectively [159, 167, 168]. Actin fibers on the borders of the cell membrane govern transport over the cell's cortex via myosin motor proteins [159, 164].⁶ When lysosomal cargo is secreted into extracellular space, lysosomes interact with the cortical actin mesh [159, 164]. In tracking experiments, the lysosomal motion appears to follow a stop-and-go-pattern, which is explained by the appearance of obstacles in the way of the vesicle, such as organelles or crossings in the cytoskeleton and the exchange of motor proteins [175]. This behavior is captured by a Lévy flight, which is an isotropic random walk with a heavy-tailed distribution of jump distances [176–178]. Lévy flights also capture common foraging patterns of animals [176], which might explain why vesicles may benefit from this transport characteristic while searching for specific targets.

⁶Non-cortical actin also plays a role in the transport of vesicles from the endo-lysosomal system [159].

1.3 Biomedical applications of nanoparticles

1.3.1 Fields of biomedical applications of nanoparticles

Nanoparticles have been applied in a wide range of therapeutic or diagnostic problems. The following paragraphs will give a brief overview of possible fields of application for nanoparticles related to biomedicine.

Fluorescence labeling with bioconjugated nanoparticles

Fluorescent nanoparticles may be used to label intracellular structures for microscopy or surface antigens for fluorescence-based assays. Semiconductor quantum dots conjugated with antibodies are well-established and commercially available fluorescence probes in flow cytometry. The striking advantages of quantum dots over conventional organic fluorochromes are the limited spectral overlap and brightness that allow for highly sensitive multicolor analyses [6]. Furthermore, a wide range of quantum dot species with different emission spectra may be excited with a single laser. These multiplexing capabilities, combined with superior photostability compared to conventional fluorophores, are also beneficial for long-term multicolor microscopy [4, 5] and particle tracking measurements [7]. While quantum dots show many beneficial features, they also possess detrimental properties compared to conventional fluorophores in some applications, such as their large size [179] and potential toxicity [5]. Blinking of quantum dots is often seen as a drawback and suppressed via surface passivation, which in turn increases the size of the quantum dot [180, 181]. While intrinsic blinking complicates the application of quantum dots in single particle tracking, it enables the use of quantum dots as an excellent fluorescent probe for specific super-resolution microscopy techniques [182, 183].

Drug delivery with nanocarriers

A drug delivery system refers to an object that controls the spatial and temporal release, as well as the rate of release, of a drug inside the body [184]. This, if done effectively, results in increased safety and efficacy of the therapeutic agent. In the context of nanomedicine, formulations of a drug delivery system include a nanoscale system as a carrier, which is loaded with a therapeutic agent. Nanoparticle-based drug delivery systems may help overcome barriers on different length scales, from systemic transport to targeting of individual organelles, and may even enable solutions in personalized medicine [185]. Great candidates for such systems are lipid nanoparticles and polymeric nanoparticles, but also, inorganic nanoparticles have been employed beyond proof-of-concept studies. In fact, nanoparticles of all the before mentioned categories are already part of FDA-approved formulations [185, 186]. Especially for cancer chemotherapy formulations that reduce the effects of the drug in off-target locations and therefore minimize the adverse drug reaction are desperately wanted.

Targeting of tumor tissue may be facilitated passively or actively. Passive targeting exploits the so-called enhanced permeability and retention (EPR) effect [187], due to which macromolecules and large particles naturally accumulate in solid tumors while small molecules are cleared from the tissue. Factors contributing to the EPR effect are the massive irregular neovascularisation, the expression of inflammatory factors, and the lack of efficient lymphatic drainage in tumors [188]. Furthermore, passive targeting strategies also aim to prolong the time a drug persists in circulation before being eliminated by the system [2, 189]. Early examples of passively targeted drug delivery systems are Doxil[®] [2] and Caelyx[™] [190], which are both formulations based on PEGylated nano-liposomes loaded with the drug doxorubicin. They have been successfully applied in the treatment of different tumor diseases, such as ovarian cancer and multiple myeloma while reducing systemic toxicity compared to free doxorubicin in some cases [186]. Nonetheless, is the success of nanoparticle-based formulations that exploit the EPR effect still an open topic of debate. In many cases, they do not show an increased efficacy compared to the free drug, and while reducing the systemic toxicity, they are sometimes the cause of new adverse drug reactions [191]. Notably, many successful passive-nanoparticle based drug delivery systems fail the translational step from proof-of-concept to clinical application [191, 192]. Thus, the need for improved drug delivery technologies does persist. Alternatively to passive targeting, the nanoparticle may be functionalized to employ a strategy of active targeting, conjugating the nanocarrier with antibodies, carbohydrates, or peptides [185]. As discussed in section 1.2.1, particles decorated with specific molecules may trigger endocytotic events that could, in turn, facilitate cell-specific uptake similar to the entry mechanisms used by viruses. Apart from modulating cell-specific uptake, drug delivery systems may also be tuned to steer their intracellular location [193] or to overcome biological barriers on a systemic level [194, 195].

Apart from drug delivery, other delivery protocols may be employed using nanoparticles. Most notably, the formulations of the mRNA vaccines from BioNTech [196] and Moderna [197] against Covid-19 include PEGylated lipid nanoparticles to encapsulate the mRNA [198]. Further applications of polymer and lipid nanoparticles as carriers for cancer vaccines and in the delivery of genome editing constructs are currently being tested [185].

Intracellular sensing with nanoparticles

Nanoparticles may also be employed as nanoscale sensors capable of measuring properties inside living cells [9]. The interaction with the environment may alter the luminescence of nanoparticles. Therefore, it is convenient to indirectly measure a physical quantity by detecting changes in a particle's luminescence lifetime or amplitude. One example of intracellular sensing with nanoparticles is nanothermometry. It has been demonstrated that changes in temperature could be correlated with changes in fluorescence intensity [199], fluorescence wavelength [200], or luminescence lifetime [201, 202] of nanoparticles.

Another branch of intracellular sensing is the application of nanoparticles as chemical sensors, which has already been demonstrated with gold nanoparticles [203], semicon-

ductor quantum dots [204], and carbon nanotubes [205], among others. Carbon nanotubes (CNTs) for instance, may be functionalized with different polymers or biomacromolecules to obtain a dependence of their fluorescence intensity or wavelength on the concentration of a specific analyte [205]. Therefore, CNTs may be used as nanoscale chemical sensors to recognize molecules such as neurotransmitters [206] or hydrogen peroxide [207]. The photometric determination of the local pH value is a very specialized type of chemical sensing that has been demonstrated many times [208–211].

1.3.2 Biomedical applications of carbon nanoparticles

CNDs (see section 1.1.4) may be engineered to have a wide variety of beneficial properties for biomedical applications, which include good solubility in water, low toxicity [110] and photostability [212, 213]. CNDs are, at least to some extent, usable in all categories of biomedical applications presented in the previous section. There has been an overwhelming amount of publications on this topic in the last decade, and due to the variety of possible CND preparation and modification methods resulting in different physicochemical properties, the results may seem to contradict each other in part. Please keep in mind that extreme care should be taken in the attempt to generalize any of the results to all CNDs. Nevertheless, the following sections are intended to provide an overview of the state of biomedical applications of CNDs to present a context for discussing the results of this work.

Toxicity and systemic distribution

Across the board, ultrasmall, hydrophilic CNDs show good biocompatibility and low toxicity in primary human cells [110, 214], cell lines [215–218], and on a systemic level [216, 217, 219, 220]. Needless to say, the toxicity of CNDs, as for all substances, is concentration dependent, and low toxicity refers to reasonable concentrations necessary for the respective application. Though, there are some cases where the toxicity of CNDs is increased compared to the general case.

The contributing factors to increased toxicity on a systemic level of CNDs presented below have been reviewed by Truskewycz et al. [221] and include hydrodynamic sizes above 6 nm, a highly positive surface charge [222] and photodegradation [223] or the generation of reactive oxygen species (ROS) [38] as a response to prolonged irradiation. Nanomaterials must be eliminated from the system via renal or hepatic excretion and not accumulate in the body over extended periods of time. The increased toxicity of larger CNDs and highly charged CNDs on a systemic level was linked to the reduced effectiveness of renal excretion [221]. Particles with a size of more than 6 nm cannot pass the glomerular basement membrane effectively, and charged particles are hindered by the negatively charged glycocalyx of the epithelial podocytes to directly pass to Bowman’s space, which impedes renal excretion, as pointed out by Truskewycz et al. Furthermore, CNDs with a positive surface charge may disrupt the endo-lysosomal system, even enter the nucleus, and interfere with the nuclear machinery, which will be discussed in the following subsection in greater detail. This may also contribute to the increased toxicity of CNDs with a positive surface charge [222]. Exposure to

light may result in cytotoxic behavior of CNDs. Liu et al. [223] showed, with a transcriptional analysis of cells exposed to photodegraded CNDs, that substances resulting from the photodegradation of their CNDs showed significant toxicity. Furthermore, the generation of ROS as a response to continuous excitation was observed for some types of CNDs [37, 38]. ROS are highly reactive oxygen-containing molecules that include hydrogen peroxide H_2O_2 , the superoxide anion O_2^- and singlet oxygen $^1\text{O}_2$ and are important for the redox-balance of the cell [224]. However, an excess of ROS is cytotoxic and may induce apoptosis [225].

Regarding the systemic distribution of CNDs, it is hard to identify properties that favor retention in specific organs. While ultrasmall CNDs are not expected to be subject to the EPR effect ⁷ due to their small size, other studies have shown significant retention in tumor tissue. Recently, Li et al. [229] demonstrated that CNDs derived from citric acid and 1,4,5,8-tetraminoanthraquinone show tumor-targeting behavior while showing negligible retention in other organs. Due to the small size (average diameter of 2.5 nm) of the CNDs employed in this study, renal excretion should have been unhindered. The uptake mechanism responsible for the accumulation proposed by the authors of this study is the transport via the large neutral amino acid transporter 1 (LAT1) prevalent in many types of tumors.

Subcellular distribution and targeting

Depending on their individual properties CNDs migrate to different terminal locations inside the cell [230]. The organelles that were found to accumulate specific types of CNDs, even without any functionalization post-synthesis, include the nucleus [231–233], the mitochondria [234], the endosomes and lysosomes [215], and the Golgi apparatus [235]. For the work discussed here, mainly targeting the nucleus and the lysosomes and the release from the endo-lysosomal pathway into the cytoplasm are of interest and thus will be discussed in greater detail in the following paragraphs.

The nucleus is a prominent target for therapeutic agents and of high interest for fluorescence labeling in basic research. Targeting the nucleus is especially challenging since multiple biological barriers must be overcome. First, the particles need to enter the cytoplasm, which makes the release from vesicles necessary. After that, the particles need to overcome the nuclear membrane, which may be, for example, achieved by diffusion through the nuclear pore complex (NPC). Passive diffusion through the NPC is only possible for very small particles, so even the diffusion of GFP with a diameter of 2.4 nm through the NPC is severely hindered [236]. Estimates for the size selectivity of the NPC are around 5 nm [237]. For larger particles, import into the nucleus is possible by the presentation of a nuclear localization sequence (NLS). An NLS is a short peptide sequence that binds to an importin and forms a complex, which is, in turn,

⁷The size ranges found in literature in which the EPR effect is at play vary significantly. While Kang et al reported a significant accumulation attributed to the EPR for spherical polyethylene glycol (PEG) particles smaller than 12 nm [226], other studies claim a lower size limit for the EPR effect of as high as 100 nm [227]. To put these findings into perspective, it may be pointed out that, besides the nanoparticles size, their shape and surface properties have also been linked to the efficiency of the EPR effect [228]. As previously discussed, the EPR effect remains a controversial topic.

transported through the NPC [238]. Furthermore, a positive surface charge has been shown to increase the interaction with the negatively charged nuclear membrane and increase the uptake rate into the nucleus [239]. Efforts have been made to functionalize CNDs with an NLS [33] or amphiphilic groups [32] to facilitate nucleus targeting beyond their inherent capabilities. Wang et al. [240] attributed the accumulation in the nucleoli they observed, which are a nuclear substructure, to the positive surface potential facilitating an interaction with the negatively charged nuclear regions and the small size (around 2 nm) of their CNDs, allowing for easy penetration of the larger nuclear pores.

There are essentially two different strategies for lysosomal targeting [241]. The first one is via the default pathway of material that is taken up via endocytosis (see section 1.2.1). The cargo inside endocytotic vesicles is transported to endosomes that may mature to or fuse with lysosomes. This pathway may be exploited by nanoparticles that are taken up via endocytosis and are unable to leave the lysosome on their own. This was demonstrated with fluorescently labeled dextran [242, 243], a polysaccharide known to be taken up via different endocytotic processes depending on its size and terminally end up in the lysosome. The distribution of some carbonaceous nanoparticles has also been explained by this pathway [241]. The second pathway to the lysosome is mainly relevant for small molecules. Since lysosomes are acidic organelles, weakly basic moieties of molecules with lipophilic facets will get protonated, which may lead to the sequestration of these molecules in the lysosome [244]. Functionalization of CNDs with lipophilic amines resulted in lysosomal targeting in past studies [245, 246]. The exit of entrapped nanoparticles from the endo-lysosomal pathway is described as endosomal escape and may be facilitated by a positive ζ -potential or rather many proton-accepting groups. The strategy for endosomal escape that utilizes proton-accepting groups is called the proton sponge effect (illustrated in Fig. 1.7 [247, 248]). The buffering effect of cationic particles or polymers, removing protons from the endosome, triggers the V-ATPase pump in the endosomal membrane to facilitate an influx of H^+ to maintain the desired pH value that will, in turn, lead to a Cl^- influx [247]. The increased intra-endosomal concentration of Cl^- results in an increased osmotic pressure. Besides osmotic pressure, factors that may play a role are polymer swelling [249] and the destabilization of the endosomal membrane [250]. This may ultimately lead to penetration of the leaky vesicle membrane or even endosomal rupture [251]. This strategy of endosomal escape based on proton-accepting groups has been recently applied to release CNDs into the cytoplasm [252, 253].

Proof of principle applications

When the questions of biocompatibility, uptake, and distribution are answered, CNDs may be applied in proof of principle experiments that demonstrate their applicability in biomedical use cases. One of the most straightforward applications of fluorescent nanoparticles that target specific organelles is the staining of those organelles for imaging. The capabilities of CNDs to target specific subcellular structures have been outlined in the previous section and will thus not be addressed extensively here. Advantages that CNDs may have over other conventional fluorophores, depending on

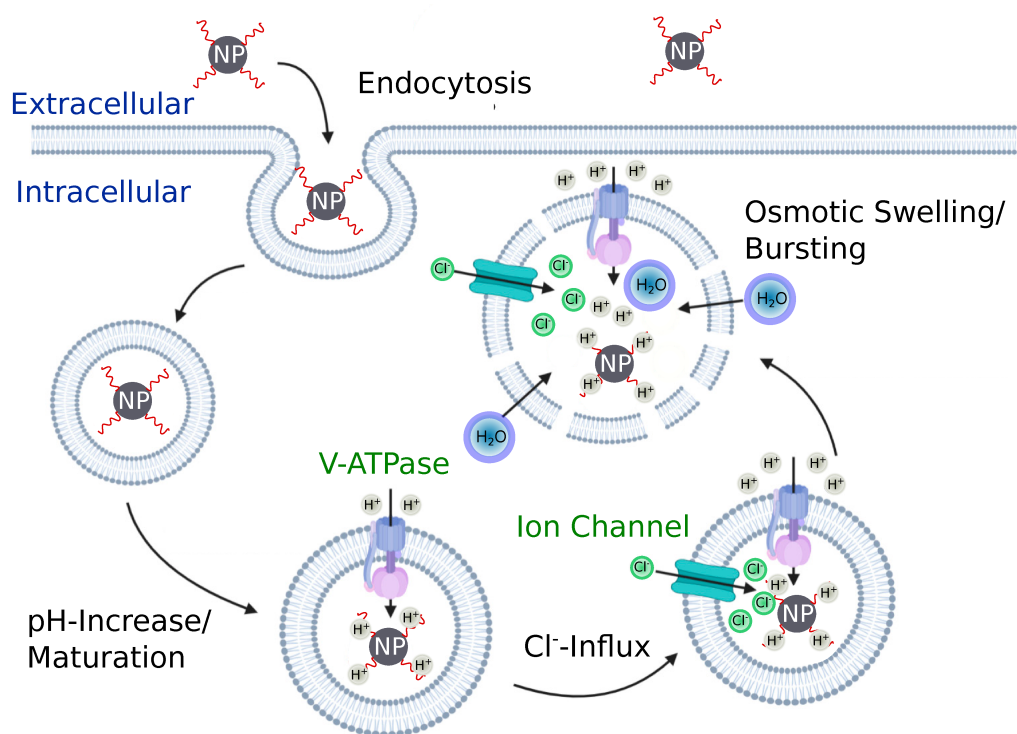


Figure 1.7: Schematic illustration of the endosomal escape facilitated by the proton sponge effect. Adapted and modified from [254], which is distributed under a CC BY 4.0 license by MDPI.

their synthesis route, include a wide cross-section for two-photon excitation [218,255], emission that can be tuned to the near-infrared region [216], and excellent photostability [121,256]. While these are all properties that CNDs share with semiconductor quantum dots, CNDs are considerably smaller and less toxic. A disadvantage of most CNDs, compared to semiconductor quantum dots, is the broad emission spectrum, which hinders applications in multicolor imaging due to crosstalk. CNDs have also been applied in single particle tracking experiments, as demonstrated by Wang et al. [257] in a membrane receptor tracking study. Due to their small size CNDs only minimally interfere with the motion of the structure they are attached to, which might be an advantage over larger single-particle tracking probes.

CNDs have also been used in first experiments that illustrate their potential as vehicles in drug or gene delivery and as therapeutic agents in experimental tumor therapies. PEI-functionalized GQDs have been successfully employed in mRNA delivery, facilitating a successful transfection [34]. Drug delivery of doxorubicin with CNDs has been facilitated on multiple occasions [32,33]. In these cases, the drug doxorubicin was loaded on the CND non-covalently via π -stacking. On a systemic level, the tumor-targeting properties of CNDs that are taken up via LAT1 have been demonstrated in human tumor xenografts in mice, as discussed above [229]. The generation of ROS may be used therapeutically in a process called photodynamic therapy which was also demonstrated with CNDs as a so-called *photosensitizer* [37,38]. Via local excitation of the CNDs administered to the body, the generation of ROS can be confined to regions

where oxidative stress is beneficial for the therapy. The excess of ROS in these regions may trigger autophagy or necrosis. Similarly, CNDs have also been employed in photothermal therapy as photothermal transducers [216, 255]. Here, the photothermal transducer converts the optical excitation energy to a large share into vibrational energy transferred as heat to the environment, resulting in a local rise in temperature [258]. Photosensitizers and photothermal transducers that absorb in the near-infrared region are especially useful for photodynamic and photothermal therapy. Since the optical window of biological tissues, where light sees only little absorption, is in the near-infrared region [259], minimally invasive therapy can be realized with particles that absorb in this region.

Similar to their semiconductor counterparts CNDs have also been used as *in vitro* and *in vivo* photometric nanosensors [22, 23]. This includes applications in temperature [24, 25], pH [26–29], and chemical sensing [30, 31] in biological environments. In conjunction with intracellular targeting, as discussed in the previous subsection, CNDs may be engineered to measure properties even in specific organelles or cellular compartments. This has been demonstrated by applying functionalized CNDs as FRET-based radiometric sensors for the prominent ROS H_2O_2 in mitochondria [31] or in the photometric measurement of the intra-lysosomal pH with lysosome-targeted CNDs with a pH-sensitive fluorescence [28, 29].

1.4 Quantitative analysis of subcellular distributions

As evident by the discussion in the previous section, knowing the target organelles of nanoparticles in biomedical applications is imperative. Comparisons between different samples can only be effectively conducted if quantitative and testable results are present. Since *Paper I* primarily focuses on the colocalization of subcellular structures with nanoparticles, the fundamental concepts related to this topic must be first introduced.

1.4.1 Colocalization

Colocalization experiments are potent tools to reveal the subcellular localization of fluorescent objects like GFP-tagged proteins or nanoparticles [260,261]. An object with a known subcellular location is stained fluorescently to reveal its location in the cell in the first channel of the microscopy image, and the fluorescent object of an unknown location is recorded in the other channel. If the fluorescence in both channels coincides or correlates spatially, the objects are colocalized. One method to evaluate this kind of data is a visual inspection of the overlay of both channels and looking for mixing colors. While this qualitative method is still applied in many cases, it is subjective and prone to a list of errors and biases [260]. Visual inspection is prone to variations in the intensity of the individual channels, leading to different mixing colors and, in turn, completely different results. A more objective way to evaluate these experiments is to employ approaches that quantify the degree of colocalization in an image. The first class of techniques discussed here is called pixel or intensity-based colocalization methods (reviewed in [260]). Here, the signals in both channels are compared or correlated for pixels that coincide spatially. The comparison or correlation with neighboring pixels in the complementary channel is disregarded entirely. One of the most simplistic metrics to evaluate colocalization is the Pearson correlation coefficient r , which measures the linear correlation between the pixel values [262]

$$r = \frac{\sum_{i=1}^n (a_i - \bar{a})(b_i - \bar{b})}{\sqrt{\sum_{i=1}^n (a_i - \bar{a})^2} \sqrt{\sum_{i=1}^n (b_i - \bar{b})^2}}. \quad (1.15)$$

Here, the covariance of the signals in the first (a_i) and the second (b_i) channel for each pixel i is divided by the product of the standard deviations of the signals in each channel. Please note that this coefficient is only applicable for linear relations between pixel intensities. The Pearson correlation coefficient can take a maximum value of 1 corresponding to complete colocalization, a value of 0 for no correlation, and a minimum value of -1 for complete exclusion. Midrange values are hard to interpret, and intensities from the whole image are considered with equal weight. This metric should be used to indicate if a high amount of colocalization is present in the sample and has only limited use in quantifying the amount of partial colocalization in an image [263]. The Manders colocalization coefficients [264] M_1 and M_2 are a more

suitable metric for evaluating partial correlation and may be understood as pixel-based colocalization quantifiers [263].

$$M_1 = \frac{\sum_i^n a_{i,coloc}}{\sum_i^n a_i}, \quad M_2 = \frac{\sum_i^n b_{i,coloc}}{\sum_i^n b_i}, \quad (1.16)$$

where $a_{i,coloc} = a_i$ if $b_i > 0$ and $a_{i,coloc} = 0$ if $b_i = 0$. Accordingly, $b_{i,coloc} = b_i$ if $a_i > 0$ and $b_{i,coloc} = 0$ if $a_i = 0$. Other thresholds than zero may be used to determine the colocalized signals $a_{i,coloc}$ and $b_{i,coloc}$. The coefficients M_1 and M_2 are good quantifiers of the overlap between both channels and may also be employed to distinguish between partial and complete colocalization. One drawback is that they are sensitive to noise since it distorts the correct determination of $a_{i,coloc}$ and $b_{i,coloc}$ [261].

While quantitative pixel-based methods are a significant improvement over pure visual inspection, they also have some drawbacks. The most notable flaw is that information from neighboring pixels that still contains information about the distribution of the objects is disregarded. Colocalization between objects that move significantly between the acquisition of the two fluorescence channels is, therefore, systematically underestimated. To address this issue, object-based colocalization methods have been developed. Here, objects are first extracted from the image by, for instance, segmentation or fitting. Then, the distribution of objects is analyzed or correlated. There is a wide range of object-based colocalization approaches, from simple overlap analysis [265] to complex techniques such as clustering by Voronoi tessellation [266, 267]. The object-based colocalization approach used in *Paper I* is based in spatial statistics, which will be introduced in the next section.

1.4.2 Spatial point pattern analysis

Spatial point pattern analysis is an area of spatial statistics and is extensively treated in [268]. A *spatial point pattern* is a dataset that contains the locations of a set of points together with additional information, such as the domain the pattern resides on and covariates that may relate to the point pattern and marks. Marks are attributes of each point in the dataset and may be either continuous or categorical. A dataset may, for example, contain the locations of trees in a forest. Here, the domain may specify the area that was considered, and a possible covariate may be given by the terrain elevation or the pollution level of the ground specified on the whole domain. An example of a categorical mark is the species of the tree, and the height of each tree would be an example of a continuous mark.

Point patterns may be generated by stochastic point processes. There is a vast theory on stochastic point processes that can not be adequately reviewed in this setting. Instead, only the most relevant topics to this work will be touched on here. The point process that generates complete spatial randomness (CSR) data is the homogeneous Poisson point process. The two defining properties are namely the homogeneity, describing that there is no preference for any location, and the independence of the densities from any arbitrary region of the outcome of any other. As a result, the expectation value of the number of points in an arbitrary region is proportional to its area A . If the region is divided into small areas of equal size, the number of points in

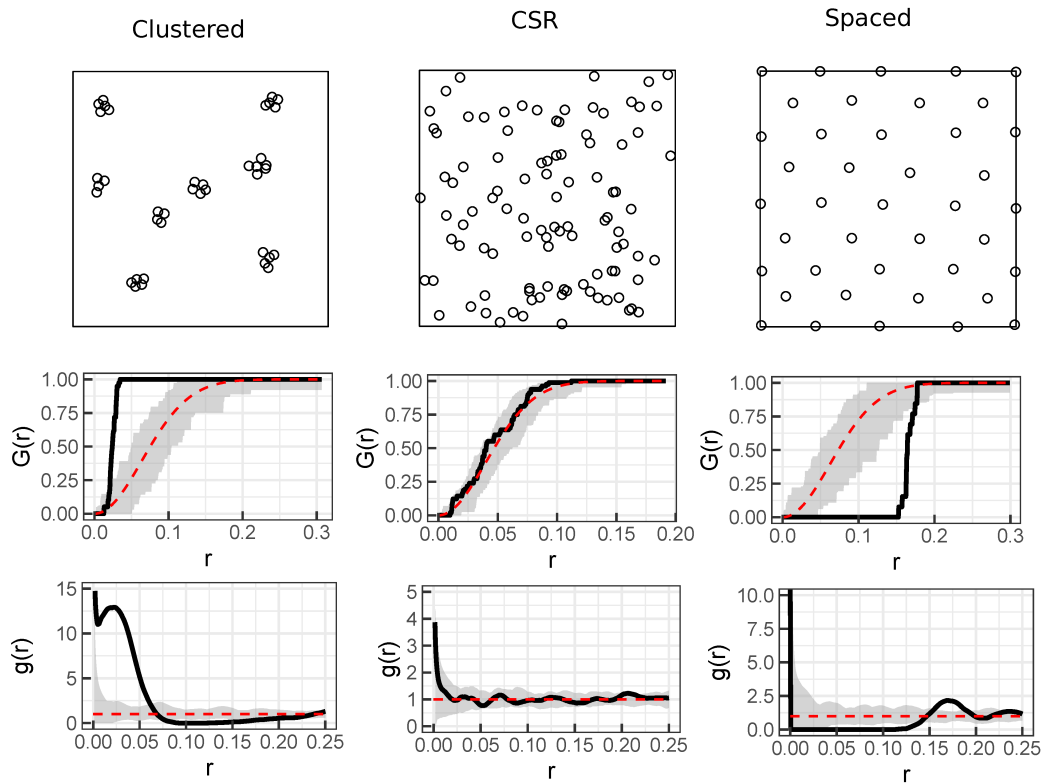


Figure 1.8: Spatial point pattern analysis with univariate spatial statistics. In the top row point patterns of manually generated clustered data (left column), complete spatial random data generated by a Poisson point process (middle column), and a manually generated spaced point pattern (right column) are shown. In the rows below, the nearest neighbor function $G(r)$ (middle row) and the pair correlation function $g(r)$ (bottom row) are displayed as solid black lines. The grey envelopes correspond to the 95 % least extreme cases of simulations of complete spatial randomness (CSR), while the dashed red line marks the mean values for the summary functions of the simulated ensemble.

those divisions should follow a Poisson distribution. In practice, this can be realized by sampling points from a uniform random distribution on the given domain. Similar to the definition of the homogeneous Poisson point process, other point processes may be defined, such as the Gibbs and the Cox model [269], which treat different realizations of non-independent stochastic point processes that result in clustered or spaced data.

To describe this kind of data, summary statistics functions are calculated. Summary statistics capture features of a point pattern, such as the spacing to the nearest neighbor or the local density. One of the most well-known summary functions is the K -function introduced by Ripley [270], which counts the number of points within a circle of radius r around every point in the point pattern. The empirical K -function is given by

$$K(r) = \frac{\Omega}{n(n-1)} \sum_{i=0}^n \sum_{j \neq i}^n \mathbf{I}\{d_{ij} \leq r\} b_{ij}(r). \quad (1.17)$$

Here, d_{ij} denotes the distance between the point with the index i and the point with the index j , n is the number of points in the point pattern, and Ω is the size of the domain the point process is defined on. The function $\mathbf{I}\{\cdot\}$ is the indicator function that takes a value of zero if its argument is false and a value of one if its argument is true, and $b_{ij}(r)$ is an optional boundary correction. The K -function indicates clustering or spacing in different distance regimes as a deviation from CSR, which can be summarized under the general term correlation. Data generated by a homogeneous Poisson process results in a parabolic K -function. Note that events at small distances affect the value of the K -function at large distances. To avoid the cumulative character of the K -function the pair correlation function may be introduced as

$$g(r) = \frac{K'(r)}{2\pi r}. \quad (1.18)$$

In practice, the empirical pair correlation function is calculated via an estimator like

$$g(r) = \frac{\Omega}{2\pi r n(n-1)} \sum_{i=0}^{n_1} \sum_{j=0}^{n_2} \kappa_h(r - d_{ij}) b_{ij}(r), \quad (1.19)$$

where $\kappa_h(r)$ is a rescaled smoothing kernel or via the numerical differentiation of the smoothed K -function. The nearest neighbor function $G(r)$ indicates what fraction of points have a nearest neighbor distance value of less than or equal to r . The estimator of $G(r)$ may be written as

$$G(r) = \frac{1}{n} \sum_i^n \mathbf{I}\{d_i \leq r\}, \quad (1.20)$$

where d_i is the nearest neighbor distance of the i -th point.

While summary functions contain information about the point pattern, they are, on their own, insufficient for statistical inference. Statistical inference may be conducted by testing a point pattern's summary functions against point patterns that are generated under a model assumption. One of the ways to perform such a test is called envelope testing. Essentially, the envelope is constructed via a Monte-Carlo simulation that generates point patterns under an assumption, the null hypothesis H_0 , and calculates a summary function for each simulated point pattern. For the ensemble of simulated summary functions at each distance r the $1 - \alpha$ least extreme points are used to construct the envelope for the hypothesis test, where α is the significance level. If the summary function lies outside of the envelope in a given interval $[r_1, r_2]$, the null hypothesis may be rejected for this interval with a p -value of $p = \alpha$. To give an example, if a measured point pattern is hypothesized to show spatially non-independent behavior in an interval $[r_1, r_2]$, H_0 may state that the point pattern was generated by complete spatial randomness. As a significance level, one might choose $\alpha = 0.05$. To test this hypothesis, 1000 simulations of a homogeneous Poisson process may be generated, and a suited summary statistics like the K -Function may be calculated for each simulated point pattern. For each r , the 950 points closest to the mean value of the summary function are used to construct the envelope. If the summary function of the measured data lies outside of the envelope within the interval $[r_1, r_2]$, H_0 may be rejected, and the measured data is different from CSR with $p = 0.05$. The behavior

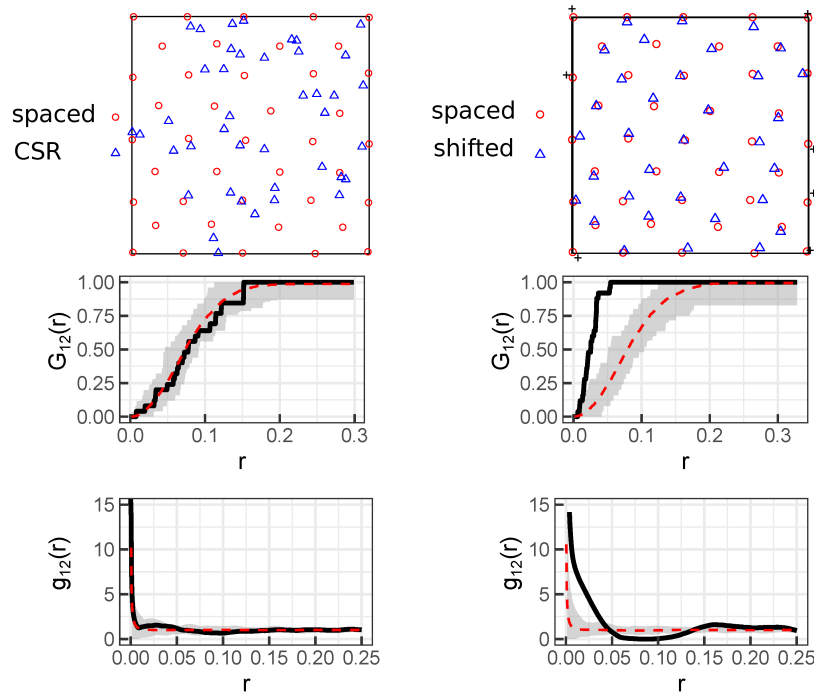


Figure 1.9: Spatial point pattern analysis with bivariate spatial statistics. In the top row marked point patterns are displayed. The left point pattern consists of manually generated spaced points with one categorical mark (red) and points generated by a Poisson point process with an other mark (blue). The point pattern on the right side consists of the same spaced pattern (red), and the individual points shifted by a vector sampled from a 2D Gaussian distribution (blue). In the rows below, the bivariate nearest neighbor function $G_{12}(r)$ (middle row) and the bivariate pair correlation function $g_{12}(r)$ (bottom row) are displayed as solid black lines. The grey envelopes correspond to the 95 % least extreme cases of simulations of complete spatial randomness (CSR) in the blue channel, while the dashed red line marks the mean values for the summary functions of the simulated ensemble.

of the summary functions for selected cases together with the envelopes for CSR is displayed in Fig. 1.8.

For colocalization problems, the centers of the measured distribution are considered as a marked point pattern, where the marks are categorical and indicate the channel of acquisition of each point. Spatial statistics has been successfully applied in object-based colocalization analysis before [271–273]. Similarly to the univariate summary functions introduced above, bivariate versions of the nearest neighbor function, the K -function, and the pair correlation function can be introduced. The bivariate summary functions give information about the correlation and distance between points with different marks. In the following paragraph, n_1 is the number of points in the first

and n_2 is the number of points in the second channel. The estimator for the bivariate K -function may be written as

$$K_{12}(r) = \frac{\Omega}{n_1 n_2} \sum_{i=0}^{n_1} \sum_{j=0}^{n_2} \mathbf{I}\{d_{ij} \leq r\} b_{ij}(r) \quad (1.21)$$

Analogously, the bivariate pair correlation function is given by

$$g_{12}(r) = \frac{K'_{12}(r)}{2\pi r}. \quad (1.22)$$

Indicating correlations between the points of different marks, $g_{12}(r)$ indicates clustering or spacing relative to CSR between points from the first and second channel. The estimator for the bivariate nearest neighbor function is defined as

$$G_{12}(r) = \frac{1}{n_1} \sum_{i=0}^{n_1} \mathbf{I}\{d_i^{[12]} \leq r\} b_{ij}(r). \quad (1.23)$$

Here, $d_i^{[12]}$ is the distance of the i -th point from the first channel to its nearest neighbor in the second channel. The function $G_{12}(r)$ indicates how many points originating from the first channel have a nearest neighbor distance of less than or equal to r . Similar to Fig. 1.8, the behavior of bivariate summary statistics for independent and correlated marked point patterns is illustrated in Fig. 1.9.

Chapter 2

Experimental methods

2.1 Carbon nanoparticles used in this work

2.1.1 Microwave-assisted synthesis

The CNDs used throughout the work related to this thesis have been prepared via a solvent-free microwave-assisted synthesis approach based on the method published initially by Qu et al. [74], which was adapted to a microwave reactor by Fasbender et al. [110]. This procedure uses citric acid and DETA as precursors for the bottom-up assembly of carbon nanodots. First, 210 mg anhydrous citric acid and 340 mg DETA are mixed by stirring in a microwave reaction vessel. The vessel is then sealed and placed in a CEM Discover microwave reactor to heat it to a target temperature of 180 °C with a maximum power of 300 W under continuous mixing with a magnetic stirrer. After a hold time of 150 s at the target temperature, the vessel is cooled by pressurized air to quench the reaction. The product is subsequently dispersed in DI water and placed in a 10 ml dialysis tube with a cut-off size of 100–500 Da and dialyzed against 2 l of DI-water. The water is exchanged three times within the timespan of 48 h. The dialysis product may be lyophilized for redistribution in the desired solvent or as a preparation for further modifications.

2.1.2 Modification via EDC and NHS

The modification of the as-synthesized nanoparticles bearing carboxylic moieties on their surface with molecules that are terminated with amino groups is often desirable. The application of EDC/NHS coupling chemistry was initially proposed and performed by Serap Üçlü from Laura Hartmann’s lab for glycofunctionalization of the CNDs from our lab. Meanwhile, Kai Lennard Fastabend also successfully applied this synthesis route to functionalize CNDs with PEI to yield CNDs with a positive ζ -potential. The quantities of the reactants vary based on the desired degree of functionalization and specific molecules. However, the general procedure with the amounts used by Kai Lennard Fastabend [274] for the conjugation with PEI is as follows.

First, 400 mg of EDC is dissolved in 2 ml water and mixed under continuous stirring with 4 ml of an aqueous CND solution with a concentration of 20 mg/ml in a 10 ml beaker. After 10 min, 400 mg NHS and the compound that should bind to the surface, which is, in this case, 40 mg corresponding to 50 μmol branched PEI-800, are added. The beaker is closed with sealing film to prevent evaporation, and the mixture is incubated for 24 h under continuous stirring and ambient conditions. The product is dialyzed afterwards to remove residual reactants and excess functionalization compounds. In the given case, this may be done with a dialysis of 10 ml of the product solution against 2 l of DI water with a 3.5 – 5 kDa membrane for 48 h with three water exchanges. The effectiveness of the process may be validated by Nuclear Magnetic Resonance (NMR) spectroscopy.

2.1.3 Characterization

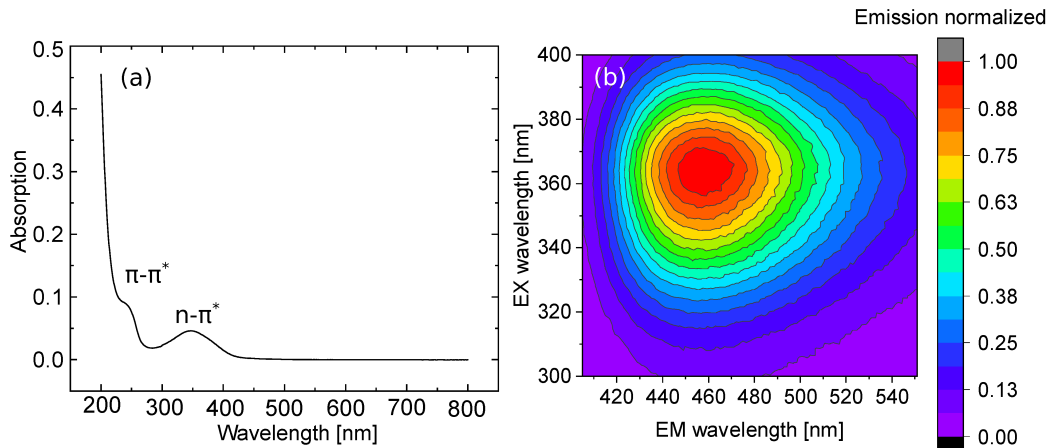


Figure 2.1: Optical spectra of the CNDs used in the work related to this thesis. (a) Absorption spectrum of a typical CND solution. The peak around 350 nm is commonly attributed to the $n-\pi^*$ -transition, while the shoulder around 230 nm is linked to the $\pi-\pi^*$ transition in the literature [74,108]. (b) 2D excitation-emission matrix of the CNDs at a concentration of 75 $\mu\text{g}/\text{ml}$.

The as-prepared CNDs have been extensively characterized regarding their composition and their structural properties by Stefan Fasbender in work related to his dissertation using transmission electron microscopy (TEM), atomic force microscopy (AFM), X-ray photoelectron spectroscopy (XPS), Raman spectroscopy, and CHN elemental analysis [110,275]. To briefly summarize his findings, the as-synthesized CNDs contain mass fractions of 40 % carbon, 8 % hydrogen, and 19 % nitrogen, as revealed by CHN elemental analysis. The remaining part was mainly attributed to oxygen, which is consistent with the XPS data. Raman spectroscopy revealed the existence of a pronounced G-band around 1596 cm^{-1} corresponding to graphitic sp^2 -carbon, a D-band that is attributed to disordered sp^2 -carbon and a D1-, D2-, and D3-band at (1375,

1195, 1264, and 1412 cm^{-1}) that may be attributed to different sp^3 -carbon containing groups [276]. Regarding the geometrical features of the particles, the CNDs showed an average diameter of 3.3 nm and possess a regular lattice with a hexagonal symmetry and a lattice constant of 0.223 nm according to TEM measurements on an amorphous carbon grid. AFM revealed that the height varies from 1 nm to 2 nm, corresponding to two to three layers of graphene. The absorption spectrum and an excitation-emission matrix of the nanoparticles are shown in figure 2.1. The particles show the typical pattern in the absorption spectrum of a peak that is attributed to an $n - \pi^*$ -transition around 350 nm and a shoulder around 230 nm that originates from a $\pi - \pi^*$ -transition according to the literature [74, 108]. The maximum emission at about 460 nm is found at an excitation wavelength of around 360 nm. The quantum yield, as determined by the method of Williams et al. [277], takes values around 25 %. The employed nanoparticles furthermore show a concentration-dependent emission wavelength, as shown in Fig. 2.2. While this may be at least in part attributed to the primary and secondary inner filter effect, this may also be partly attributed to the formation of aggregates, as previously hypothesized by Chen et al. [278].

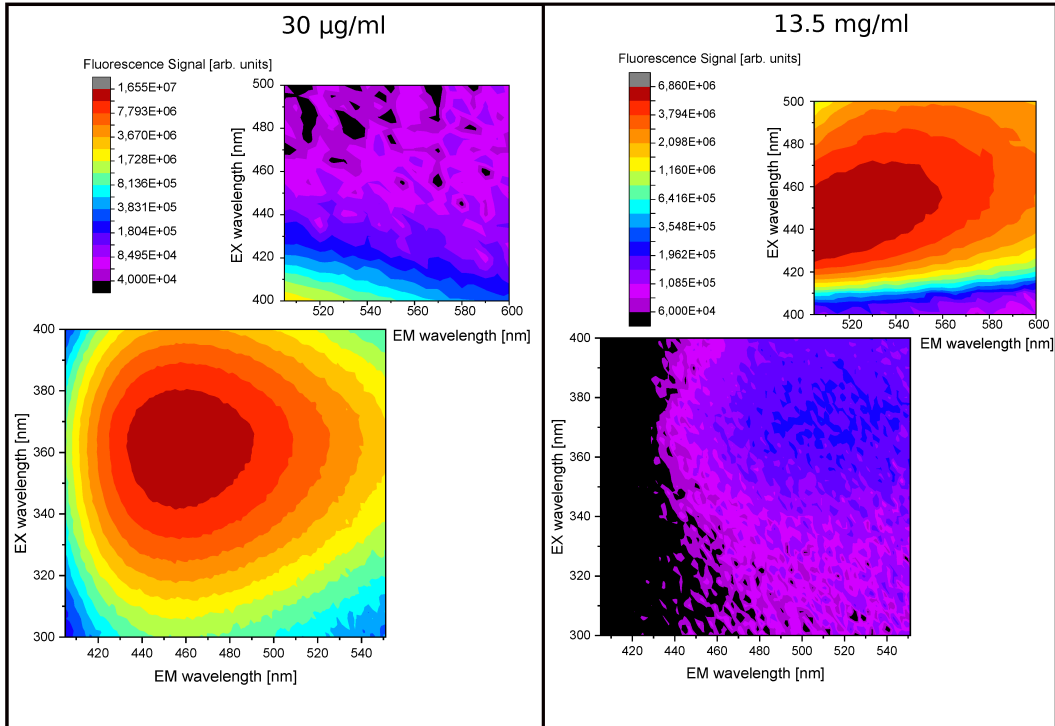


Figure 2.2: Concentration dependence of the emission spectra of the CNDs. Excitation emission matrices for CNDs at a concentration of 30 $\mu\text{g}/\text{ml}$ (left side) and 13.5 mg/ml (right side). The colorbar for the emission signal is scaled logarithmically. Please note that the emission peak shifts from blue to yellow when increasing the concentration.

2.2 Confocal fluorescence microscopy

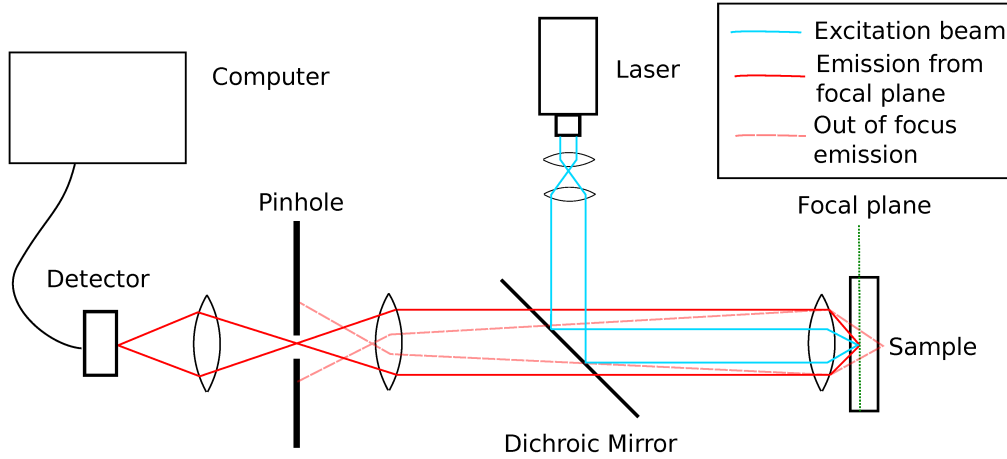


Figure 2.3: Beam path in the confocal set-up. The excitation beam is focused on the sample by the objective. Fluorescence light from the focal volume passes the pinhole, while out-of-focus light is blocked by the aperture. Light from the focal volume finally reaches the detector.

The confocal microscope was invented by Minsky, who filed the patent application in 1955 [279, 280]. Even though confocal microscopy is a basic technique that has been known and available in commercial set-ups for a long time, it will be briefly introduced here since it was used as a critical tool to explore the subcellular distribution of CNDs in the context of this thesis. Furthermore, Airy scanning microscopy, discussed in the next section and used in *Paper I*, is based on confocal microscopy. The instrumentation is reviewed in detail by other sources, for example, in Müller’s book [281], which this section is heavily based on. To understand the advantages of confocal laser scanning microscopes over traditional widefield microscopes, namely the ability of optical sectioning and a superior Signal-to-Noise Ratio (SNR), the confocal arrangement (depicted in Fig. 2.3) has to be discussed first. Light emitted from a laser is collimated and reflected by a dichroic mirror onto the objective lens, which focuses the excitation beam onto the sample. Fluorophores in the sample are excited by the incident light and reemit photons in random directions. The back-focus of the objective lens and the focus of the tube lens coincide in the confocal set-up. Due to this arrangement, beams from the sample-sided focus of the objective lens arrive at the tube lens as parallel beams and are thereby focused in the back-focus of the tube lens. An aperture (pinhole) is placed in the focal plane of the tube lens, blocking light paths originating from above and below the focal plane of the objective. The light is guided to a detector, commonly a photomultiplier tube or an avalanche photodiode in modern systems. The pinhole size determines the size of the Point Spread Function (PSF), which is the response of the optical system to a point-like entity in the focal plane. The confocal PSF is the product of the excitation and the detection PSF, and is, therefore, typically narrower than the excitation PSF found in comparable non-confocal microscopes. An

optical image $D(r)$ is constructed by the convolution of the confocal PSF $PSF_{conf}(r)$ of the system and the object $O(r)$. With the addition of noise $N(r)$, the equation for the construction of the image is given by [282]

$$D(r) = O(r) \otimes PSF_{conf}(r) + N(r). \quad (2.1)$$

Therefore, the width of the PSF directly impacts the resolution of the system. On the other hand, the size of the pinhole also limits the number of photons that reach the detector and contribute to the signal. A trade-off between a high signal (wide pinhole) and a high resolution (small pinhole) has to be made. While arguments for other pinhole sizes can be made under particular circumstances, a pinhole size of one Airy unit is considered a good standard value for imaging. With a confocal arrangement, only light from the confocal volume is collected. In order to obtain a complete image, scanning is required. While specimen scanning, i.e., moving the specimen in relation to the optical set-up, can be used, this method is relatively slow and may interfere with the integrity of the sample. With improvements in the manufacturing of optical systems, the method of laser scanning, i.e., moving the excitation spot over the sample, has become the standard technique for confocal image construction today. This scanning technique can be realized by implementing a pair of scanning mirrors in the beam path. The drawback of laser scanning compared to specimen scanning is that the beam path to the excitation spot is now off-axis, which may lead to optical aberrations. Alongside the demand for high-quality optics, this drawback can be minimized by placing the region of interest in the specimen close to the optical axis. The advantage of laser scanning is the improved scanning speed and the minimization of sample movement. An appropriate spatial sampling rate has to be chosen to avoid aliasing due to undersampling and overexposure, possibly leading to photodamage and unnecessarily prolonged total acquisition times due to oversampling. According to the Nyquist-Shannon-Theorem, the sampling rate has to be more than twice as high as the maximum signal frequency. To prevent aliasing artifacts, the scanning process must be adjusted so that more than two (a typical recommended value is 2.3) pixels fit inside the resolution limit. The exclusion of light from planes neighboring the focal plane allows three-dimensional imaging scanning microscopy.

2.2.1 Airyscan microscopy

The principle of Airy scanning may be used on a confocal set-up to enhance its scanning speed [283] or to perform super-resolution microscopy [284]. This section will focus on the latter and is heavily based on Weisshart's paper [282]. The Airyscan method employs a detector array arranged in a facet eye fashion (see Fig. 2.4), where the central detector element is placed on the optical axis and thus corresponds to the detector of a traditional confocal microscope. The non-central detector elements are displaced relative to the optical axis and therefore sample the point spread function at different positions simultaneously. Each detector element records a different mode of the same image by acting as an individual pinhole with sub Airy unit size. Taking the values of the ZEISS LSM 880, this allows imaging at a pinhole as small as 0.2 AU while collecting photon numbers comparable to a pinhole size of 1.25 AU with the whole

detector array. To yield a single image, the signals from every detector element are deconvolved with their individual PSF and subsequently compounded by a weighted sum. The deconvolution step is performed by linear Wiener filtering. The reconstructed image has a significantly enhanced resolution by a maximum factor of 1.7.

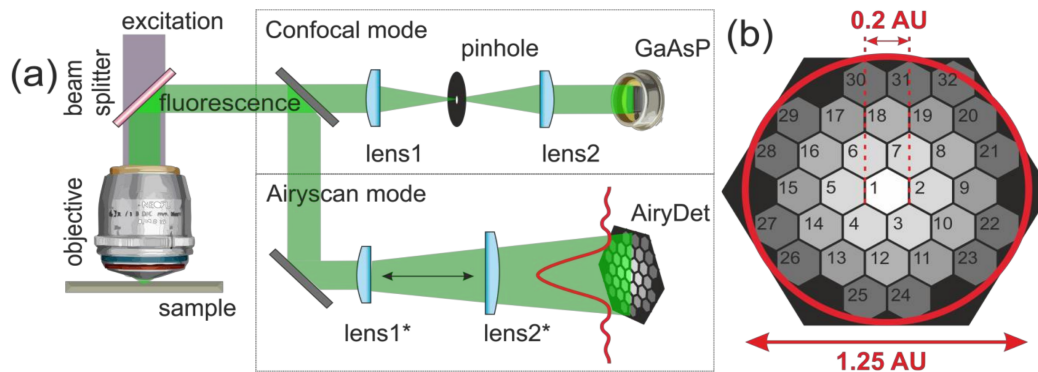


Figure 2.4: (a) Beam path of the traditional confocal arrangement compared to the beam path in Airy scanning. (b) Arrangement of the detector elements in the ZEISS LSM 880 Airyscan. Both figures are reprinted from [285] and are distributed under a CC BY 4.0 license by MDPI.

2.3 Flow Cytometry

In flow cytometry, an ensemble of cells is characterized in regard to multiple parameters with single cell resolution. The size, granularity, and expression level of antigens presented on the surface or the number of fluorescently tagged intracellular structures can be inferred for each cell. A flow cytometer (schematically illustrated in Fig. 2.5) generally consists of a fluidic, an optical, and an electronic system. Cells are prepared to be available in single cell suspension, so tissues must be broken up. Adherent cells must be treated with detachment agents such as trypsin before analysis. The as-prepared cell suspension is placed in a reservoir and guided into a channel. To measure one cell at a time, the cells must be aligned in the center of the channel and individually pass the laser beam at the interrogation point. This is realized by hydrodynamic focusing [286]. Here the sample stream containing the cells is surrounded by a coaxial sheath stream [287, 288]. The pressure in the sample stream is always higher than the pressure in the sheath stream. The flow rate is controlled by the pressure in the inner sample stream and can be varied depending on the number of cells per volume. Higher pressure in the sample stream results in a higher flow rate and, therefore, an increased amount of measured cells per time unit. However, it also leads to an increased diameter of the sample stream due to an increased differential pressure compared to the sheath stream. The increased diameter at higher sample stream pressures may lead to out-of-focus events when passing the interrogation point with the optical system resulting in data of suboptimal quality.

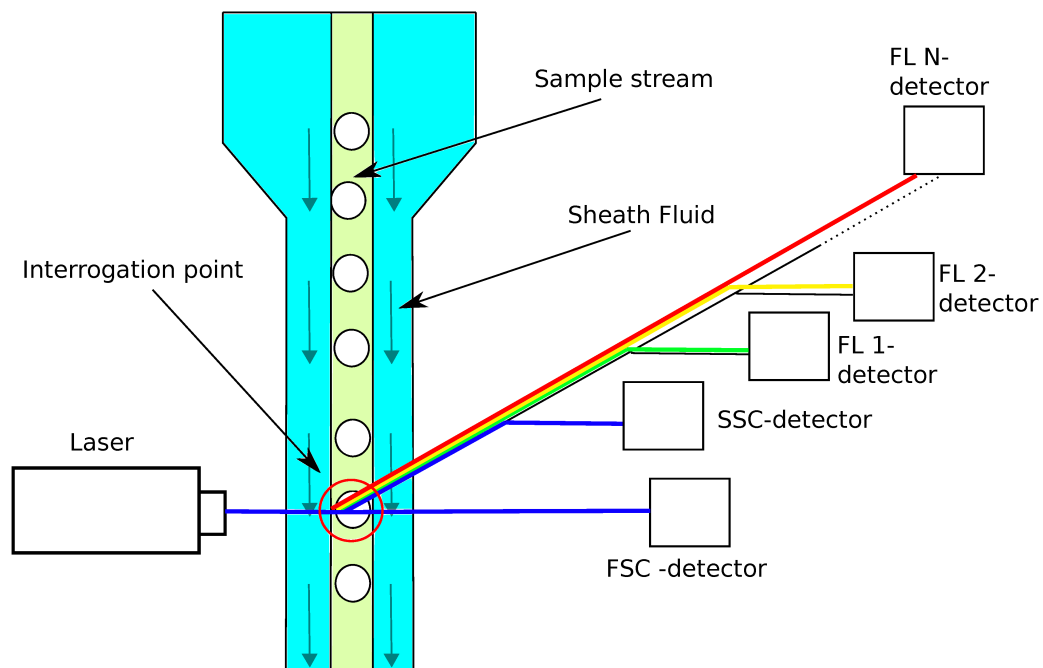


Figure 2.5: Simplified representation of the fluidic and optical system of a flow cytometry set-up. Single cells are aligned in the sample stream by hydrodynamic focusing. At the interrogation point, the laser beam coincides with the cells from the sample stream. The forward scattered (FSC) light is collected in parallel to the excitation beam, while the side scattered (SSC) light and the signal in fluorescence channels (FL-1, FL-2, ..., FL-N) is measured perpendicular to the excitation beam.

This trade-off has to be considered in experiment design and sample preparation. When a cell crosses the interrogation point and enters the focus of the excitation laser beams, the forward scattered light (FSC), the side scattered light (SSC), and the fluorescence emission are measured. The FSC provides information about the size of the cells and is measured parallel to the excitation beam, while the SSC correlates with the cells' granularity and is measured perpendicular to the excitation. Furthermore, a list of fluorescence channels is recorded that quantify the amount of fluorescent antibodies on the cell's surface or fluorescent molecules and particles inside the cell. Modern devices usually employ more than one laser for the excitation to allow the selection from a broader panel of fluorophores to be used on the same cell. This information is then transmitted to and stored by a computer (electronic system) for each cell. The resulting dataset has a number of dimensions equal to the number of channels recorded, typically larger than ten on modern devices [289, 290].

Due to the high dimensionality of flow cytometric data, the raw data is hard to interpret by pure visual inspection. Classically, the data is processed with a method called *gating*. Here, a human operator labels the data by viewing two-dimensional scatter plots and finding clusters as well as remarkable marker combinations in each subplot. Different cell types are then typically selected via polygonal windows in these scatter plots and labeled regarding the expression level of the given markers. Prior to that,

debris and doublets are typically removed in a pre-gating step. While time-consuming and requiring a high degree of proficiency by the operator, this process is still the standard in modern-day clinical routines. In the last decade, other algorithmic approaches using clustering for automatic gating and dimensionality reduction for visualizations entered the field [290,291]. Automatic detection of clusters is possible with algorithms like SPADE [292] and FlowSOM [293] that, in turn, also provide more accessible representations of the dataset. A common approach for non-linear dimensionality reduction for data visualization that has also been employed in flow cytometry is t -distributed stochastic neighbor embedding (tSNE) [294,295]. The tSNE algorithm was also applied in our work for the visualization of high-dimensional data in *Paper II*.

Chapter 3

Subcellular distribution of carbon nanodots

Information about the subcellular location of a nanoparticle is crucial to assess its applicability in biomedicine, as discussed in chapter 1.3. In that chapter, it was also discussed that the target organelle of CNDs varies depending on the properties of the nanoparticle. To determine the target location and thereby shed light on the applicability of the CNDs used here, colocalization experiments were conducted using Airy scanning microscopy, which was treated in chapter 2.2.1. Furthermore, an object-based colocalization method based on spatial statistics, introduced in chapter 1.4.2, is presented here. The instruments of spatial statistics help to address common shortcomings of traditional colocalization methods since the analyzed objects do not need to overlap in both channels. This method allows for testing of the distribution of objects in the measurement against a model assumption. It is especially suited for microscopy methods with a high spatial resolution but poor temporal resolution, which results in a significant time lag between the acquisition of both channels.

3.1 Paper I

Reference

Reproduced from [C. Wimmenauer and T. Heinzel (2023). Identification of nanoparticles as vesicular cargo via Airy scanning fluorescence microscopy and spatial statistics. *Nanoscale Advances*. <https://doi.org/10.1039/d3na00188a>], with the permission of The Royal Society of Chemistry

Copyright statement

This article is published under a CC BY 3.0 licence. Material from this article can be used in other publications provided that the correct acknowledgement is given with the reproduced material.


Contributions

I performed all the experiments and data analysis and wrote the main body of the manuscript.



Cite this: DOI: 10.1039/d3na00188a

Identification of nanoparticles as vesicular cargo via Airy scanning fluorescence microscopy and spatial statistics†

Christian Wimmenauer and Thomas Heinzel *

Many biomedical applications of nanoparticles on the cellular level require a characterisation of their subcellular distribution. Depending on the nanoparticle and its preferred intracellular compartment, this may be a nontrivial task, and consequently, the available methodologies are constantly increasing. Here, we show that super-resolution microscopy in combination with spatial statistics (SMSS), comprising the pair correlation and the nearest neighbour function, is a powerful tool to identify spatial correlations between nanoparticles and moving vesicles. Furthermore, various types of motion like for example diffusive, active or Lévy flight transport can be distinguished within this concept via suitable statistical functions, which also contain information about the factors limiting the motion, as well as regarding characteristic length scales. The SMSS concept fills a methodological gap related to mobile intracellular nanoparticle hosts and its extension to further scenarios is straightforward. It is exemplified on MCF-7 cells after exposure to carbon nanodots, demonstrating that these particles are stored predominantly in the lysosomes.

Received 24th March 2023
Accepted 8th June 2023

DOI: 10.1039/d3na00188a

rsc.li/nanoscale-advances

1 Introduction

To employ nanoparticles in biomedical applications such as drug or gene delivery, it is mandatory to determine their subcellular location after uptake. A common approach relies on using fluorescent or fluorescence-marked particles in combination with staining the candidate organelles, after which the system is studied by fluorescence imaging and subsequent colocalization analysis. This powerful concept has provided many highly relevant results, like the clarification of viral uptake mechanisms^{1,2} or the characterisation of a variety of potential nanoparticle systems for drug delivery and photodynamic therapy.^{3–5} However, the technique experiences also several limitations. One of these arises in a typical scenario, where the two fluorescence channels have to be detected with the same sensor, thus requiring sequential sampling of the two images for each channel and subsequent data analysis. In this case, the measured spatial correlation can be disturbed by the motion of the nanoparticles and vesicles during the single image data acquisition time. *Object based colocalization methods* have been established which relate spatially the structures in both channels after a segmentation step. Prominent methods from this field include Voronoi tessellation,⁶ trajectory

correlation⁷ and overlap analysis.⁸ More recently, methods from spatial statistics found their way into this field, with the best known example being the bivariate version of Ripley's *K*-function.^{9,10} Further numerical instruments such as the pair correlation function¹¹ (PCF), the estimation of interaction probabilities based on point patterns^{10,12,13} or the nearest neighbour function (NNF)⁸ have also been successfully applied to co-localization problems. In some cases, however, these powerful methods also experience limitations, in particular for vesicles that move significantly on the time scale set by the microscopy scans and regarding the spatial resolution limits by conventional confocal microscopy.

In the present work, we show that these problems can be reduced or avoided altogether, respectively, by a combination of super-resolution microscopy, here in the form of Airy scanning fluorescence microscopy, with a subsequent spatial statistics analysis which we denote by SMSS in the following. Airy scanning microscopy yields a higher resolution and superior signal-to-noise ratio compared to conventional confocal imaging, as required for vesicles with sizes below ≈ 500 nm. We apply the PCF and the NNF to the measured data and create envelopes representing 95%-confidence intervals. They are based on Monte-Carlo-simulations of complete spatial randomness (CSR) and a model for transport with heavily tailed jump distances. It is shown that these envelopes are of relevance for hypothesis testing and for proving consistency of the measured data with an underlying assumption.^{14,15}

As a topical model system, MCF-7 cells incubated with ultra-small carbon nanodots (CNDs) are used. Even though the family

Institute of Experimental Condensed Matter Physics, Heinrich-Heine-University, Universitätsstr. 1, 40225 Düsseldorf, Germany. E-mail: thomas.heinzel@uni-duesseldorf.de

† Electronic supplementary information (ESI) available. See DOI: <https://doi.org/10.1039/d3na00188a>



of CNDs is relatively diverse,¹⁶ common features such as good solubility in water,^{17,18} low toxicity^{19,20} and accessible functionalization protocols^{21,22} put them in the focus for biomedical applications. Proof of principle experiments for drug delivery,^{23–25} photosensitizing,^{26,27} deep tissue imaging^{28,29} and intracellular sensing^{18,29} have been reported. Their intracellular storage in different target organelles depends on the composition, surface functional groups and periphery of the particle.³⁰ While several groups have identified the vesicles of the endolysosomal system as primary location,^{31,32} they appear to be stored in the Golgi apparatus,³³ mitochondria³⁴ or in the nuclei³⁵ in other experiments. We have designed a study of the colocalization of CNDs with lysosomes. The computed statistical functions are compared with model envelopes and are discussed in the context of a positive control (double labelled lysosomes) and a negative control (labelled lysosomes and Golgi apparatus).

The same detector is used for both fluorescence channels to be compared, which thus have to be acquired by sequential scanning. Sequential scanning is favored in some colocalization problems, since it minimizes the bleed through from a fluorophore with a broad emission spectrum into the other channel, which is detrimental to colocalization analysis. Especially for nanoparticles with intrinsic fluorescence properties it may be, therefore, hard to optimize for a simultaneous acquisition. Furthermore, limitations in the available instrumentation may pose a problem since for sophisticated methods like Airy scanning or STED simultaneous acquisition of multiple fluorophores, while possible, sets high requirements on the setup. Since the acquisition of an image takes up to 2 s, intensity correlation based colocalization analysis fails due to the vesicular motion by a distance comparable to, or even larger than, their size within the acquisition time of one frame, see Fig. 3 (zoom-in, second row). Therefore, in this typical scenario, an object based analysis method needs to be applied.

2 Materials and methods

2.1 Carbon nanodots

2.1.1 Synthesis. CNDs were prepared *via* a slightly modified version of the bottom up synthesis method proposed by Qu *et al.*¹⁷ as described in detail elsewhere.¹⁹ 0.21 g anhydrous citric acid (Alfa Aesar) and 0.34 g diethylenetriamine (Merck) were mixed and treated in a closed microwave reaction chamber (CEM Discover) at 180 °C for 150 s under continuous stirring. The resulting product was dissolved in DI water, placed in a 100–500 Da dialysis tube (Float-A-Lyser) and dialysed against 2 L of DI water for 48 hours. The water was exchanged three times during the process. The dialysis product was lyophilized to obtain the dry mass and redissolved in phosphate-buffered saline (PBS, Gibco) and sterile filtered (pore size 0.22 µm, Satorius).

2.1.2 Characterisation. The as prepared CNDs were characterized *via* Raman spectroscopy, transmission electron microscopy (TEM), X-ray photoelectron spectroscopy (XPS), CHN elemental analysis, fluorescence spectroscopy and atomic force microscopy (AFM) in previous work.¹⁹ This section will

briefly summarize the already published findings. In Raman spectroscopy a pronounced G-band around 1596 cm^{−1} corresponding to graphitic sp²-carbon as well as a D-, D1-, D2- and D3-band at (1375, 1195, 1264 and 1412 cm^{−1}) corresponding to different sp³-carbon containing groups were found. In TEM measurements on an amorphous carbon substrate nanoparticles with an average diameter of 3.3 nm and a lattice with an hexagonal symmetry and a lattice constant of 0.223 nm were found. Taking lattice strain due to impurities and the limited size of the particles into account, this value is in good agreement with the lattice constant of bulk graphene (0.246 nm). In CHN elemental analysis the mass fractions were determined to be 40% carbon, 8% hydrogen and 19% nitrogen. Attributing the remaining mass fractions to oxygen is consistent with the results from the XPS measurement. From AFM measurements on silicon oxide the height was determined to range between 1 nm and 2 nm, which is in good agreement with the height of two to three layers of graphene on this kind of substrate.

The absorbance spectrum shows two pronounced peaks in the UV-region, one around 230 nm commonly attributed to the π–π*-transition of the graphitic carbon domains and one around 350 nm which is attributed to the n–π*-transition of C=O moieties.¹⁷ The employed CNDs display their strongest emission around 460 nm, if excited at 360 nm. A quantum yield of 23% was obtained for these particles.

2.2 Cell experiments

2.2.1 Cell culture. MCF-7 cells, a breast cancer cell line from an invasive breast ductal carcinoma, were cultivated in medium consisting of RPMI 1640, 10% fetal bovine serum and 1% penicillin streptomycin solution. The cells were maintained at 37 °C and 5% CO₂ in a Heracell 150i (ThermoFisher Scientific™) incubator in a 75 cm² cell culture flask. The culture was split every three to four days using a trypsin/EDTA solution (Sigma-Aldrich).

2.2.2 Transfection and incubation with CNDs. MCF-7 cells are seeded out at a density of (10 000–15 000) cells per well in an 8 well µ-slide (no. 1.5 polymer coverslip, tissue culture treated, Ibidi™) 48 hours prior to imaging. CNDs are added to respective wells to yield a concentration of 500 µg mL^{−1}. The cells in the respective chambers were transfected with reagents from the CellLight™ BacMam 2.0 product series (Invitrogen™) 24 hours prior to imaging. To label the lysosomes CellLight™ Lysosomes-RFP and CellLight™ Lysosomes-GFP was used yielding MCF-7 cells expressing a fusion protein of LAMP1 and the respective fluorescent protein. To label the Golgi apparatus CellLight™ Golgi-GFP was used yielding MCF-7 cells expressing a fusion protein of the human Golgi resident enzyme *N*-acetylgalactosaminyltransferase and GFP. One hour before imaging the samples were washed with PBS and the medium was exchanged with fresh full medium. Between the preparation steps the sample was kept in the incubator at 37 °C and 5% CO₂.

2.2.3 Microscopy. The as treated specimen were imaged using a Zeiss LSM 880 Airyscan confocal microscope with an 63× oil objective (Planachromat, NA 1.4) at 37 °C. Owing to the



employed 32-channel gallium arsenide phosphide photo-multiplier tube (GaAsP-PMT) area detector with each detector element collecting a full confocal image the Zeiss LSM 880 Airyscan has an improved signal-to-noise ratio compared to conventional confocal microscopy. It can be run in *super-resolution mode* with a lateral resolution of down to 140 nm or in *fast mode* collecting multiple line scans in parallel resulting in a significantly reduced scan time.^{36,37} The images were acquired in *superresolution mode* and time series in *fast mode*. To image the CNDs, a 405 nm laser diode was used for excitation. For GFP excitation, an argon laser with a wavelength of 488 nm was used for excitation and RFP was excited by a 561 nm diode pumped solid state laser was used for excitation. In all measurements channels were acquired frame wise.

2.3 Data analysis

A schematic representation of the SMSS protocol is shown in Fig. 1.

Wavelet segmentation is performed *via* the implementation of the open image analysis platform Icy.³⁸ The watershed method is then applied to the binary image, and the point pattern is extracted with the analyze particles function implemented in Fiji.³⁹

2.3.1 Bivariate spatial statistics. Programs to perform the spatial point pattern analysis make extensive use of functions from the *spatstat* package⁴⁰ for the R programming language.

The bivariate *G*-function

$$G_{12}(r) = \frac{1}{n_1} \sum_{i=0}^{n_1} \mathbf{I}\{d_i^{[12]} \leq r\} \quad (1)$$

measures the number of spots with a nearest neighbour distance below r , and $d_i^{[12]}$ denotes the nearest neighbor distance between spot i of type 1 and the type 2 spots. Here, $\mathbf{I}\{Y\}$ is the indicator function that takes the value of one if the statement Y is true and gets zero if Y is false.

The bivariate pair correlation function is related to the probability of finding a spot of type 1 a given distance r from a spot of type 2. It is defined *via* the derivative of the bivariate *K*-function

$$g_{12}(r) = \frac{K'_{12}(r)}{2\pi r}, \quad (2)$$

with the bivariate *K*-function

$$K_{12}(r) = \frac{\Omega}{n_1 n_2} \sum_{i=0}^{n_1} \sum_{j=0}^{n_2} \mathbf{I}\{d_{ij} \leq r\} b_{ij}(r), \quad (3)$$

which measures the number of type 2 spots inside of a circle with radius r and around a type 1 spot the area of the region of interest (ROI) is denoted by Ω and the number of spots is denoted by n . The expression $b_{ij}(r)$ corrects for edge effects. In our particular case, the translation correction⁴¹ is applied. The manually estimated borders of the cell from the auto-fluorescence were selected as ROI. The nucleus was excluded from the ROI to prevent artificial inflation of the summary functions (images of the ROIs are available in the ESI†). Model calculations of $G_{12}(r)$ and $g_{12}(r)$ for clustered and for periodically

arranged spots are reproduced in the ESI.† Since in contrast to $g_{12}(r)$, $G_{12}(r)$ neglects points beyond the nearest neighbor but has a more intuitive interpretation, giving the share of points that found their nearest neighbor up to a distance of r , these two summary functions are complementary and we discuss both of them below.

For the interpretation, the spatial statistical functions as obtained from the measured data are compared to *reference envelopes*. To construct them, an ensemble of $N = 100$ simulated point patterns is generated under a model assumption. For these simulated point patterns an ensemble of summary functions is calculated, capturing the behaviour of the model. For a significance level $\alpha = 0.05$ the 5% that deviate the most from the mean are excluded from the ensemble of simulated summary functions at each distance r . The minimum and maximum of the remaining points describe the borders of the envelope. If the respective summary function of the measured data lies outside of the envelope inside of a certain interval in r , the p -value is greater than the significance level ($p > \alpha$) and the underlying model (null hypothesis) is rejected in this interval. The first tested model was a uniform random distribution inside the ROI of the type 2 spots (red channel), while the type 1 spots had the same distribution as the measured data. The underlying null hypothesis is that the positions of the type 2 spots are independent of the type 1 spots. In the second tested model the positions of the type 1 spots are again the same as for the measured data. To test the null hypothesis of transport with a lognormal distribution of jump distances the simulated type 2 spots were generated by shifting each of the type 1 spots by a vector \vec{s}_i . Length $|\vec{s}_i|$ was sampled from a lognormal distribution that was fitted to the jump distance distribution of the measured data and the angle θ that describes the direction was sampled from a uniform distribution. If a simulated point of type 2 was generated outside of the ROI a new vector \vec{s}_i was generated. To ensure that the number of type 2 points in every simulation (n_s) corresponds to the number of type 2 points in the measurement (n_m), spots in random locations were added (if $n_m > n_s$) or the set of simulated points was sub-sampled to match n_m (if $n_m < n_s$).

2.3.2 Single particle tracking and trajectory analysis. To determine the particle trajectories from the microscopy data the *TrackMate* plugin⁴² for the open source image analysis platform *Fiji*³⁹ is used. The particle positions were detected with the *Laplacian of Gaussians* detector ($d = 0.8 \mu\text{m}$) and detected objects were filtered afterwards based on mean intensity and quality. With the *Simple Linear Assignment Problem Tracker*⁴³ with a linking distance of $1 \mu\text{m}$, a maximum gap of 2 frames and a gap closing distance of $2 \mu\text{m}$, the lysosomal trajectories are constructed. Merging or splitting events were disregarded. Trajectories with less than ten time points or more than five gaps were excluded.

3 Results and discussion

3.1 Single particle tracking of lysosomes

Lysosomes are actively transported *via* kinesin and dynein along the microtubuli,⁴⁶ which manifests itself in short bursts of



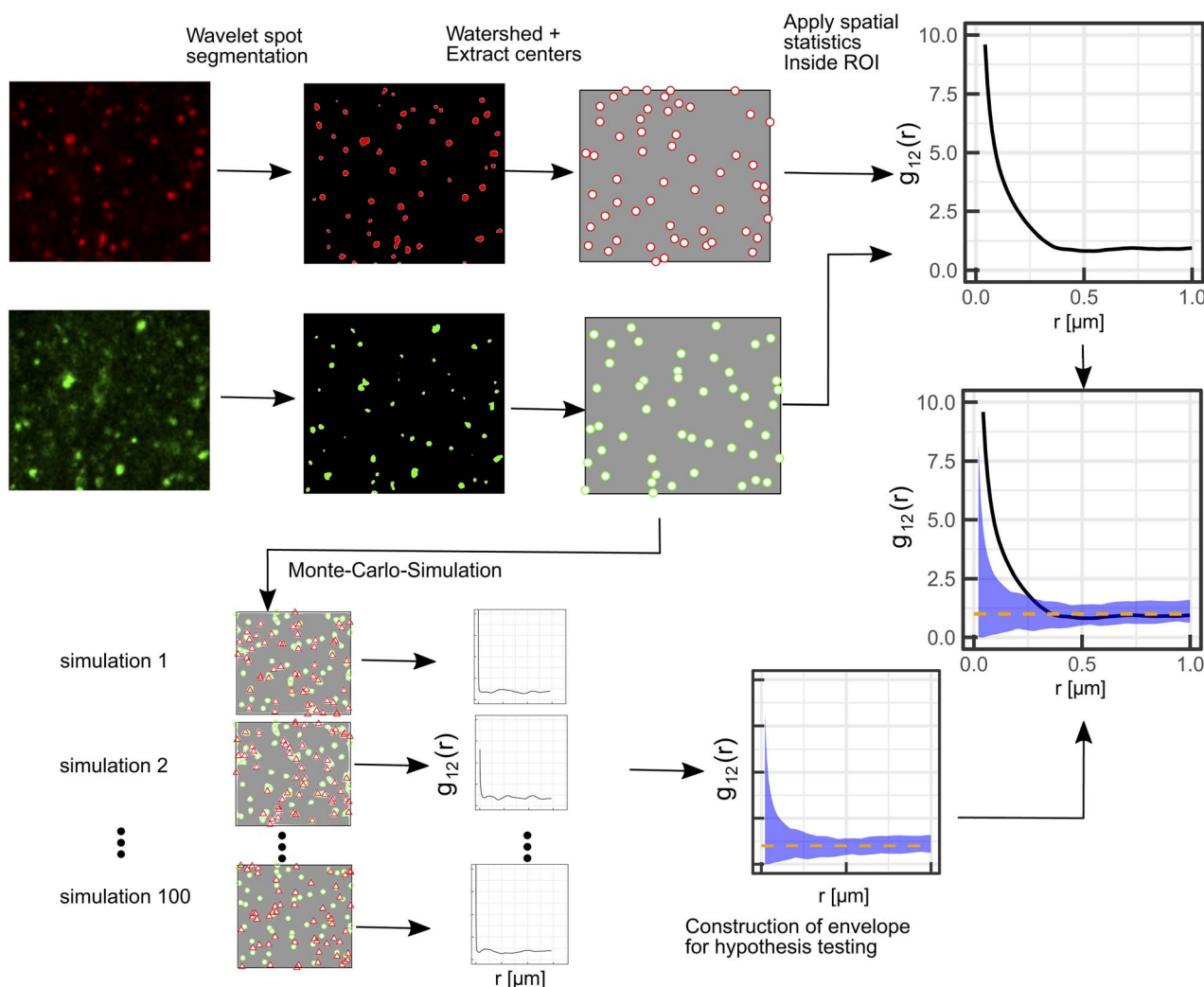


Fig. 1 Illustration of the proposed protocol comprising Airy scanning fluorescence microscopy in the superresolution mode in combination with spatial statistics (SMSS). First, a wavelet segmentation is applied to extract the spots in each channel, then the watershed method is applied and the centers of the spots are extracted. Bivariate spatial statistics is applied to yield the summary function, *i.e.* $g_{12}(r)$ in this illustration. To test the distribution against a random distribution of lysosomes in the red channel, the green points are used as a starting point for a Monte-Carlo-simulation. From the Monte-Carlo-simulations for spatial randomness (red triangles in the frames to the lower left) an envelope is constructed that encloses the 95 least extreme values of the summary functions from the simulations (blue shaded area). The dashed orange line denotes the mean value of the simulated summary functions for spatial randomness.

directed motion. In between these intervals of active transport, lysosomes show (sub-) diffusive behaviour, which has been attributed to lingering at the intersections of microtubuli.⁴⁷

This bimodal motion resembles a Lévy walk.^{48–50} To construct envelopes for the assumption of transport, knowledge about the jump distance distribution is necessary. To obtain insight in the underlying transport dynamics, single particle tracking was performed on a time series measurement over 100 time points with an acquisition time of 827 ms per frame. After excluding trajectories shorter than 8.3 s, 763 trajectories remain, which form the input of the analysis. Typical trajectories are reproduced in Fig. 2(a).

The distribution of frame-to-frame jump distances is heavy tailed and can be described reasonably well by a log-normal

distribution with $\sigma = 0.94$ and $\mu = -1.87$, see Fig. 2(b), in agreement with recent results.⁵⁰ Following a similar workflow to the method presented by Pinholt *et al.*,⁵¹ the trajectories are classified prior to an analysis of their time dependent ensemble mean square displacement (MSD) as follows. Eight descriptive features, *i.e.*, the mean, standard deviation, skewness and kurtosis of the jump distance distribution, as well as the straightness, sinuosity, average MSD and turn angle correlation⁵² are calculated for each trajectory, providing a space for classification *via* the density based clustering algorithm *density-based spatial clustering of applications with noise* (DBSCAN).⁴⁵ A non-linear dimensionality reduction *via t-distributed stochastic neighbor embedding* (tSNE)⁴⁴ was applied prior to the clustering. From the six emerging clusters, see the ESI† for detailed



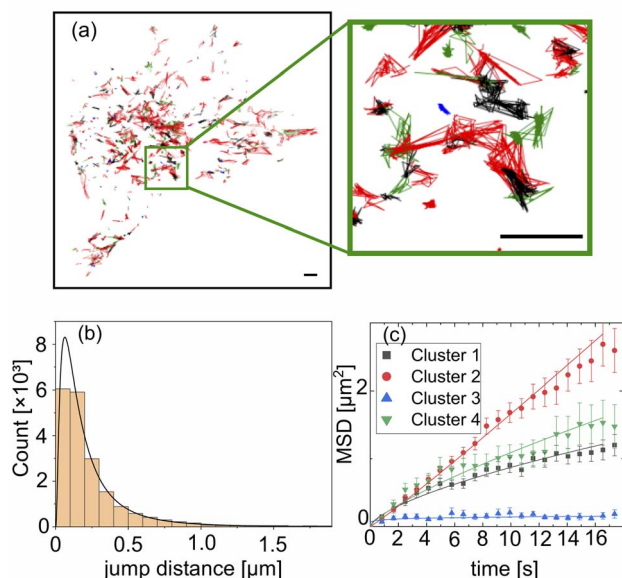


Fig. 2 Single particle tracking of lysosomes. (a) Extracted single particle trajectories colored according to the identified cluster via cluster analysis with *t*-distributed stochastic neighbor embedding (tSNE)⁴⁴ and *density-based spatial clustering of applications with noise* (DBSCAN).⁴⁵ The size of the scale bar amounts to 5 μm. (b) A lognormal distribution was fitted to the frame to frame jump distance for all trajectories. (c) Three different subtypes of lysosomal motion, namely immobile, subdiffusive and diffusive, were identified for the four clusters by inspection of their MSD scaling.

information, two consisted of very few points and where therefore excluded from the subsequent MSD analysis. Fig. 2(c) shows the resulting averaged MSD curves for the three clearly distinguishable extracted states (full curves in ESI†). Fitting the data to the standard expression $\text{MSD} = 4Dt^\alpha$ gives the fit parameters as summarized in displayed in Table 1. Class 1 (cluster 2, red), which forms by far the largest group, is diffusive, *i.e.*, $\alpha \approx 1$. The trajectories of class 2 (cluster 3, blue) are immobile to a good approximation, while class 3 (cluster 1, black and cluster 4, green) is subdiffusive.

Typical sample trajectories of the three classes are shown in Fig. 2(a). Class 1 trajectories correspond to lysosomes travelling predominantly along filaments without changes of the direction by large angles. The lysosomes with class 2 trajectories are

essentially captured at some structure, for example a filament junction. Lysosomes travelling along the filaments with frequent large-angle changes of the path form class 3. The values for the diffusion constant are within a reasonable range compared to the literature.^{50,53} It should be noted that this classification treats the trajectories globally, in contrast to segmentation of the trajectories into different diffusive states, in which bursts of directed motion appear on smaller time scales below 10 s.⁵⁰ A finer temporal resolution in combination with a more sophisticated segmentation algorithm may provide more insight into the lysosomal movement patterns on a single particle level, but is beyond the scope of this work. These studies show that a significant fraction of the lysosomes move farther than their size within the capture time of a picture frame, which suggests them a suitable test bed for the SMSS analysis.

3.2 Control experiments

To validate the SMSS protocol, we perform two control experiments and determine their corresponding reference envelopes. In the positive control experiment, MCF-7 cells are transfected to express a fusion protein of the lysosome resident protein LAMP1 and RFP as well as a fusion protein of LAMP1 and GFP. Fig. 3(a)–(d) reproduce characteristic fluorescence microscope images. Since both channels capture the location of the same subcellular structure the employed method is expected to yield maximum colocalisation under the present experimental conditions. The two bivariate functions $G_{12}(r)$ and $g_{12}(r)$ of the experimental data should therefore reside inside the reference envelope for the transport model, *i.e.* spatial correlation. As can be seen in Fig. 4(a) and (b), respectively, the measured bivariate functions lie inside the confidence intervals for $r \leq 500$ nm, deviate slightly from them for larger distances, but remain close up to the largest distances studied, *i.e.* 3.3 μm. The reference envelope for spatial independence, on the other hand, is distinctly separated from the experimental data, showing some overlap only at large distances above $r = 1.8$ μm for $G_{12}(r)$, and in the range $r = 1.2$ μm for $g_{12}(r)$. As an interpretation example, we evaluate that therefore, for distances $r < 1.2$ μm, the null hypothesis of the spatial randomness can be rejected with $p < 0.05$. From $G_{12}(r = 1.2 \text{ μm}) \approx 0.8$, on the other hand, we can infer that 80% of points in the green channel have a nearest neighbor distance of less than 1.2 μm to points in the red channel. This positive control experiment shows how a close to perfect cross-correlation will look like in our experiments. We explain the deviations between the measured trace and the reference envelope for correlation at larger distances with the three-dimensional character of the cell. As soon as lysosomes move into or out of the focal plane, the correlation is blurred. This will set in at the focal length of the microscope, which in our case equals approximately 500 nm. Furthermore, the treatment of points exiting the edge of the ROI in the simulation may also introduce a bias. If a simulated point is generated outside of the ROI, a new point is generated until it lies inside of the ROI. This treatment may introduce a bias that favours small jump distances for points close to the cellular border.

Table 1 Results of the power law fit to the MSD functions displayed in Fig. 2(d). Displayed are the type of motion, the effective diffusion constant D and the exponent α from the expression $\text{MSD} = 4Dt^\alpha$, the number of trajectories in the cluster N and the coefficient of determination R^2

Cluster	Type	$D [\mu\text{m}^2 \text{s}^{-1}]$	α	N	R^2
1	Subdiffusive	0.048 ± 0.003	0.66 ± 0.03	147	0.98
2	Diffusive	0.036 ± 0.002	1.06 ± 0.019	466	0.99
3	Immobile	0.025 ± 0.003	0.14 ± 0.06	33	0.30
4	Subdiffusive	0.047 ± 0.004	0.77 ± 0.05	108	0.95

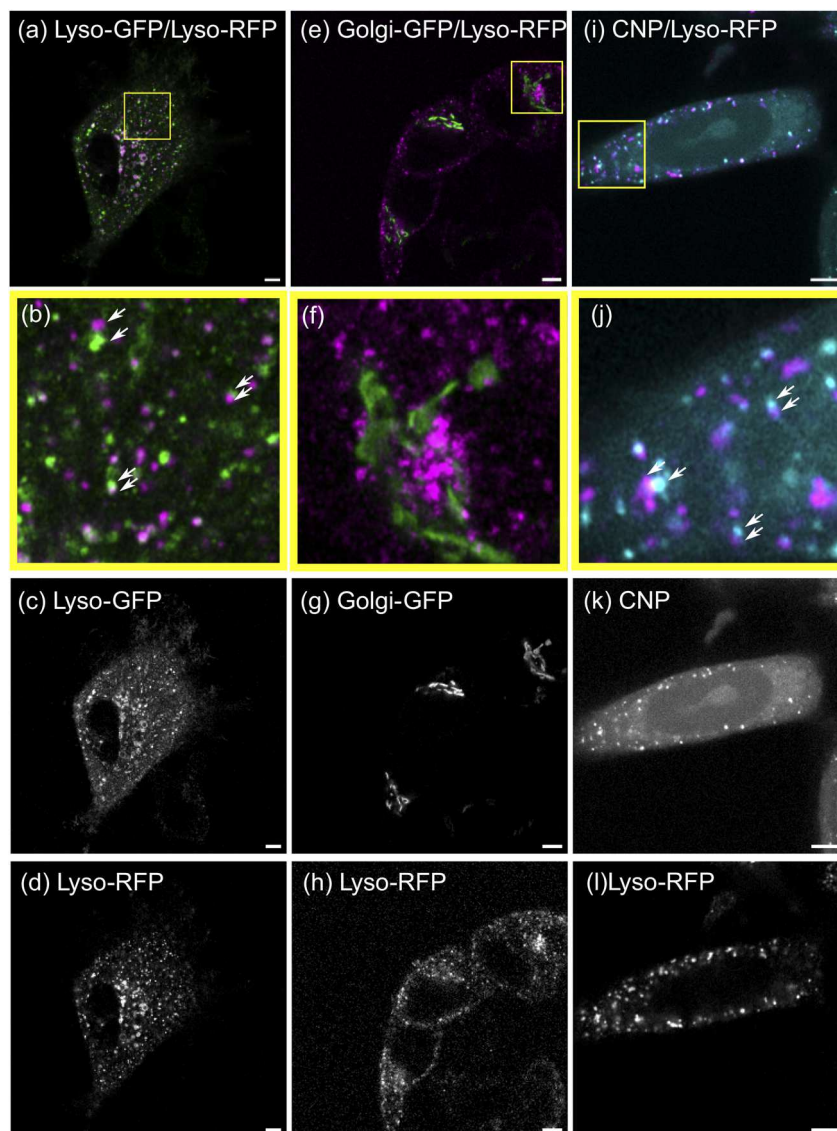


Fig. 3 Microscopy images of MCF-7 cells with RFP- and GFP-labeled lysosomes (left column, (a)–(d)), RFP-labeled lysosomes and a GFP-labeled Golgi apparatus (middle column, (e)–(h)) and RFP-labeled lysosomes post CNP incubation (right column, (i)–(l)). The top row (a, e, i) displays the overlay of both channels, while the individual channels are shown in the lowermost two rows (c, g, k and d, h, l, respectively). The second row (b, f, j) shows a zoom in on the yellow bordered region in the composite images. The white arrows indicate spots in different channels of same size and shape that are in close proximity. These indicated spots supposedly correspond to the same object that is shifted due to movement between the acquisitions of both channels. The length of all scale bars amounts to 5 μm .

Nonetheless, reasonable agreement of the measured data with the transport model persists.

For the negative control experiment, the cells were transfected to express a LAMP1/RFP fusion protein labeling the lysosomes, but this time co-labeled with a fusion protein for an enzyme resident in the Golgi, namely *N*-acetylgalactosaminyl-transferase with GFP, see Fig. 3(e)–(h) for fluorescence microscopy images. The labeled organelles are spatially disjunct and correlate only in the sense that their locations mutually exclude each other. Therefore, the bivariate functions are expected to reside inside the reference envelope for spatial independence. As can be seen in Fig. 4(c) and (d), both $G_{12}(r)$ and $g_{12}(r)$ lie inside the reference envelope, *i.e.*, the null hypothesis can not

be rejected. It can therefore be inferred that the spatial spot pattern for the negative control is indistinguishable from an independent distribution for the two spot types.

3.3 Spatial correlation between CNDs and lysosomes

With the control experiments at hand, we apply the SMSS protocol to quantify the subcellular localisation of the CNDs. MCF-7 cells are transfected to express the LAMP1/RFP fusion protein and are afterwards incubated with CNDs for 48 h, leading to typical bicolor fluorescence patterns as shown in Fig. 3(i)–(l). The resulting bivariate functions are reproduced in Fig. 4(e) and (f) together with the reference envelopes. For distances $r < 0.5 \mu\text{m}$, both spatial statistical functions lie outside



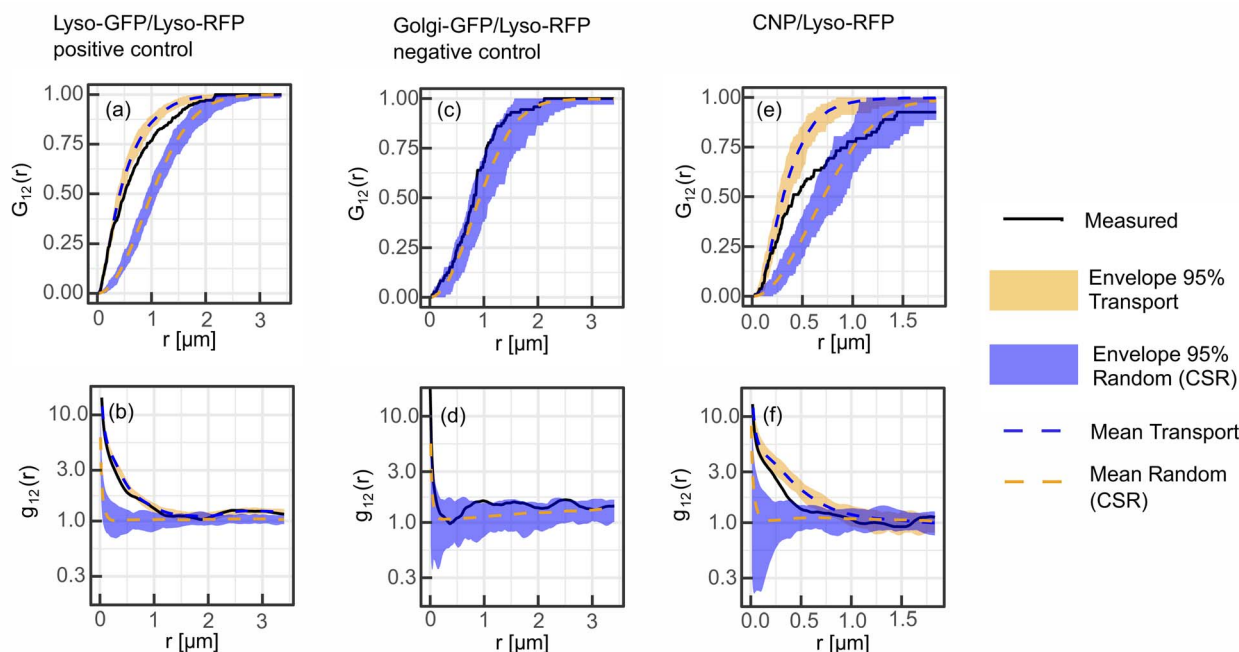


Fig. 4 Results of point pattern analysis. Bivariate spatial statistics was applied to all three conditions namely the positive control with lysosomes labelled in both channels (left column, (a) and (b)), the negative control displaying lysosomal markers in channel 1 and the Golgi apparatus in channel 2 (middle column, (c) and (d)) and the condition with lysosomal staining visible in channel 1 and the distribution of the CNDs in channel 2 (right column, (e) and (f)). The set of summary functions comprises of the nearest neighbor function $G_{12}(r)$ (top row, (a), (c) and (e)) and the pair correlation function $g_{12}(r)$ (bottom row, (b), (d) and (f)). The summary functions are displayed as solid black lines, while the envelopes for uniform randomization of the lysosomal channel and a model for transport with a heavy tailed jump distance distribution are displayed in blue and orange respectively.

the reference envelope for independent motion. Thus, the hypothesis of the lysosomal distribution being independent of the CND distribution can be rejected with $p < 0.05$. Rather, $G_{12}(r)$ and $g_{12}(r)$ are found inside the envelope functions for correlated motion for small distances. From $G_{12}(r = 0.5 \mu\text{m}) > 0.5$, see Fig. 4(e), we conclude that more than 50% of the nearest neighbor distances between CNDs and lysosomes are smaller than $0.5 \mu\text{m}$. At larger distances, G_{12} runs outside this reference envelope but, as we have seen during the study of the correlated reference envelope, this is the case even for perfect correlation and can be explained by lysosomes CNDs entering or leaving the focal plane within the period set by the single picture acquisition time. These results show that with a significance level of 0.05, more than 50% of the fluorescent CNDs are captured in the lysosomes in our experiments, which therefore form the dominant host for the CNDs.

3.4 Generalizability and critical evaluation of the method

The proposed SMSS protocol can be applied to explore the subcellular distribution of a wide variety of nanoparticles, since it requires simply that the nanoparticle possess intrinsic fluorescence and a moderate photostability, in order not to bleach out on the time scale of the acquisition. It may be furthermore useful for nanoparticles with a wide emission spectrum, which benefit from sequential scanning in colocalization experiments to minimize bleed through. The presented workflow is modular

and may be adapted to a given problem. First of all, the presented segmentation pipeline may not be appropriate in all situations. Wavelet based segmentation was used since it is known that this approach is well-suited to extract small spots even for varying levels of intensity. For more specialized problems, other segmentation pipelines^{54,55} may be employed. Second, the transport characteristic that is used to model the envelope for transport has to be evaluated on a case-by-case basis. While a log-normal distribution of jump distances is well-suited for the presented problem, this cannot be applied to all transport process in a cellular context. In the case of normal diffusion, for example, a Gaussian distribution of the displacement in x - and y -direction would be more appropriate. We illustrate the analysis of diffusive objects on synthetic data found in the ESI† Directed motion with a negligible diffusive component, for example, has to be treated differently again.

Furthermore, application of the SMSS concept requires sufficiently dilute objects in the following sense. The mean spacing between the objects to be traced sets the length scale of the objects' motion distance in between two consecutive recording times: if objects move more than the mean spacing during this time interval, complete spatial randomness (CSR) and the underlying transport process can no longer be distinguished, leading to a significant overlap of the respective envelopes. This is illustrated by synthetic data in the ESI† showing the analysis of points subject to a radial drift. At high



object densities, the directed motion of the ensemble becomes indistinguishable from CSR. Finally, optical aberrations may interfere with the spatial statistics analysis. Chromatic aberrations in particular may present a problem since they distort the location of the objects in both fluorescence channels differently. As for all fluorescence colocalization experiments it is essential to minimize this effect by centering the region of interest on the optical axis of the imaging system and using achromatic objectives. If a significant amount of chromatic aberration is present, the image would be subject to stretching that increases from the center to the periphery.

4 Conclusions

It has been demonstrated that Airy scanning fluorescence microscope in combination with spatial statistics functions and reference envelopes provides a powerful tool to quantify correlated motion of nanoparticles and/or vesicles on a subcellular level. It is particularly suited for setups where locations measured in subsequent pictures may be correlated, which may be for instance necessary to minimize bleed through when fluorophores with a broad emission spectrum must be used. The reference envelopes corresponding to the hypotheses to be tested (here: uncorrelated motion and motion with a log-normal distribution) enable the specification of significance levels according to the requirements (set to the frequently used value of 0.05 in our work). This rather broadly applicable scheme, with selectable targets for labelling as well as several established spatial statistical functions, has been exemplified by a study the spatial colocalization of carbon nanodots in lysosomes. The results do not exclude that a fraction of the CNDs reside inside the Golgi apparatus or the nucleoli, for example. This would require additional experiments along the lines discussed above. However, it can be concluded that the major fraction of the CNDs is localized inside mobile lysosomes with a significance level of 0.05. The experienced limitations of the SMSS protocol in its present form have been identified being mainly due to motion of the detected fluorescent units into or out of the focal length of the microscope. Therefore, confinement of the system under study to a plane with a thickness of about 500 nm appears to be one promising future way to improve the presented protocol.

Conflicts of interest

There are no conflicts to declare.

Acknowledgements

C. W. gratefully acknowledges the support of the Jürgen Manchot Stiftung. The authors thank the Center of Advanced Imaging (CAI) of the HHU for providing their microscopes, laboratories and support. Cornelia Monzel is gratefully thanked for the fruitful discussion in the early stages of this work and for providing access to the laboratories of the chair for experimental medical physics at the HHU.

Notes and references

- 1 Q. Li, W. Li, W. Yin, J. Guo, Z.-P. Zhang, D. Zeng, X. Zhang, Y. Wu, X.-E. Zhang and Z. Cui, *ACS Nano*, 2017, **11**, 3890–3903.
- 2 K. Gorshkov, K. Susumu, J. Chen, M. Xu, M. Pradhan, W. Zhu, X. Hu, J. C. Breger, M. Wolak and E. Oh, *ACS Nano*, 2020, **14**, 12234–12247.
- 3 Y. Cheng, A. C. Samia, J. Li, M. E. Kenney, A. Resnick and C. Burda, *Langmuir*, 2010, **26**, 2248–2255.
- 4 L. P. Fernando, P. K. Kandel, J. Yu, J. McNeill, P. C. Ackroyd and K. A. Christensen, *Biomacromolecules*, 2010, **11**, 2675–2682.
- 5 Y. Wang, G. Wei, X. Zhang, X. Huang, J. Zhao, X. Guo and S. Zhou, *Small*, 2018, **14**, 1702994.
- 6 L. Andronov, I. Orlov, Y. Lutz, J.-L. Vonesch and B. P. Klaholz, *Sci. Rep.*, 2016, **6**, 1–9.
- 7 D. Vercauteren, H. Deschout, K. Remaut, J. F. Engbersen, A. T. Jones, J. Demeester, S. C. De Smedt and K. Braeckmans, *ACS Nano*, 2011, **5**, 7874–7884.
- 8 J.-F. Gilles, M. Dos Santos, T. Boudier, S. Bolte and N. Heck, *Methods*, 2017, **115**, 55–64.
- 9 B. D. Ripley, *J. Appl. Probab.*, 1976, **13**, 255–266.
- 10 T. Lagache, N. Sauvonnnet, L. Danglot and J.-C. Olivo-Marin, *Cytometry, Part A*, 2015, **87**, 568–579.
- 11 C. Coltharp, X. Yang and J. Xiao, *Curr. Opin. Struct. Biol.*, 2014, **28**, 112–121.
- 12 J. A. Helmuth, G. Paul and I. F. Sbalzarini, *BMC Bioinf.*, 2010, **11**, 1–12.
- 13 S. Mukherjee, C. Gonzalez-Gomez, L. Danglot, T. Lagache and J.-C. Olivo-Marin, *IEEE Signal Process. Lett.*, 2020, **27**, 1085–1089.
- 14 B. D. Ripley, *J. Roy. Stat. Soc. B*, 1977, **39**, 172–192.
- 15 T. Wiegand, P. Grabarnik and D. Stoyan, *Ecosphere*, 2016, **7**, e01365.
- 16 S. Zhu, Y. Song, X. Zhao, J. Shao, J. Zhang and B. Yang, *Nano Res.*, 2015, **8**, 355–381.
- 17 D. Qu, M. Zheng, J. Li, Z. Xie and Z. Sun, *Light: Sci. Appl.*, 2015, **4**, e364.
- 18 Z. L. Wu, M. X. Gao, T. T. Wang, X. Y. Wan, L. L. Zheng and C. Z. Huang, *Nanoscale*, 2014, **6**, 3868–3874.
- 19 S. Fasbender, L. Zimmermann, R.-P. Cadeddu, M. Luysberg, B. Moll, C. Janiak, T. Heinzel and R. Haas, *Sci. Rep.*, 2019, **9**, 1–13.
- 20 F. Chen, W. Gao, X. Qiu, H. Zhang, L. Liu, P. Liao, W. Fu and Y. Luo, *Frontiers in Laboratory Medicine*, 2017, **1**, 192–199.
- 21 R. Buiculescu, D. Stefanakis, M. Androulidaki, D. Ghanotakis and N. A. Chaniotakis, *Analyst*, 2016, **141**, 4170–4180.
- 22 Z. Ji, A. Sheardy, Z. Zeng, W. Zhang, H. Chevva, K. Allado, Z. Yin and J. Wei, *Molecules*, 2019, **24**, 152.
- 23 X. Sun, Z. Liu, K. Welscher, J. T. Robinson, A. Goodwin, S. Zaric and H. Dai, *Nano Res.*, 2008, **1**, 203–212.
- 24 L. He, T. Wang, J. An, X. Li, L. Zhang, L. Li, G. Li, X. Wu, Z. Su and C. Wang, *CrystEngComm*, 2014, **16**, 3259–3263.



- 25 I. J. Gomez, B. Arnaiz, M. Cacioppo, F. Arcudi and M. Prato, *J. Mater. Chem. B*, 2018, **6**, 5540–5548.
- 26 A. Cadranet, J. T. Margraf, V. Strauss, T. Clark and D. M. Guldi, *Acc. Chem. Res.*, 2019, **52**, 955–963.
- 27 R. Knoblauch and C. D. Geddes, *Materials*, 2020, **13**, 4004.
- 28 Q. Liu, B. Guo, Z. Rao, B. Zhang and J. R. Gong, *Nano Lett.*, 2013, **13**, 2436–2441.
- 29 P. Lesani, G. Singh, C. M. Viray, Y. Ramaswamy, D. M. Zhu, P. Kingshott, Z. Lu and H. Zreiqat, *ACS Appl. Mater. Interfaces*, 2020, **12**, 18395–18406.
- 30 H. Liu, J. Guo, A. A. Aryee, L. Hua, Y. Sun, Z. Li, J. Liu and W. Tang, *Front. Chem.*, 2021, **9**, 784851.
- 31 D. Kersting, S. Fasbender, R. Pilch, J. Kurth, A. Franken, M. Ludescher, J. Naskou, A. Hallenberger, C. von Gall, C. J. Mohr, *et al.*, *Nanotechnology*, 2019, **30**, 395101.
- 32 C. Nollmann, C. Wimmenauer, S. Fasbender, S. Mayer, R.-P. Cadeddu, P. Jäger, T. Heinzl and R. Haas, *RSC Adv.*, 2021, **11**, 26303–26310.
- 33 M. Yuan, Y. Guo, J. Wei, J. Li, T. Long and Z. Liu, *RSC Adv.*, 2017, **7**, 49931–49936.
- 34 X.-W. Hua, Y.-W. Bao, Z. Chen and F.-G. Wu, *Nanoscale*, 2017, **9**, 10948–10960.
- 35 Z. Zhu, Q. Li, P. Li, X. Xun, L. Zheng, D. Ning and M. Su, *PLoS One*, 2019, **14**, e0216230.
- 36 J. Huff, *Nat. Methods*, 2015, **12**, i–ii.
- 37 K. Weisschart, *Zeiss Technology Note*, 2014, vol. 22.
- 38 F. De Chaumont, S. Dallongeville, N. Chenouard, N. Hervé, S. Pop, T. Provoost, V. Meas-Yedid, P. Pankajakshan, T. Lecomte, Y. Le Montagner, *et al.*, *Nat. Methods*, 2012, **9**, 690–696.
- 39 J. Schindelin, I. Arganda-Carreras, E. Frise, V. Kaynig, M. Longair, T. Pietzsch, S. Preibisch, C. Rueden, S. Saalfeld, B. Schmid, *et al.*, *Nat. Methods*, 2012, **9**, 676–682.
- 40 A. Baddeley, E. Rubak and R. Turner, *Spatial Point Patterns: Methodology and Applications with R*, Chapman and Hall/CRC Press, London, 2015.
- 41 J. Ohser, *Statistics*, 1983, **14**, 63–71.
- 42 J.-Y. Tinevez, N. Perry, J. Schindelin, G. M. Hoopes, G. D. Reynolds, E. Laplantine, S. Y. Bednarek, S. L. Shorte and K. W. Eliceiri, *Methods*, 2017, **115**, 80–90.
- 43 K. Jaqaman, D. Loerke, M. Mettlen, H. Kuwata, S. Grinstein, S. L. Schmid and G. Danuser, *Nat. Methods*, 2008, **5**, 695–702.
- 44 L. Van der Maaten and G. Hinton, *J. Mach. Learn. Res.*, 2008, **9**, 2579–2605.
- 45 M. Ester, H.-P. Kriegel, J. Sander, X. Xu, *et al.*, *Data Min. Knowl. Discov.*, 1998, **2**, 169–194.
- 46 B. Cabukusta and J. Neefjes, *Traffic*, 2018, **19**, 761–769.
- 47 Š. Bálint, I. V. Vilanova, Á. S. Álvarez and M. Lakadamyali, *Proc. Natl. Acad. Sci. U. S. A.*, 2013, **110**, 3375–3380.
- 48 K. Chen, B. Wang and S. Granick, *Nat. Mater.*, 2015, **14**, 589–593.
- 49 V. Zaburdaev, S. Denisov and J. Klafter, *Rev. Mod. Phys.*, 2015, **87**, 483.
- 50 K. Polev, D. V. Kolygina, K. Kandere-Grzybowska and B. A. Grzybowski, *Cells*, 2022, **11**, 270.
- 51 H. D. Pinholt, S. S.-R. Bohr, J. F. Iversen, W. Boomsma and N. S. Hatzakis, *Proc. Natl. Acad. Sci. U. S. A.*, 2021, **118**, e2104624118.
- 52 J. Signer, J. Fieberg and T. Avgar, *Ecol. Evol.*, 2019, **9**, 880–890.
- 53 W. Durso, M. Martins, L. Marchetti, F. Cremisi, S. Luin and F. Cardarelli, *Int. J. Mol. Sci.*, 2020, **21**, 3397.
- 54 A. Rizk, G. Paul, P. Incardona, M. Bugarski, M. Mansouri, A. Niemann, U. Ziegler, P. Berger and I. F. Sbalzarini, *Nat. Protoc.*, 2014, **9**, 586–596.
- 55 D. Ershov, M.-S. Phan, J. W. Pylvänäinen, S. U. Rigaud, L. Le Blanc, A. Charles-Orszag, J. R. Conway, R. F. Laine, N. H. Roy, D. Bonazzi, *et al.*, *Nat. Methods*, 2022, **19**, 829–832.



Supplementary Information: Identification of nanoparticles as vesicular cargo via Airy scanning fluorescence microscopy and spatial statistics

Christian Wimmenauer^a and Thomas Heinzl^{*,a}

^a*Institute of Experimental Condensed Matter Physics, Heinrich-Heine-University, Universitätsstr. 1, 40225 Düsseldorf, Germany, E-Mail: thomas.heinzl@uni-duesseldorf.de*

1 Details Spatial Statistics

1.1 Spatial statistics summary functions

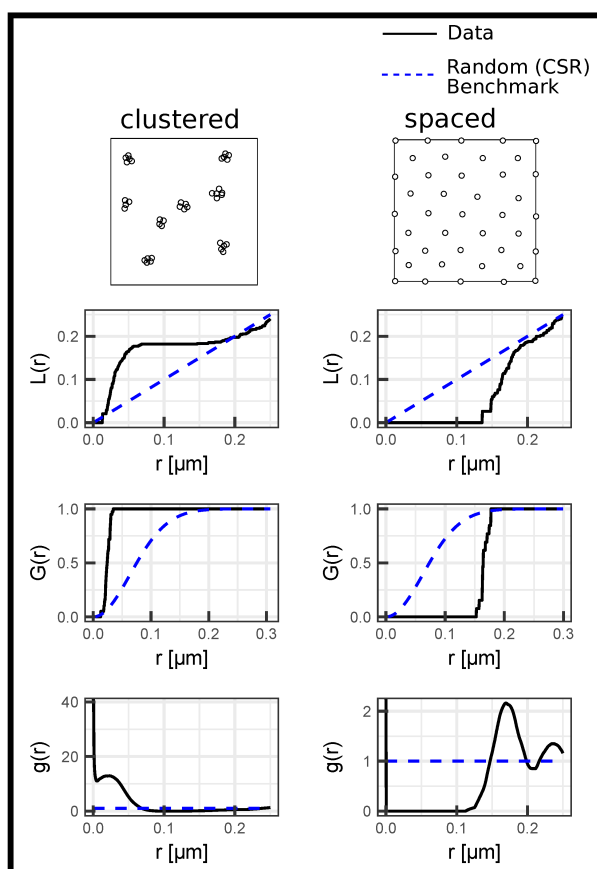


Figure 1: Univariate summary functions of a manually generated clustered (left) and a spaced (right) point pattern to illustrate the respective behaviour in these cases.

1.2 Monte Carlo Simulations

1.2.1 Complete Spatial Randomization of a single channel

To generate point patterns that display complete spatial randomness in one of the color channels the points in color channel 2 are sampled from a continuous uniform distribution inside the region of interest (ROI), while the positions of the points in channel 1 in the generated pattern match the positions in the measured data. The number of generated random points was chosen to match the number of points from the measurement.

1.2.2 Transport Simulation

First a lognormal distribution

$$lnorm_{\mu,\sigma}(x) = \frac{1}{\sqrt{2\pi}\sigma x} \exp \left[-\frac{(\log(x) - \mu)^2}{2\sigma^2} \right]$$

is fitted to the histogram of nearest neighbour distances between the first and second color channel points in the point pattern, to estimate reasonable parameters for the mean μ and standard deviation σ on the logarithmic scale. The positions of the channel 1 points in the simulation are unaltered compared to the measurement $\vec{r}'_{1,i} = \vec{r}_{1,i}$. The positions of the channel 2 points in the simulation $\vec{r}'_{2,i}$ are calculated by shifting the positions of the channel 1 points $\vec{r}_{1,i}$ by $\Delta\vec{r}_{\mu,\sigma,i}$.

$$\vec{r}'_{2,i} = \Delta\vec{r}_{\mu,\sigma,i} + \vec{r}_{1,i}$$

The shift vector $\Delta\vec{r}_{\mu,\sigma,i}$ is randomly sampled

$$\Delta\vec{r}_{\mu,\sigma,i} = \rho_{\mu,\sigma} \begin{pmatrix} \cos(\theta) \\ \sin(\theta) \end{pmatrix}$$

, where $\rho_{\mu,\sigma}$ is sampled from $lnorm_{\mu,\sigma}(x)$ and $\theta \in [0, 2\pi]$ is sampled from a continuous uniform distribution. If the resulting $\vec{r}'_{2,i}$ lies outside of the defined ROI a new shift vector $\Delta\vec{r}_{\mu,\sigma,i}$ is sampled until the resulting $\vec{r}'_{2,i}$ lies inside of the ROI. This process is repeated for every channel 1 point $\vec{r}_{1,i}$.

The number of generated points is subsequently altered to ensure that the number of generated points in channel 2 is equal to the number of measured points in channel 2. If the number of points in channel 2 in the measurement n_m is greater than the number points in channel 2 in the simulation n_s ($n_m > n_s$), a total of $n_m - n_s$ channel 2 points sampled from a continuous uniform distribution in the ROI are added to the simulated point pattern in channel 2. If on the other hand $n_m < n_s$, a total of $n_s - n_m$ randomly selected channel 2 points are removed from the simulated point pattern.

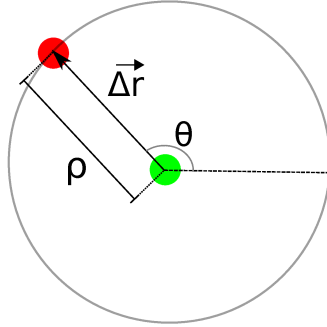


Figure 2: Construction of the shift vector $\Delta\vec{r}$ from the randomly sampled variables ρ and θ

2 Colocalisation: Supporting Data

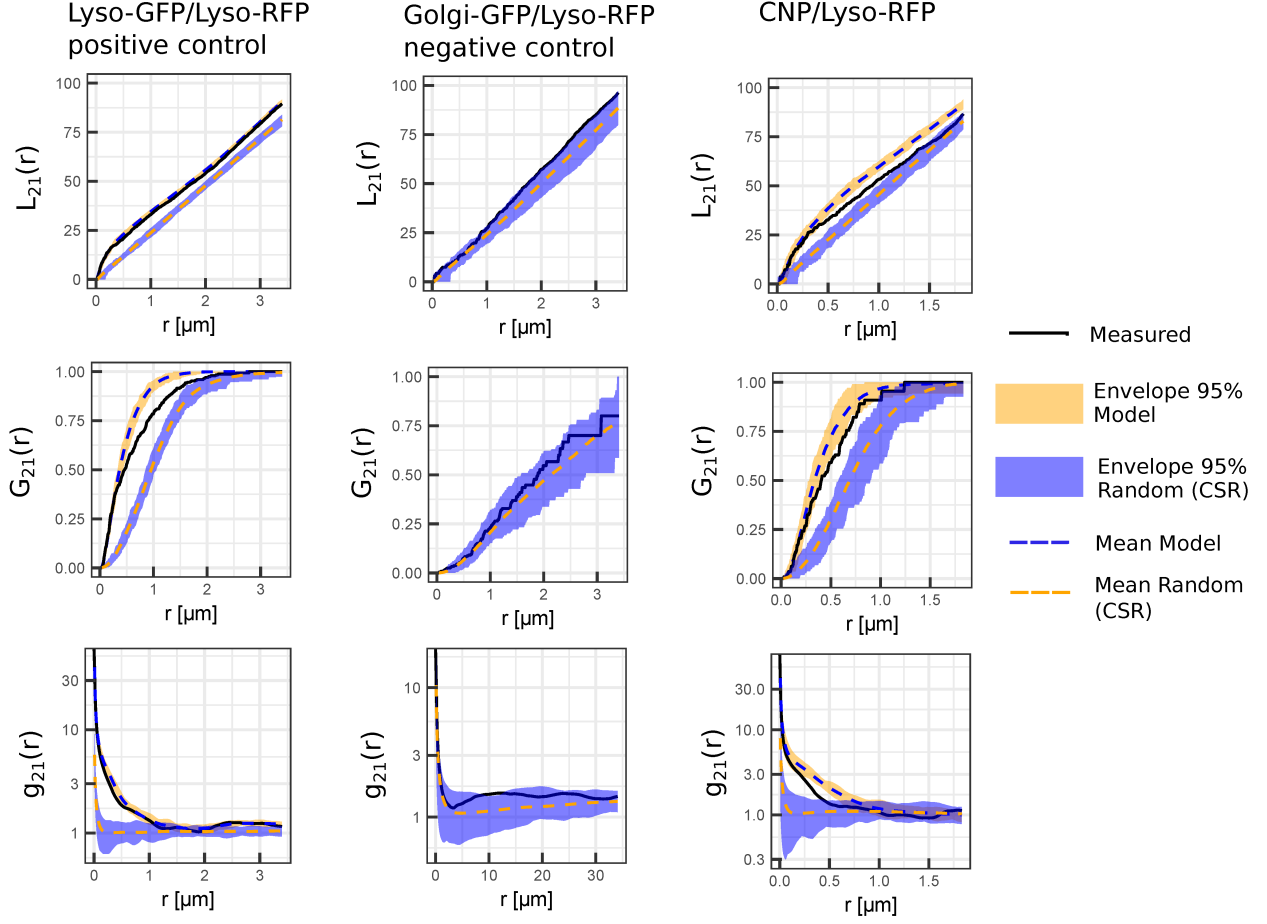


Figure 3: Complementary summary functions to the panel in the main article. Here the color channels 1 and 2 have been exchanged in the calculation of the bivariate summary functions (e.g. $g_{21}(r)$ is shown instead of $g_{12}(r)$). It becomes apparent, that the character of the summary functions persists. Furthermore, the L-Function is shown in this panel, which is in large parts redundant to the pair correlation function and is thus not discussed in the main article.

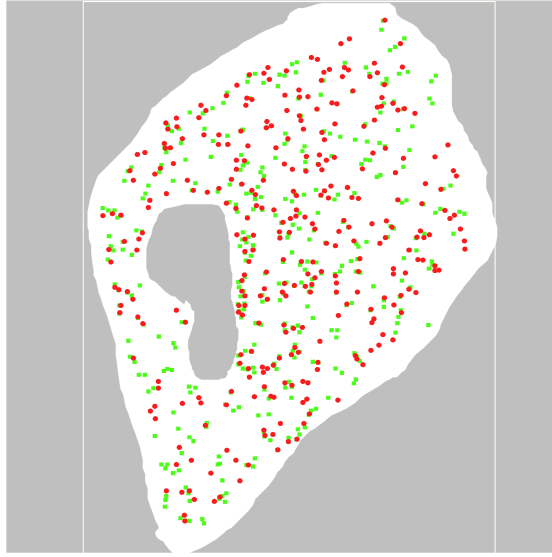


Figure 4: Point pattern with ROI for Lysosomes-GFP/Lysosomes-RFP for the case discussed in the main article.

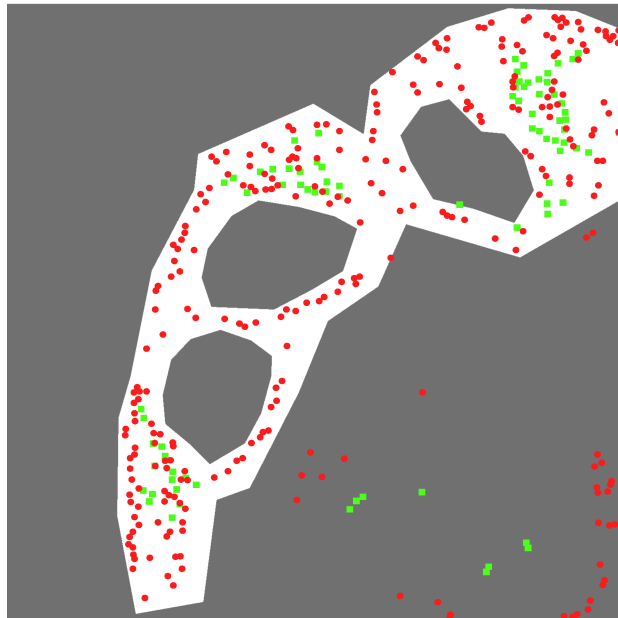


Figure 5: Point pattern with ROI for Golgi-GFP/Lysosomes-RFP for the case discussed in the main article.

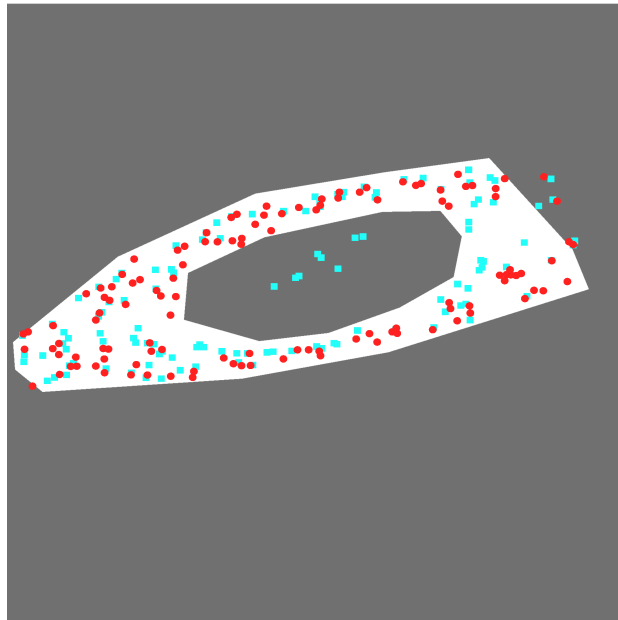


Figure 6: Point pattern with ROI for CND/Lysosomes-RFP for the case discussed in the main article.

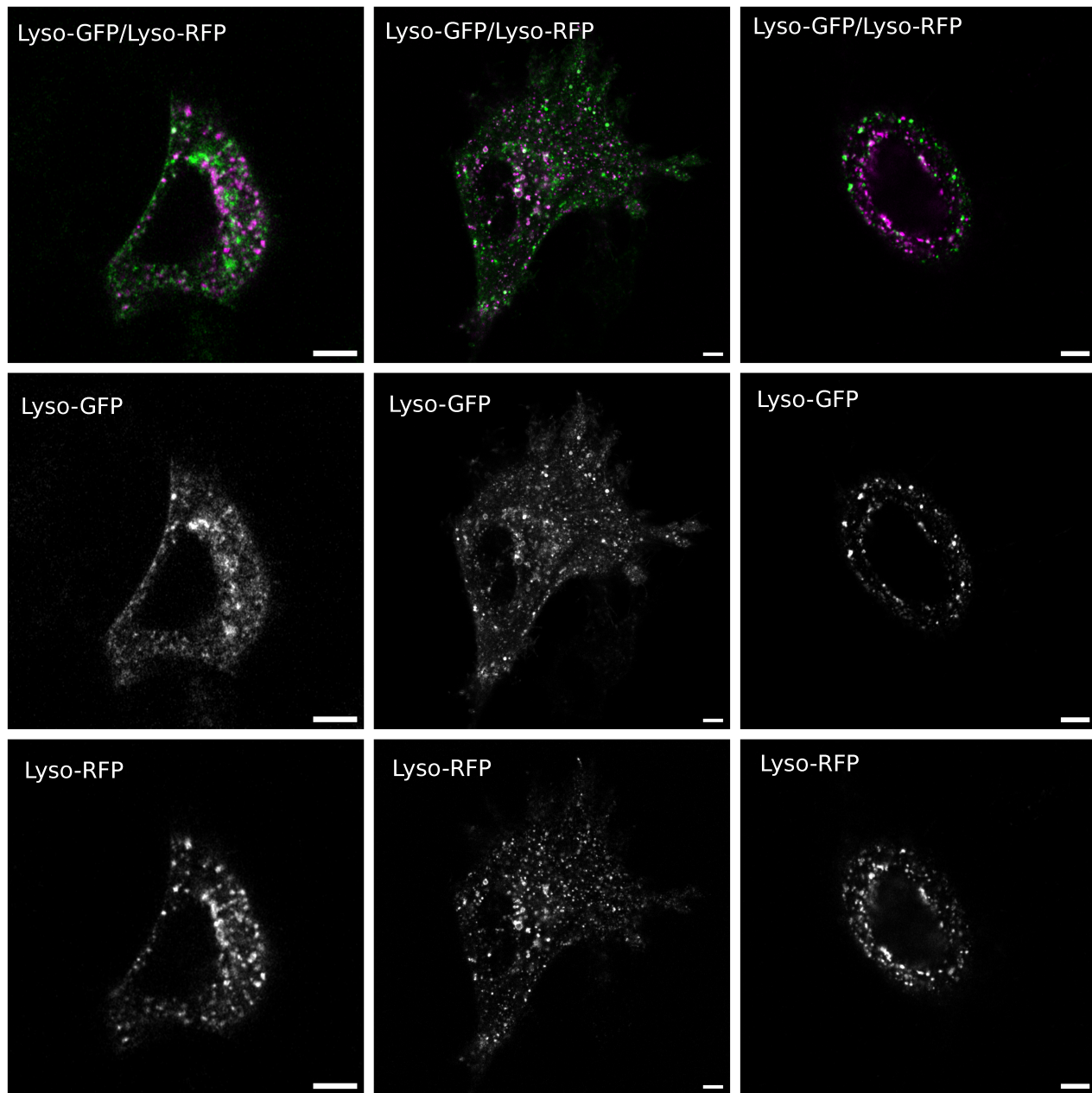


Figure 7: Further microscopy images for Lysosomes-GFP/Lysosomes-RFP. The size of the shown scale bars amounts to 5 μm .

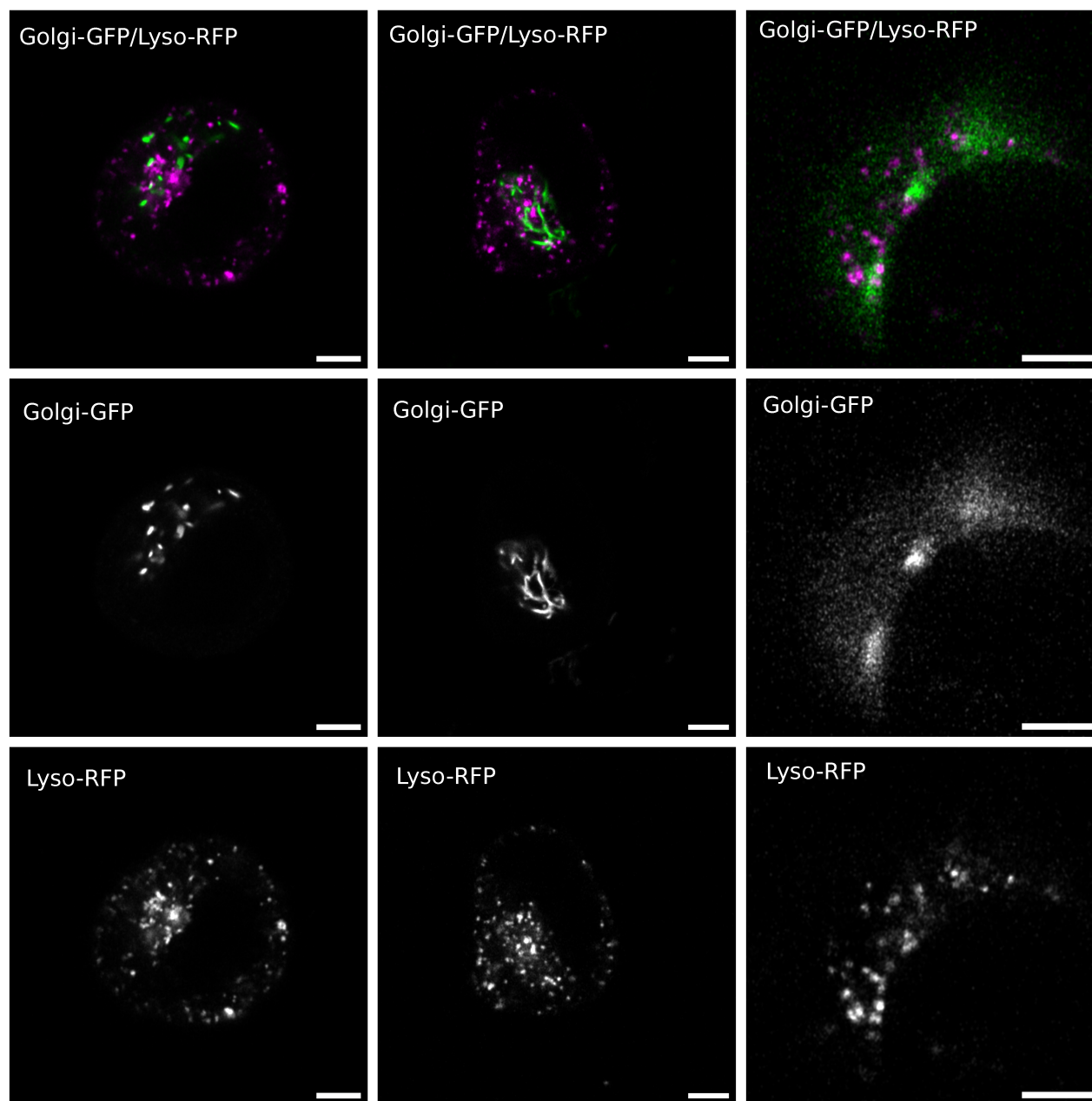


Figure 8: Further microscopy images for Golgi-GFP/Lysosomes-RFP. The size of the shown scale bars amounts to 5 μ m.

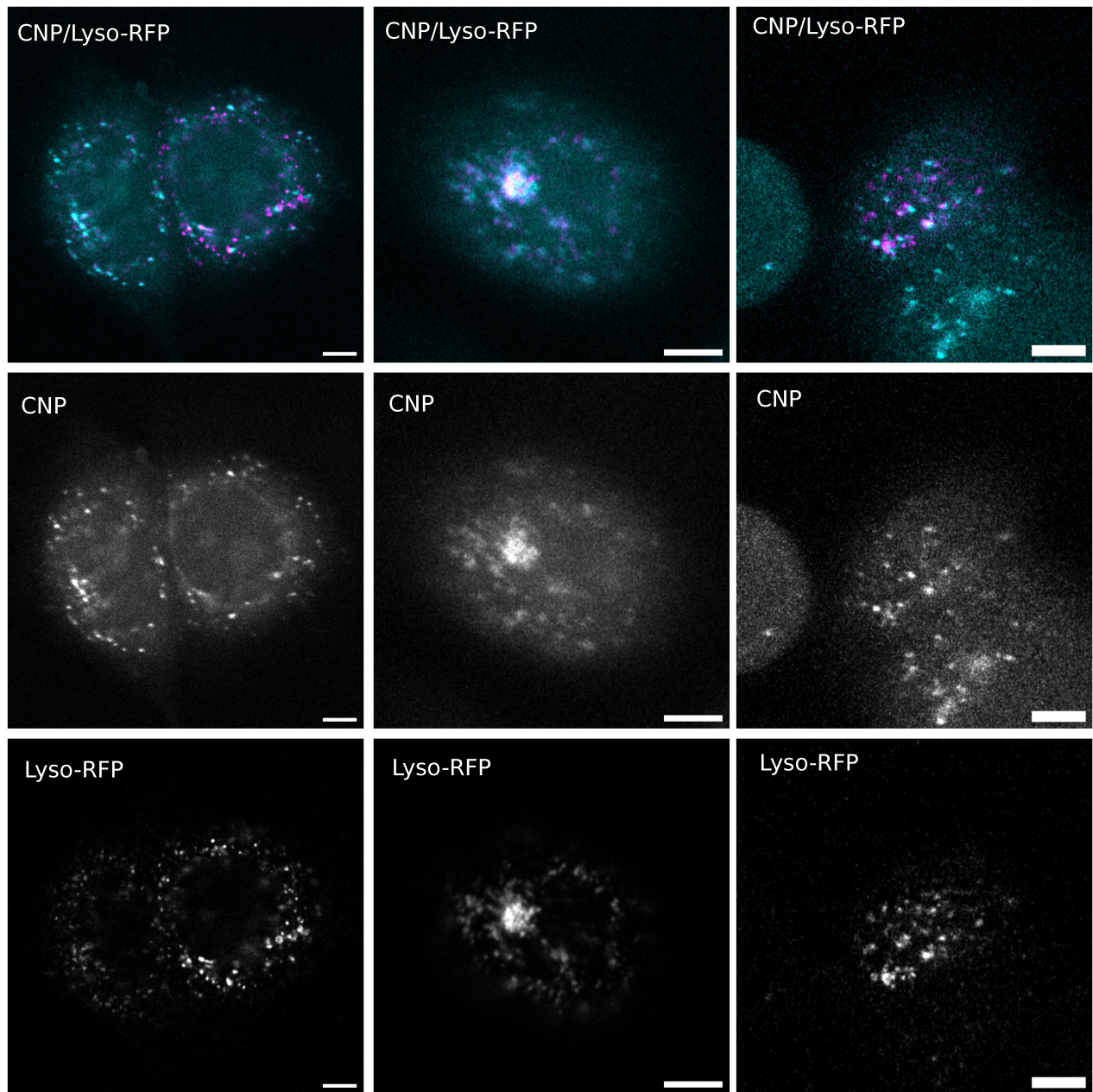


Figure 9: Further microscopy images for CNP/Lysosomes-RFP. The size of the shown scale bars amounts to 5 μm .

3 Single Particle Tracking

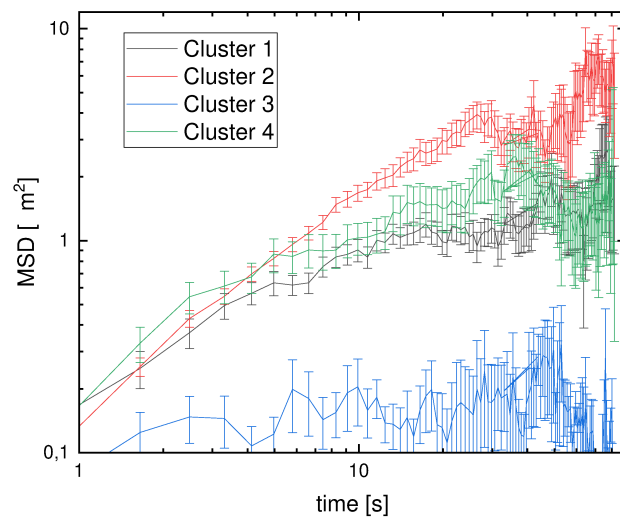


Figure 10: Ensemble averaged mean square displacement plotted against time for all 100 time points.

3.1 Identification of movement patterns via cluster analysis on particle tracking data

3.1.1 Cluster Analysis via tSNE and DBSCAN

To distinguish between different types of motion in the single particle tracking data eight different metrics were calculated. The first four are moments of the distribution of jump distances, namely the mean, the standard deviation, the skewness and the kurtosis of the jump distances in a single track. The four other metrics are global characteristics of the tracks namely the mean squared displacement msd ¹, the turn angle correlation tac ², the straightness¹ and the sinuosity³ that were calculated with the *movement_metrics()* function from the *amt-package*¹. The metrics are given by:

$$msd = \frac{1}{N} \sum_{i=1}^N [(x_i - \bar{x})^2 + (y_i - \bar{y})^2] \quad (1)$$

$$tac = \frac{1}{N} \sum_{i=1}^{N-1} [(\cos(\alpha_{i+1}) - \cos(\alpha_i))^2 + (\sin(\alpha_{i+1}) - \sin(\alpha_i))^2] \quad (2)$$

$$\text{straightness} = \frac{\text{total distance}}{\text{cumulative distance}} \quad (3)$$

$$\text{sinuosity} = 2 \left[p \left(\frac{1 - c^2 - s^2}{(1 - c)^2 + s^2} + b^2 \right) \right]^{-0.5} \quad (4)$$

With the number of points in a track N , the i -th x- (y-)Koordinate x_i (y_i), the i -th turn angle α_i , the mean step length p , the mean cosine (sine) of α (c (s)) and the coefficient of variation of step length b . A point in the eight-dimensional space spanned by these metrics is calculated for each track. Prior to the cluster analysis the dimensionality reduction algorithm tSNE⁴ is applied mapping the data to two coordinates while preserving the local properties of the eight-dimensional dataset. Clusters are analysed with DBSCAN⁵. For tSNE a perplexity of $perp = 30$ was chosen and for DBSCAN the hyperparameters $\epsilon = 1.9$ and $minPts = 5$ were chosen. The resulting clusters are displayed in Figure 11. The ensemble averaged mean squared displacement at time t was calculated for each individual cluster (Figure 10).

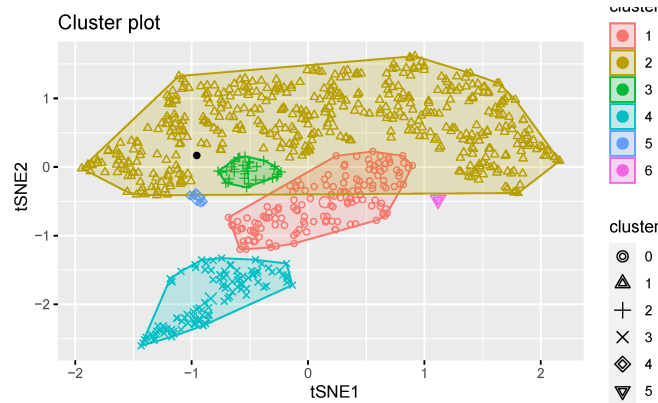


Figure 11: Plot of the DBSCAN clustering on the tSNE-transformed movement metrics for the particle trajectories.

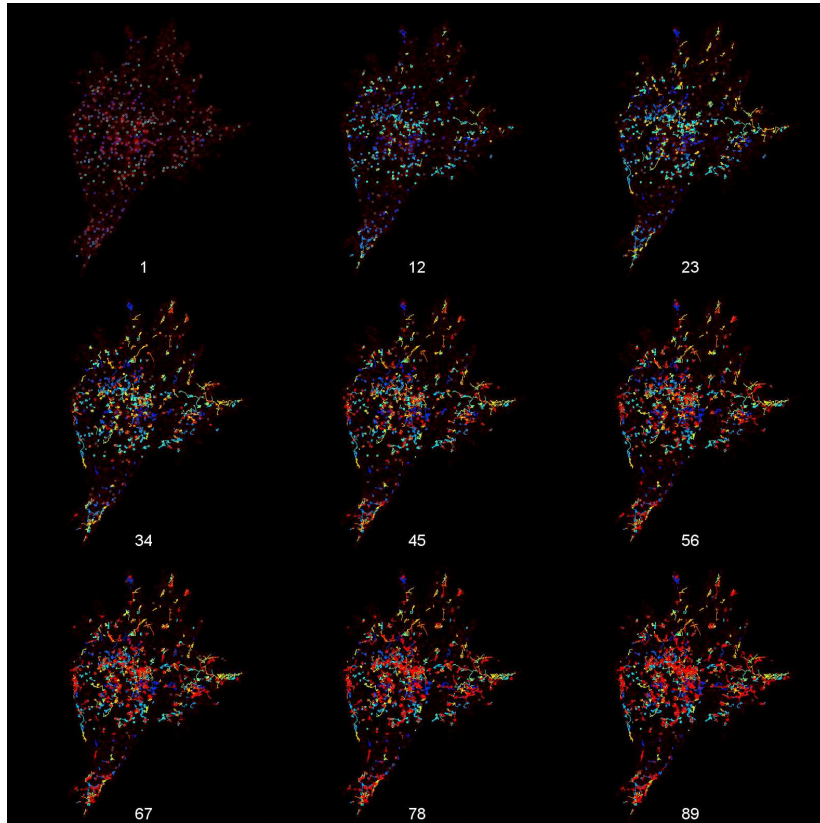


Figure 12: Single particle tracking time series data. The index of the image indicating the position in the time series is displayed in the lower right corner.

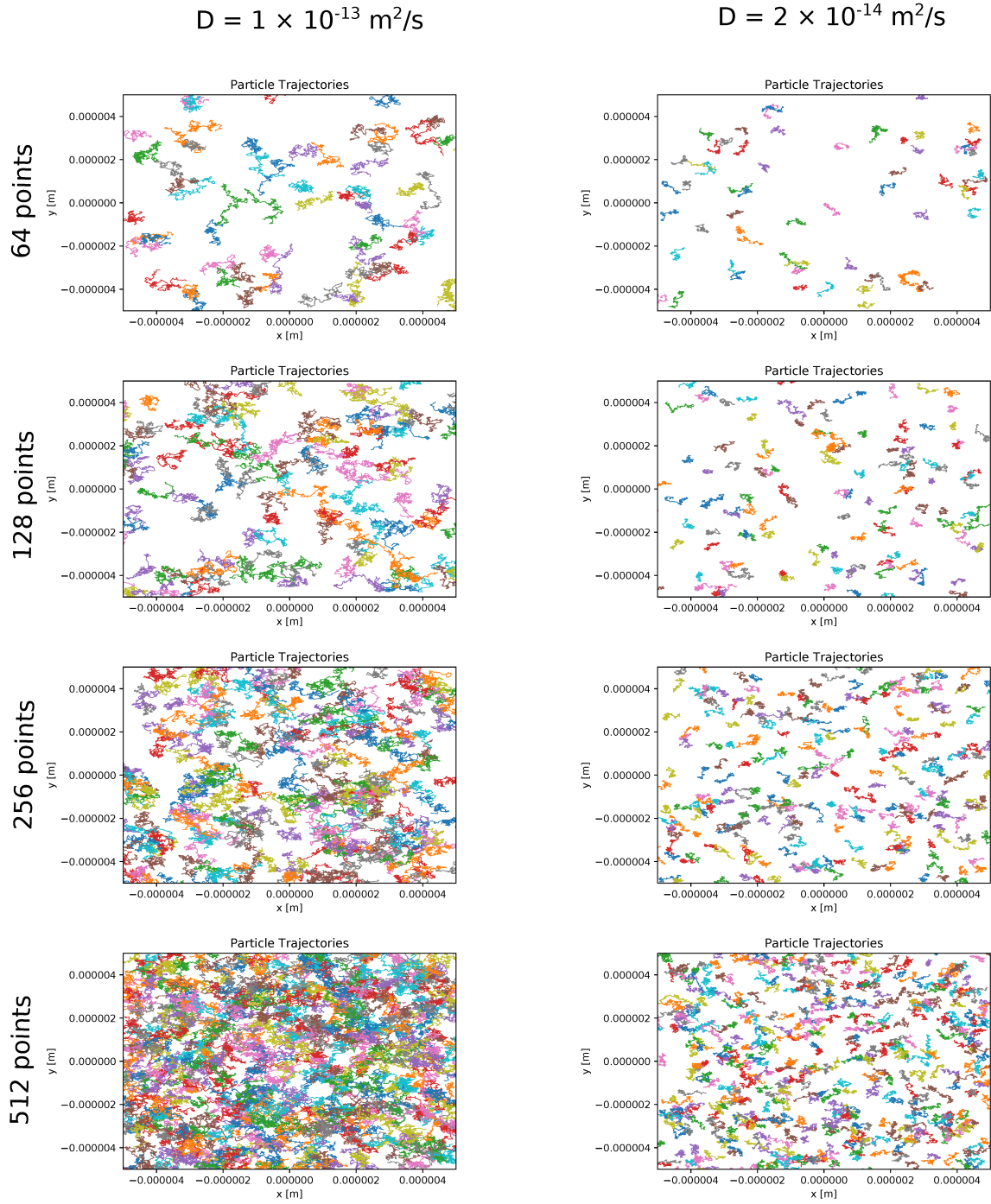


Figure 13: Synthetic data of a diffusion process with a diffusion constant of $D = 1 \times 10^{-13} \frac{\text{m}^2}{\text{s}}$ (left column) and $D = 2 \times 10^{-14} \frac{\text{m}^2}{\text{s}}$ (right column) on a $10\mu\text{m} \times 10\mu\text{m}$ region of interest. The positions of the particles were initialized with a Poisson point process. The number of particles, and therefore the degree of crowding, here increase from top to bottom.

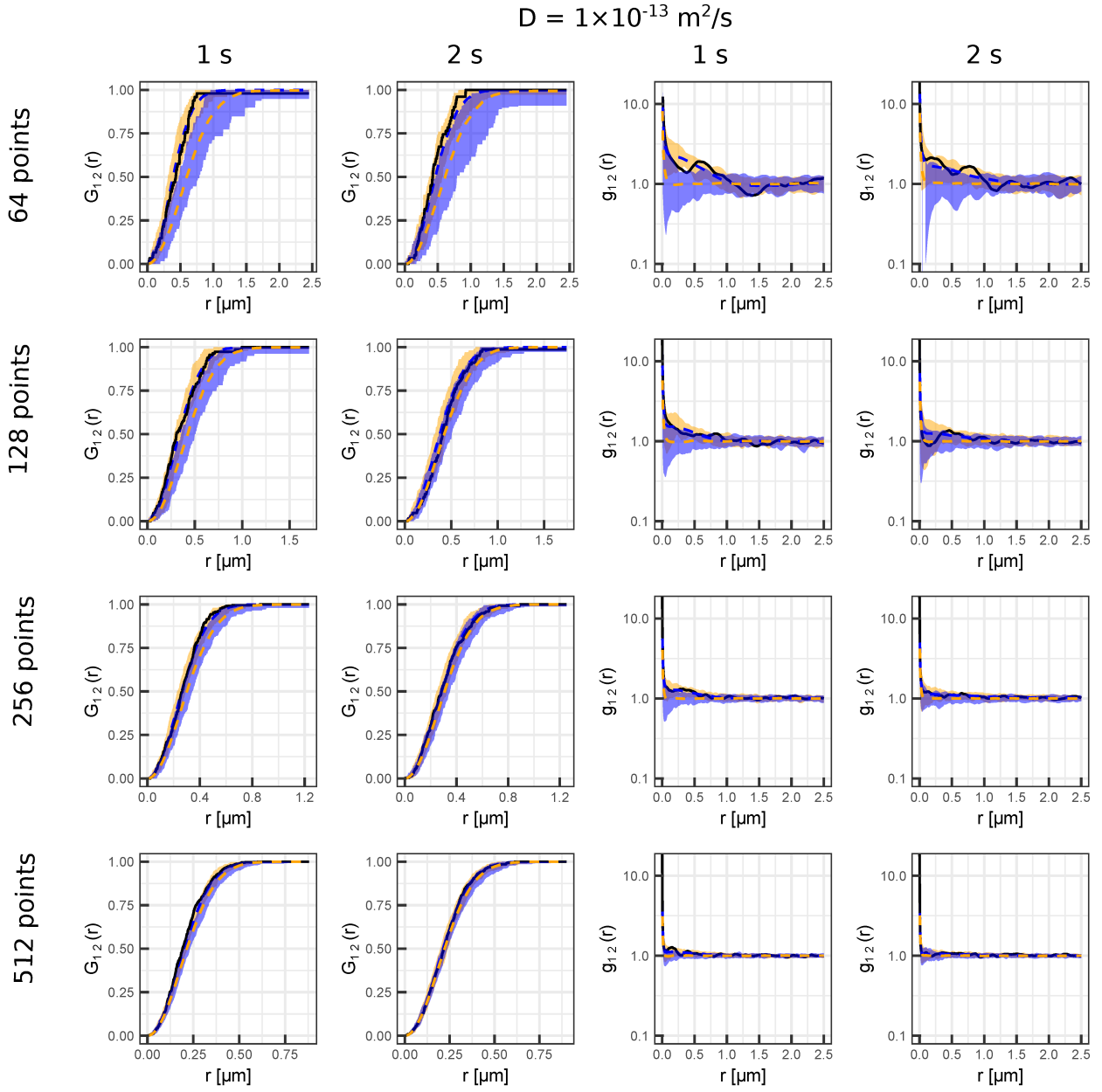


Figure 14: Bivariate pair correlation functions $g_{12}(r)$ and nearest neighbor functions $G_{12}(r)$ (shown as solid black line) calculated from the synthetic data displaying diffusion shown in the left column ($D = 1 \cdot 10^{-13} \frac{\text{m}^2}{\text{s}}$) of figure 13 after 1 s and 2 s correlated with the starting distribution, respectively. The envelope of CSR is displayed in blue, while the envelope of a Monte Carlo simulation of diffusive transport via a 2D Gaussian function is drawn in orange. The number of particles increases from top to bottom illustrating the effect of crowding on the spatial statistics analysis.

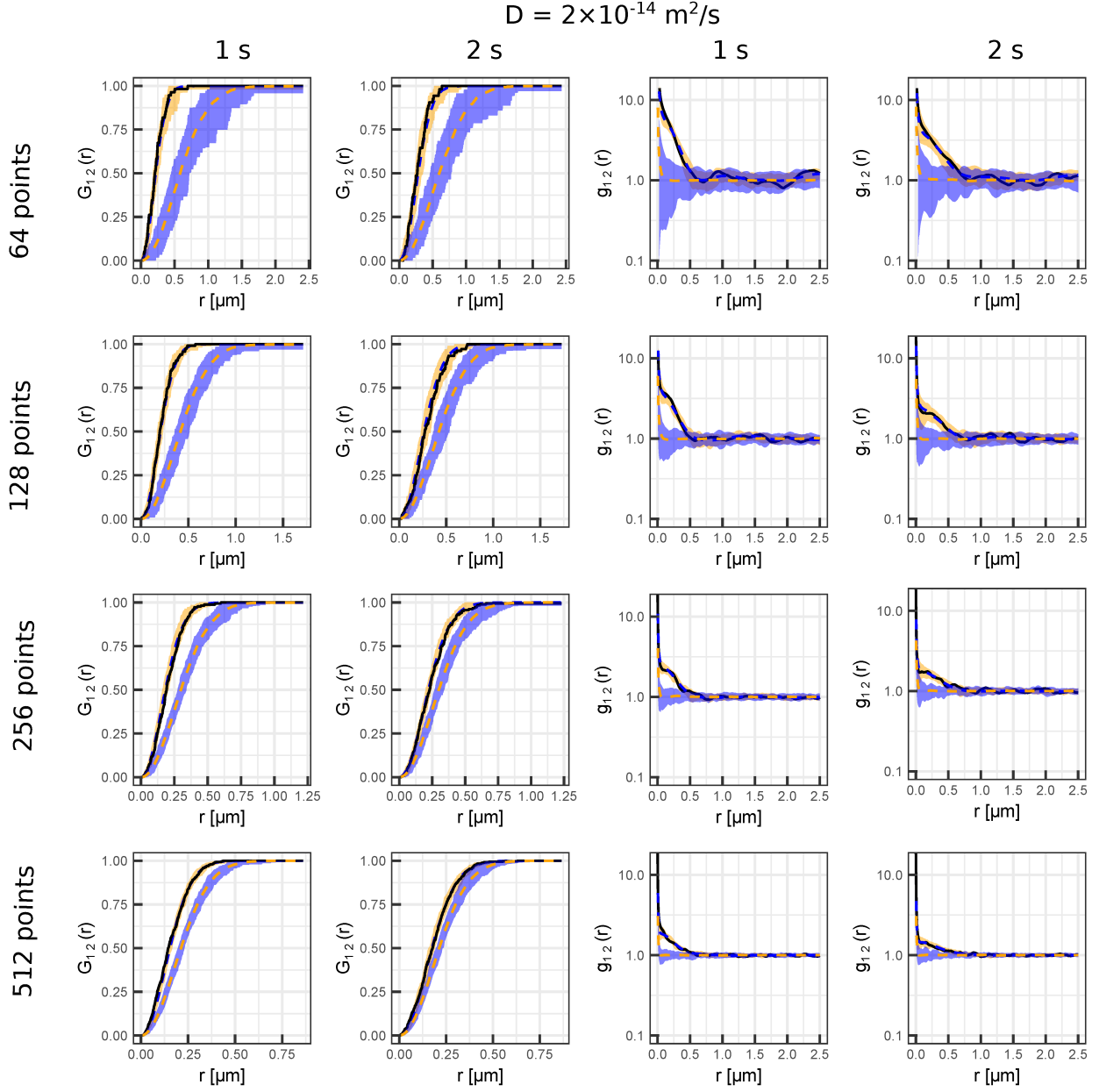


Figure 15: Bivariate pair correlation functions $g_{12}(r)$ and nearest neighbor functions $G_{12}(r)$ (shown as solid black line) calculated from the synthetic data displaying diffusion shown in the right column ($D = 2 \times 10^{-14} \frac{\text{m}^2}{\text{s}}$) of figure 13 after 1s and 2s correlated with the starting distribution, respectively. The envelope of CSR is displayed in blue, while the envelope of a Monte Carlo simulation of diffusive transport via a 2D Gaussian function is drawn in orange. The number of particles increases from top to bottom illustrating the effect of crowding on the spatial statistics analysis.

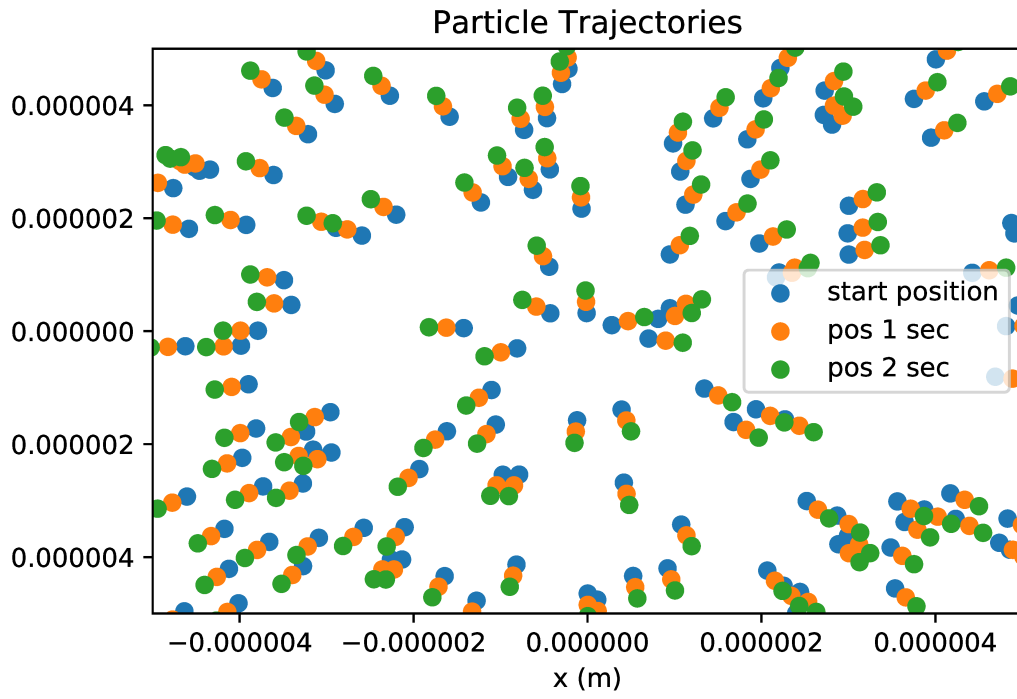


Figure 16: Synthetic bivariate point pattern generated by radial drift as an example of a purely directed motion. The point pattern at $t = 0$ is sampled from a random uniform distribution on a $10\mu m \times 10\mu m$ region of interest. The patterns at $t = 1s$ and $t = 2s$ are generated by shifting the points in radial direction with a velocity of $2 \times 10^{-9} \frac{m}{s}$.

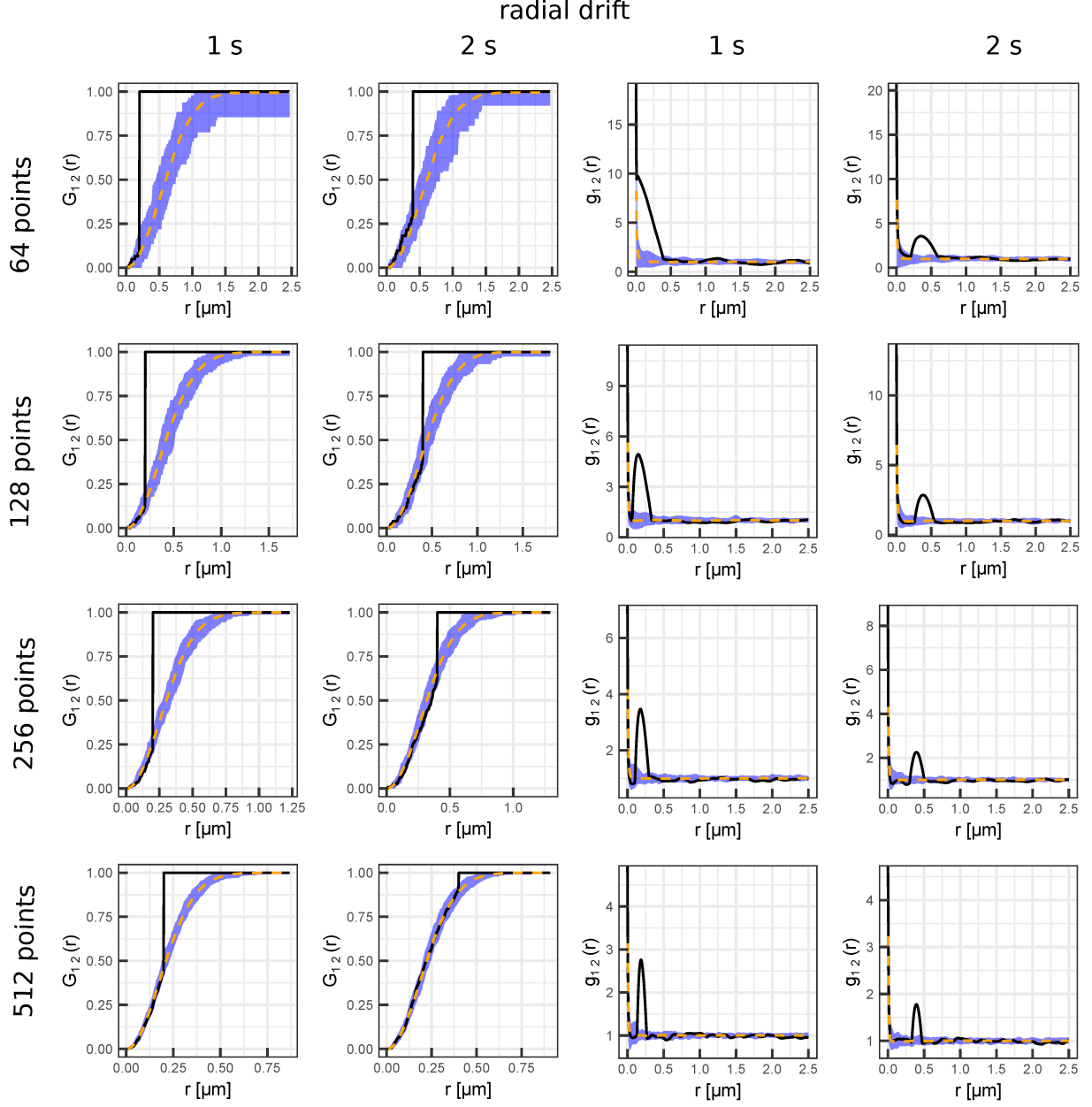


Figure 17: Bivariate pair correlation functions $g_{12}(r)$ and nearest neighbor functions $G_{12}(r)$ (shown as solid black line) calculated from the synthetic data of the point pattern from figure 16, which is subject to a radial drift of a constant velocity of $2 \times 10^{-9} \frac{\text{m}}{\text{s}}$. The summary functions $G_{12}(r)$ and $g_{12}(r)$ were calculated between the starting distribution and the distributions after $t = 1 \text{ s}$ and $t = 2 \text{ s}$, respectively. The envelope of CSR in channel 2 is shown in blue. The number of particles increases from top to bottom illustrating the effect of crowding on the spatial statistics analysis. Note that $G_{12}(r)$ becomes indistinguishable from CSR with increasing particle density.

References

- [1] J. Signer, J. Fieberg and T. Avgar, *Ecology and evolution*, 2019, **9**, 880–890.
- [2] B. Abrahms, D. P. Seidel, E. Dougherty, E. L. Hazen, S. J. Bograd, A. M. Wilson, J. Weldon McNutt, D. P. Costa, S. Blake, J. S. Brashares *et al.*, *Movement ecology*, 2017, **5**, 1–11.
- [3] P. J. Almeida, M. V. Vieira, M. Kajin, G. Forero-Medina and R. Cerqueira, *Zoologia (Curitiba)*, 2010, **27**, 674–680.
- [4] L. Van der Maaten and G. Hinton, *Journal of machine learning research*, 2008, **9**, 2579–2605.
- [5] M. Ester, H.-P. Kriegel, J. Sander, X. Xu *et al.*, *kdd*, 1996, pp. 226–231.

Chapter 4

Differential uptake of carbon nanodots

For some applications, such as drug delivery in tumor chemotherapy (briefly presented in section 1.3), it is desirable that nanoparticles show a differential uptake. Ultimately, the selective addressing of different subgroups, such as healthy and malignant cells, is of interest. Before any attempts are made to functionalize the particles, in order to facilitate cell-specific uptake, it is useful to first examine the uptake of the unmodified particles. Thus, the differential uptake into different subsets of samples from healthy donors and samples from AML patients was investigated in *Paper II*. Here, flow cytometry that was introduced in section 2.3 was used to characterize the individual cells. Furthermore, in an attempt to modify the cell-specific uptake, CNDs were glycofunctionalized with the sugar monomers mannose and galactose as well as with sugar-decorated oligomers. This study is presented in *Paper III*. While no differential uptake between the investigated cell types was observed, the different nanoparticle conjugates showed altered uptake rates across all tested cell lines.

4.1 Paper II

Reference

Reproduced from [C. Nollmann, C. Wimmenauer, S. Fasbender, S. Mayer, R. P. Cadeddu, P. Jäger, T. Heinzl and R. Haas (2021). Uptake of carbon nanodots into human AML cells in comparison to primary hematopoietic cells. RSC advances, 11(42), 26303-26310. <https://doi.org/10.1039/D1RA05033H>], with the permission of The Royal Society of Chemistry

Copyright statement

This article is licensed under a Creative Commons Attribution 3.0 Unported License. Material from this article can be used in other non-commercial publications provided that the correct acknowledgement is given with the reproduced material.

Contributions

I participated in the preparation of the nanoparticles and data analysis related to the flow cytometry measurements together with CN and SM, from planning to execution. I planned and performed the microscopy experiments and took a minor role in manuscript writing. Furthermore, I have taken over administrative tasks concerning the ethics vote.


Cite this: *RSC Adv.*, 2021, **11**, 26303

Uptake of carbon nanodots into human AML cells in comparison to primary hematopoietic cells†

Cathrin Nollmann,^a Christian Wimmenauer,^a Stefan Fasbender,^a Saskia Mayer,^b Ron-Patrick Cadeddu,^b Paul Jäger,^b Thomas Heinzel^{id}*^a and Rainer Haas^{*,b}

Carbon nanodots (CNDs) comprise a class of next generation nanomaterials with a wide variety of potential applications. Here, we report on their uptake into primary hematopoietic cells from three normal donors and malignant cells from five patients with *de novo* acute myeloid leukemia (AML). A significant CND uptake was observed in all cell types of the normal and leukemic cells. Still, the uptake was significantly smaller for the CD34⁺ and CD33⁺ myeloid subsets of the malignant cell population as compared to the normal blood-derived CD34⁺ and CD33⁺ cells. For the T and B lymphoid cell populations as defined by CD3 and CD19 within the leukemic and normal samples a similar uptake was observed. The CNDs accumulate preferentially in small clusters in the periphery of the nucleus as already shown in previous studies for CD34⁺ progenitor/stem cells and human breast cancer cells. This particular subcellular localization could be useful for targeting the lysosomal compartment, which plays a pivotal role in the context of autophagy associated survival of AML cells. Our results demonstrate the usability of CNDs beyond their application for *in vitro* and *in vivo* fluorescence labeling or drug delivery into normal and malignant cells.

Received 29th June 2021

Accepted 27th July 2021

DOI: 10.1039/d1ra05033h

rsc.li/rsc-advances

1. Introduction

Carbon nanodots, the family of carbon based, nanometer-sized particles which includes graphene quantum dots as well as small graphitic crystallites, have a large surface to volume ratio and excellent biocompatibility,^{1,2} and studying new ways for their production is still an active field of research.^{3–6} Since they also show fluorescence with advantageous properties in an aqueous environment, CNDs have been widely used in biomedical studies,^{3,7–9} although the origin of the fluorescence is still under debate.^{10–13} As far as living cells are concerned, CNDs enter the cytoplasm of many human cell lines as well as of primary human blood cells, without significant effects on the cell viability.^{14–19} As for other nanoparticles, CNDs have been used in studies for cancer diagnosis or drug delivery.^{20–26} In this context, the question arises whether the uptake of CNDs by malignant primary cells differs from that observed for healthy cells.

We therefore investigated the uptake of CNDs into leukemic cells that were freshly obtained from patients with *de novo* acute myeloid leukemia. In the majority of patients with this kind of leukemia, the pathological blasts resemble their normal

counterparts to some extent, in particular with respect to the expression of particular lineage- and differentiation associated surface molecules. Between those, CD34 and CD33 are prominent representatives reflecting an early stemness phenotype and myeloid differentiation, respectively. Our focus was on the aspect whether there is a differential uptake between primary human blood cells and leukemic cells, which could be of translational relevance.

2. Experimental section

2.1 Patients according to AML classification

The AML can be divided into different subtypes. The most commonly used classification schemes are the French–American–British (FAB)²⁷ and the World Health Organization (WHO)²⁸ system. The FAB classification is based on cytomorphological and cytochemical criteria, while the more recent WHO classification combines the FAB classification with immunological, cyto- as well as molecular genetic alterations. Table 1 lists the WHO and FAB classifications of the AML samples used in our study, as well as the percentage of blasts in the bone marrow and peripheral blood. The AML samples fall into different FAB categories permitting to some extent a subtype related assessment of the uptake.

2.2 Materials

Citric acid (ACS reagent, ≥99.5%), Diethylentriamine (DETA, 99%), Dulbecco's Phosphate Buffered Saline (DPBS), Lysis

^aCondensed Matter Physics Laboratory, Heinrich-Heine-University, 40204 Düsseldorf, Germany. E-mail: Thomas.Heinzel@hhu.de

^bDepartment of Haematology, Oncology and Clinical Immunology, Heinrich-Heine-University, 40204 Düsseldorf, Germany. E-mail: Haas.med@uni-duesseldorf.de

† Electronic supplementary information (ESI) available. See DOI: 10.1039/d1ra05033h



Table 1 WHO and FAB classifications of the five AML samples and the percentage of blasts in bone marrow (BM) and peripheral blood (PB)

Sample	WHO classification	FAB classification	Percentage of blasts
AML 1	AML with MDS-associated modifications	AML M0	PB: 39% BM: 32%
AML 2	AML with MDS-associated modifications	AML M2	PB: 65% BM: 69%
AML 3	Acute leukemia, assignment unclear	AML M4/5	PB: 10% BM: 40%
AML 4	AML without further cytometric or molecular genetic specification	AML M2	PB: 1% BM: 57%
AML 5	AML without further cytometric or molecular genetic specification	AML M1	PB: 77% BM: 85%

Buffer, Float-A-Lyzer dialysis devices (100–500 Da). Antibodies against CD45-PE-Cy7, CD34-PerCP-Cy5.5, CD33-PE, CD19-APC-R700 and CD3-APC-H7 were purchased from BD biosciences. Stem SPAN™ SFEM medium was bought at STEMCELL™ Technologies and microwave reaction vessels were obtained from CEM GmbH. NucBlue™ Live ReadyProbes™ Reagent (Invitrogen™), Poly-L-Lysine coated 8 well μ -slide was obtained from ibidi.

2.3 Preparation and characterization of CNDs

The CNDs were prepared and characterized exactly as described in detail elsewhere.¹⁸ In brief, fluorescent CNDs were synthesized according to the method of Qu *et al.*²⁹ with slight modifications. 210 mg citric acid and 340 mg Diethylenetriamine (DETA) were mixed and heated to 180 °C for 150 s in a closed microwave reaction chamber (CEM Discover). The resulting viscous liquid was dissolved in 10 ml DI water. Citric acid, DETA and very small particles were removed by dialysis for 72 h, using a 100–500 Da membrane, with two water exchanges every 24 h. Afterwards, the CND solution was freeze-dried and dissolved for further use. The CNDs were characterized by scanning probe microscopy, transmission electron microscopy as well as by Raman- and XPS spectroscopy. These measurements indicate that the CNDs are composed of the mass fractions 40% C, 33% O, 19% N and 8% H. About 30% of the carbon bonds are C–C bonds, and the Raman spectra reveal their mixture of sp^2 with sp^3 hybridization. The average size of the CNDs was (3.3 ± 0.6) nm. Some particles showed a hexagonal crystal symmetry in the TEM with a lattice constant of approximately 220 pm, which is 10% smaller than that one of free-standing graphene. Hence, we conclude that the CNDs are particles with mixed crystal structures of graphene-, graphite- and possible diamond-type sections. Their photoluminescence properties are most relevant for the present study. They were measured using a Horiba FluoroMax®-4 spectrofluorometer, while the absorbance spectra were taken with an Agilent Cary 4000 spectrophotometer. The absorbance shows a peak around 360 nm wavelength of approximately 80 nm linewidth (full width at half maximum-FWHM). To avoid UV exposure of the cells, we excited the CNDs with light of $\lambda = 400$ nm, yielding a fluorescence spectrum centered at $\lambda = 460$ nm (FWHM ≈ 100 nm), which fits well into the V450 channel of the flow cytometer (see below), which we used for their detection. The quantum yield of the CNDs was 23%.²⁰ Since our particles do not show a fluorescence wavelength that differs from the values expected for size quantization and furthermore contain structural elements, like sp^3 hybridizations, that should be absent in graphene, we refer to

them as carbon nanodots. These nanoparticles are selected for the present study for several reasons. First of all, it has been shown earlier that they have a small toxicity and almost no influence on the gene expression of the exposed cells.¹⁹ Second, they have a small mass and are thus expected to exert only a marginal influence on the dynamics of attached macromolecules of interest. Finally, they are relatively simple to prepare, show a competitive quantum yield and have a long shelf life of several months.

2.4 Collection of leukapheresis derived blood samples from normal donors

Primary hematopoietic cells were obtained from leukapheresis products (LP) of three healthy individuals who served as HLA-identical donors for an allogeneic blood stem cell transplantation using the granulocyte colony stimulating factor (G-CSF) at a dose of 480 μ g per day over a period of five days. This increases the number of circulating human progenitor and stem cells (HSCs) – as characterised by the expression of CD34 on the cell surface – in the peripheral blood. This kind of LP samples are furthermore enriched with mononuclear blood cells (MNCs) including T and B cells, monocytes and CD34⁺ HSCs.^{30–32} The samples also contain a significant percentage of granulocytes which are activated due to the exposure to G-CSF for five days.³³

2.5 Cell preparation

Blood samples from LPs of three healthy donors and AML samples from five patients *de novo* AML were used for the *in vitro* studies. In order to remove the erythrocytes, the samples from the donors and from the patients were lysed with 50 ml ammonium chloride, once and twice, respectively. For all samples, the remaining leukocytes were resuspended in 50 ml PBS and centrifuged for 5 min at 300 g. Cell pellets were resuspended in 2 ml PBS. 3 ml per well of StemSpan™ Serum-Free Expansion Medium (SFEM) were dispensed in six well plates and appropriate amounts of cell suspension were added, resulting in a final concentration of 2×10^6 cells per ml.

2.6 Cultivation of the cells for CND uptake studies

CNDs were dissolved in PBS at concentrations of 20 mg ml^{−1}. The obtained solutions were sterile filtered. 75 μ l of CND solution, corresponding to a concentration of 500 μ g ml^{−1}, was added to the cell culture. The same amount of PBS without CNDs was added to the wells serving as negative control. The cells were cultivated in a Heracell™ 150i incubator in



a humidified atmosphere at 5% CO₂ and 37 °C. After 24 h, all samples were washed twice with PBS (centrifugation for 5 minutes at 300 g) and stained with antibodies as described in detail below.

2.7 Flow cytometry workflow

To study the differential uptake of CNDs in the various subpopulations of primary human blood cells and leukemic cells, monoclonal antibodies directed against lineage and differentiation specific antigens, *i.e.*, CD45-PE-Cy7, CD34-PerCP-Cy5.5, CD33-PE, CD19-APC-R700 and CD3-APC-H7 were used. The cells were incubated for 15 minutes in the dark with 2 μ l diluted CD45 (1 : 10 with PBS), 2.5 μ l CD34, 2.5 μ l CD33, 1 μ l CD19 and 1 μ l CD3 per sample. Afterwards, they were washed with 2 ml PBS (centrifugation for 5 minutes at 300 g) and fixed with 200 μ l 0.5% formaldehyde. To exclude results that do not originate from viable cells (*e.g.*, cell fragments or clumps), a gate was set in a forward vs. side scatter plot (FSC vs. SSC, see Fig. S1† in the ESI for examples). The FSC strength allows the discrimination of the cells by their size, while the SSC signal distinguishes the cell types by their granularity. Our gating strategy is exemplified for one AML sample and one donor sample each in Fig. 1. For an overall characterization of the sample composition, all viable cells from each sample are represented in a CD45 vs. SSC scatter plot (Fig. 1A and F). This also allows us to set blast gates for the AML samples later on.^{34–36} Afterwards, the CD33⁺ cells were gated out in a CD33 vs. CD45 plot, see Fig. 1B and G. Since the AML samples were extracted from the bone marrow (BM), the CD33⁺ gate of the AML samples contains both myeloid progenitor cells and malignant blasts. The donor samples, on the other hand, are collected from the peripheral blood (PB), and hence the CD33⁺ cells are mainly monocytes, mixed with some basophils (a subtype of granulocytes). In the next step, the stem and progenitor cells (CD45⁺/CD34⁺) were selected with a CD34 vs. CD45 plot as shown in Fig. 1C and H, respectively. The CD34⁺ cells of the AML samples include the malignant blasts. Even though some of the CD33⁺ cells of the donor samples have a high fluorescence intensity in the CD34 PerCP-Cy5.5 channel, they were not included in the CD34⁺ gate since CD34⁺/CD33⁺ cells are absent in the peripheral blood. To distinguish between the lymphocyte subpopulations, CD3⁺/CD19[−] cells (T cells) as well as CD19⁺/CD3[−] cells (B cells) were gated out in a CD45 vs. CD3 respectively CD45 vs. CD19 plot. In order to distinguish between the different types of blasts, further gates were set which are detailed in Section 2.7.

FACS analysis was performed using a BD FACSLyric™ flow cytometer. It is equipped with a 488 nm and a 640 nm laser to measure the fluorescence intensities in the PE, PerCP-Cy5.5, PE-Cy7, APC-R700 and APC-H7 channels and a laser with an excitation wavelength of 405 nm, allowing the measurement of the CND induced fluorescence in the V450 channel. For each sample, at least 50 000 events were recorded. The analysis was carried out using the BD FACSuite™ software.

The ratio of the mean V450 fluorescence intensity measured for the samples with CNDs to that one in the control samples was calculated, resulting in the uptake factor as the parameter,

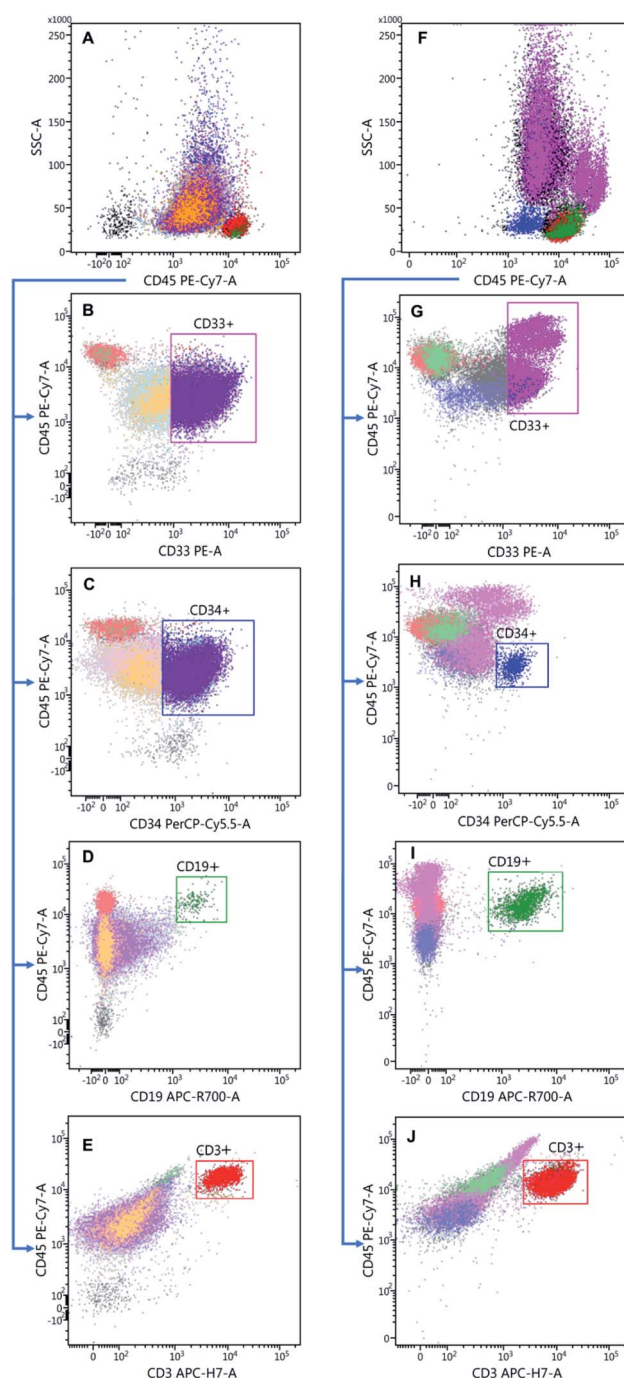


Fig. 1 Gating strategy of the AML samples in the left column and of the donor samples in the right column: scatter plots of the viable cells of AML 2 (A) and donor 3 (F) which are further differentiated using CD markers. Gating of the myeloid progenitor cells and CD33⁺ malignant blasts (B) and the monocytes (G). (C) CD34⁺ blasts respectively stem and progenitor cells gate (H). Differentiation between CD3[−]/CD19⁺ B cells and CD19[−]/CD3⁺ T cells of AML 2 (D and E) and of donor 3 (I and J).

which quantifies the cellular uptake of CNDs for each specific subpopulation. We thereby postulate that the CND fluorescence intensity represents a suitable parameter reflecting the local particle number. This implies that the intensity is not

concentration- or pH-dependent. Concentration-dependent studies have shown that for the CND concentrations used here, the fluorescence intensity is linear as a function of the concentrations, while a significant pH dependence is observed only for unphysiologically low or high pH values (not shown).

2.8 Confocal fluorescence microscopy

The AML cell line HL-60 (passage number 18) was selected for the microscopy experiments. The cells were incubated in appropriate nutrition medium with a concentration of $500 \mu\text{g ml}^{-1}$ CNDs at 37°C and $5\% \text{CO}_2$ for 48 h in a Poly-L-Lysine coated 8 well μ -slide, the nuclei were stained using NucBlue™ Live ReadyProbes™ Reagent (Invitrogen™) and the nutrition medium was exchanged for fresh medium without CNDs. The cells were imaged using a Zeiss LSM 710 confocal microscope evaluating the Hoechst 33342 channel (excitation 405 nm, emission 410–495 nm), the CND channel (excitation 488 nm, emission 495–530 nm) in framewise acquisition mode. A $63\times$ oil objective with NA 1.40 was used.

2.9 t-SNE representation of the ensembles

Visualization of the multi-labelled cell ensembles in two dimensions by t-distributed stochastic neighbour embedding (t-SNE) has been carried out.^{37,38} The FlowJo™ software has been used for this purpose. The perplexity was set to 30 and the number of iterations to 1000, respectively. The learning rate was automatically adjusted for every sample by FlowJo™ software. In our t-SNE plots, the cell subtypes appear in clusters, while a colour scale represents the CND fluorescence intensity. In order to attribute partially overlapping clusters to the corresponding cell types in the AML ensembles, overlays with the gated $\text{CD}33^+$, $\text{CD}34^+$, $\text{CD}19^+$ and $\text{CD}3^+$ populations are created, and the thereby identified populations are framed in the t-SNE plots accordingly.

2.10 Ethical statement

All experiments were performed in compliance with the relevant laws and institutional guidelines and have been approved by the ethical committee of the Heinrich Heine University (Study-no.: 2018-50_1). All donors had given their informed consent according to the guidelines of the ethical committee specified above.

3. Results and discussion

3.1 Subset analysis of AML samples

To investigate the CND uptake by the blasts depending on their maturity level, four categories were defined based on the expression level of CD33 and CD34. Undifferentiated blasts almost only express CD34 antigens on their surface, while CD33 gradually emerges at a later stage of maturation when CD34 is vanishing. To investigate the influence of the maturity level on the CND uptake, the blasts were gated within a $\text{CD}45$ vs. SSC plot for every AML sample (Fig. 2A and B). Afterwards, the blasts were classified according to the expression of CD33 and CD34 in

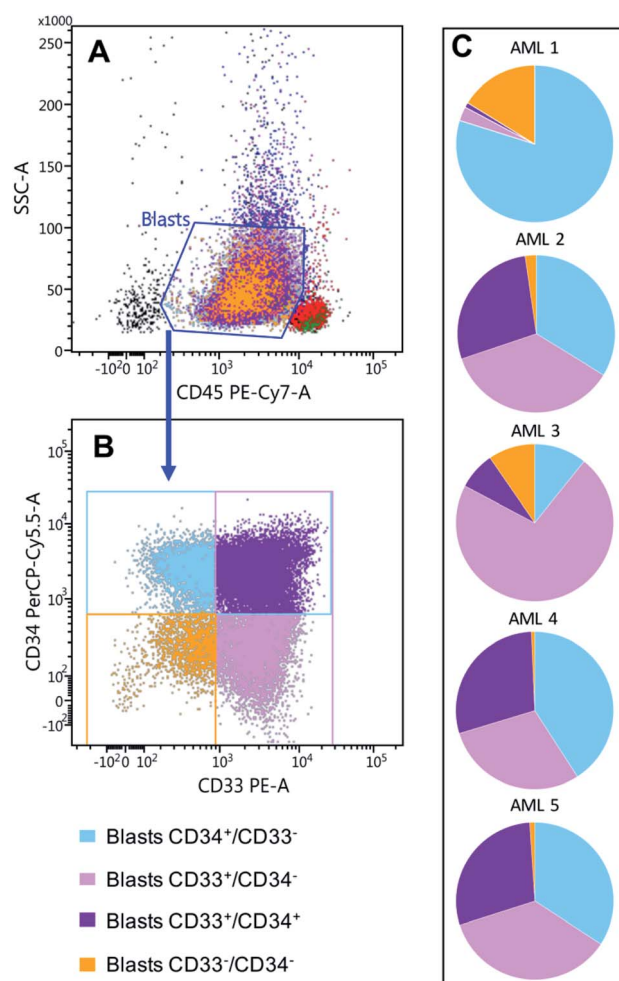


Fig. 2 AML samples characteristics: gating of the different blasts subsets, firstly all blasts were gated out in a $\text{CD}45$ vs. SSC plot (A). Secondly four categories were defined: $\text{CD}33^+/ \text{CD}34^-$ blasts, $\text{CD}34^+/ \text{CD}33^-$ blasts, blasts that were positive for both antibodies ($\text{CD}33^+/ \text{CD}34^+$) and those that were not positive for either antibody ($\text{CD}33^-/ \text{CD}34^-$) (B). (C) Distributions of the four blasts categories are shown for the five AML samples.

four subsets depending on whether they were positive or negative for the respective antigen.

The resulting distribution varied significantly between the different AML samples (Fig. 2C). While the $\text{CD}33^+/ \text{CD}34^-$, $\text{CD}34^+/ \text{CD}33^-$ or $\text{CD}33^+/ \text{CD}34^+$ blasts are nearly equally distributed in AML 2, AML 4 and AML 5, $\text{CD}34^+/ \text{CD}33^-$ blasts predominated in AML 1 and $\text{CD}33^+/ \text{CD}34^-$ blasts in AML 3, reflecting the degree of relative maturity of the blasts within their pathological boundaries. The results correspond to some degree with the classifications of the AMLs (Table 1). AML 1 was classified as M0, *i.e.*, a predominantly undifferentiated acute myeloblastic leukemia ($\text{CD}34^+/ \text{CD}33^-$), whereas AML 2 and 4 belong to the M2 class (AML with maturation). AML 5 belongs to M1, an acute myeloblastic leukemia with some maturation, as indicated by the increase of the $\text{CD}33^+/ \text{CD}34^+$ and $\text{CD}33^+/ \text{CD}34^-$ blasts. Finally, in AML 3, the $\text{CD}33^+/ \text{CD}34^-$ blasts were dominant reflecting the M4/M5 classification (acute myelomonocytic/monocytic leukemia).



3.2 Cellular uptake of CNDs

We proceed by examining whether there is a differential uptake between primary human blood cells and the leukemic cells collected from the bone marrow, as well as between different subpopulations of the samples. In order to quantify and compare the uptake, we defined the uptake factor as the ratio of the mean fluorescence signal after CND exposure to that one of the negative control.

First, healthy and leukemic cells show an uptake of CNDs, reflected by a significant increase in signal intensity in the cells cultivated in the presence of CNDs as compared to the controls. The mean fluorescence signal in the V450 channel is increased by at least a factor of four. Representative examples are given in Fig. 3 for AML 2 (C) and for donor 3 (D). In more detail, the uptake factor for the CD34⁺ cells (HSCs) from the donor samples is 1.7 – fold greater as compared to that one of the AML samples. The uptake factors of the CD33⁺ populations differ even more between AML and donor samples, as the mean uptake factor for the donor samples is increased by 3.2. These findings indicate that the leukemic cells CD33⁺ and CD34⁺ leukemic cells have an apparently reduced ability to take up small compounds such as CNDs from the extracellular space.

Next, we have studied whether one of the four blast subpopulations (as obtained from the gating protocol shown in Fig. 2) shows a selective uptake behaviour. The resulting uptake

factors do not show any differences between the various blast categories (see Fig. S2† of the ESI). This finding indicates that the degree of differentiation of the blasts is not related to the uptake capability of the CNDs, suggesting that a subset specific targeting of blasts without further modifications of the CNDs is not feasible.

Having a closer look on the intensity histogram of the CD33⁺ population (Fig. 3(B) and (C)) it becomes apparent that the intensity of the donor CD33⁺ cells show two peaks, one around 2×10^3 counts and a second one around 10^4 counts. This split was not found in the negative control, which represents the autofluorescence. Hence, the splitting indicates that two different CD33⁺ cell types are present which differ with regard to their CND uptake behaviour, which can be related to CD33⁺ monocytes only present in the LP products of the normal donors. This cell type is a prototype for a phagocytic cell implying that the CNDs are engulfed by vesicles related to the endolysosomal pathway, as suggested in earlier work.¹⁹ On the other hand, the first peak is probably related to a small proportion of CD33⁺ progenitor cells contained within the population of mobilized CD34⁺ cells (see Fig. S3† in the ESI).

For the CD19⁺ and CD3⁺ populations, there was no significant difference between the uptake factors of AML and donor samples. Still, for both, AML as well as donor samples, the uptake factor for the CD19⁺ subpopulation is significantly

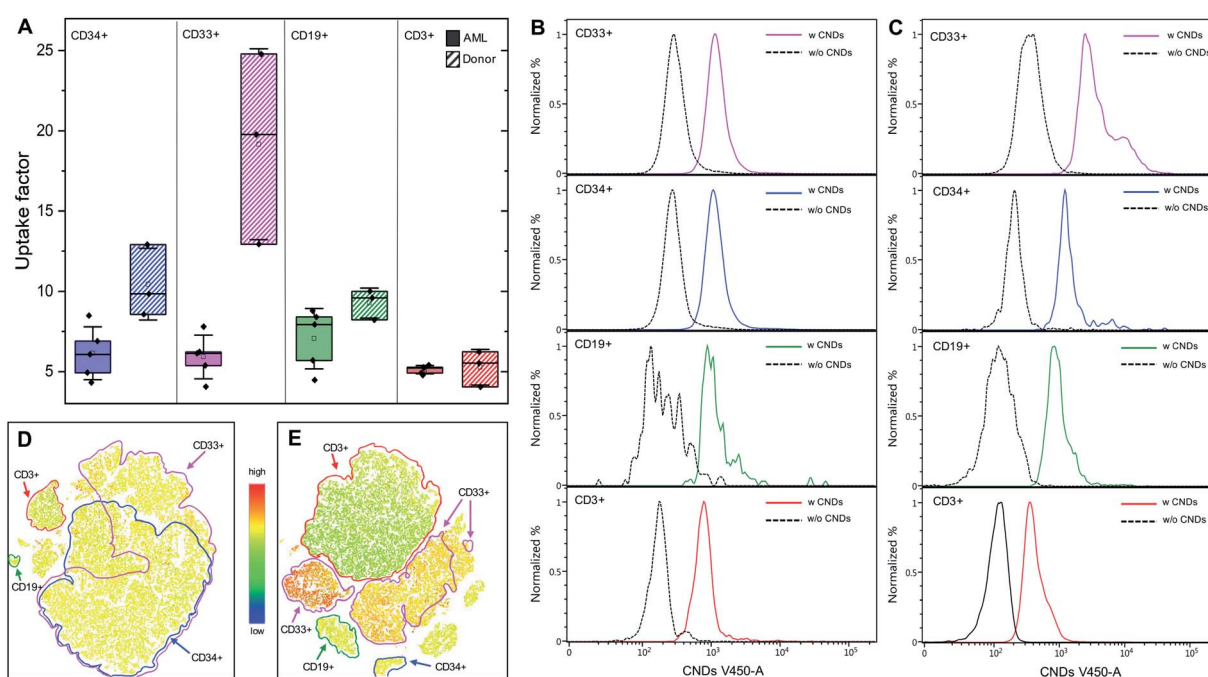


Fig. 3 (A) The sample-averaged uptake factors as determined for the four cell types and the corresponding statistical properties. The black squares denote the uptake factors of the individual samples, the horizontal bars are the median values and the unfilled squares are the mean values. The error bars indicate the standard deviation, and the lower and upper edge correspond to the first and the third quartile of the data. Please note that the CD34⁺ population from the AML samples contains the CD34⁺/CD33⁺ and the CD34⁺/CD33⁻ cells. Likewise, the CD33⁺ population is composed of the CD34⁺/CD33⁺ and the CD34⁻/CD33⁺ cells. Examples of the CND uptake by an AML (AML 2, (B)) and a healthy donor (donor 3, (C)) sample, as observed in the populations characterized by four CD antibodies. The intensity histograms are all normalized to a maximum value of 1 for better comparability. The t-SNE plots for the AML 2 and donor 3 samples are shown in (D) and (E), respectively as examples. Here, the colour scale quantifies the fluorescence intensity in the V450 A channel. The identified CD populations (CD33⁺, CD34⁺, CD19⁺ and CD3⁺) have been framed manually.

greater in comparison to the CD3⁺ cells. For the AML and the normal donor samples, the mean uptake factors of the CD19⁺ cells are about 1.38 and 1.76 times greater, respectively. A smaller uptake avidity of CD3⁺ T and T helper cells compared to CD19⁺ B cells from healthy donors was already observed in our previous study.¹⁹ The difference between these two types of lymphoid cells may relate to the phagocytic ability of activated B cells.³⁹

The t-SNE plots (Fig. 3(D) (for AML 2) and (E) (for donor 3)) permit a very informative illustration of our findings, as the fluorescence intensity of the CND signal in the V450 channel is color-coded. With regard to the AML samples, the relatively homogeneous intensity of colour across all subpopulations represents the similar uptake behaviour of the various cell types with a strong overlap of the CD33⁺ and the CD34⁺ cells. In contrast, the populations of the healthy samples are distinguishable in the t-SNE map, each of them characterized by a particular colour-coded uptake activity, which corresponds to the distinct peaks shown in Fig. 3C.

3.3 Subcellular distribution of CNDs in AML cells

In order to compare the intracellular distribution of the CNDs in AML cells, confocal microscopy images of HL-60 cells (corresponding to AML FAB M2 cells) were taken after 48 h of incubation with CNDs (Fig. 4). The CNDs accumulate preferentially in small clusters in the periphery of the nucleus. Based on the results of previous studies in HSCs and human breast cancer cells using a counterstaining method these clusters could be localized to lysosomes.^{19,40} It is therefore conceivable that the CNDs following ingestion into the leukemic blasts are stored in the lysosomes, suggesting that the endolysosomal

pathway is also effective in AML cells. In the light of this finding the results of Folkerts *et al.* are interesting and of potential therapeutic relevance.⁴¹ They could show decreased survival upon HCQ 20 μ M hydroxychloroquine (HCQ) treatment for leukemic cell lines as well as primary sorted AML CD34⁺ cells ($n = 36$) compared to normal bone marrow CD34⁺ cells ($N = 6$; NBM CD34⁺: 41.7% \pm 7.1 vs. AML CD34⁺: 21.3% \pm 3.2, $p = <0.05$).

Microscopy images of the control samples are contained within in the ESI (see Fig. S4[†] and S5 in the ESI).

4. Conclusions

We compared the cellular uptake of small graphene quantum dots into normal blood cells with that into primary leukemic cells from patients with AML. Based on the intensity of the CNDs related autofluorescence recorded following a 24 h exposure time in an *in vitro* culture, a significantly smaller uptake was noted into leukemic cells compared to normal cells. This was true for both, the CD34⁺ as well as CD33⁺ subset. With regard to the uptake into lymphoid cells, a similar degree of uptake was observed for normal and leukemic cells, while a significant difference was only found between CD19⁺ B cells and CD3⁺ T cells irrespective of the sample source. This decreased differential uptake by the malignant cells studied here in comparison to their healthy counterparts forms a challenge for a selective addressing of those cells to which, *e.g.*, a drug should be delivered. Suitable drug delivery systems based on our CNDs therefore may require some functionalization which increases the uptake by the target cells, like antigens or sugars, for example by preferential binding to the target cells. Alternatively, one might

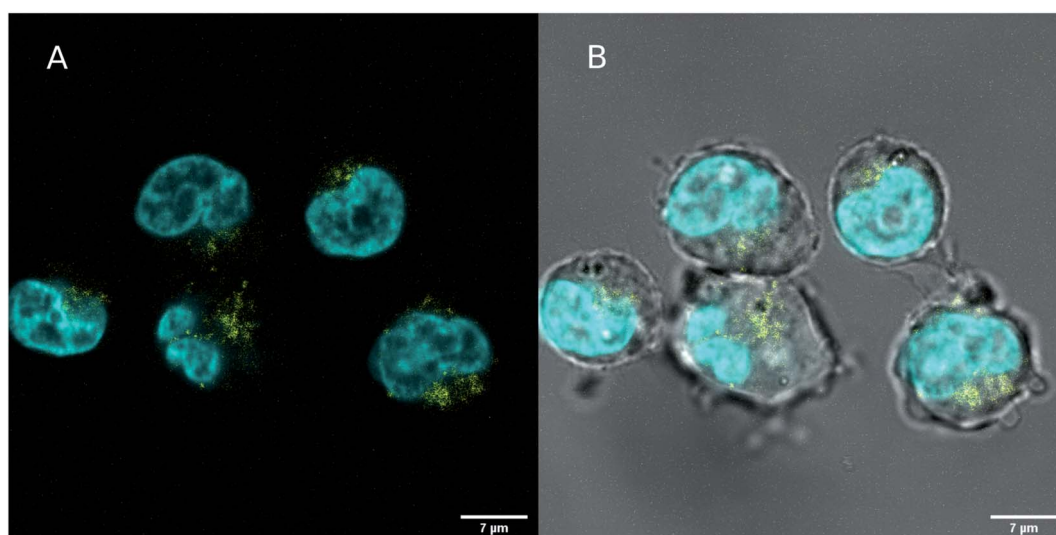


Fig. 4 Microscopy image of HL-60 cells taken 48 h after incubation with 500 μ g ml⁻¹ CNDs taken with a Zeiss LSM 710 confocal microscope (63 \times oil, NA 1.40). The nucleus was stained with Hoechst 33342, which was excited with a 405 nm UV diode laser and emission light was detected between 410 nm and 495 nm (cyan). The CNDs were excited with a 488 nm line from a multiline argon laser and the fluorescence was detected between 495 nm and 530 nm (yellow). The images have been acquired framewise. Image (A) displays only the fluorescence channels, while an overlay of the transmitted light from the CND channel and the fluorescence channels is shown in (B). Images of the control samples, taken with the same imaging parameters, are shown in the ESI.[†]



imagine selective inhibitor schemes where the CNDs protect the healthy cells from the impact of a drug. These issues are, however, beyond our scope here and will be the topic of future studies. It should be noted in this context that the reduced uptake of quantum dots in the malignant cell type studied here cannot be generalized to malignant cells of other organs, such as solid tumors of the breast or lung. The latter ones are epithelial in nature by their germline affiliation and thus may well differ with regard to their uptake properties from leukemia cells of mesenchymal origin.

Following their uptake, the CNDs reside in close proximity to endosomal-lysosomal machinery, which is involved in the uptake of extracellular particles *via* endocytosis. This subcellular location could be useful for therapeutic targeting involving the lysosomal compartment, which plays a pivotal role in the context of autophagy.⁴¹ Watson and colleagues demonstrated the dual function of autophagy for the balance between cell death and cell survival.⁴² They found that the complete blockade of autophagy induced the death of leukemic cells, while a reduction of this pathway increased their proliferation, which was associated with a significantly reduced latency of the disease. The dual role of autophagy for cancer progression and resistance is complex and therefore challenging when a targeted therapy is envisaged. Therefore, one direction of further work may be geared towards methods mediating a more specific leukemic uptake to assess functional effects on autophagy related processes in a dose-dependent manner.

List of abbreviations

AML	Acute myeloid leukemia
t-SNE	t-Distributed stochastic neighbour embedding
CNDs	Carbon nanodots
LP	Leukapheresis products

Author contributions

CN prepared the carbon nanodots, collected the AML and apheresate cytometry data, participated in the data analysis, wrote the initial draft and prepared the figures. CW took the confocal microscopy pictures, participated in the preparation and characterization of the CNDs and the data analysis. He furthermore initiated the t-SNE representation. SF contributed to the CND preparation setup and the flow cytometry. SM contributed to the recording of the cytometric data. RPD guided and supervised the cytometry and the gating of the cell ensembles. PJ collected the samples and evaluated the medical aspects of the AML data. TH co-designed the experiments, participated in the interpretation of the data and co-wrote the manuscript. RH initiated the study, interpreted the data and co-wrote the manuscript.

Conflicts of interest

There are no conflicts to declare.

Acknowledgements

Access to the confocal microscope at the Center for Advanced Imaging (CAI) of HHU Düsseldorf is gratefully acknowledged. C. N. and C. W. gratefully acknowledge the support by the Jürgen Manchot Stiftung. The authors thank Cornelia Monzel for providing access to her laboratories.

Notes and references

- 1 Y. Yan, J. Gong, J. Chen, Z. Zeng, W. Huang, K. Pu, J. Liu and P. Chen, *Adv. Mater.*, 2019, **31**, e1808283.
- 2 H. Singh, S. Sreedharan, K. Tiwari, N. H. Green, C. Smythe, S. K. Pramanik, J. A. Thomas and A. Das, *Chem. Commun.*, 2019, **55**, 521.
- 3 K. Yadav, M. Das, N. Hassan, A. Mishra, J. Lahiri, A. K. Dubey, S. K. Yadav and A. S. Parmar, *RSC Adv.*, 2021, **11**, 976.
- 4 B. H. Lee, R. L. McKinney, M. T. Hasan and A. V. Naumov, *Materials*, 2021, **14**, 616.
- 5 M. J. Deka, P. Dutta, S. Sarnia, O. K. Medhi, N. C. Talukdar and D. Chowdhury, *Heliyon*, 2019, **5**, e01985.
- 6 P. Roy, P.-C. Chen, A. P. Periasamy, Y.-N. Chen and H.-T. Chang, *Mater. Today*, 2015, **18**, 447.
- 7 N. Panwar, A. M. Soehartono, K. K. Chan, S. Zeng, G. Xu, J. Qu, P. Coquet, K. Yong and X. Chen, *Chem. Rev.*, 2019, **119**, 9559.
- 8 J. Du, N. Xu, J. Fan, W. Sun and X. Peng, *Small*, 2019, **15**, 1805087.
- 9 W. Su, H. Wu, H. Xu, Y. Zhang, Y. Li, X. Li and L. Fan, *Mater. Chem. Front.*, 2020, **4**, 821.
- 10 R. Ludmerczki, S. Mura, C. M. Carbonaro, I. M. Mandity, M. Carraro, N. Senes, S. Garroni, G. Granozzi, L. Calvillo, S. Marras, L. Malfatti and P. Innocenzi, *Chem.-Eur. J.*, 2019, **25**, 11963.
- 11 J. Schneider, C. J. Reckmeier, Y. Xiong, M. von Seckendorff, A. S. Susha, P. Kasák and A. L. Rogach, *J. Phys. Chem. C*, 2017, **121**, 2014.
- 12 W. Kasprzyk, T. Świergosz, S. Bednars, K. Walas, N. V. Bashmakova and D. Bogdał, *Nanoscale*, 2018, **10**, 13889.
- 13 W. Wang, B. Wang, H. Embrechts, C. Damm, A. Cadranel, V. Strauss, M. Distaso, V. Hinterberger, D. M. Guldi and W. Peukert, *RSC Adv.*, 2017, **7**, 24771.
- 14 L. Cao, X. Wang, M. J. Mezziani, F. Lu, H. Wang, P. G. Luo, Y. Lin, B. A. Harruff, L. M. Vaca, D. Murray, S. Xie and Y. Sun, *J. Am. Chem. Soc.*, 2007, **129**, 11318.
- 15 C. Liu, P. Zhang, F. Tian, W. Li, F. Lib and W. Liu, *J. Mater. Chem.*, 2011, **21**, 13163.
- 16 S. Zhu, J. Zhang, C. Qiao, S. Tang, Y. Li, W. Yuan, B. Li, L. Tian, F. Liu, R. Hu, H. Gao, H. Wei, H. Zhang, H. Sun and B. Yang, *Chem. Commun.*, 2011, **47**, 6858.
- 17 W. Shang, X. Zhang, M. Zhang, Z. Fan, Y. Sun, M. Han and L. Fan, *Nanoscale*, 2014, **6**, 5799.
- 18 S. Fasbender, S. Allani, C. Wimmenauer, R. P. Cadeddu, K. Raba, J. C. Fischer, B. Bulat, M. Luysberg, C. A. M. Seidel, T. Heinzel and R. Haas, *RSC Adv.*, 2017, **7**, 12208.

- 19 S. Fasbender, L. Zimmermann, R. P. Cadeddu, M. Luysberg, B. Moll, C. Janiak, T. Heinzel and R. Haas, *Sci. Rep.*, 2019, **9**, 12018.
- 20 C. Zhao, X. Song, Y. Liu, Y. Fu, L. Ye, N. Wang, F. Wang, L. Li, M. Mohammadniaei, M. Zhang, Q. Zhang and J. Liu, *J. Nanobiotechnol.*, 2020, **18**, 142.
- 21 Q. Liu and A. Atrens, *Corros. Rev.*, 2013, **31**, 85.
- 22 M. Zhang, L. Bai, W. Shang, W. Xie, H. Ma, Y. Fu, D. Fang, H. Sun, L. Fan, M. Han, C. Liu and S. Yang, *J. Mater. Chem.*, 2012, **22**, 7461.
- 23 I. Al-Ogaidi, H. Gou, Z. P. Aguilar, S. Guo, A. K. Melconian, A. K. A. Al-Kazaz, F. Meng and N. Wu, *Chem. Commun.*, 2014, **50**, 1344.
- 24 Z. L. Wu, M. X. Gao, T. T. Wang, X. Y. Wan, L. L. Zhenga and C. Z. Huang, *Nanoscale*, 2014, **6**, 3868.
- 25 X. Sui, C. Luo, C. Wang, F. Zhang, J. Zhang and S. Guo, *Nanomedicine*, 2016, **12**, 1997.
- 26 X. Gong, Q. Zhang, Y. Gao, S. Shuang, M. M. F. Choi and C. Dong, *ACS Appl. Mater. Interfaces*, 2016, **8**, 11288.
- 27 J. M. Bennett, D. Catovsky, M. T. Daniel, G. Flandrin, D. A. Galton, H. R. Gralnick and C. Sultan, *Ann. Intern. Med.*, 1985, **103**, 620.
- 28 S. H. Swerdlow, E. Campo, N. L. Harris, E. S. Jaffe, S. A. Pileri, H. Stein, J. Thiele and J. W. Vardiman, *WHO Classification of Tumours of Haematopoietic and Lymphoid Tissues*, WHO Press, Geneva, Switzerland, 2008.
- 29 D. Qu, M. Zheng, J. Li, Z. Xie and Z. Sun, *Light: Sci. Appl.*, 2015, **4**, e364.
- 30 R. Möhle, M. Pförsich, S. Fruehauf, B. Witt, A. Krämer and R. Haas, *Bone Marrow Transplant.*, 1994, **14**, 827.
- 31 K. Theilgaard-Mönch, K. Raaschou-Jensen, H. Palm, K. Schødt, C. Heilmann, L. Vindeløv, N. Jacobsen and E. Dickmeiss, *Bone Marrow Transplant.*, 2001, **28**, 1073.
- 32 M. D'Aveni, J. Rossignol, T. Coman, S. Sivakumaran, S. Henderson, T. Manzo, P. S. E. Sousa, J. Bruneau, G. Fouquet, F. Zavala, O. Alegria-Prvot, M. Garfa-Traor, F. Suarez, H. Trebeden-Ngre, M. Mohty, C. L. Bennett, R. Chakraverty, O. Hermine and M. T. Rubio, *Sci. Transl. Med.*, 2015, **7**, 281ra42.
- 33 S. Murea, S. Fruehauf, W. J. Zeller and R. Haas, *J. Hematother.*, 1996, **5**, 351.
- 34 M. J. Borowitz, K. L. Guenther, K. E. Shults and G. T. Stelzer, *Am. J. Clin. Pathol.*, 1993, **100**, 534.
- 35 G. T. Stelzer, K. E. Shults and M. R. Loken, *Ann. N. Y. Acad. Sci.*, 1993, **677**, 265.
- 36 F. Lacombe, F. Durrieu, A. Briais, P. Dumain, F. Belloc, E. Bascans, J. Reiffers, M. R. Boisseau and P. Bernard, *Leukemia*, 1997, **11**, 1878.
- 37 L. van der Maaten and G. Hilton, *J. Mach. Learn. Res.*, 2008, **9**, 2579.
- 38 E. D. Amir, K. L. Davis, M. D. Tadmor, E. F. Simonds, J. H. Levine, S. C. Bendall, D. K. Shenfeld, S. Krishnaswamy, G. P. Nolan and D. Pe'er, *Nat. Biotechnol.*, 2013, **31**, 545.
- 39 Q. Zhu, M. Zhang, M. Shi, Y. Liu, Q. Zhao, W. Wang, G. Zhang, L. Yang, J. Zhi, L. Zhang, G. Hu, P. Chen, Y. Yang, W. Dai, T. Liu, Y. He, G. Feng and G. Zhao, *Immunobiology*, 2016, **221**, 558.
- 40 D. Kersting, S. Fasbender, R. Pilch, J. Kurth, A. Franken, M. Ludescher, J. Naskou, A. Hallenberger, C. von Gall, C. J. Mohr, R. Lukowski, K. Raba, S. Jaschinski, I. Esposito, J. C. Fischer, T. Fehm, D. Niederacher, H. Neubauer and T. Heinzel, *Nanotechnology*, 2019, **30**, 39.
- 41 H. Folkerts, B.-J. Wieringa, P. J. Coffey, J. J. Schuringa and E. Vellenga, *Blood*, 2015, **126**, 3831.
- 42 A. S. Watson, T. Riffelmacher, A. Stranks, O. Williams, J. de Boer, K. Cain, M. MacFarlane, J. McGouran, B. Kessler, S. Khandwala, O. Chowdhury, D. Puleston, K. Phadwal, M. Mortensen, D. Ferguson, E. Soilleux, P. Woll, S. E. W. Jacobsen and A. K. Simon, *Cell Death Discovery*, 2015, **1**, 15008.



Supplementary Information

Uptake of carbon nanodots into human AML cells in comparison to primary hematopoietic cells

Cathrin Nollmann^a, Christian Wimmenauer^a, Stefan Fasbender^a, Saskia Mayer^b, Ron-Patrick Caddedu^b, Paul Jäger^b, Thomas Heinzel^{*a}, and Rainer Haas^{*b}

a. Condensed Matter Physics Laboratory, Heinrich-Heine-University, 40204 Düsseldorf, Germany.

E-Mail: Thomas.Heinzel@hhu.de

b. Department of Haematology, Oncology and Clinical Immunology, Heinrich-Heine-University, 40204 Düsseldorf, Germany.

E-Mail: Haas.med@uni-duesseldorf.de

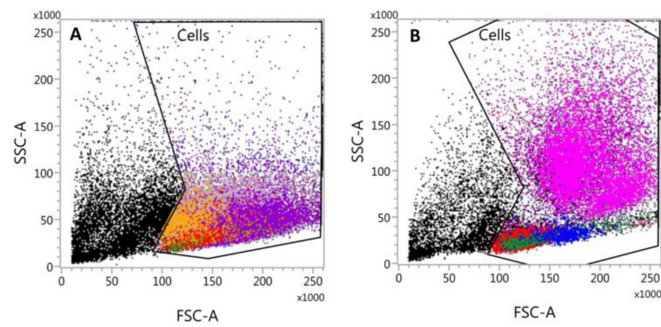


Fig. S1: Examples of FSC vs. SSC plots by which the cell population was selected via suitable gates. Shown are AML 2 in (A) and donor 3 in (B). The colours represent the rear projections of further gates that have been set, namely CD33+ (pink), CD34+ (blue), CD19+ (green), and CD3+ (red).

Tab. S1: Percentage distribution of the CD33+, CD34+, CD19+ and CD3+ populations for all samples.

sample	CD33+	CD34+	CD19+	CD3+
AML 1	7,96%	14,40%	0,25%	0,84%
AML 2	77,01%	72,55%	0,55%	4,87%
AML 3	88,16%	3,82%	1,69%	6,33%
AML 4	42,11%	35,50%	1,11%	31,30%
AML 5	84,82%	77,05%	0,08%	1,21%
donor 1	33,14%	1,89%	2,48%	43,87%
donor 2	43,94%	3,56%	8,75%	36,93%
donor 3	24,15%	2,13%	4,64%	47,12%

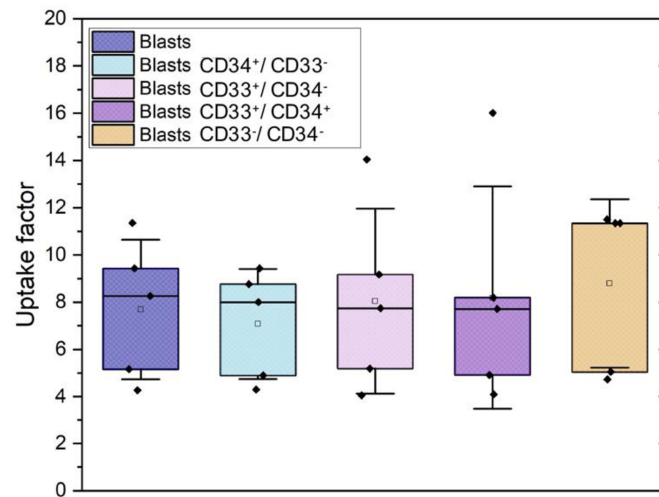


Fig. S2: Uptake factors for all blasts and four subsets which were defined by means of the CD34 and CD33 markers.

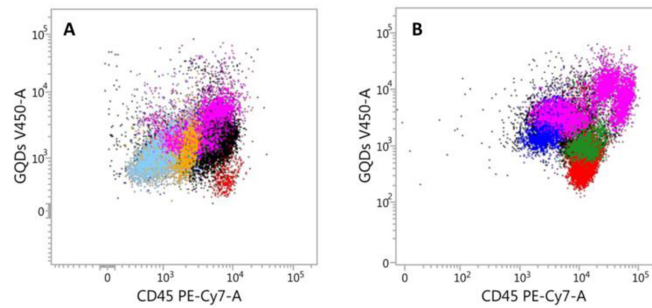


Fig. S3: CD45 vs. V450 plot, shown exemplarily for AML 1 (A) and donor 3 (B). The colours are rear projections of other set gates CD33+ (pink), CD34+ (blue), CD19+ (green), and CD3+ (red).

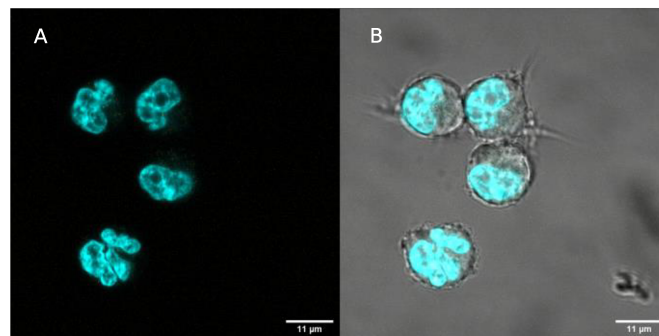


Fig. S4: Control samples (HL-60 cells) without CNDs. The nuclei are stained with Hoechst 33342.

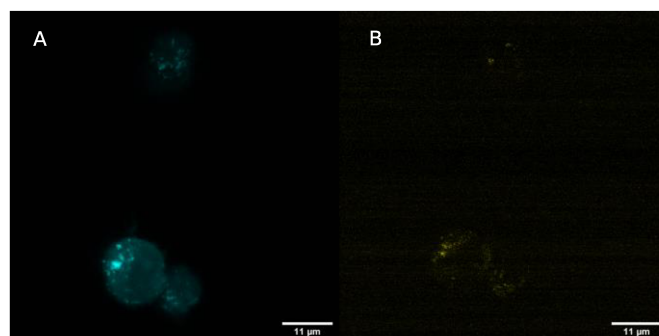


Fig. S5: Control sample of CND-exposed HL-60 cells with the nuclei unstained. The CNDs show fluorescence in the blue (a) and in the olive (B) channel.

4.2 Paper III

Reference

S. Üclü, C. Wimmenauer, C. Nollmann, A. Liu, S. A. Hill, N. L. Snyder, T. Heinzel and L. Hartmann (2023). Sweet carbon dots: synthesis of sugar-functionalized carbon nanoparticles and their cellular uptake. *To be resubmitted*.

Copyright statement

This manuscript is a preprint we are currently planning to resubmit to a journal of the Royal Chemical Society. The Royal Chemical Society explicitly allows the original authors in their "Journal policy on prior publication" to share their research ahead of publication as part of their dissertation or thesis for an academic or professional qualification.

Contributions

I prepared the non-functionalized nanoparticles, that were further processed by SÜ. I performed the optical characterisation of the functionalized nanoparticles. I performed the confocal microscopy experiments. I prepared the samples for flow cytometry together with CN that were finally measured by CN. I performed the viability assay together with SÜ and contributed to the data analysis and planning of all bioexperiments. I contributed to manuscript writing together with SÜ, LH and TH.

Sweet carbon dots: synthesis of sugar functionalized carbon nanoparticles and their cellular uptake

Serap Üclü,^{†a} Christian Wimmenauer,^{†b} Cathrin Nollmann,^b Andrea Liu,^c Stephen A. Hill,^a Nicole L. Snyder,^c Thomas Heinzel^{*b} and Laura Hartmann^{*a}

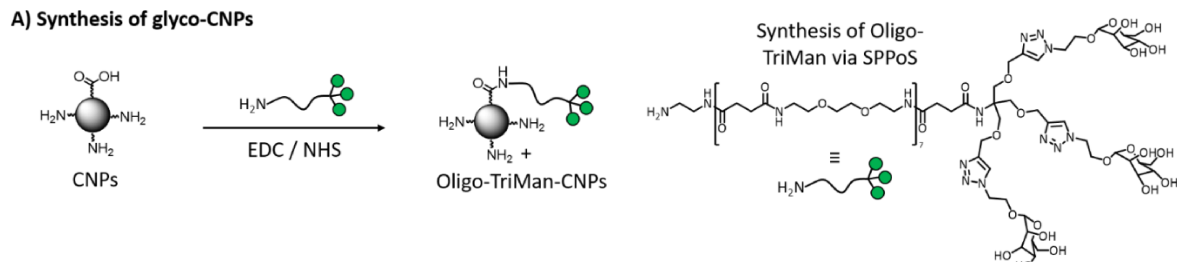
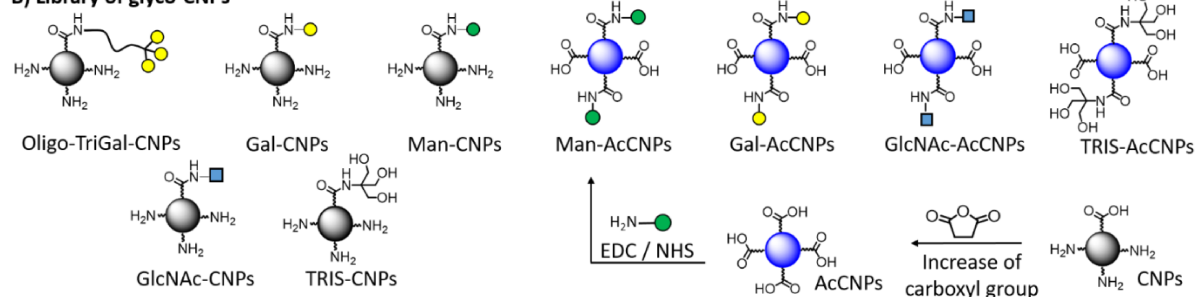
a. Department for Organic Chemistry and Macromolecular Chemistry, Heinrich Heine University Düsseldorf, Universitätsstraße 1, Düsseldorf 40225, Germany. E-mail: laura.hartmann@hhu.de

b. Institute for Experimental Condensed Matter Physics, Heinrich Heine University Düsseldorf, Universitätsstraße 1, Düsseldorf 40225, Germany. E-mail: thomas.heinzel@hhu.de

c. Department of Chemistry Davidson College 102 North Main Street, Davidson, NC 28035 USA E-mail: nisnyder@davidson.edu

Carbon nanoparticles are coupled covalently to various monosaccharides as well as glycooligomers and studied for their interaction with different tumor cell lines overexpressing carbohydrate-recognizing lectin receptors. Monosaccharide-conjugated carbon nanoparticles show an enhanced uptake rate as compared to both pristine as well as glycooligomer-coated particles. However, coating with mannose, galactose, N-acetylglucosamine or glycooligomers derived thereof does not influence the intracellular distribution of the nanoparticles showing that they are preferably stored in the endolysosomal pathway.

Functionalized nanoparticles and their application in biomedical research have developed into a mature scientific field over the last two decades.¹⁻³ Multicolor fluorescence spectroscopy based on quantum dots is used routinely within various diagnostic medical protocols.⁴⁻⁶ Carbon nanoparticles (CNPs) are a promising complement to conventional semiconducting quantum dots in these respects, due to their low mass, intrinsic water solubility, easy functionalization and low toxicity.^{7,8} They have been used as intracellular pH meter,⁹ selectivity enhancers during cisplatin¹⁰ or doxorubicin¹¹ uptake, or in confocal fluorescence microscopy¹²⁻¹⁴, to name just a few examples. One important advancement in the development of nanomaterials for biomedical applications is their selectivity, e.g., for cancer vs. healthy cells.^{15,17} Such selectivity can enable more efficient drug delivery and thus reduced side effects in anti-cancer therapy.¹⁸⁻²⁰ Interactions between carbohydrates and lectins as receptors have been shown to allow for such selectivity and have been successfully applied to derive various glycofunctionalized nanomaterials for use in biomedicine.²¹⁻²² Examples of glycofunctionalization for cell specific targeting include galactose (Gal) ligands addressing the asialoglycoprotein receptor, sialic acid (Neu5Ac) ligands targeting Siglecs,²³ and hyaluronic acid (HA) functionalization for binding to CD44 receptors,²⁴; each receptor is overexpressed in a specific cell type. Another carbohydrate recognizing C-type lectin receptor (CLR) with relevance for targeting cancer cells is the Mannose Receptor (MR). MR recognizes mannose (man), fucose (fuc) and N-acetylglucosamine (GlcNAc) in a calcium-dependent manner.^{25,26} Different types of cancer cells are known to overexpress MR,²⁷ and it has been shown that by targeting the MR e.g., through binding with its carbohydrate ligands, cancer cells can be distinguished from healthy cells.²⁸ In this study we aim to combine the advantages of CNPs and glycofunctionalization, with a special focus on targeting MR overexpressing cancer cells, and investigate the cellular uptake of glyco-CNPs in dependence of the type of glycofunctionalization using used and comparing different monosaccharides as well as glycooligomers.

A) Synthesis of glyco-CNPs**B) Library of glyco-CNPs****C) Degree of functionalization**

Man-CNP	Gal-CNP	GlcNAc-CNP	Oligo-TriMan-CNP	Oligo-TriGal-CNP	Man-AcCNP	Gal-AcCNP	GlcNAc-AcCNP
1.04 μmol/ mg	1.00 μmol/ mg	0.90 μmol/ mg	2.95 μmol/ mg	2.49 μmol/ mg	0.59 μmol/ mg	0.45 μmol/ mg	0.68 μmol/ mg

Figure 1: A) Synthesis of glyco-CNPs: SPPoS of Oligo-TriMan functionalization of CNPs via activation the carboxyl groups by EDC/NHS. B) Library of synthesized glyco-CNPs including the extension of carboxyl group of CNPs through succinic anhydride to gain higher level of functionalization degree (AcCNPs) and their glyco-conjugated derivatives. C) Functionalization degrees of glyco-CNPs.

Here, we present the preparation and characterization of the glyco-CNPs (Figure 1A), followed by uptake studies using three ubiquitous cell lines, which were exposed to a set of CNPs coupled to different monosaccharides as well as glycooligomers. We opted to use CNPs prepared by microwave assisted pyrolysis from citric acid and diethylenetriamine as described in detail the ESI, leading to free acid- and primary amine groups at the surface of the CNPs. A second fraction of the particles was first coupled to succinic anhydride (AcCNPs) thereby reacting with amine groups also present on the CNP surface and increase the degree of carboxylic groups, which are required for conjugation of the carbohydrate derivatives and glycooligomers. (Figure 1B) In addition to acceptable fluorescence properties, these CNPs are very small with diameters of roughly 3 nm, and extremely stable. Furthermore, they are known to have only a marginal toxicity, even on the gene expression level.²⁹ For glycofunctionalization, a set of monosaccharides were used: Man and GlcNAc as known MR ligands, and Gal as a negative control.

Additionally, glycooligomers presenting multiple copies of Man or Gal were synthesized and applied for the functionalization of the CNPs. Cancer cells such as MDA-MB-231 breast cancer can be targeted by receptor-mediated endocytosis through overexpressed MR.^{30,31} The multivalent presentation of Man is expected to increase binding and thus cell uptake, through the statistical possibility of a Man molecule encountering a CRD, resulting in binding enhancement.³² Thus, glycooligomers were synthesized by previously established solid-phase polymer synthesis (SPPoS, see ESI).^{33,34} In brief, stepwise conjugation of tailor-made building blocks using standard Fmoc-peptide coupling protocols on resin provided access to sequence-defined oligo(amidoamines) with alkyne side chains, which were used for further conjugation of carbohydrate-azide derivatives via a copper-mediated click reaction (CuAAC).³⁵ Glycooligomers used for subsequent conjugation to NPs carry a long hydrophilic chain and three terminal Man ligands. For later use as negative control, glycooligomers presenting Gal were synthesized accordingly.

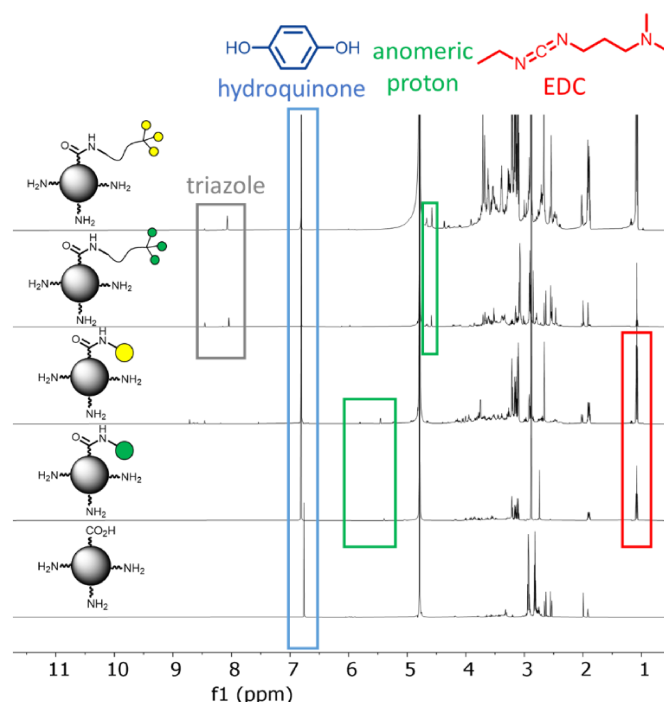


Figure 2: ^1H NMR spectra of pristine and functionalized CNPs. Hydroquinone was used as internal standard (blue frame). Green frame: anomer proton signal of Man/Gal. Grey frame: signal from the protons of the triazole ring of the glycooligomers. The EDC signal is framed in red.

Conjugation of both, monosaccharides and glycooligomers to the CNPs were achieved by activation of carboxylic groups on the CNPs via 1-ethyl-3-(3-dimethylaminopropyl)carbodiimide (EDC) and *N*-hydroxysuccinimide (NHS) followed by subsequent reaction with free amine groups either from amino-functionalized monosaccharides (see ESI for synthesis and analytical data of the amino sugars) or on the C-terminal position of the oligomer. The hydrophilic chain of the glycooligomer provides flexibility and may potentially increase the accessibility of the carbohydrate ligands in binding to cell surface receptors (see the ESI for further details on the synthesis and analytical data of the products).

The degree of functionalization of the glycol-CNPs was studied by ^1H NMR, see Figure 2. Hydroquinone was used as an internal standard and compared to either the anomer protons of the sugar (green frame) or the protons of the triazole ring of the glycooligomers (grey frame), which provided the overall sugar concentration. Successful glycofunctionalization was demonstrated for both AcCNPs and CNPs, but with different degrees of functionalization. While the AcCNPs have a larger number of acid groups indicating a higher degree of functionalization, they have a lower sugar concentration as compared to the glycofunctionalized CNP system, see Figure 1 C. We attribute this to steric effects, since succinic anhydride functionalization limits the accessibility of the acid groups. In the CNP system, on the other hand, the acid groups have more space on the CNP surface, which results in better accessibility for glycofunctionalization. Additionally, the CNP system was used for functionalization with glycooligomers, confirming and quantifying the degree of functionalization via NMR (see Figure 2). In the NMR spectra, we also identified an EDC contamination (red frame in Figure 2) for the monosaccharide functionalized CNPs. Since we were unable to remove this contamination with extensive washing protocols, this is likely either covalently attached to the surface of the CNPs or located in between the carbohydrates through ionic interactions. Since the EDC remained present also after dialysis against high ionic buffer (PBS), covalent binding strikes us as more plausible. This contamination is not seen in the CNPs functionalized with glyco-oligomers, which could be because the flexible chain covers a larger surface area on the CNPs, thus preventing EDC binding to the surface. Diffusion ordered spectroscopy (DOSY) measurements were performed to evaluate the change of the

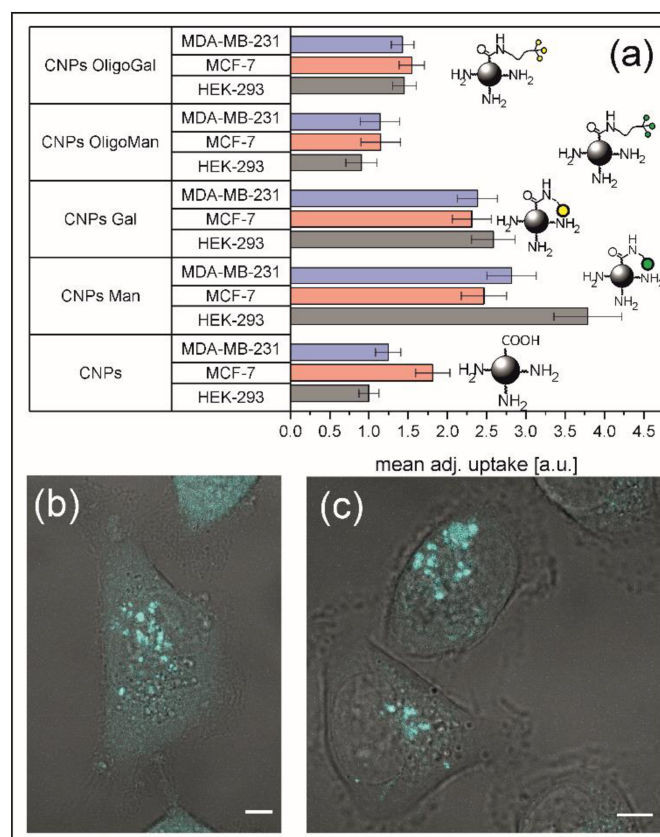


Figure 3: (a) CNP uptake as determined from flow cytometry measurements. Confocal microscopy on MDA-MB-231 cells after uptake of pristine (b) and mannose-conjugated (c), CNPs. The size of the scale bars is 5 μ m.

hydrodynamic radii before and after the functionalization. All diffusion coefficients lie in the range $[4 - 6] \times 10^{-10} \text{ m}^2 \text{ s}^{-1}$, corresponding to hydrodynamic radii around 0.4 nm, almost independent of the functionalization (see Table 1 in the ESI). Fluorescence spectroscopy reveals that all functionalized CNPs show a weak but noticeable redshift of the fluorescence maximum, while the shape of the spectrum remains approximately constant (see ESI Table 2).

With this set of glyco-CNPs in hand, we then performed flow cytometry, confocal microscopy, and XTT assays to determine their cellular uptake rates, subcellular distribution, and cell toxicity, respectively. Two breast cancer cell lines MCF-7 and MDA-MB-231 as well as the embryonic kidney cell line HEK-293 were employed in these experiments based on their expression of MRs: HEK-293 cells were shown to present few MR in previous work, while MDA-MB-231 are known to possess a high expression of MRs.³⁶ MCF-7 cells were selected due to their high uptake of CNPs shown in previous studies.¹³ To quantify cellular uptake, measured in terms of the total mass of nanoparticles per cell, the fluorescence intensity of an event detected in flow cytometry was corrected with the brightness of each particle species (see ESI Table 2). Here, the quantum yield under an excitation wavelength of 360 nm was determined using Coumarin 1 with a quantum yield of 0.5 as a reference. The extinction coefficient is obtained from a fit of Lambert-Beer's law to the concentration dependence of the absorption. We define the brightness of a particle type as the product of the quantum yield and the extinction coefficient. Increased uptake rates of CNPs functionalized with monosaccharides compared to non-functionalized CNPs were observed as shown in Figure 3 (a). This effect is independent of the cell type and therefore of the receptor expression. This was confirmed by additional receptor-specific studies with HepG2 cells, which are widely used for drug development and toxicity testing and overexpress the asialoglycoprotein receptor (ASGPR)³⁷ and MR³⁸. Here, the specific uptake of Gal-CNPs targeting ASGPR of HepG2 cells were investigated, and showed the same uptake rate as the negative control cell line HEK293 (see the ESI). In addition, the influence of glycofunctionalization on the subcellular distribution of the glyco-CNPs was investigated, see Figure 3 (b), (c). Confocal microscopy revealed that

they accumulate in small sub-spaces inside the cell, which most likely correspond to vesicles in the endo-lysosomal pathway, an observation that has been confirmed via other studies.¹³ Pristine and glycofunctionalized CNPs were observed to share this characteristic subcellular distribution 24 h after the incubation. Co-staining of the lysosomes with CellLight Lysosomes-RFP (Invitrogen) reveals a high correlation of the distribution of the lysosome resident protein LAMP1 and the CNPs (See ESI, Figure S36 + S37), indicating that all the CNPs used in our studies tend to accumulate in the lysosomes. Furthermore, glycofunctionalization does not lead to a decrease in cell viability 24 h post incubation, as measured via XTT assay (see the ESI Figure S38 for details). Surprisingly, CNPs functionalized with glycooligomers show uptake rates similar to the pristine CNPs. We tentatively explain this uptake behaviour using the following, qualitative picture: During endocytosis, both pristine and oligomer-conjugated CNPs are taken up from the encapsulated extracellular solution; the uptake rate is proportional to the density of the CNPs in solution. In addition to this process, monosaccharide-conjugated CNPs may adhere to the outer membrane surface. This picture is commensurate with a quantitative estimation (see ESI). Since the uptake rates are independent of the cell type and hence of the densities of the sugar receptors at the cell surface, we conclude that interactions with receptors do not play a major role in CNP uptake. Rather, we conjecture that the increased uptake rate of monosaccharide-conjugated CNPs may originate from non-specific, physical interactions. The fact that glycoconjugation of the CNPs does not influence the viability of the cells supports the picture that the nanoparticles are captured in the endolysosomal pathway, where they exert only a marginal influence on cellular metabolism.

In conclusion, we have presented protocols for the glycofunctionalization of carbon nanoparticles with different monosaccharides, as well as glycooligomers. NMR studies have been used to verify the nanoparticle-sugar coupling. Uptake studies with different cancer cell lines reveal that the uptake rate does not correlate with the cell-specific expression of lectin receptors nor the type of carbohydrate. Rather, CNPs functionalized with sugar monomers show an approximately two- to threefold increase of the uptake rate in comparison to the pristine nanoparticles, which is similar to the uptake rate for oligomer-functionalized CNPs. This behaviour is tentatively explained using a geometric picture where the uptake takes place in an unspecific combination of CNPs in solution and those which adhere to the cell membrane. Confocal microscopy shows that glycofunctionalization does not modify the intracellular distribution, where the nanoparticles are preferably stored in the endolysosomal pathway. While carbohydrate functionalization has not led to an increase in cell selectivity, cell uptake increased with monosaccharide functionalization, making these glyco-CNPs potentially interesting for cell imaging or drug delivery applications. To achieve a more selective uptake, future studies could explore the effects of using more complex oligosaccharide ligands or non-carbohydrate ligands such as antibodies.

The authors acknowledge the CeMSA@HHU (Center for Molecular and Structural Analytics @ Heinrich Heine University) for recording the mass-spectrometric and the NMR-spectroscopic data, the Center for Advanced Imaging (CAi) at Heinrich-Heine-University Düsseldorf for providing access to the Zeiss LSM 710. L.H. acknowledges funding through the DFG (HA5950/5-2). C.W. and C. N. gratefully acknowledge the founding by the Jürgen Manchot Stiftung.

There are no conflicts to declare.

References

- 1 X. Michalet et al., *Science*, 2005, **307**, 538.
- 2 I. L. Medintz et al., *Nature Materials*, 2005, **4**, 435.
- 3 W. R. Algar et al., *Chem. Rev.*, 2021, **121**, 9243.
- 4 J. Kim et al., *Chem. Soc. Rev.*, 2009, **38**, 372-390.
- 5 L.-L. Chen et al., *Small*, 2022, **18**, 2104567.
- 6 R. Thangam et al., *Nanomaterials*, 2021, **12**, 18.
- 7 J. Shen et al., *Chem. Commun.*, 2012, **48**, 3686.
- 8 L. Cao et al., *J. Am. Chem. Soc.*, 2007, **129**, 11318.

- 9 Wu, Z. L. et al., *Nanoscale* **6**, 3868 (2014).
- 10 Sui, X. et al., *Nanomedicine: Nanotech., Biol. Med.*, 2016, **12**,1997.
- 11 Gong, X. et al., *ACS Appl. Mater. Interfaces*, 2016, **8**, 11288.
- 12 J. Du, N. Xu, J. Fan, W. Sun and X. Peng, *Small*, 2019, **15**, 1805087.
- 13 D. Kersting et al., *Nanotechnology*, 2019, **30**, 39.
- 14 N. Panwar et al., *Chem. Rev.*, 2019, **119**, 9559.
- 15 J. Chen et al., *Adv. Sci. (Weinh.)*, 2016, **3**, 1600270.
- 16 Yim et al., *Chem. Commun.*, 2021, **57**, 9820.
- 17 J. Sun et al., *Chem. Commun.*, 2021, **57**, 1989.
- 18 C. Wang et al., *J. Colloid Interface Sci.*, 2018, **516**, 332.
- 19 D. Rosenblum et al., *Nat. Commun.*, 2018, **9**, 1410.
- 20 R. Lima-Sousa et al., *Carbohydrate Polymers*, 2018, **200**, 93.
- 21 N. Kong et al., *ACS Appl. Bio Mater.*, 2019, **2**, 284.
- 22 D. Sharma et al., *Colloid Polymer Science*, 2020, **298**, 365.
- 23 M.P. Lenza et al., *Cells*, 2020, **9**, 2691.
- 24 J.M. Rios de la Rosa et al., *Adv. Healthcare Mater.*, 2019, **8**, 1901182.
- 25 M. E. Taylor et al., *J. Biol. Chem.*, 1992, 267, 1719.
- 26 P. R. Taylor et al., *Immunol*, 2005, 26, 104.
- 27 E. D. Vedove et al., *Adv Healthc. Mater.*, 2018, **7**, 1701398.
- 28 L. Li et al., *Nanomedicine*, 2018, **14**, 2355.
- 29 S. Fasbender et al., *Sci. Rep.*, 2019, **9**, 12018.
- 30 D. Brevet et al., *Chem. Commun.* 2009, **12**, 1475.
- 31 Y.-H. Tang et al., *Biosens. Bioelectron.* 2018, **116**, 100.
- 32 L. Raviv et al., *Mol. Pharmaceutics*, 2015, **12**, 453.
- 33 F. Wojcik et al., *Chemistry - A European Journal* **2013**, **19**, 3090-3098.
- 34 Ponader et al., *J. Am. Chem. Soc.*, **2014**, **136**, 2008–2016.
- 35 S. Hill and M. C. Galan, *Beilstein J. Org. Chem.*, 2017, **13**, 1136.
- 36 Ye et al., *Chem. Eur. J.*, 2016, **22**, 15216–15221.
- 37 Y. Li et al., *Curr. Drug Delivery* 2008, **5**, 299.
- 38 K. Staines et al., *PLoS One* 2014, **9**, e110330.

Chapter 5

Multilayer graphene quantum dots

The aggregation of GQDs to multilayer structures may affect their fluorescence properties. Aggregation of nanoparticles may occur as a result of high concentrations. As illustrated in Fig. 2.2 the CNDs used in the work related to this thesis also display concentration dependent fluorescence. While this concentration dependence may be explained by other factors such as inner filter effects, aggregation may be a contribution factor. Environmental factors such as the pH value, the solvent polarity, or salt concentration that vary inside biological matter may also play a role in the aggregation. Moreover, multilayer structures have also been shown to natively play a role in different types of CNDs (as discussed in section 1.1.4). To gain a better understanding of the fluorescence mechanisms of carbon nanoparticles and their behavior as a response to aggregation, we performed tight-binding simulations of multilayer GQDs in *Paper IV*. The physical fundamentals for these calculations and their interpretation are introduced in chapter 1.1. Besides the size-dependent energy spectra, the optical absorption spectra were calculated. The results are discussed with a particular focus on the geometry and edge structure of the layers.

5.1 Paper IV

Reference

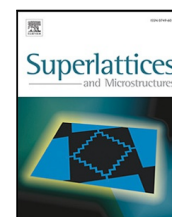
Reproduced from [C. Wimmenauer, J. Scheller, S. Fasbender and T. Heinzl, Single-particle energy–and optical absorption–spectra of multilayer graphene quantum dots. *Superlattices and Microstructures* 132 (2019): 106171. <https://doi.org/10.1016/j.spmi.2019.106171>], with the permission of Elsevier

Copyright statement

The author of this Elsevier article retains the right to include it in a thesis or dissertation, provided it is not published commercially. Theses and dissertations which contain embedded PJAs as part of the formal submission can be posted publicly by the awarding institution with DOI links back to the formal publications on ScienceDirect.

Contributions

I performed the numerical simulations together with JS and wrote the manuscript together with TH.



Single-particle energy – and optical absorption – spectra of multilayer graphene quantum dots

C. Wimmenauer, J. Scheller, S. Fasbender, T. Heinzl^{*}

Solid State Physics Laboratory, Heinrich-Heine-Universität, Universitätsstr.1, 40225 Düsseldorf, Germany



ARTICLE INFO

Keywords:

Quantum dots
Tight binding model
Energy spectra
Carbon nanodot
Multilayer graphene
Absorption spectra

ABSTRACT

The energy spectra of quantum dots formed by stacked disks of graphene are calculated as a function of the disk shape and size, the number of disk layers and the edge type (zigzag/armchair) within a tight-binding approach in the single-particle picture. Stacks formed by up to seven disks of hexagonal, rhombic and triangular shape are considered. For both edge types, we find a monotonously decreasing energy gap as the number of stacked disks or the disk size is increased, with the exception of triangular dots with zigzag edges, which have a metallic character. In some cases, simple scaling relations for the energy gaps can be formulated. Furthermore, the optical absorption spectra within the dipole approximation are calculated. The results are interpreted with the help of selected HOMO wave functions that form inside the stacks.

1. Introduction

A single layer of graphite, also known as graphene, has a variety of remarkable properties due to the linear energy dispersion of the electronic states close to the Fermi level, which implies a description of the electronic dynamics in terms of massless Dirac fermions [1,2]. One branch of graphene research focuses on graphene quantum dots (GQDs), comprising preparation techniques, fundamental optical and transport properties [3–7] as well as applications [8] like photovoltaics [9,10] and photocatalysis [11], sensing [12–14] or storage of energy [15,16]. Recently, GQDs have been used for imaging in biological and medical studies [17–22], where their intrinsic water solubility and their small size [8,23] in combination with their low toxicity [24] offer advantages in comparison to conventional quantum dots composed of binary semiconductors [25,26]. In this field, tailoring the optical properties to the specific requirements of the experiment is desirable. For example, living cells suffer from UV irradiation, such that an absorption peak of the GQDs in the blue or green range is often to be preferred. Clearly, the diameter of the graphene disks, their edge type (zigzag or armchair) as well as the number m of stacked disks are relevant parameters that influence the energy spectra of the GQDs. Unfortunately, however, even though a wide variety of GQDs, including GQD stacks, has been prepared according to different recipes and subsequently used in many experiments, the tailoring of the optical properties of GQDs by the preparation parameters is still in its infancy. Even though different absorption maxima in the range between 320 nm and 450 nm as well as fluorescence emission maxima between 450 nm and 650 nm have been reported [27,28], a relation of the experimentally observed absorption and fluorescence energies with the GQD parameters stated above has not yet been established, despite remarkable recent progress in relation to single-layer, triangular dots with armchair edges [29]. Rather, the optical properties have been explained qualitatively in terms of moieties like amines or hydroxy groups, as well as by crystal defects. The vision of being able to tailor the optical properties of GQDs with respect to a specific application thus requires a wide variety of experimental and theoretical

^{*} Corresponding author.

E-mail address: thomas.heinzl@hhu.de (T. Heinzl).

studies, one element of which are numerical calculations of the energy spectra of stacked graphene disks, preferably carried out for various disk shapes and sizes, as well as for various stack heights.

Several authors have reported the formation of multilayer GQDs with up to three graphene layers [30–32], while nanoparticles with many more layers are conceptually feasible [33]. On the theory side, GQD energy spectra were calculated analytically within certain approximations for single layer [34] and double layer [35] graphene disks, both with an infinite mass boundary (i.e neglecting the edge structure). Besides the infinite mass boundary condition, armchair and zigzag boundary conditions were also used in the Dirac–Weyl-Model [36], where it has been established that the edge structure is highly relevant [37–40]. A comprehensive comparison between the analytic (Dirac) and the tight-binding approach for hexagonal and triangular GQDs has been presented in Ref. [36], showing that the solutions for the energy eigenstates in the Dirac-Model and the tight binding model are qualitatively similar but deviate quantitatively. These calculations have shown that the tight-binding model does give reliable results, including the influence of the edge structure, while an inclusion of states not belonging to the π -bands, like impurities or adsorbates, is by no means straightforward and should be carried out using different approaches like density functional theory or ab-initio models. However, even disregarding defects and adsorbates, calculations have been hitherto presented only for stacks of up to three graphene disks [41–43].

The objective of the present manuscript is to move one step forward in this direction by elucidating how the energy gap depends on the number m of graphene disks that form the quantum dot, and how these dependencies are reflected in the optical absorption spectra. We use the tight-binding model to calculate the single-particle energy spectra of defect-free, Bernal-stacked GQDs of hexagonal, rhombic and triangular shape, with the number of stacked layers $m \leq 7$, and for both zigzag and armchair edges. Our results are also supposed to serve as an estimate for the band gaps that can be expected for ideal systems, as well as a reference for more elaborate simulations that may include, for example, defects or electron–electron interactions [44–46]. They extend previous results for quantum dots with smaller m , and in some cases allow the formulation of an empirical scaling relation for the dependence of the energy gap on the size of the graphene disk and on m .

2. Description of the numerical implementation

Three different geometries are considered, namely hexagonal (see Fig. 1(a, b)), triangular (see Fig. 1(c, d)) and rhombic (see Fig. 1(e, f)). The geometry determines the number of edge defects in the corners and thereby influences the character of some states, most prominently of the edge states in the disks with zigzag edges. As one moves along the edge and crosses a corner, the angle between the edges is given by the condition $\theta = n \cdot \pi/3$ in our structures, where $n \in \mathbb{N}$. If n is odd, the corner is commensurate with the edge type. If, on the other hand, n is even, the corner is incommensurate with the edge type and represents an impurity inside the otherwise pristine edge. Therefore, we find in our geometries edge defects in all six corners of hexagonal GQDs, no edge defects in the triangular GQDs and edge defects in two of the corners of the rhombic GQDs. Equations that relate the length of the edge L , the number of atoms at the edge N_S and the number of atoms per disk N are given in Fig. 1, as well as in the supplement (S1). In all equations $a = 0.142 \text{ nm}$ denotes the bond length between two neighboring carbon atoms in graphene.

We proceed with the introduction of our model Hamiltonian used for all simulations, and with the description of the numerical implementation. The stacking geometry and the coupling energies used are illustrated in Fig. 1, where exemplarily bilayer hexagonal GQDs with zigzag (a) and armchair (b) edges are shown. Stacks with larger m can be formed by a periodic repetition of the Bernal stacking. Neighboring carbon atoms within one disk are coupled via the hopping energy $t = 2.7 \text{ eV}$ [47]. Atoms in sublattice A of the top layer are located directly on top of the sublattice A atoms of the bottom layer, with a corresponding coupling energy of $\gamma_1 = 0.4 \text{ eV}$ [47]. The atoms that form sublattice B in the top layer couple to three atoms of sublattice B of the bottom layer with a hopping energy of $\gamma_3 = 0.3 \text{ eV}$ [47]. All other interlayer coupling energies amount to $\approx 0.04 \text{ eV}$ and below, which are neglected in the following, in accordance with common practice [47]. Also, coupling effects between non-nearest neighbor layers are disregarded. It should be noted that such a stack of graphene disks is identical to a small column of conventional graphite with an edge configuration that corresponds to the Bernal stacking.

The resulting tight-binding Hamiltonian H reads

$$H = - \sum_{\langle i,j \rangle, m} t(a_{m,i}^\dagger b_{m,j} + h.c.) - \sum_{i, \langle m1, m2 \rangle} \gamma_1(a_{m1,i}^\dagger a_{m2,i} + h.c.) - \sum_{\langle i,j \rangle, \langle m1, m2 \rangle} \gamma_3(b_{m1,i}^\dagger b_{m2,j} + h.c.) \quad (1)$$

Here, $a_{m,i}^\dagger (b_{m,i}^\dagger)$ denote the creation operator at sublattice A(B) in layer $m1$ or $m2$ with $m1, m2 \in \{1, \dots, 7\}$ at the site \mathbf{R}_i . The corresponding annihilation operators are denoted by $a_{m,i}$ and $b_{m,i}$, respectively. The reference energy ($E = 0$) is chosen to be the on-site electrostatic potential. Furthermore, spin is not included, i.e., all states computed show an additional two-fold spin degeneracy.

The KWANT package [48] was used for computing the energy eigenvalues as well as the optical transition matrix elements. The energy bands of the multi-layered quantum dots were computed, and the energy gaps were determined from the states with the lowest (highest) energy in the conduction (valence) band (named LUMO and HOMO, respectively) as a function of the parameters m and the disk size, which we parameterize by N (see above). To check our implementation, we have reproduced earlier results reported for hexagonal monolayer GQDs, both with armchair and zigzag edges. The energy gaps we obtain are in quantitative agreement with Ref. [36] (not shown).

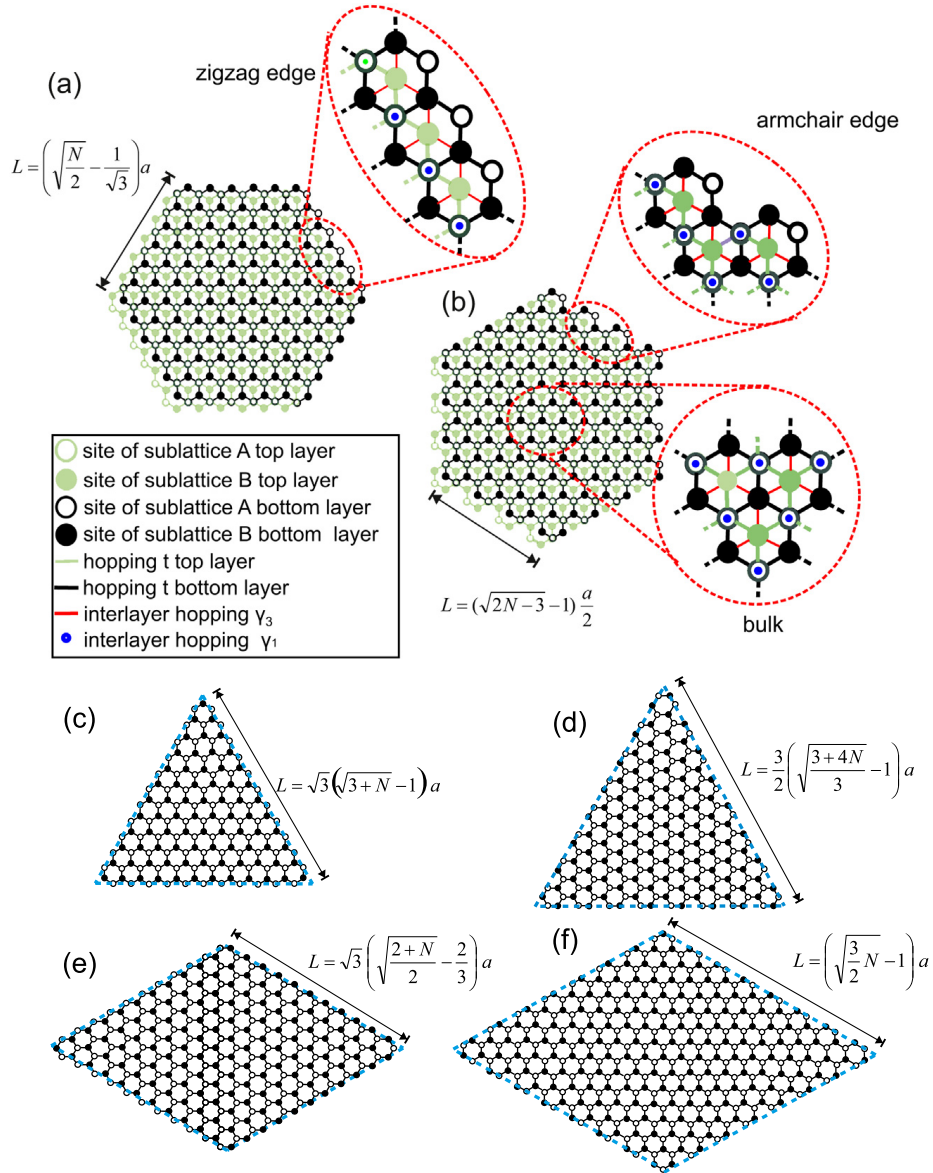


Fig. 1. Scheme and designations of the considered stacking for hexagonal zigzag (a) and armchair (b) graphene quantum dots (GQDs). Illustrations of a single layer of zigzag (c) and armchair (d) triangular GQDs as well as (e) zigzag and (f) armchair rhombic GQDs are shown as well. The dashed blue border drawn in the triangular and rhombic dots indicates the geometry for which the length L , as used in the expression for its relation to the number of sites N , is measured. The constant $a = 0.142$ nm denotes the bond length between two neighboring carbon atoms in graphene.

The absorption spectra $A(\omega)$ were calculated using [49]

$$A(\omega) = \sum_{i,f} |\langle \Psi_f | P | \Psi_i \rangle|^2 \delta(\hbar\omega - (E_f - E_i)) \quad (2)$$

Here, $\hbar\omega$ denotes the photon energy. The expression $|\langle \Psi_f | P | \Psi_i \rangle|^2$ is the transition matrix element from the initial state $|\Psi_i\rangle$ to the final state $|\Psi_f\rangle$, with the corresponding energy eigenvalues E_i and E_f and the dipole operator P . Only transitions from occupied initial states to unoccupied final states were considered in the summation, assuming a Fermi-Dirac distribution in the low temperature limit. The implementation was tested by reproducing published tight-binding spectra of triangular zigzag GQDs [49].

Multilayer graphene quantum dots composed of 1 to 7 disks are considered, with N ranging from 24 (corresponding to a disk diameter of approximately 0.8 nm) to 1986 (disk diameter approximately 8.8 nm), both for the hexagonal shape. Triangular and rhombic GQDs of comparable sizes were considered. Also, the limit of $m \rightarrow \infty$ has been calculated using the *physics.bands* method from the KWANT package, which is based on implementing the discrete translational symmetry for the stacking direction in the tight-binding Hamiltonian [48].

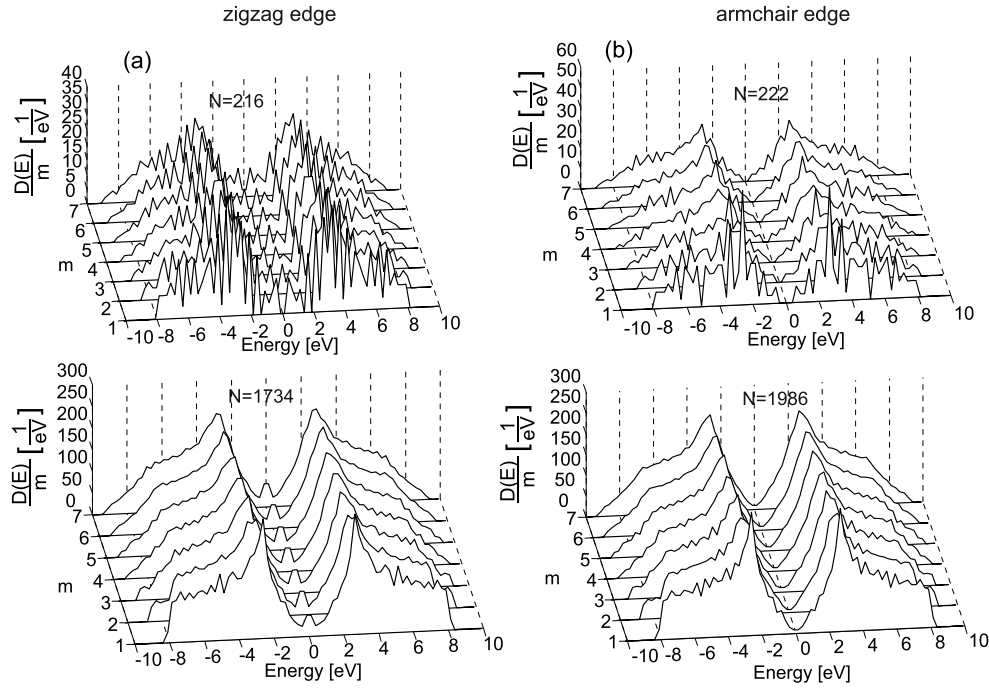


Fig. 2. Waterfall plots of typical computed densities of states $D(E)$ of hexagonal GQDs, normalized to the number m of disk layers, and their evolution as a function of m , for a small ($N = 216$) and large ($N = 1734$) disk with zigzag edges (a), and for armchair dots with $N = 222$ and $N = 1986$, respectively (b).

3. Results and discussion

Both hexagonal and rhombic GQD disks contain edge defects at their corners in the sense as described above. This leads to similarities in the electronic structures, and therefore, hexagonal and rhombic GQDs are discussed jointly. The defect-free edges of triangular GQDs, on the other hand, give rise to a somewhat different energy spectrum and are discussed separately thereafter.

In Fig. 2, the densities of states $D(E)$ for hexagonal GQDs as they emerge from the computed energy spectra are illustrated. We have calculated all energy levels that develop from the $2p_z$ states of the carbon atoms, such that the number of (spin-degenerate) energy levels forming $D(E)$ equals N . A bin size of 0.25 eV has been used for all plots in order to keep the number of states per bin sufficiently large. For small zigzag dots (upper part in Fig. 2(a)), an energy gap E_g around $E = 0$ is resolvable in between two weak DOS peaks that correspond to the edge states, in agreement with results obtained earlier [37].

As m increases, the band broadens and E_g gets smaller. For large N , (lower part in Fig. 2(a)), the edge states tend to merge and form a peak around $E = 0$. An energy gap is still present but is not visible here, since its energy has dropped below the bin size. In Fig. 2(b), the densities of states are shown for a comparable small and a large hexagonal armchair dot. The small dot (upper part of Fig. 2(b)) shows a pronounced energy gap which decreases as m is increased, while the low energy peak in $D(E)$, which is characteristic for the edge state in zigzag dots, is absent. Also here, the band broadens as m increases. For the large armchair GQD, E_g has again dropped below the resolution threshold of this plot, while $D(E)$ has developed its typical, approximately parabolic shape close to $E = 0$. In rhombic GQDs, $D(E)$ shows a similar behavior, the most prominent difference being a higher peak around $E = 0$ due to lower E_g at comparable sizes, see Fig. S2 in the supplement. In the following, we focus on the dependence of E_g on m , N , the geometry and on the edge type.

For sufficiently large N , E_g of the hexagonal and rhombic zigzag GQDs depends approximately exponentially on N , i.e., $E_g \propto e^{-\sqrt{N} \cdot \gamma}$, see Fig. 3(a, c). In the case of hexagonal zigzag GQDs, the exponent γ takes the value of 0.16 for $m = 1$ and increases towards 0.2 as m is increased, see the inset. For rhombic zigzag GQDs, a value for γ of 0.78 for $m = 1$ is found, which increases towards 0.86 with increasing m . The exponential dependence indicates that the penetration of the edge state wave function into the bulk of the dot, or in other words, the degree of localization of the edge state, determines the energy gap [50], and that the increase of the circumference with N is not the dominant factor for the size of the energy gap. The data also suggest that this localization gets stronger as m is increased. We note that our data fit significantly worse to an algebraic model as used in Ref. [40], albeit in a somewhat different setting.

The energy gap of hexagonal and rhombic armchair dots, on the other hand, show an algebraic dependence on N , i.e., $E_g \propto N^{-\alpha/2}$ with the well-known exponent of $\alpha = 1$ for $m = 1$, which increases towards 2 as m is increased, see Fig. 3(b, d). This increase can be regarded as an indication that the electronic states develop a quasi-three dimensional character as m is increased. Furthermore, the energy gaps of armchair GQDs of comparable size are generally significantly larger, with a ratio which increases as N is increased. This difference reflects the fact that in the dots with zigzag edged, the gap energy is determined by the disturbance of the edge states by the edge defects at the corners, after which their energies remain relatively close to zero.

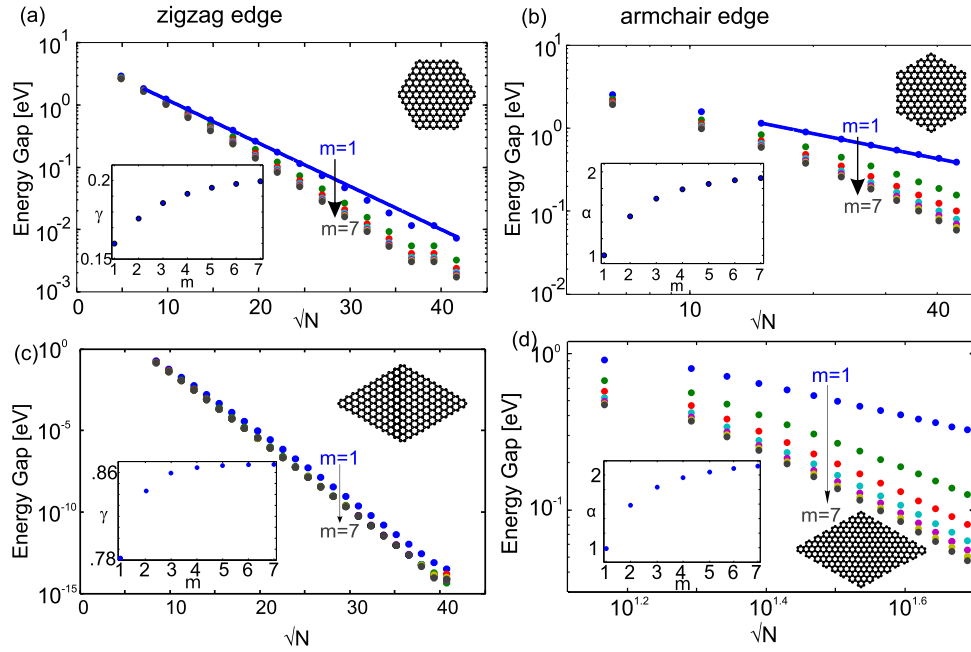


Fig. 3. Energy gap of the stacks of hexagonal zigzag (a) and of armchair (b), as well as rhombic zigzag (c) and armchair (d) graphene quantum dots as a function of the number N of atomic sites per disk for different m .

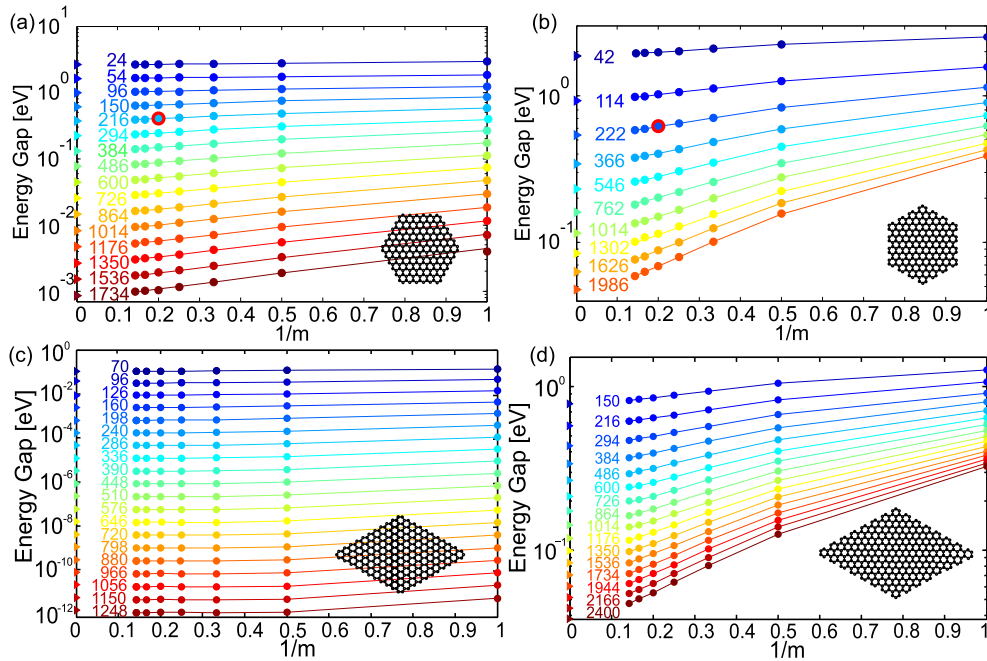


Fig. 4. Energy gap of the stacks of hexagonal zigzag (a) and of armchair (b), as well as rhombic zigzag (c) and armchair (d) graphene quantum dots as a function of the inverse number of layers $1/m$ for disks with a different number of atomic sites N .

The dependence of E_g on m for fixed N , see Fig. 4(b, d), is stronger in armchair GQDs as compared to that one of zigzag GQDs, see Fig. 4(a, c). Neither an exponential nor a simple algebraic dependence on m , of the form $E_g \propto m^\alpha$, is observed in any type of GQD. Furthermore, the energy gaps for $m \rightarrow \infty$ agree reasonably well with the extrapolation of the evolution of $E_g(1/m)$ towards $1/m \rightarrow 0$ for both edge types, such that an educated guess for the value of the energy gap for arbitrary m is possible from Fig. 4.

To shed some light on the different scaling of GQDs with zigzag and with armchair edges, we take a look at the HOMO/LUMO wave functions of selected, hexagonal GQDs, shown via the respective probability densities $|\Psi(\mathbf{r})|^2$ as a function of the spatial coordinate \mathbf{r} , see Fig. 5. The HOMO wavefunction in the hexagonal zigzag GQDs is concentrated at the side walls of the dots, as can be seen in Fig. 5(a), whereas that one of the hexagonal armchair GQDs is extended more homogeneously across the bulk of the column, see Fig. 5(b). For comparison, the corresponding $|\Psi(\mathbf{r})|^2$ of the two degenerate ground states in a single disk of the same type

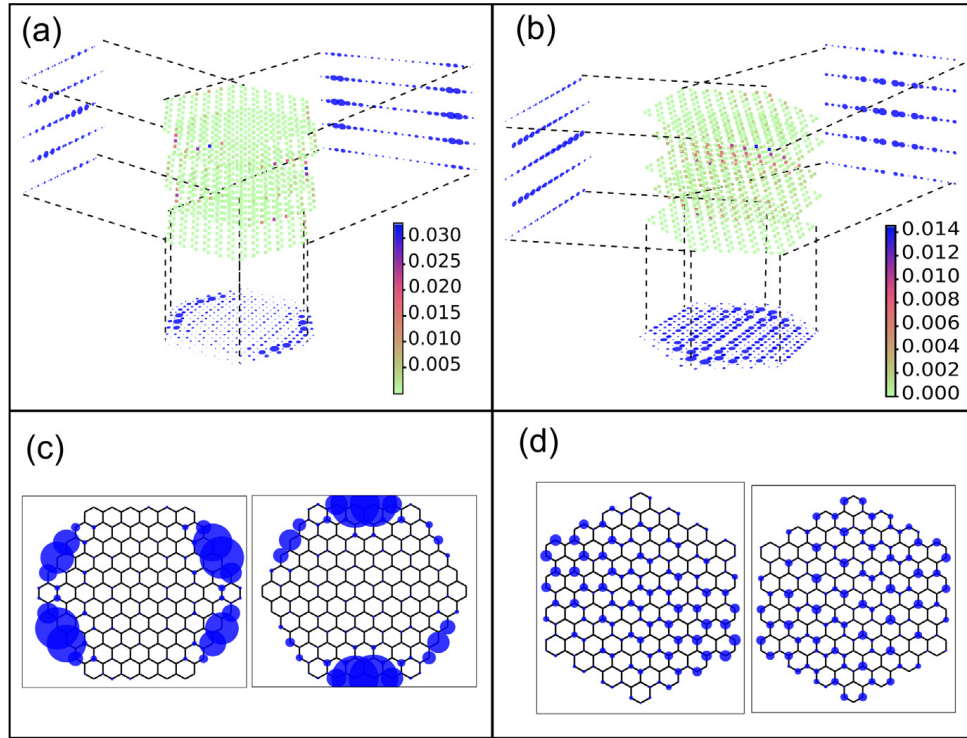


Fig. 5. Illustration of the electronic highest occupied molecular orbital HOMO state probability densities $|\Psi(\mathbf{r})|^2$ for hexagonal quantum dots formed by stacks of five zigzag (a) and armchair (b) disks, respectively. The projection planes contain the integrated $|\Psi(\mathbf{r})|^2$ along the directions perpendicular to the plane. In (c) and (d), $|\Psi(\mathbf{r})|^2$ of the two degenerate HOMO wave functions are shown for single disks which form the two types of dots.

and size are depicted in Fig. 5(c) and (d), respectively. Here, the characteristic edge state is seen for the zigzag GQD, while the wave functions of the ground state in the armchair disk have a more two-dimensional character. Thus, as the zigzag or armchair disks are stacked to form the three-dimensional quantum dots, this character of the HOMO state wave function is maintained, resulting in a quasi-two-dimensional state in the case of zigzag stacks, approximately confined to a cylinder mantle, and a quasi-three-dimensional state for stacks of armchair disks. It should be noted that the symmetry under rotation about the z axis by π reflects the symmetry of the stacked layers [40].

The absorption spectra were calculated for exemplary GQDs to illustrate the relation of the calculated energy spectra to the optical properties. In Fig. 6, the spectra, more specifically the optical joint density of states (JDOS), of hexagonal $N = 216$ zigzag (a, c) and $N = 222$ armchair (b, d) GQDs consisting of up to seven layers are shown. Peak amplitudes that are more than three orders of magnitude smaller than the main transition may originate from numerical noise and are neglected. For the excitation radiation polarized perpendicularly to the stacking direction (upper row in Fig. 6), the energy of the main transition (marked in red) is larger than the energy gap for both GQDs. Due to the symmetry of the HOMO and LUMO wave functions, an optical dipole transition at E_g is not possible. In the zigzag GQD, see Fig. 6(a), the main transition peak shifts from 0.66 eV for $m = 1$ to 0.57 eV for $m = 7$, while the energy gap shifts from 0.58 eV to 0.39 eV. For the armchair GQD (see Fig. 6(b)) on the other hand, the main transition peak shifts from 1.31 eV for $m = 1$ to 1.12 eV for $m = 7$, while the energy gap decreases from 1.14 eV to 0.58 eV. The decrease of the transition energy of the main peak with increasing m thus correlates with the decrease of E_g , but the relation is not linear. For polarization in stacking direction, we find main transition peaks slightly closer to the energy gap. Interestingly, for the armchair GQD we find a blue shift of the absorption edge as m increases, while the HOMO and LUMO levels do show a red shift. The corresponding JDOS plots for rhombic GQDs can be found in the supplement (S3).

We continue by describing the properties of the triangular GQDs and stacks thereof. In Fig. 7, their density of states $D(E)$, normalized to the number m of layers, is shown for selected examples. A bin size of 0.25 eV is used. For the zigzag edge type, a peak at zero energy in $D(E)$ is present for all GQDs. This peak is larger compared to the other geometries for comparable sizes, due to the presence of true zero energy states for all sizes, which has its origin in the absence of edge defects at the corners. The degeneracy of the zero energy state increases according to $g = (N_S - 1)m = (\sqrt{3} + N - 3)m$, which is consistent with the well known degeneracy for $m = 1$ [51]. The magnitude of the peak at $E = 0$ in $D(E)/m$ does not change with increasing m , since g depends linearly on m . The density of states for small ($N = 216$, Fig. 7(b)) and large ($N = 2268$, Fig. 7(d)) triangular armchair GQDs shows a behavior similar to that one of hexagonal and rhombic armchair GQDs (see above). A broadening in $D(E)$ for an increasing number of layers can be observed for both edge types.

The HOMO and LUMO states in triangular GQDs with zigzag edges are true zero energy states. Hence, E_g equals zero and is not suited to parameterize the evolution of the electronic spectrum as a function of N and m . Thus, in order to be able to characterize the evolution of the energy spectrum also in this case by a characteristic energy difference, we study the energy gap between the

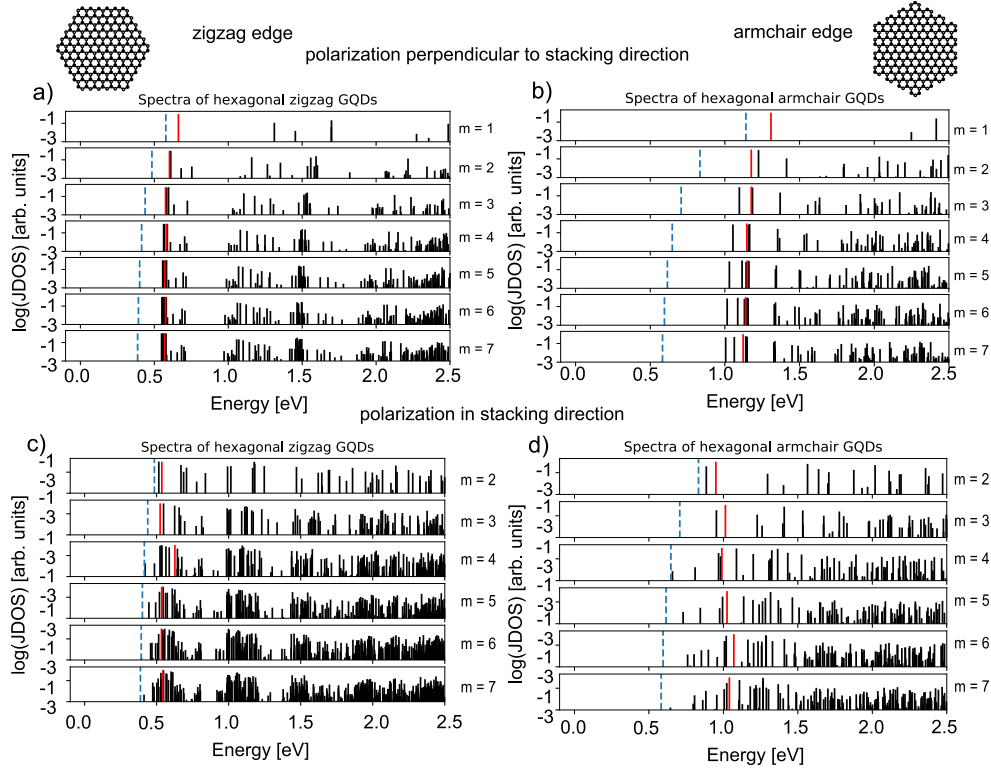


Fig. 6. Absorption spectra of hexagonal graphene quantum dots (GQDs). The optical joint density of states (JDOS) is plotted semilogarithmically against the photon energy for $N = 216$ zigzag (a, c) and $N = 222$ armchair (b, d) GQDs. The polarization of the excitation in the plane of the disks (a, b) and perpendicular to it (c, d) are shown in the upper and lower row, respectively. The value of the energy gap is tagged with a dashed blue line for comparison. The transition with the highest probability is marked in red.

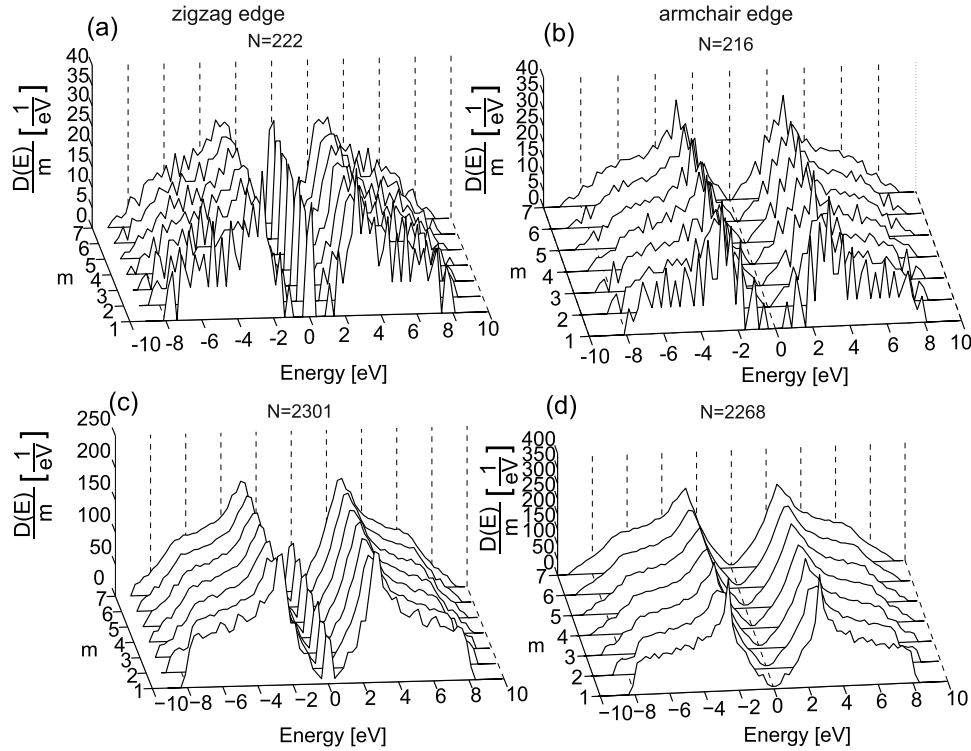


Fig. 7. Waterfall plots of typical computed densities of states $D(E)$ for triangular GQDs, normalized to the number m of disk layers, and their evolution as a function of m , for a small ($N = 222$) and large ($N = 2301$) disks with zigzag edges (a, c), and for armchair dots with $N = 216$ and $N = 2268$, respectively (b, d).

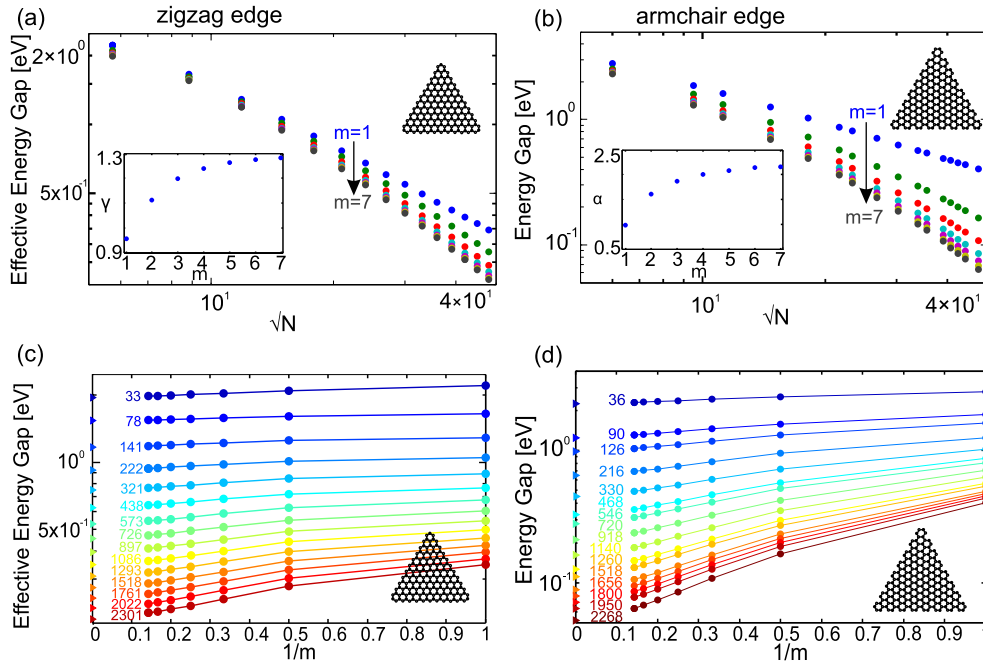


Fig. 8. Energy gap E_g and effective energy gap E_g^* of triangular GQDs with armchair end zigzag edges, respectively. In contrast to E_g , which is the HOMO/LUMO energy gap, the effective energy gap E_g^* denotes the energy gap between the conduction band states and the zero energy states in triangular zigzag GQDs. The dependence of E_g (E_g^*) on the number of atoms per disk N for zigzag (a) and armchair (b) is shown in the upper panel. The dependence of E_g (E_g^*) on the inverse number of disks $1/m$ for zigzag (c) and armchair (d) GQDs is shown in the lower panel.

edge states and the nearest energy level in the conduction band, which we denote by E_g^* in Fig. 8. We find an algebraic dependence with the exponent α ranging approximately from $\alpha = 0.96$ for $m = 1$ to $\alpha = 1.3$ for E_g^* as a function of N , see Fig. 8(a). This difference to the behavior of hexagonal and rhombic zigzag GQDs can be explained by the absence of edge states with non-zero energy. The lowermost conduction band state above the edge state is not localized at the edges, and therefore, the scaling of E_g^* is determined by the scaling of the volume rather than the penetration of an edge state into the bulk. Armchair triangular GQDs, on the other hand, show a very similar behavior to hexagonal and rhombic GQDs. The dependence of E_g on N also follows an algebraic dependence, with α values ranging from $\alpha = 1$ for $m = 1$ to $\alpha = 2$ for $m = 7$, see Fig. 8(b). As discussed in relation to the previous geometries, we are unable to find a simple functional description for the monotonous decrease of E_g with an increasing number of layers for both edge types, see Fig. 8(c, d).

For comparison, the optical absorption spectra of triangular $N = 222$ zigzag and $N = 216$ armchair GQDs were calculated, see Fig. 9. The dominant peak in the zigzag GQD (a, c) is at zero energy. This peak has no impact on the optical properties of the GQD and can be understood as a transition between edge state wave functions in response to a time-independent electric field, reminiscent of a DC Stark effect. The lower threshold for optical absorption of radiation polarized in the disk plane is approximately at E_g^* , corresponding to a transition between the zero energy states and the non-edge state with the lowest energy. For polarization in stacking direction, the JDOS at the absorption edge is about two orders of magnitude smaller than the transition peak at $E = 0$. For polarization in the disk plane the main transition peak, which is equal to the absorption edge in this case, shifts towards E_g^* with increasing m , see Fig. 9(a). The absorption edge for polarization in stacking direction shows a red shift, which is smaller than that one for light with polarization in the disk plane. We mention that computing the eigenfunctions of the edge state for the triangular dots with zigzag edges is hampered by numerical difficulties, which originate in the nominally zero, but numerically extremely small numbers for the energy eigenvalues. This fluctuation may also impact the calculated transition probabilities from and into zero energy states. For the triangular armchair GQD (b, d) the main transition peak is well above the calculated energy gap. The main transition peak shifts from 1.43 eV for $m = 1$ to 1.25 eV for $m = 7$, while E_g decreases from 1.25 eV to 0.96 eV, see Fig. 9(b). As in the case of hexagonal armchair GQDs, the red shift of E_g can be used to qualitatively estimate the red shift of the absorption edge as well as the main transition peak, for polarization in the disk plane. For the polarization in the stacking direction, however, a blue shift of the main transition peak is observed as m is increased, indicating that the transition between the HOMO and LUMO level violates the dipole selection rule.

We conclude this section with a comparison of our numerical results to some published experimental data and to numerical results obtained by other techniques. Subramaniam et al. [52] performed low-temperature scanning tunneling spectroscopy on graphene islands prepared on Ir(111) surfaces. The monolayer disks have a distorted hexagonal shape with edge lengths of ≈ 4.6 nm (corresponding to approximately 2200 carbon atoms per dot), and predominantly with zigzag edges. In this system, the band gap depends on the Ir-graphene distance and approaches a value of ≈ 320 meV for large distances. This value lies in between our values for the energy gaps of hexagonal single layer disks of this size for zigzag ($E_{g(\text{zigzag}, N = 1734, L = 4.1 \text{ nm})} = 4$ meV) and for armchair ($E_{g(\text{armchair}, N = 1986, L = 4.4 \text{ nm})} = 400$ meV). An extrapolation via the obtained power law yields that

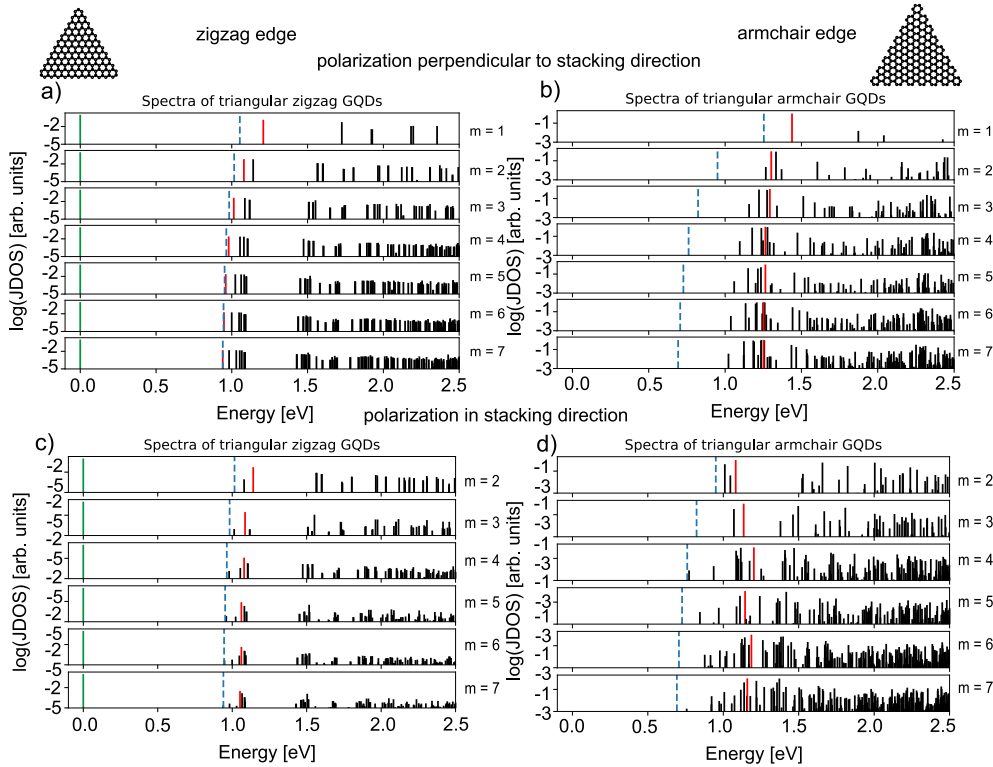


Fig. 9. Absorption spectra of triangular graphene quantum dots (GQDs). The optical joint density of states (JDOS) is plotted semilogarithmically against the photon energy for $N = 222$ zigzag (a, c) and $N = 216$ armchair (b, d) GQDs. Polarized excitation in the plane of the disks (a, b) and perpendicular to the disk plane (c, d) was considered. The value of the (effective) energy gap E_g (E_g^*) is tagged with a dashed blue line for comparison. The non zero energy transition peak with the highest probability is marked in red. The transitions between zero energy states are shown in green.

$E_g(\text{armchair}, N = 2200) = 370 \text{ meV}$. This comparison indicates that the zigzag edges of the quantum dots in this implementation are not perfect but contain defects, thereby shifting the band gap energy to larger values, towards that one for armchair edges. Moreover, the spectra of the excited states in such systems scale with the dot size in rough agreement with our calculations [53]. Kastler et al. have reported the synthesis of very small GQDs (containing 42 carbon atoms) from aromatic hydrocarbon molecules [54]. The shapes of these dots comprise clean as well as distorted hexagons, with predominantly armchair edges. The authors observe optical transition energies in the range of 2.7 eV, which depend slightly on the shape of the dots as well as on the adsorbates at the edges. For the smallest hexagonal GQDs we find energy gaps of $E_g(\text{zigzag}, N = 24) \approx 2 \text{ eV}$ and $E_g(\text{armchair}, N = 42) = 2.5 \text{ eV}$, see Fig. 4(a, b). This is in reasonable agreement with comparable particles in Ref. [54]. In a recent work, the preparation of triangular GQDs with armchair edges of high quality has been reported [29]. The authors have compared the experimental absorption spectra with numerical simulations by density functional theory. Their results for GQDs without functionalization correspond to the assumption of hydrogen termination at the edges within the tight-binding model. For example, the quantum dot labeled T-CQDs-3 represents a triangular GQD with armchair edges of $L = 1.7 \text{ nm}$, containing 60 carbon atoms. A transition wavelength of 500 nm is found, corresponding to a photon energy of 2.5 eV, in very good agreement with our results, see Fig. 9(b,d). It should be emphasized that our tight-binding model is a single particle model which disregards the excitonic binding energies, which will decrease the absorption edges by a value of a few tens of meV [29]. Finally, we mention the work of Chen et al. [55], who have reported a red shift of the absorption spectra of GQDs with sizes around 20 nm as a consequence of aggregation, which can be interpreted as a form of disordered stacking, in qualitative agreement with our numerical results.

4. Summary and conclusions

We have presented tight-binding calculations for graphitic quantum dots formed by stacked graphene disks in the shape of hexagons, rhombuses and triangles, both with armchair and zigzag edges. The energy spectra as well as the optical absorption spectra of these systems were calculated as a function of the disk size as well as of the number of stacked disks. In the absence of zero-energy edge states, the energy gaps decrease monotonously as the number of carbon atoms per disk or the number of disks per stack is increased. Zigzag quantum dots show a significantly smaller band gap as compared to armchair quantum dots with an identical number of disks and a similar number of carbon atoms. For the zigzag dots, the dependence of E_g on m is weaker and that one on N is stronger than for armchair dots. This behavior can be qualitatively understood in terms of the character of the ground state wave function of a single disk. Stacking the disk transforms the quasi-one-dimensional edge state in zigzag disks into a state that is localized at the mantle of the dot, while the ground state wave functions of the armchair disk has a more two-dimensional

character, which transforms into a three-dimensional wave function when the stack is formed. Triangular dots with zigzag edges are a special case due to the presence of edge states exactly at zero energy. This property originates from the corners which do not disturb the zigzag geometry of the edge in this shape. Since the limiting case of $m \rightarrow \infty$ has also been considered, our data hopefully provide a guideline for estimating the single-particle energy gap for graphitic nanoparticles over a wide range of sizes.

Acknowledgments

The authors would like to thank HHU Düsseldorf for financial support. S. F. acknowledges funding by the Düsseldorf School of Oncology (DSO), Germany. C. W. acknowledges funding by the Jürgen Manchot Stiftung, Germany.

Appendix A. Supplementary data

Supplementary material related to this article can be found online at <https://doi.org/10.1016/j.spmi.2019.106171>.

References

- [1] K.S. Novoselov, A.K. Geim, S.V. Morozov, D. Jiang, M.I. Katsnelson, I.V. Grigorieva, Two-dimensional gas of massless dirac fermions in graphene, *Nature* 438 (2005) 197.
- [2] Y. Zhang, Y.-W. Tan, H.L. Stormer, P. Kim, Experimental observation of the quantum hall effect and berry's phase in graphene, *Nature* 438 (2005) 201.
- [3] A.V. Rozhkov, F. Nori, Exact wave functions for an electron on a graphene triangular quantum dot, *Phys. Rev. B* 81 (2010) 155401.
- [4] P. Recher, B. Trauzettel, Quantum dots and spin qubits in graphene, *Nanotechnology* 21 (2010) 302001.
- [5] Z.Z. Zhang, K. Chang, F.M. Peeters, Tuning of energy levels and optical properties of graphene quantum dots, *Phys. Rev. B* 77 (2008) 235411.
- [6] J. Güttinger, T. Frey, C. Stampfer, T. Ihn, K. Ensslin, Spin states in graphene quantum dots, *Phys. Rev. Lett.* 105 (2010) 116801.
- [7] A.D. Güçlü, P. Potasz, M. Korkusinski, P. Hawrylak, *Graphene Quantum Dots*, Springer, New York, 2014.
- [8] H. Li, Z. Kang, Y. Liu, S.-T. Lee, Carbon nanodots: Synthesis, properties and applications, *J. Mat. Chem.* 22 (2012) 24230.
- [9] Y. Li, Y. Hu, Y. Zhao, G. Shi, L. Deng, Y. Hou, L. Qu, An electrochemical avenue to green-luminescent graphene quantum dots as potential electron-acceptors for photovoltaics, *Adv. Mater.* 23 (2011) 776.
- [10] V. Gupta, N. Chaudhary, R. Srivasta, G.D. Sharma, R. Bhardwaj, S. Chand, Luminescent graphene quantum dots for organic photovoltaic devices, *J. Am. Chem. Soc.* 133 (2011) 9960.
- [11] S. Bhattacharyya, F. Ehrat, P. Urban, R. Teves, R. Wyrwich, M. Döblinger, J. Feldmann, A.S. Urban, J.K. Stolarczyk, Effect of nitrogen atom positioning on the trade-off between emissive and photocatalytic properties of carbon dots, *Nature Commun.* 8 (2017) 1401.
- [12] H. Sun, L. Wu, W. Wei, X. Xu, Recent advances in graphene quantum dots for sensing, *Mater. Today* 16 (2013) 433.
- [13] A. Ananthanarayanan, X. Wang, P. Routh, B. Sana, S. Lim, D.-H. Kim, K.-H. Kim, J. Li, P. Chen, Facile synthesis of graphene quantum dots from 3d graphene and their application for Fe³⁺-sensing, *Adv. Funct. Mater.* 24 (2014) 3021.
- [14] B. Kong, A. Zhu, C. Ding, X. Zhao, B. Li, Y. Tian, Carbon dot-based inorganic-organic nanosystem for two-photon imaging and biosensing of ph variation in living cells and tissues, *Adv. Mater.* 24 (2012) 5844.
- [15] W.-W. Liu, Y.Q. Feng, X.-B. Yan, J.-T. Chen, Q.-J. Xue, Superior micro-supercapacitors based on graphene quantum dots, *Adv. Funct. Mater.* 23 (2013) 4111.
- [16] Z. Zhu, J. Ma, Z. Wang, C. Mu, Z. Fan, L. Du, Y. Bai, L. Fan, H. Yan, D.L. Phillips, Efficiency enhancement of perovskite solar cells through fast electron extraction: the role of graphene quantum dots, *J. Am. Chem. Soc.* 136 (2014) 3760.
- [17] Z.L. Wu, M.X. Gao, T.T. Wang, X.Y. Wan, L.L. Zheng, C.Z. Huang, A general quantitative ph sensor developed with dicyandiamide n-doped high quantum yield graphene quantum dots, *Nanoscale* 6 (2014) 3868.
- [18] L. Cao, X. Wang, M.J. Mezziani, F. Lu, H. Wang, P.G. Luo, Y. Lin, B.A. Harruff, L.M. Veca, D. Murray, S. Xie, Y. Sun, Carbon dots for multiphoton bioimaging, *J. Am. Chem. Soc.* 129 (2007) 11318.
- [19] C. Liu, P. Zhang, F. Tian, W. Li, F. Li, W. Liu, One-step synthesis of surface passivated carbon nanodots by microwave assisted pyrolysis for enhanced multicolor photoluminescence and bioimaging, *J. Mater. Chem.* 21 (2011) 13163.
- [20] S. Zhu, J. Zhang, C. Qiao, S. Tang, Y. Li, W. Yuan, B. Li, L. Tian, F. Liu, H. Gao, H. Wei, H. Zhang, H. Sun, B. Yang, Strongly green-photoluminescent graphene quantum dots for bioimaging applications, *Chem. Commun.* 47 (2011) 6858.
- [21] W. Shang, X. Zhang, M. Zhang, Z. Fang, Y. Sun, M. Han, L. Fan, The uptake mechanism and biocompatibility of graphene quantum dots with human neural stem cells, *Nanoscale* 6 (2014) 5799.
- [22] S. Nandi, R. Malishev, K.P. Kootery, Y. Mirsky, S. Kolusheva, R. Jelinek, Membrane analysis with amphiphilic carbon dots, *Chem. Commun.* 50 (2014) 10299.
- [23] S. Fasbender, S. Allani, C. Wimmenauer, R.-P. Cadetdu, K. Raba, J.C. Fischer, B. Bulat, M. Luysberg, C.A.M. Seidel, T. Heinzel, R. Haas, Uptake dynamics of graphene quantum dots into primary human blood cells following in vitro exposure, *RSC Adv.* 7 (2017) 12208.
- [24] S.N. Baker, G.A. Baker, Luminescent carbon nanodots: Emergent nanolights, *Angew. Chem. Int. Ed.* 49 (2010) 6726.
- [25] J.K. Jaiswal, H. Mattoussi, J.M. Mauro, S.M. Simon, Long-term multiple color imaging of live cells using quantum dot bioconjugates, *Nat. Biotechnol.* 21 (2002) 47–51.
- [26] X. Michalet, F.F. Pinaud, L.A. Bentolila, J.M. Tsay, S. Doose, J.J. Li, G. Sundaresan, A.M. Wu, S.S. Gambhir, S. Weiss, Quantum dots for live cells, in vivo imaging, and diagnostics, *Science* 307 (2005) 538.
- [27] S.J. Zhu, Y.B. Song, X.H. Zhao, J.R. Shao, J.H. Zhang, B. Yang, The photoluminescence mechanism in carbon dots (graphene quantum dots, carbon nanodots, and polymer dots): current state and future perspective, *Nano Res.* 8 (2015) 355.
- [28] D. Qu, M. Zheng, J. Li, Z. Xie, Z. Sun, Tailoring color emissions from n-doped graphene quantum dots for bioimaging applications, *Light Sci. Appl.* 4 (2015) e364.
- [29] F. Yuan, T. Yuan, L. Sui, Z. Wang, Z. Xi, Y. Li, X. Li, L. Fan, Z. Tan, A. Chen, M. Jin, S. Yang, Engineering triangular carbon quantum dots with unprecedented narrow bandwidth emission for multicolored LEDs, *Nature Commun.* 9 (1) (2018) 2249.
- [30] T.F. Yeh, C.Y. Teng, S.J. Chen, H.S. Teng, Nitrogen-doped graphene oxide quantum dots as photocatalysts for overall watersplitting under visible light illumination, *Adv. Mater.* 26 (2014) 3297.
- [31] D.Y. Pan, J.C. Zhang, Z. Li, M.H. Wu, Hydrothermal route for cutting graphene sheets into blue-luminescent graphene quantum dots, *Adv. Mater.* 22 (2010) 734.
- [32] J. Wang, X.K. Xin, Z.Q. Lin, Cu(2)znsns(4) nanocrystals and graphene quantum dots for photovoltaics, *Nanoscale* 3 (2011) 3040.

- [33] C.D. Simpson, J.S. Wu, M.D. Watson, K. Mullen, From graphite molecules to columnar superstructures—an exercise in nanoscience, *J. Mat. Chem.* 14 (2004) 494.
- [34] S. Schnez, K. Ensslin, M. Sigrist, T. Ihn, Analytic model of the energy spectrum of a graphene quantum dot in a perpendicular magnetic field, *Phys. Rev. B* 78 (2008) 195427.
- [35] S. Tamandani, G. Darvish, R. Faez, Analytical calculation of energy levels of mono-and bilayer graphene quantum dots used as light absorber in solar cells, *Appl. Phys. A* 122 (2016) 37.
- [36] M. Zarenia, A. Chaves, G.F.F. Peeters, Energy levels of triangular and hexagonal graphene quantum dots: a comparative study between the tight-binding and dirac equation approach, *Phys. Rev. B* 84 (2011) 245403.
- [37] T. Espinosa-Ortega, I.A. Lukyanchuk, Y.G. Rubo, Density of states in randomly shaped graphene quantum dots, *Superlattices Microstruct.* 49 (2011) 283.
- [38] K.A. Ritter, J.W. Lyding, The influence of edge structure on the electronic properties of graphene quantum dots and nanoribbons, *Nat. Mater.* 8 (2009) 235.
- [39] M. Wimmer, A.R. Akhmerov, F. Guinea, Robustness of edge states in graphene quantum dots, *Phys. Rev. B* 82 (2010) 045409.
- [40] D. daCosta, M. Zarenia, A. Chaves, G. Farias, F. Peeters, Energy levels of bilayer graphene quantum dots, *Phys. Rev. B* 92 (2015) 115437.
- [41] D. daCosta, M. Zarenia, A. Chaves, J.M. Pereira, G. Farias, F. Peeters, Hexagonal-shaped monolayer-bilayer quantum disks in graphene: A tight-binding approach, *Phys. Rev. B* 94 (2016) 035415.
- [42] M. Mirzakhani, M. Zarenia, D. daCosta, S. Ketabi, F. Peeters, Energy levels of abc-stacked trilayer graphene quantum dots with infinite-mass boundary conditions, *Phys. Rev. B* 94 (2016) 165423.
- [43] A.D. Güçlü, P. Potasz, P. Hawrylak, Electric-field controlled spin in bilayer triangular graphene quantum dots, *Phys. Rev. B* 84 (2011) 035425.
- [44] M.A. Sk, A. Ananthanarayanan, L. Huang, K.H. Lim, P. Chen, Revealing the tunable photoluminescence properties of graphene quantum dots, *J. Mat. Chem. C* 2 (2014) 6954.
- [45] I. Ozfidan, M. Korkusinski, A.D. Güçlü, J.A. McGuire, P. Hawrylak, Microscopic theory of the optical properties of colloidal graphene quantum dots, *Phys. Rev. B* 89 (2014) 085310.
- [46] I. Ozfidan, M. Korkusinski, P. Hawrylak, Theory of biexcitons and biexciton-exciton cascade in graphene quantum dots, *Phys. Rev. B* 91 (2015) 115314.
- [47] M.S. Dresselhaus, G. Dresselhaus, Intercalation compounds of graphite, *Adv. Phys.* 51 (2002) 1.
- [48] C.W. Groth, M. Wimmer, A.R. Akhmerov, X. Waintal, Kwant: a software package for quantum transport, *New J. Phys.* 16 (2014) 063065.
- [49] A.D. Güçlü, P. Potasz, P. Hawrylak, Excitonic absorption in gate-controlled graphene quantum dots, *Phys. Rev. B* 82 (2010) 155445.
- [50] M. Fujita, K. Wakabayashi, K. Nakada, K. Kusakabe, Peculiar localized state at zigzag graphite edge, *J. Phys. Soc. Japan* 65 (1996) 1920.
- [51] P. Potasz, A.D. Güçlü, P. Hawrylak, Zero-energy states in triangular and trapezoidal graphene structures, *Phys. Rev. B* 81 (2010) 033403.
- [52] D. Subramaniam, F. Libisch, Y. Li, C. Pauly, V. Geringer, R. Reiter, T. Mashoff, M. Liebmann, J. Burgdörfer, C. Busse, T. Michely, R. Mazzarello, M. Pratzer, M. Morgenstern, Wave-function mapping of graphene quantum dots with soft confinement, *Phys. Rev. Lett.* 108 (2012) 046801.
- [53] F. Craes, S. Runte, J. Klinkhammer, M. Kralj, T. Michely, C. Busse, Mapping image potential states on graphene quantum dots, *Phys. Rev. Lett.* 111 (2013) 056804.
- [54] M. Kastler, J. Schmidt, W. Pisula, D. Sebastiani, K. Müllen, From armchair to zigzag peripheries in nanographenes, *J. Am. Chem. Soc.* 128 (2006) 9526–9534.
- [55] S. Chen, J. Liu, M. Chen, X. Chen, J. Wang, Unusual emission transformation of graphene quantum dots induced by self-assembled aggregation, *Chem. Commun.* 48 (2012) 7637–7639.

Single-particle energy spectra of multilayer graphene quantum dots

C. Wimmenauer, J. Scheller, S. Fasbender, T. Heinzel

Solid State Physics Laboratory, Heinrich-Heine-Universität, Universitätsstr.1, 40225 Düsseldorf, Germany

1. Supplement

Table S1: Equations that express the relations between the number of sites per disk N , the number of sites at one edge N_S and the length of an edge L , for triangular, hexagonal and rhombic graphene quantum dots. The constant $a = 0.142\text{ nm}$ denotes the bond length in graphene.

		hexagonal	triangular	rhombic
$N(N_S)$	zigzag	$N = 6N_S^2$	$N = N_S^2 + 4N_S + 1$	$N = 2N_S^2 + 4N_S$
	armchair	$N = \frac{9}{2}N_S^2 - 9N_S + 6$	$N = \frac{3}{4}N_S^2 + \frac{3}{2}N_S$	$N = \frac{3}{2}N_S^2$
$L(N_S)$	zigzag	$L = \sqrt{3}(N_S - \frac{1}{3})a$ [1]	$L = \sqrt{3}(N_S + 1)a$ [1]	$L = \sqrt{3}(N_S + \frac{1}{3})a$
	armchair	$L = (3N_S - 4)\frac{a}{2}$ [1]	$L = \frac{3}{2}N_S a$ [1]	$L = (3N_S - 2)\frac{a}{2}$
$L(N)$	zigzag	$L = (\sqrt{\frac{N}{2}} - \frac{1}{\sqrt{3}})a$	$L = \sqrt{3}(\sqrt{3 + N} - 1)a$	$L = \sqrt{3}(\sqrt{\frac{2+N}{2}} - \frac{2}{3})a$
	armchair	$L = (\sqrt{2N - 3} - 1)\frac{a}{2}$	$L = \frac{3}{2}(\sqrt{\frac{3+4N}{3}} - 1)a$	$L = (\sqrt{\frac{3}{2}N} - 1)a$

Email address: thomas.heinzel@hhu.de (T. Heinzel)

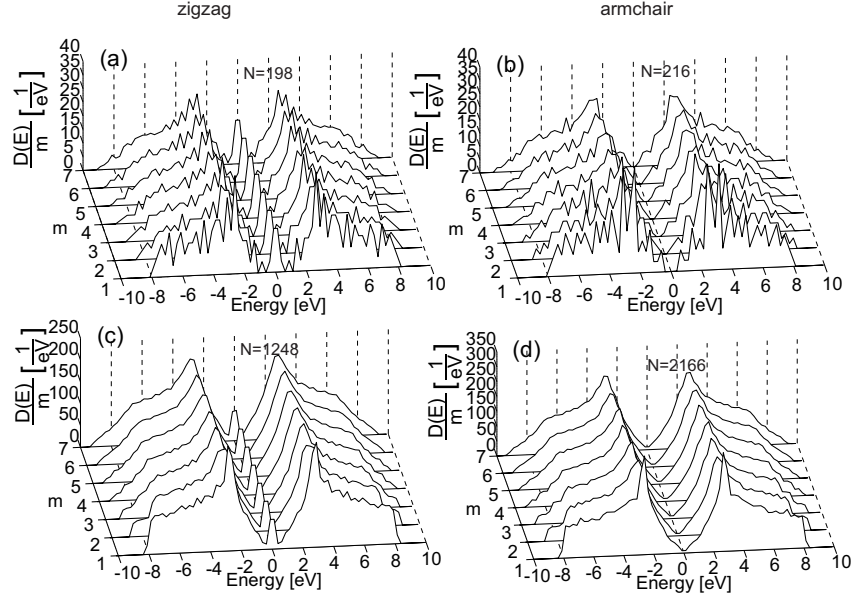


Figure S2: (color online) Waterfall plots of typical computed densities of states $D(E)$ of rhombic GQDs, normalized to the number m of disk layers, and their evolution as a function of m , for a small ($N = 198$) and large ($N = 1248$) disks with zigzag edges (a), and for armchair dots with $N = 216$ and $N = 2166$, respectively (b).

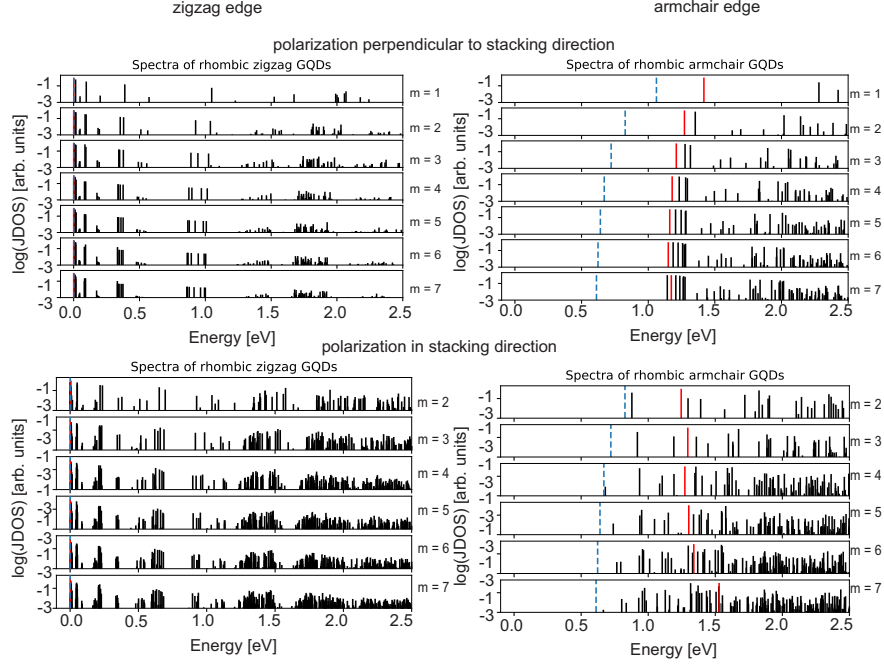


Figure S3: (color online) Absorption spectra of rhombic graphene quantum dots (GQDs). The optical joint density of states (JDOS) is plotted against the photon energy for $N = 198$ zigzag (left) and $N = 222$ armchair (right) GQDs. The polarization of the excitation in the plane of the disks and perpendicular to it are shown in the upper and lower row, respectively. The value of the energy gap is tagged with a dashed blue line for comparison. The transition with the highest probability is marked in red.

References

- [1] M. Zarenia, A. Chaves, G. F. F. Peeters, Energy levels of triangular and hexagonal graphene quantum dots: a comparative study between the tight-binding and dirac equation approach, Phys. Rev. B 84 (2011) 245403.

Chapter 6

Conclusion and outlook

The CNDs prepared by solvent-free microwave-assisted pyrolysis of citric acid and DETA have been characterized regarding their uptake and subcellular distribution. As presented in chapter 3, a data processing pipeline using spatial statistics was developed and successfully validated with a positive and negative control. This procedure was applied to super-resolution microscopy images of the CNDs, with RFP-tagged lysosomes that were acquired via Airy scanning microscopy. It was shown that the CNDs are predominately located in the lysosomes after 48 h of incubation. The method introduced here addresses many common problems in quantitative colocalization analysis. It provides an object-based approach that does not rely on the particles to overlap and is, additionally, testable for statistical significance. Moreover, the presented workflow is not limited to Airy scanning microscopy data. It may be applied to colocalization problems with data from other super-resolution microscopy techniques based on confocal scanning microscopy, such as stimulated emission depletion (STED) imaging.

A differential uptake between healthy primary hematopoietic cells and human AML cells was found, as reported in chapter 4.1. While all cells showed significant uptake of the nanoparticles, the $CD33^+$ and $CD34^+$ subsets of the malignant cells showed a reduced uptake. It was therefore demonstrated that CNDs may, in principle, selectively address specific cell subsets. Furthermore, the effect of glycofunctionalization of these nanoparticles on the cellular uptake rate has been studied, as presented in section 4.2. While no differential uptake into different cell types depending on their receptor expression according to literature was observed, there was a difference in uptake regarding the different molecules tested. Namely, CNDs that were functionalized with mannose- and galactose-decorated oligomers were taken up in similar quantities compared to non-functionalized CNDs. CNDs functionalized with mannose and galactose monomers, on the other hand, showed a two- to threefold increase in uptake compared to the other conjugates. Increased adsorption to the surface of the cell was given as a preliminary explanation for the increased uptake of the monomer-functionalized CNDs, which may be explained by electrostatic interaction or selective binding to sites present on all investigated cell lines.

Finally, as reported in chapter 5, the effect of stacking of GQDs to multilayer nanoparticles on their optical properties, as it may be observed at high concentrations [278],

has been studied in tight-binding simulations. When the number of layers in a multi-layer GQD is increased, the absorption edge shifts to lower energies corresponding to a red shift of the energy spectrum. The edge type and geometry have been identified as major influences on the relationship between the size of the nanoparticle and its energy, which was already known for the lateral extension but was clarified for the height of the particle as well in this work.

To conclude, the initial question regarding the uptake and subcellular distribution was successfully addressed by the work related to this thesis. The information gained from the projects may be valuable for specific applications of the CNDs used here. The fact that most CNDs are localized in the lysosomes may be used to employ CNDs in sensing applications in the endolysosomal pathway or selectively address this compartment in therapeutic applications. Furthermore, it is now clear that escape from the endolysosomal pathway must be facilitated when the employed CNDs are to be used in a drug delivery system with a different target location, such as the nucleus. While first efforts in this direction have been made to utilize the proton sponge effect for endosomal escape with PEI-conjugated CNDs [274], there is still some work to do for an effective release from this compartment. Further work may go into modifying the CNDs to intensify the trend of differential uptake seen in *Paper II* or to test different ligands similar to *Paper III* to finally facilitate a differential uptake that may be exploitable for therapeutic applications. Further engaging questions address the phototoxicity of our particles. While some CNDs have indeed been shown to be phototoxic, which limits their use in some applications like live cell imaging but enables the use as a photosensitizer in photodynamic therapy [37, 38, 223], the status of the particles employed here is in this regard still unclear. Furthermore, it remains an open question if our particles may be effectively excited with two-photon excitation, which would increase the number of possibilities to apply the CNDs prepared in our group.

Bibliography

- [1] R. P. Feynman, “There’s plenty of room at the bottom: An invitation to enter a new field of physics,” *Miniaturization, Reinhold*, 1961.
 - [2] Y. C. Barenholz, “Doxil®—the first fda-approved nano-drug: Lessons learned,” *Journal of controlled release*, vol. 160, no. 2, pp. 117–134, 2012.
 - [3] X. Huang, N. Kong, X. Zhang, Y. Cao, R. Langer, and W. Tao, “The landscape of mrna nanomedicine,” *Nature Medicine*, pp. 1–15, 2022.
 - [4] J. K. Jaiswal, H. Mattoussi, J. M. Mauro, and S. M. Simon, “Long-term multiple color imaging of live cells using quantum dot bioconjugates,” *Nature biotechnology*, vol. 21, no. 1, pp. 47–51, 2003.
 - [5] I. L. Medintz, H. T. Uyeda, E. R. Goldman, and H. Mattoussi, “Quantum dot bioconjugates for imaging, labelling and sensing,” *Nature materials*, vol. 4, no. 6, pp. 435–446, 2005.
 - [6] P. K. Chattopadhyay, D. A. Price, T. F. Harper, M. R. Betts, J. Yu, E. Gostick, S. P. Perfetto, P. Goepfert, R. A. Koup, S. C. De Rosa, *et al.*, “Quantum dot semiconductor nanocrystals for immunophenotyping by polychromatic flow cytometry,” *Nature medicine*, vol. 12, no. 8, pp. 972–977, 2006.
 - [7] F. Pinaud, S. Clarke, A. Sittner, and M. Dahan, “Probing cellular events, one quantum dot at a time,” *Nature methods*, vol. 7, no. 4, pp. 275–285, 2010.
 - [8] D. Jin, P. Xi, B. Wang, L. Zhang, J. Enderlein, and A. M. van Oijen, “Nanoparticles for super-resolution microscopy and single-molecule tracking,” *Nature methods*, vol. 15, no. 6, pp. 415–423, 2018.
 - [9] J. Liu, J. Wen, Z. Zhang, H. Liu, and Y. Sun, “Voyage inside the cell: Microsystems and nanoengineering for intracellular measurement and manipulation,” *Microsystems & Nanoengineering*, vol. 1, no. 1, pp. 1–15, 2015.
 - [10] B. Neuhaus, B. Tosun, O. Rotan, A. Frede, A. M. Westendorf, and M. Epple, “Nanoparticles as transfection agents: a comprehensive study with ten different cell lines,” *Rsc Advances*, vol. 6, no. 22, pp. 18102–18112, 2016.
 - [11] Z. Glass, Y. Li, and Q. Xu, “Nanoparticles for crispr-cas9 delivery,” *Nature biomedical engineering*, vol. 1, no. 11, pp. 854–855, 2017.
 - [12] W. Li, G. S. Kaminski Schierle, B. Lei, Y. Liu, and C. F. Kaminski, “Fluorescent nanoparticles for super-resolution imaging,” *Chemical Reviews*, vol. 122, no. 15, pp. 12495–12543, 2022.
-

-
- [13] I. P. Novoselova, A. Neusch, J.-S. Brand, M. Otten, M. R. Safari, N. Bartels, M. Karg, M. Farle, U. Wiedwald, and C. Monzel, "Magnetic nanoprobe for spatio-mechanical manipulation in single cells," *Nanomaterials*, vol. 11, no. 9, p. 2267, 2021.
- [14] X. Xu, R. Ray, Y. Gu, H. J. Ploehn, L. Gearheart, K. Raker, and W. A. Scrivens, "Electrophoretic analysis and purification of fluorescent single-walled carbon nanotube fragments," *Journal of the American Chemical Society*, vol. 126, no. 40, pp. 12736–12737, 2004.
- [15] L.-s. Li and X. Yan, "Colloidal graphene quantum dots," *The Journal of Physical Chemistry Letters*, vol. 1, no. 17, pp. 2572–2576, 2010.
- [16] C. Hu, M. Li, J. Qiu, and Y.-P. Sun, "Design and fabrication of carbon dots for energy conversion and storage," *Chemical Society Reviews*, vol. 48, no. 8, pp. 2315–2337, 2019.
- [17] Z. Li, Y. Zhang, Q. Niu, M. Mou, Y. Wu, X. Liu, Z. Yan, and S. Liao, "A fluorescence probe based on the nitrogen-doped carbon dots prepared from orange juice for detecting Hg^{2+} in water," *Journal of Luminescence*, vol. 187, pp. 274–280, 2017.
- [18] Y. Xie, D. Cheng, X. Liu, and A. Han, "Green hydrothermal synthesis of n-doped carbon dots from biomass highland barley for the detection of Hg^{2+} ," *Sensors*, vol. 19, no. 14, p. 3169, 2019.
- [19] A. Bhati, S. R. Anand, Gunture, A. K. Garg, P. Khare, and S. K. Sonkar, "Sunlight-induced photocatalytic degradation of pollutant dye by highly fluorescent red-emitting mg-n-embedded carbon dots," *ACS Sustainable Chemistry & Engineering*, vol. 6, no. 7, pp. 9246–9256, 2018.
- [20] A. Bhati, S. R. Anand, D. Saini, and S. K. Sonkar, "Sunlight-induced photoreduction of cr (vi) to cr (iii) in wastewater by nitrogen-phosphorus-doped carbon dots," *npj Clean Water*, vol. 2, no. 1, p. 12, 2019.
- [21] X. Miao, D. Qu, D. Yang, B. Nie, Y. Zhao, H. Fan, and Z. Sun, "Synthesis of carbon dots with multiple color emission by controlled graphitization and surface functionalization," *Advanced materials*, vol. 30, no. 1, p. 1704740, 2018.
- [22] F. Lin, C. Jia, and F.-G. Wu, "Carbon dots for intracellular sensing," *Small Structures*, vol. 3, no. 9, p. 2200033, 2022.
- [23] T. S. Atabaev, "Doped carbon dots for sensing and bioimaging applications: a minireview," *Nanomaterials*, vol. 8, no. 5, p. 342, 2018.
- [24] J.-R. Macairan, D. B. Jaunky, A. Piekny, and R. Naccache, "Intracellular ratio-metric temperature sensing using fluorescent carbon dots," *Nanoscale Advances*, vol. 1, no. 1, pp. 105–113, 2019.
- [25] S. Kalytchuk, K. Poláková, Y. Wang, J. P. Froning, K. Cepe, A. L. Rogach, and R. Zbořil, "Carbon dot nanothermometry: intracellular photoluminescence lifetime thermal sensing," *ACS nano*, vol. 11, no. 2, pp. 1432–1442, 2017.
- [26] Z. L. Wu, M. X. Gao, T. T. Wang, X. Y. Wan, L. L. Zheng, and C. Z. Huang, "A general quantitative ph sensor developed with dicyandiamide n-doped high
-

- quantum yield graphene quantum dots,” *Nanoscale*, vol. 6, no. 7, pp. 3868–3874, 2014.
- [27] E. Shuang, Q.-X. Mao, X.-L. Yuan, X.-L. Kong, X.-W. Chen, and J.-H. Wang, “Targeted imaging of the lysosome and endoplasmic reticulum and their ph monitoring with surface regulated carbon dots,” *Nanoscale*, vol. 10, no. 26, pp. 12788–12796, 2018.
- [28] Q. Q. Zhang, T. Yang, R. S. Li, H. Y. Zou, Y. F. Li, J. Guo, X. D. Liu, and C. Z. Huang, “A functional preservation strategy for the production of highly photoluminescent emerald carbon dots for lysosome targeting and lysosomal ph imaging,” *Nanoscale*, vol. 10, no. 30, pp. 14705–14711, 2018.
- [29] Q. Liu, X. Niu, Y. Zhang, Y. Zhao, K. Xie, B. Yang, Q. He, S. Lv, and L. Li, “Carbon dots for lysosome targeting and imaging of lysosomal ph and cys/hcy in living cells,” *Nanoscale*, vol. 12, no. 24, pp. 13010–13016, 2020.
- [30] A. Salinas-Castillo, M. Ariza-Avidad, C. Pritz, M. Camprubí-Robles, B. Fernández, M. J. Ruedas-Rama, A. Megia-Fernández, A. Lapresta-Fernández, F. Santoyo-Gonzalez, A. Schrott-Fischer, *et al.*, “Carbon dots for copper detection with down and upconversion fluorescent properties as excitation sources,” *Chemical Communications*, vol. 49, no. 11, pp. 1103–1105, 2013.
- [31] F. Du, Y. Min, F. Zeng, C. Yu, and S. Wu, “A targeted and fret-based ratiometric fluorescent nanoprobe for imaging mitochondrial hydrogen peroxide in living cells,” *Small*, vol. 10, no. 5, pp. 964–972, 2014.
- [32] Y. K. Jung, E. Shin, and B.-S. Kim, “Cell nucleus-targeting zwitterionic carbon dots,” *Scientific reports*, vol. 5, no. 1, pp. 1–9, 2015.
- [33] L. Yang, Z. Wang, J. Wang, W. Jiang, X. Jiang, Z. Bai, Y. He, J. Jiang, D. Wang, and L. Yang, “Doxorubicin conjugated functionalizable carbon dots for nucleus targeted delivery and enhanced therapeutic efficacy,” *Nanoscale*, vol. 8, no. 12, pp. 6801–6809, 2016.
- [34] Y. Liu, C. Zhao, A. Sabirsh, L. Ye, X. Wu, H. Lu, and J. Liu, “A novel graphene quantum dot-based mrna delivery platform,” *ChemistryOpen*, vol. 10, no. 7, pp. 666–671, 2021.
- [35] J. Li, L. Zhang, J. Chen, R. Zhang, Z. Liu, J. Zhao, B. Liu, M.-y. Han, G. Han, and Z. Zhang, “One-step synthesized amphiphilic carbon dots for the super-resolution imaging of endoplasmic reticulum in live cells,” *RSC advances*, vol. 12, no. 30, pp. 19424–19430, 2022.
- [36] X. Sun and N. Mosleh, “Fluorescent carbon dots for super-resolution microscopy,” *Materials*, vol. 16, no. 3, p. 890, 2023.
- [37] S. Mandal, S. R. Prasad, D. Mandal, and P. Das, “Bovine serum albumin amplified reactive oxygen species generation from anthracycline-derived carbon dot and concomitant nanoassembly for combination antibiotic–photodynamic therapy application,” *ACS applied materials & interfaces*, vol. 11, no. 36, pp. 33273–33284, 2019.
- [38] J. Yue, L. Li, C. Jiang, Q. Mei, W.-F. Dong, and R. Yan, “Riboflavin-based car-
-

- bon dots with high singlet oxygen generation for photodynamic therapy,” *Journal of Materials Chemistry B*, vol. 9, no. 38, pp. 7972–7978, 2021.
- [39] P. R. Wallace, “The band theory of graphite,” *Physical review*, vol. 71, no. 9, p. 622, 1947.
- [40] K. S. Novoselov, A. K. Geim, S. V. Morozov, D. Jiang, Y. Zhang, S. V. Dubonos, I. V. Grigorieva, and A. A. Firsov, “Electric field effect in atomically thin carbon films,” *science*, vol. 306, no. 5696, pp. 666–669, 2004.
- [41] K. S. Novoselov, A. K. Geim, S. V. Morozov, D. Jiang, M. I. Katsnelson, I. Grigorieva, S. Dubonos, and A. Firsov, “Two-dimensional gas of massless dirac fermions in graphene,” *nature*, vol. 438, no. 7065, pp. 197–200, 2005.
- [42] G. W. Semenoff, “Condensed-matter simulation of a three-dimensional anomaly,” *Physical Review Letters*, vol. 53, no. 26, p. 2449, 1984.
- [43] D. DiVincenzo and E. Mele, “Self-consistent effective-mass theory for intralayer screening in graphite intercalation compounds,” *Physical Review B*, vol. 29, no. 4, p. 1685, 1984.
- [44] Y. Zhang, Y.-W. Tan, H. L. Stormer, and P. Kim, “Experimental observation of the quantum hall effect and berry’s phase in graphene,” *nature*, vol. 438, no. 7065, pp. 201–204, 2005.
- [45] M. Katsnelson, K. Novoselov, and A. Geim, “Chiral tunnelling and the klein paradox in graphene,” *Nature physics*, vol. 2, no. 9, pp. 620–625, 2006.
- [46] N. Stander, B. Huard, and D. Goldhaber-Gordon, “Evidence for klein tunneling in graphene p- n junctions,” *Physical review letters*, vol. 102, no. 2, p. 026807, 2009.
- [47] A. C. Neto, F. Guinea, N. M. Peres, K. S. Novoselov, and A. K. Geim, “The electronic properties of graphene,” *Reviews of modern physics*, vol. 81, no. 1, p. 109, 2009.
- [48] A. J. Leggett, “Lecture 5: Graphene: Electronic band structure and dirac fermions,” *Physics 769. Selected topics in condensed matter physics*, 2010.
- [49] K. Wakabayashi, K.-i. Sasaki, T. Nakanishi, and T. Enoki, “Electronic states of graphene nanoribbons and analytical solutions,” *Science and technology of advanced materials*, vol. 11, no. 5, p. 054504, 2010.
- [50] M. Fujita, K. Wakabayashi, K. Nakada, and K. Kusakabe, “Peculiar localized state at zigzag graphite edge,” *Journal of the Physical Society of Japan*, vol. 65, no. 7, pp. 1920–1923, 1996.
- [51] C. W. Groth, M. Wimmer, A. R. Akhmerov, and X. Waintal, “Kwant: a software package for quantum transport,” *New Journal of Physics*, vol. 16, no. 6, p. 063065, 2014.
- [52] S. Schnez, K. Ensslin, M. Sigrist, and T. Ihn, “Analytic model of the energy spectrum of a graphene quantum dot in a perpendicular magnetic field,” *Physical Review B*, vol. 78, no. 19, p. 195427, 2008.
- [53] P. Recher, J. Nilsson, G. Burkard, and B. Trauzettel, “Bound states and magnetic
-

- field induced valley splitting in gate-tunable graphene quantum dots,” *Physical Review B*, vol. 79, no. 8, p. 085407, 2009.
- [54] N. M. Freitag, L. A. Chizhova, P. Nemes-Incze, C. R. Woods, R. V. Gorbachev, Y. Cao, A. K. Geim, K. S. Novoselov, J. Burgdörfer, F. Libisch, *et al.*, “Electrostatically confined monolayer graphene quantum dots with orbital and valley splittings,” *Nano letters*, vol. 16, no. 9, pp. 5798–5805, 2016.
- [55] M. Zarenia, A. Chaves, G. Farias, and F. Peeters, “Energy levels of triangular and hexagonal graphene quantum dots: a comparative study between the tight-binding and dirac equation approach,” *Physical Review B*, vol. 84, no. 24, p. 245403, 2011.
- [56] P. Potasz, A. Güçlü, and P. Hawrylak, “Zero-energy states in triangular and trapezoidal graphene structures,” *Physical Review B*, vol. 81, no. 3, p. 033403, 2010.
- [57] A. Güçlü, P. Potasz, and P. Hawrylak, “Excitonic absorption in gate-controlled graphene quantum dots,” *Physical Review B*, vol. 82, no. 15, p. 155445, 2010.
- [58] T. Latychevskaia, S.-K. Son, Y. Yang, D. Chancellor, M. Brown, S. Ozdemir, I. Madan, G. Berruto, F. Carbone, A. Mishchenko, *et al.*, “Stacking transition in rhombohedral graphite,” *Frontiers of Physics*, vol. 14, pp. 1–7, 2019.
- [59] M. S. Dresselhaus and G. Dresselhaus, “Intercalation compounds of graphite,” *Advances in physics*, vol. 51, no. 1, pp. 1–186, 2002.
- [60] F. Yuan, T. Yuan, L. Sui, Z. Wang, Z. Xi, Y. Li, X. Li, L. Fan, Z. Tan, A. Chen, *et al.*, “Engineering triangular carbon quantum dots with unprecedented narrow bandwidth emission for multicolored leds,” *Nature communications*, vol. 9, no. 1, pp. 1–11, 2018.
- [61] K. A. Ritter and J. W. Lyding, “The influence of edge structure on the electronic properties of graphene quantum dots and nanoribbons,” *Nature materials*, vol. 8, no. 3, pp. 235–242, 2009.
- [62] D. Subramaniam, F. Libisch, Y. Li, C. Pauly, V. Geringer, R. Reiter, T. Mashoff, M. Liebmann, J. Burgdörfer, C. Busse, *et al.*, “Wave-function mapping of graphene quantum dots with soft confinement,” *Physical review letters*, vol. 108, no. 4, p. 046801, 2012.
- [63] F. Craes, S. Runte, J. Klinkhammer, M. Kralj, T. Michely, and C. Busse, “Mapping image potential states on graphene quantum dots,” *Physical review letters*, vol. 111, no. 5, p. 056804, 2013.
- [64] S. Zhao, J. Lavie, L. Rondin, L. Orcin-Chaix, C. Diederichs, P. Roussignol, Y. Chassagneux, C. Voisin, K. Müllen, A. Narita, *et al.*, “Single photon emission from graphene quantum dots at room temperature,” *Nature communications*, vol. 9, no. 1, pp. 1–5, 2018.
- [65] S. Zhu, Y. Song, X. Zhao, J. Shao, J. Zhang, and B. Yang, “The photoluminescence mechanism in carbon dots (graphene quantum dots, carbon nanodots, and polymer dots): current state and future perspective,” *Nano research*, vol. 8, no. 2, pp. 355–381, 2015.
-

-
- [66] A. Sciortino, A. Cannizzo, and F. Messina, “Carbon nanodots: a review—from the current understanding of the fundamental photophysics to the full control of the optical response,” *C*, vol. 4, no. 4, p. 67, 2018.
- [67] C. Reckmeier, J. Schneider, A. Susha, and A. Rogach, “Luminescent colloidal carbon dots: optical properties and effects of doping,” *Optics Express*, vol. 24, no. 2, pp. A312–A340, 2016.
- [68] D. Reyes, M. Camacho, M. Camacho, M. Mayorga, D. Weathers, G. Salamo, Z. Wang, and A. Neogi, “Laser ablated carbon nanodots for light emission,” *Nanoscale research letters*, vol. 11, no. 1, pp. 1–11, 2016.
- [69] H. Gonçalves, P. A. Jorge, J. Fernandes, and J. C. E. da Silva, “Hg (ii) sensing based on functionalized carbon dots obtained by direct laser ablation,” *Sensors and Actuators B: Chemical*, vol. 145, no. 2, pp. 702–707, 2010.
- [70] Q.-L. Zhao, Z.-L. Zhang, B.-H. Huang, J. Peng, M. Zhang, and D.-W. Pang, “Facile preparation of low cytotoxicity fluorescent carbon nanocrystals by electrooxidation of graphite,” *Chemical Communications*, no. 41, pp. 5116–5118, 2008.
- [71] Y. Xu, J. Liu, J. Zhang, X. Zong, X. Jia, D. Li, and E. Wang, “Chip-based generation of carbon nanodots via electrochemical oxidation of screen printed carbon electrodes and the applications for efficient cell imaging and electrochemiluminescence enhancement,” *Nanoscale*, vol. 7, no. 21, pp. 9421–9426, 2015.
- [72] S. Kumar, S. T. Aziz, O. Girshevitz, and G. D. Nessim, “One-step synthesis of n-doped graphene quantum dots from chitosan as a sole precursor using chemical vapor deposition,” *The Journal of Physical Chemistry C*, vol. 122, no. 4, pp. 2343–2349, 2018.
- [73] J. M. Ha, N. E. Lee, Y. J. Yoon, S. H. Lee, Y. S. Hwang, J. K. Suk, C. Y. Lee, C. R. Kim, and S. Yeo, “Universal dry synthesis and patterning of high-quality and-purity graphene quantum dots by ion-beam assisted chemical vapor deposition,” *Carbon*, vol. 186, pp. 28–35, 2022.
- [74] D. Qu, M. Zheng, J. Li, Z. Xie, and Z. Sun, “Tailoring color emissions from n-doped graphene quantum dots for bioimaging applications,” *Light: Science & Applications*, vol. 4, no. 12, pp. e364–e364, 2015.
- [75] A. Pankaj, K. Tewari, S. Singh, and S. P. Singh, “Waste candle soot derived nitrogen doped carbon dots based fluorescent sensor probe: An efficient and inexpensive route to determine Hg (ii) and Fe (iii) from water,” *Journal of environmental chemical engineering*, vol. 6, no. 4, pp. 5561–5569, 2018.
- [76] W. L. Ang, C. A. Boon Mee, N. S. Sambudi, A. W. Mohammad, C. P. Leo, E. Mahmoudi, M. Ba-Abbad, and A. Benamor, “Microwave-assisted conversion of palm kernel shell biomass waste to photoluminescent carbon dots,” *Scientific reports*, vol. 10, no. 1, pp. 1–15, 2020.
- [77] J. B. Essner, C. H. Laber, S. Ravula, L. Polo-Parada, and G. A. Baker, “Pee-dots: biocompatible fluorescent carbon dots derived from the upcycling of urine,” *Green Chemistry*, vol. 18, no. 1, pp. 243–250, 2016.
-

-
- [78] M. Tan, L. Zhang, R. Tang, X. Song, Y. Li, H. Wu, Y. Wang, G. Lv, W. Liu, and X. Ma, "Enhanced photoluminescence and characterization of multicolor carbon dots using plant soot as a carbon source," *Talanta*, vol. 115, pp. 950–956, 2013.
- [79] M. Zulfajri, H. N. Abdelhamid, S. Sudewi, S. Dayalan, A. Rasool, A. Habib, and G. G. Huang, "Plant part-derived carbon dots for biosensing," *Biosensors*, vol. 10, no. 6, p. 68, 2020.
- [80] L. Wang and H. S. Zhou, "Green synthesis of luminescent nitrogen-doped carbon dots from milk and its imaging application," *Analytical chemistry*, vol. 86, no. 18, pp. 8902–8905, 2014.
- [81] Z.-C. Yang, M. Wang, A. M. Yong, S. Y. Wong, X.-H. Zhang, H. Tan, A. Y. Chang, X. Li, and J. Wang, "Intrinsically fluorescent carbon dots with tunable emission derived from hydrothermal treatment of glucose in the presence of monopotassium phosphate," *Chemical communications*, vol. 47, no. 42, pp. 11615–11617, 2011.
- [82] Q. Xu, B. Li, Y. Ye, W. Cai, W. Li, C. Yang, Y. Chen, M. Xu, N. Li, X. Zheng, *et al.*, "Synthesis, mechanical investigation, and application of nitrogen and phosphorus co-doped carbon dots with a high photoluminescent quantum yield," *Nano Research*, vol. 11, no. 7, pp. 3691–3701, 2018.
- [83] S. A. Hill, D. Benito-Alifonso, S. A. Davis, D. J. Morgan, M. Berry, and M. C. Galan, "Practical three-minute synthesis of acid-coated fluorescent carbon dots with tuneable core structure," *Scientific reports*, vol. 8, no. 1, pp. 1–10, 2018.
- [84] M. Moniruzzaman, B. A. Lakshmi, S. Kim, and J. Kim, "Preparation of shape-specific (trilateral and quadrilateral) carbon quantum dots towards multiple color emission," *Nanoscale*, vol. 12, no. 22, pp. 11947–11959, 2020.
- [85] M. Zhang, L. Hu, H. Wang, Y. Song, Y. Liu, H. Li, M. Shao, H. Huang, and Z. Kang, "One-step hydrothermal synthesis of chiral carbon dots and their effects on mung bean plant growth," *Nanoscale*, vol. 10, no. 26, pp. 12734–12742, 2018.
- [86] Q. Liu, N. Zhang, H. Shi, W. Ji, X. Guo, W. Yuan, and Q. Hu, "One-step microwave synthesis of carbon dots for highly sensitive and selective detection of copper ions in aqueous solution," *New Journal of Chemistry*, vol. 42, no. 4, pp. 3097–3101, 2018.
- [87] X. Zhai, P. Zhang, C. Liu, T. Bai, W. Li, L. Dai, and W. Liu, "Highly luminescent carbon nanodots by microwave-assisted pyrolysis," *Chemical communications*, vol. 48, no. 64, pp. 7955–7957, 2012.
- [88] H. Li, F.-Q. Shao, S.-Y. Zou, Q.-J. Yang, H. Huang, J.-J. Feng, and A.-J. Wang, "Microwave-assisted synthesis of n, p-doped carbon dots for fluorescent cell imaging," *Microchimica Acta*, vol. 183, no. 2, pp. 821–826, 2016.
- [89] T. V. de Medeiros, J. Manioudakis, F. Noun, J.-R. Macairan, F. Victoria, and R. Naccache, "Microwave-assisted synthesis of carbon dots and their applications," *Journal of Materials Chemistry C*, vol. 7, no. 24, pp. 7175–7195, 2019.
- [90] D. Michael P áMingos *et al.*, "Tilden lecture. applications of microwave dielectric heating effects to synthetic problems in chemistry," *Chemical society reviews*,
-

- vol. 20, no. 1, pp. 1–47, 1991.
- [91] R. Gedye, F. Smith, K. Westaway, H. Ali, L. Baldisera, L. Laberge, and J. Rousell, “The use of microwave ovens for rapid organic synthesis,” *Tetrahedron letters*, vol. 27, no. 3, pp. 279–282, 1986.
- [92] J.-S. Schanche, “Microwave synthesis solutions from personal chemistry,” *Molecular diversity*, vol. 7, no. 2-4, p. 293, 2003.
- [93] F. Yan, Y. Jiang, X. Sun, Z. Bai, Y. Zhang, and X. Zhou, “Surface modification and chemical functionalization of carbon dots: a review,” *Microchimica Acta*, vol. 185, no. 9, pp. 1–34, 2018.
- [94] X. Sun, Z. Liu, K. Welsher, J. T. Robinson, A. Goodwin, S. Zaric, and H. Dai, “Nano-graphene oxide for cellular imaging and drug delivery,” *Nano research*, vol. 1, no. 3, pp. 203–212, 2008.
- [95] W. Dong, S. Zhou, Y. Dong, J. Wang, X. Ge, and L. Sui, “The preparation of ethylenediamine-modified fluorescent carbon dots and their use in imaging of cells,” *Luminescence*, vol. 30, no. 6, pp. 867–871, 2015.
- [96] L. Yang, W. Jiang, L. Qiu, X. Jiang, D. Zuo, D. Wang, and L. Yang, “One pot synthesis of highly luminescent polyethylene glycol anchored carbon dots functionalized with a nuclear localization signal peptide for cell nucleus imaging,” *Nanoscale*, vol. 7, no. 14, pp. 6104–6113, 2015.
- [97] M. J. Fischer, “Amine coupling through edc/nhs: a practical approach,” in *Surface plasmon resonance*, pp. 55–73, Springer, 2010.
- [98] Y. Jiang, Z. Wang, and Z. Dai, “Preparation of silicon-carbon-based dots@dopamine and its application in intracellular ag+ detection and cell imaging,” *ACS applied materials & interfaces*, vol. 8, no. 6, pp. 3644–3650, 2016.
- [99] C. X. Guo, D. Zhao, Q. Zhao, P. Wang, and X. Lu, “Na (+)-functionalized carbon quantum dots: a new draw solute in forward osmosis for seawater desalination,” *Chem. Commun*, vol. 50, no. 55, pp. 7318–7321, 2014.
- [100] W.-R. Zhuang, Y. Wang, P.-F. Cui, L. Xing, J. Lee, D. Kim, H.-L. Jiang, and Y.-K. Oh, “Applications of π - π stacking interactions in the design of drug-delivery systems,” *Journal of controlled release*, vol. 294, pp. 311–326, 2019.
- [101] Q.-X. Mao, S. E, J.-M. Xia, R.-S. Song, Y. Shu, X.-W. Chen, and J.-H. Wang, “Hydrophobic carbon nanodots with rapid cell penetrability and tunable photoluminescence behavior for in vitro and in vivo imaging,” *Langmuir*, vol. 32, no. 46, pp. 12221–12229, 2016.
- [102] K. M. Omer, S. A. Idrees, A. Q. Hassan, and L. A. Jamil, “Amphiphilic fluorescent carbon nanodots as a selective nanoprobe for nitrite and tetracycline both in aqueous and organic solutions,” *New Journal of Chemistry*, vol. 44, no. 13, pp. 5120–5126, 2020.
- [103] P. Kumari, B. Ghosh, and S. Biswas, “Nanocarriers for cancer-targeted drug delivery,” *Journal of drug targeting*, vol. 24, no. 3, pp. 179–191, 2016.
- [104] B. Wang and S. Lu, “The light of carbon dots: From mechanism to applications,”
-

- Matter*, vol. 5, no. 1, pp. 110–149, 2022.
- [105] W. P. Kasprzyk, T. Świergosz, P. P. Romańczyk, J. Feldmann, and J. Stolarczyk, “The role of molecular fluorophores in photoluminescence of carbon dots derived from citric acid: current state of the art and future perspectives,” *Nanoscale*, 2022.
- [106] M. Fu, F. Ehrat, Y. Wang, K. Z. Milowska, C. Reckmeier, A. L. Rogach, J. K. Stolarczyk, A. S. Urban, and J. Feldmann, “Carbon dots: a unique fluorescent cocktail of polycyclic aromatic hydrocarbons,” *Nano letters*, vol. 15, no. 9, pp. 6030–6035, 2015.
- [107] X. Zhou, Y. Zhang, C. Wang, X. Wu, Y. Yang, B. Zheng, H. Wu, S. Guo, and J. Zhang, “Photo-fenton reaction of graphene oxide: a new strategy to prepare graphene quantum dots for dna cleavage,” *ACS nano*, vol. 6, no. 8, pp. 6592–6599, 2012.
- [108] M. Sudolska, M. Dubecky, S. Sarkar, C. J. Reckmeier, R. Zboril, A. L. Rogach, and M. Otyepka, “Nature of absorption bands in oxygen-functionalized graphitic carbon dots,” *The Journal of Physical Chemistry C*, vol. 119, no. 23, pp. 13369–13373, 2015.
- [109] Y. Dong, C. Chen, X. Zheng, L. Gao, Z. Cui, H. Yang, C. Guo, Y. Chi, and C. M. Li, “One-step and high yield simultaneous preparation of single-and multi-layer graphene quantum dots from cx-72 carbon black,” *Journal of Materials Chemistry*, vol. 22, no. 18, pp. 8764–8766, 2012.
- [110] S. Fasbender, L. Zimmermann, R.-P. Cadetdu, M. Luysberg, B. Moll, C. Janiak, T. Heinzl, and R. Haas, “the low toxicity of graphene quantum dots is reflected by marginal gene expression changes of primary human hematopoietic stem cells,” *Scientific reports*, vol. 9, no. 1, pp. 1–13, 2019.
- [111] C. Wimmenauer, J. Scheller, S. Fasbender, and T. Heinzl, “Single-particle energy-and optical absorption-spectra of multilayer graphene quantum dots,” *Superlattices and Microstructures*, vol. 132, p. 106171, 2019.
- [112] S. H. Jin, D. H. Kim, G. H. Jun, S. H. Hong, and S. Jeon, “Tuning the photoluminescence of graphene quantum dots through the charge transfer effect of functional groups,” *ACS nano*, vol. 7, no. 2, pp. 1239–1245, 2013.
- [113] S. Tao, S. Zhu, T. Feng, C. Zheng, and B. Yang, “Crosslink-enhanced emission effect on luminescence in polymers: advances and perspectives,” *Angewandte Chemie*, vol. 132, no. 25, pp. 9910–9924, 2020.
- [114] S. Tao, C. Zhou, C. Kang, S. Zhu, T. Feng, S.-T. Zhang, Z. Ding, C. Zheng, C. Xia, and B. Yang, “Confined-domain crosslink-enhanced emission effect in carbonized polymer dots,” *Light: Science & Applications*, vol. 11, no. 1, pp. 1–10, 2022.
- [115] S. Zhu, L. Wang, N. Zhou, X. Zhao, Y. Song, S. Maharjan, J. Zhang, L. Lu, H. Wang, and B. Yang, “The crosslink enhanced emission (cee) in non-conjugated polymer dots: from the photoluminescence mechanism to the cellular uptake mechanism and internalization,” *Chemical communications*, vol. 50, no. 89,
-

- pp. 13845–13848, 2014.
- [116] Y. Xiong, J. Schneider, E. V. Ushakova, and A. L. Rogach, “Influence of molecular fluorophores on the research field of chemically synthesized carbon dots,” *Nano Today*, vol. 23, pp. 124–139, 2018.
- [117] A. Behrmann and A. Hofmann, “Ueber die amide der citronensäure; umwandlung derselben in pyridinverbindungen,” *Berichte der deutschen chemischen Gesellschaft*, vol. 17, no. 2, pp. 2681–2699, 1884.
- [118] W. Sell and T. Easterfield, “Lxxiii.—studies on citrazinic acid. part i,” *Journal of the Chemical Society, Transactions*, vol. 63, pp. 1035–1051, 1893.
- [119] J. Schneider, C. J. Reckmeier, Y. Xiong, M. von Seckendorff, A. S. Susa, P. Kasák, and A. L. Rogach, “Molecular fluorescence in citric acid-based carbon dots,” *The Journal of Physical Chemistry C*, vol. 121, no. 3, pp. 2014–2022, 2017.
- [120] M. Otten, M. Hildebrandt, R. Kühnemuth, and M. Karg, “Pyrolysis and solvothermal synthesis for carbon dots: Role of purification and molecular fluorophores,” *Langmuir*, 2022.
- [121] M. Sun, C. Liang, Z. Tian, E. V. Ushakova, D. Li, G. Xing, S. Qu, and A. L. Rogach, “Realization of the photostable intrinsic core emission from carbon dots through surface deoxidation by ultraviolet irradiation,” *The journal of physical chemistry letters*, vol. 10, no. 11, pp. 3094–3100, 2019.
- [122] S. N. Baker and G. A. Baker, “Luminescent carbon nanodots: emergent nanolights,” *Angewandte Chemie International Edition*, vol. 49, no. 38, pp. 6726–6744, 2010.
- [123] S. Khan, A. Gupta, N. C. Verma, and C. K. Nandi, “Time-resolved emission reveals ensemble of emissive states as the origin of multicolor fluorescence in carbon dots,” *Nano letters*, vol. 15, no. 12, pp. 8300–8305, 2015.
- [124] Z. Gan, H. Xu, and Y. Hao, “Mechanism for excitation-dependent photoluminescence from graphene quantum dots and other graphene oxide derivatives: consensus, debates and challenges,” *Nanoscale*, vol. 8, no. 15, pp. 7794–7807, 2016.
- [125] S. K. Cushing, M. Li, F. Huang, and N. Wu, “Origin of strong excitation wavelength dependent fluorescence of graphene oxide,” *ACS nano*, vol. 8, no. 1, pp. 1002–1013, 2014.
- [126] M. Kaksonen and A. Roux, “Mechanisms of clathrin-mediated endocytosis,” *Nature reviews Molecular cell biology*, vol. 19, no. 5, pp. 313–326, 2018.
- [127] M. A. Edeling, C. Smith, and D. Owen, “Life of a clathrin coat: insights from clathrin and AP structures,” *Nature reviews Molecular cell biology*, vol. 7, no. 1, pp. 32–44, 2006.
- [128] M. Kaksonen, C. P. Toret, and D. G. Drubin, “Harnessing actin dynamics for clathrin-mediated endocytosis,” *Nature reviews Molecular cell biology*, vol. 7, no. 6, pp. 404–414, 2006.
- [129] B. Marks, M. H. Stowell, Y. Vallis, I. G. Mills, A. Gibson, C. R. Hopkins, and
-

- H. T. McMahon, "GTPase activity of dynamin and resulting conformation change are essential for endocytosis," *Nature*, vol. 410, no. 6825, pp. 231–235, 2001.
- [130] X. Cheng, K. Chen, B. Dong, M. Yang, S. L. Filbrun, Y. Myoung, T.-X. Huang, Y. Gu, G. Wang, and N. Fang, "Dynamin-dependent vesicle twist at the final stage of clathrin-mediated endocytosis," *Nature cell biology*, vol. 23, no. 8, pp. 859–869, 2021.
- [131] D. Manzanares and V. Ceña, "Endocytosis: the nanoparticle and submicron nanocompounds gateway into the cell," *Pharmaceutics*, vol. 12, no. 4, p. 371, 2020.
- [132] M. Simionescu, A. Gafencu, and F. Antohe, "Transcytosis of plasma macromolecules in endothelial cells: a cell biological survey," *Microscopy research and technique*, vol. 57, no. 5, pp. 269–288, 2002.
- [133] S. Mayor, R. G. Parton, and J. G. Donaldson, "Clathrin-independent pathways of endocytosis," *Cold Spring Harbor perspectives in biology*, vol. 6, no. 6, p. a016758, 2014.
- [134] J. P. Cheng and B. J. Nichols, "Caveolae: one function or many?," *Trends in cell biology*, vol. 26, no. 3, pp. 177–189, 2016.
- [135] E. Uribe-Querol and C. Rosales, "Phagocytosis: our current understanding of a universal biological process," *Frontiers in Immunology*, vol. 11, p. 1066, 2020.
- [136] R. C. May and L. M. Machesky, "Phagocytosis and the actin cytoskeleton," *Journal of cell science*, vol. 114, no. 6, pp. 1061–1077, 2001.
- [137] J. P. Lim and P. A. Gleeson, "Macropinocytosis: an endocytic pathway for internalising large gulps," *Immunology and cell biology*, vol. 89, no. 8, pp. 836–843, 2011.
- [138] J. A. Swanson and C. Watts, "Macropinocytosis," *Trends in cell biology*, vol. 5, no. 11, pp. 424–428, 1995.
- [139] M. C. Kerr and R. D. Teasdale, "Defining macropinocytosis," *Traffic*, vol. 10, no. 4, pp. 364–371, 2009.
- [140] A. Verma and F. Stellacci, "Effect of surface properties on nanoparticle–cell interactions," *small*, vol. 6, no. 1, pp. 12–21, 2010.
- [141] S. Salatin, S. Maleki Dizaj, and A. Yari Khosroushahi, "Effect of the surface modification, size, and shape on cellular uptake of nanoparticles," *Cell biology international*, vol. 39, no. 8, pp. 881–890, 2015.
- [142] R. Augustine, A. Hasan, R. Primavera, R. J. Wilson, A. S. Thakor, and B. D. Kevadiya, "Cellular uptake and retention of nanoparticles: Insights on particle properties and interaction with cellular components," *Materials Today Communications*, vol. 25, p. 101692, 2020.
- [143] B. D. Chithrani, A. A. Ghazani, and W. C. Chan, "Determining the size and shape dependence of gold nanoparticle uptake into mammalian cells," *Nano letters*, vol. 6, no. 4, pp. 662–668, 2006.
- [144] A. E. Nel, L. Mädler, D. Velegol, T. Xia, E. Hoek, P. Somasundaran, F. Klaessig,
-

- V. Castranova, and M. Thompson, "Understanding biophysicochemical interactions at the nano-bio interface," *Nature materials*, vol. 8, no. 7, pp. 543–557, 2009.
- [145] R. Toy, P. M. Peiris, K. B. Ghaghada, and E. Karathanasis, "Shaping cancer nanomedicine: the effect of particle shape on the in vivo journey of nanoparticles," *Nanomedicine*, vol. 9, no. 1, pp. 121–134, 2014.
- [146] C. He, Y. Hu, L. Yin, C. Tang, and C. Yin, "Effects of particle size and surface charge on cellular uptake and biodistribution of polymeric nanoparticles," *Biomaterials*, vol. 31, no. 13, pp. 3657–3666, 2010.
- [147] S. B. Hartono, W. Gu, F. Kleitz, J. Liu, L. He, A. P. Middelberg, C. Yu, G. Q. Lu, and S. Z. Qiao, "Poly-L-lysine functionalized large pore cubic mesostructured silica nanoparticles as biocompatible carriers for gene delivery," *Acs Nano*, vol. 6, no. 3, pp. 2104–2117, 2012.
- [148] P. J. Hernando, S. Dedola, M. J. Marín, and R. A. Field, "Recent developments in the use of glyconanoparticles and related quantum dots for the detection of lectins, viruses, bacteria and cancer cells," *Frontiers in Chemistry*, vol. 9, 2021.
- [149] A. Anas, T. Okuda, N. Kawashima, K. Nakayama, T. Itoh, M. Ishikawa, and V. Biju, "Clathrin-mediated endocytosis of quantum dot-peptide conjugates in living cells," *ACS nano*, vol. 3, no. 8, pp. 2419–2429, 2009.
- [150] N. Bertrand, P. Grenier, M. Mahmoudi, E. M. Lima, E. A. Appel, F. Dormont, J.-M. Lim, R. Karnik, R. Langer, and O. C. Farokhzad, "Mechanistic understanding of in vivo protein corona formation on polymeric nanoparticles and impact on pharmacokinetics," *Nature communications*, vol. 8, no. 1, pp. 1–8, 2017.
- [151] J. Kolosnjaj-Tabi, C. Wilhelm, O. Clément, and F. Gazeau, "Cell labeling with magnetic nanoparticles: opportunity for magnetic cell imaging and cell manipulation," *Journal of nanobiotechnology*, vol. 11, no. 1, pp. 1–19, 2013.
- [152] M. Luo, "Influenza virus entry," *Viral Molecular Machines*, pp. 201–221, 2012.
- [153] S. Han, T. Zal, and K. V. Sokolov, "Fate of antibody-targeted ultrasmall gold nanoparticles in cancer cells after receptor-mediated uptake," *ACS nano*, vol. 15, no. 6, pp. 9495–9508, 2021.
- [154] X. Gao, T. Wang, B. Wu, J. Chen, J. Chen, Y. Yue, N. Dai, H. Chen, and X. Jiang, "Quantum dots for tracking cellular transport of lectin-functionalized nanoparticles," *Biochemical and biophysical research communications*, vol. 377, no. 1, pp. 35–40, 2008.
- [155] S. A. Hill, *Carbohydrate-based carbon dots as multivalent glycan platforms*. PhD thesis, University of Bristol, 2017.
- [156] Y. Wei, T. Tang, and H.-B. Pang, "Cellular internalization of bystander nanomaterial induced by TAT-nanoparticles and regulated by extracellular cysteine," *Nature communications*, vol. 10, no. 1, pp. 1–11, 2019.
- [157] K. He, Y. Wei, Z. Zhang, H. Chen, B. Yuan, H.-B. Pang, and K. Yang, "Membrane-curvature-mediated co-endocytosis of bystander and functional nanoparticles," *Nanoscale*, vol. 13, no. 21, pp. 9626–9633, 2021.
-

-
- [158] Y.-X. Li and H.-B. Pang, "Macropinocytosis as a cell entry route for peptide-functionalized and bystander nanoparticles," *Journal of Controlled Release*, vol. 329, pp. 1222–1230, 2021.
- [159] B. Cabukusta and J. Neefjes, "Mechanisms of lysosomal positioning and movement," *Traffic*, vol. 19, no. 10, pp. 761–769, 2018.
- [160] D. Bandyopadhyay, A. Cyphersmith, J. A. Zapata, Y. J. Kim, and C. K. Payne, "Lysosome transport as a function of lysosome diameter," *PloS one*, vol. 9, no. 1, p. e86847, 2014.
- [161] G. Griffiths, "On vesicles and membrane compartments," *Protoplasma*, vol. 195, no. 1, pp. 37–58, 1996.
- [162] J. P. Luzio, P. R. Pryor, and N. A. Bright, "Lysosomes: fusion and function," *Nature reviews Molecular cell biology*, vol. 8, no. 8, pp. 622–632, 2007.
- [163] C. Settembre, A. Fraldi, D. L. Medina, and A. Ballabio, "Signals from the lysosome: a control centre for cellular clearance and energy metabolism," *Nature reviews Molecular cell biology*, vol. 14, no. 5, pp. 283–296, 2013.
- [164] P. L. McNeil, "Repairing a torn cell surface: make way, lysosomes to the rescue," *Journal of cell science*, vol. 115, no. 5, pp. 873–879, 2002.
- [165] M. Corrotte and T. Castro-Gomes, "Lysosomes and plasma membrane repair," *Current topics in membranes*, vol. 84, pp. 1–16, 2019.
- [166] K. Honey and A. Y. Rudensky, "Lysosomal cysteine proteases regulate antigen presentation," *Nature Reviews Immunology*, vol. 3, no. 6, pp. 472–482, 2003.
- [167] I. Jordens, M. Fernandez-Borja, M. Marsman, S. Dusseljee, L. Janssen, J. Calafat, H. Janssen, R. Wubbolts, and J. Neefjes, "The Rab7 effector protein RILP controls lysosomal transport by inducing the recruitment of dynein-dynactin motors," *Current Biology*, vol. 11, no. 21, pp. 1680–1685, 2001.
- [168] C. Rosa-Ferreira and S. Munro, "Arl8 and SKIP act together to link lysosomes to kinesin-1," *Developmental cell*, vol. 21, no. 6, pp. 1171–1178, 2011.
- [169] G. H. Diering and M. Numata, "Endosomal pH in neuronal signaling and synaptic transmission: role of Na^+/H^+ exchanger NHE5," *Frontiers in physiology*, vol. 4, p. 412, 2014.
- [170] S. Ohkuma and B. Poole, "Fluorescence probe measurement of the intralysosomal pH in living cells and the perturbation of pH by various agents.," *Proceedings of the National Academy of Sciences*, vol. 75, no. 7, pp. 3327–3331, 1978.
- [171] I. Mellman, R. Fuchs, and A. Helenius, "Acidification of the endocytic and exocytic pathways," *Annual review of biochemistry*, vol. 55, no. 1, pp. 663–700, 1986.
- [172] H. Appelqvist, P. Wäster, K. Kågedal, and K. Öllinger, "The lysosome: from waste bag to potential therapeutic target," *Journal of molecular cell biology*, vol. 5, no. 4, pp. 214–226, 2013.
- [173] M. L. Jongsma, I. Berlin, R. H. Wijdeven, L. Janssen, G. M. Janssen, M. A. Garstka, H. Janssen, M. Mensink, P. A. Van Veelen, R. M. Spaapen, *et al.*,
-

- “An ER-associated pathway defines endosomal architecture for controlled cargo transport,” *Cell*, vol. 166, no. 1, pp. 152–166, 2016.
- [174] R. Jia, C. M. Guardia, J. Pu, Y. Chen, and J. S. Bonifacino, “BORC coordinates encounter and fusion of lysosomes with autophagosomes,” *Autophagy*, vol. 13, no. 10, pp. 1648–1663, 2017.
- [175] Š. Bálint, I. Verdeny Vilanova, Á. Sandoval Álvarez, and M. Lakadamyali, “Correlative live-cell and superresolution microscopy reveals cargo transport dynamics at microtubule intersections,” *Proceedings of the National Academy of Sciences*, vol. 110, no. 9, pp. 3375–3380, 2013.
- [176] V. Zaburdaev, S. Denisov, and J. Klafter, “Lévy walks,” *Reviews of Modern Physics*, vol. 87, no. 2, p. 483, 2015.
- [177] K. Chen, B. Wang, and S. Granick, “Memoryless self-reinforcing directionality in endosomal active transport within living cells,” *Nature Materials*, vol. 14, no. 6, pp. 589–593, 2015.
- [178] K. Polev, D. V. Kolygina, K. Kandere-Grzybowska, and B. A. Grzybowski, “Large-scale, wavelet-based analysis of lysosomal trajectories and co-movements of lysosomes with nanoparticle cargos,” *Cells*, vol. 11, no. 2, p. 270, 2022.
- [179] B. A. Kairdolf, A. M. Smith, T. H. Stokes, M. D. Wang, A. N. Young, and S. Nie, “Semiconductor quantum dots for bioimaging and biodiagnostic applications,” *Annual review of analytical chemistry*, vol. 6, pp. 143–162, 2013.
- [180] S. Hohng and T. Ha, “Near-complete suppression of quantum dot blinking in ambient conditions,” *Journal of the American Chemical Society*, vol. 126, no. 5, pp. 1324–1325, 2004.
- [181] O. Chen, J. Zhao, V. P. Chauhan, J. Cui, C. Wong, D. K. Harris, H. Wei, H.-S. Han, D. Fukumura, R. K. Jain, *et al.*, “Compact high-quality cdse–cds core–shell nanocrystals with narrow emission linewidths and suppressed blinking,” *Nature materials*, vol. 12, no. 5, pp. 445–451, 2013.
- [182] K. A. Lidke, B. Rieger, T. M. Jovin, and R. Heintzmann, “Superresolution by localization of quantum dots using blinking statistics,” *Optics express*, vol. 13, no. 18, pp. 7052–7062, 2005.
- [183] Y. Wang, G. Fruhwirth, E. Cai, T. Ng, and P. R. Selvin, “3d super-resolution imaging with blinking quantum dots,” *Nano letters*, vol. 13, no. 11, pp. 5233–5241, 2013.
- [184] M. L. Bruschi, “Modification of drug release,” in *Strategies to modify the drug release from pharmaceutical systems*, ch. 2, pp. 15–28, Woodhead Publishing, 2015.
- [185] M. J. Mitchell, M. M. Billingsley, R. M. Haley, M. E. Wechsler, N. A. Peppas, and R. Langer, “Engineering precision nanoparticles for drug delivery,” *Nature Reviews Drug Discovery*, vol. 20, no. 2, pp. 101–124, 2021.
- [186] D. Bobo, K. J. Robinson, J. Islam, K. J. Thurecht, and S. R. Corrie, “Nanoparticle-based medicines: a review of fda-approved materials and clinical trials to date,” *Pharmaceutical research*, vol. 33, no. 10, pp. 2373–2387, 2016.
-

-
- [187] Y. Matsumura and H. Maeda, "A new concept for macromolecular therapeutics in cancer chemotherapy: mechanism of tumoritropic accumulation of proteins and the antitumor agent smancs," *Cancer research*, vol. 46, no. 12_Part_1, pp. 6387–6392, 1986.
- [188] J. Wu, "The enhanced permeability and retention (epr) effect: the significance of the concept and methods to enhance its application," *Journal of Personalized Medicine*, vol. 11, no. 8, p. 771, 2021.
- [189] J.-S. Kim, "Liposomal drug delivery system," *Journal of Pharmaceutical investigation*, vol. 46, no. 4, pp. 387–392, 2016.
- [190] M. R. Ranson, S. Cheeseman, S. White, and J. Margison, "Caelyx (stealth liposomal doxorubicin) in the treatment of advanced breast cancer," *Critical reviews in oncology/hematology*, vol. 37, no. 2, pp. 115–120, 2001.
- [191] D. Sun, S. Zhou, and W. Gao, "What went wrong with anticancer nanomedicine design and how to make it right," *ACS nano*, vol. 14, no. 10, pp. 12281–12290, 2020.
- [192] J. W. Nichols and Y. H. Bae, "Epr: Evidence and fallacy," *Journal of Controlled Release*, vol. 190, pp. 451–464, 2014.
- [193] C. S. Paulo, R. P. das Neves, and L. S. Ferreira, "Nanoparticles for intracellular-targeted drug delivery," *Nanotechnology*, vol. 22, no. 49, p. 494002, 2011.
- [194] R. Alyautdin, I. Khalin, M. I. Nafeeza, M. H. Haron, and D. Kuznetsov, "Nanoscale drug delivery systems and the blood–brain barrier," *International journal of nanomedicine*, vol. 9, p. 795, 2014.
- [195] J. Watchorn, A. J. Clasky, G. Prakash, I. A. Johnston, P. Z. Chen, and F. X. Gu, "Untangling mucosal drug delivery: engineering, designing, and testing nanoparticles to overcome the mucus barrier," *ACS Biomaterials Science & Engineering*, vol. 8, no. 4, pp. 1396–1426, 2022.
- [196] E. M. Agency, "Committee for medicinal products for human use (chmp) assessment report. comirnaty. common name: Covid-19 mrna vaccine (nucleoside-modified) procedure no. emea/h/c/005735/0000. 19 february 2021," 2021.
- [197] E. M. Agency, "Committee for medicinal products for human use (chmp) covid-19 vaccine moderna common name: Covid-19 mrna vaccine (nucleoside-modified) procedure no. emea/h/c/005791/0000. 11 march 2021," 2021.
- [198] G. Guerrini, D. Magrì, S. Gioria, D. Medagliani, and L. Calzolari, "Characterization of nanoparticles-based vaccines for covid-19," *Nature Nanotechnology*, vol. 17, no. 6, pp. 570–576, 2022.
- [199] B. Han, W. L. Hanson, K. Bensalah, A. Tuncel, J. M. Stern, and J. A. Caddeu, "Development of quantum dot-mediated fluorescence thermometry for thermal therapies," *Annals of biomedical engineering*, vol. 37, no. 6, pp. 1230–1239, 2009.
- [200] L. M. Maestro, E. M. Rodríguez, F. S. Rodríguez, M. I.-d. la Cruz, A. Juarranz, R. Naccache, F. Vetrone, D. Jaque, J. A. Capobianco, and J. G. Solé, "Cdse quantum dots for two-photon fluorescence thermal imaging," *Nano letters*, vol. 10, no. 12, pp. 5109–5115, 2010.
-

-
- [201] X. Liu, A. Skripka, Y. Lai, C. Jiang, J. Liu, F. Vetrone, and J. Liang, "Fast wide-field upconversion luminescence lifetime thermometry enabled by single-shot compressed ultrahigh-speed imaging," *Nature communications*, vol. 12, no. 1, pp. 1–9, 2021.
- [202] L. Shang, F. Stockmar, N. Azadfar, and G. U. Nienhaus, "Intracellular thermometry by using fluorescent gold nanoclusters," *Angewandte Chemie International Edition*, vol. 52, no. 42, pp. 11154–11157, 2013.
- [203] K. Saha, S. S. Agasti, C. Kim, X. Li, and V. M. Rotello, "Gold nanoparticles in chemical and biological sensing," *Chemical reviews*, vol. 112, no. 5, pp. 2739–2779, 2012.
- [204] M. F. Frasco and N. Chaniotakis, "Semiconductor quantum dots in chemical sensors and biosensors," *Sensors*, vol. 9, no. 9, pp. 7266–7286, 2009.
- [205] J. Ackermann, J. T. Metternich, S. Herbertz, and S. Kruss, "Biosensing with fluorescent carbon nanotubes," *Angewandte Chemie International Edition*, vol. 61, no. 18, p. e202112372, 2022.
- [206] S. Kruss, M. P. Landry, E. Vander Ende, B. M. Lima, N. F. Reuel, J. Zhang, J. Nelson, B. Mu, A. Hilmer, and M. Strano, "Neurotransmitter detection using corona phase molecular recognition on fluorescent single-walled carbon nanotube sensors," *Journal of the American Chemical Society*, vol. 136, no. 2, pp. 713–724, 2014.
- [207] H. Wu, R. Nißler, V. Morris, N. Herrmann, P. Hu, S.-J. Jeon, S. Kruss, and J. P. Giraldo, "Monitoring plant health with near-infrared fluorescent h2o2 nanosensors," *Nano Letters*, vol. 20, no. 4, pp. 2432–2442, 2020.
- [208] P. T. Snee, R. C. Somers, G. Nair, J. P. Zimmer, M. G. Bawendi, and D. G. Nocera, "A ratiometric cdse/zns nanocrystal ph sensor," *Journal of the American Chemical Society*, vol. 128, no. 41, pp. 13320–13321, 2006.
- [209] H. Sun, A. M. Scharff-Poulsen, H. Gu, and K. Almdal, "Synthesis and characterization of ratiometric, ph sensing nanoparticles with covalently attached fluorescent dyes," *Chemistry of Materials*, vol. 18, no. 15, pp. 3381–3384, 2006.
- [210] F. Zhang, Z. Ali, F. Amin, A. Feltz, M. Oheim, and W. J. Parak, "Ion and ph sensing with colloidal nanoparticles: influence of surface charge on sensing and colloidal properties," *ChemPhysChem*, vol. 11, no. 3, pp. 730–735, 2010.
- [211] M. J. Marín, F. Galindo, P. Thomas, and D. A. Russell, "Localized intracellular ph measurement using a ratiometric photoinduced electron-transfer-based nanosensor," *Angewandte Chemie*, vol. 124, no. 38, pp. 9795–9799, 2012.
- [212] W. Wang, C. Damm, J. Walter, T. J. Nacken, and W. Peukert, "Photobleaching and stabilization of carbon nanodots produced by solvothermal synthesis," *Physical Chemistry Chemical Physics*, vol. 18, no. 1, pp. 466–475, 2016.
- [213] A. Alaghmandfard, O. Sedighi, N. T. Rezaei, A. A. Abedini, A. M. Khachatourian, M. S. Toprak, and A. Seifalian, "Recent advances in the modification of carbon-based quantum dots for biomedical applications," *Materials Science and Engineering: C*, vol. 120, p. 111756, 2021.
-

-
- [214] S. Fasbender, S. Allani, C. Wimmenauer, R.-P. Cadetdu, K. Raba, J. C. Fischer, B. Bulat, M. Luysberg, C. A. Seidel, T. Heinzl, *et al.*, “Uptake dynamics of graphene quantum dots into primary human blood cells following in vitro exposure,” *RSC advances*, vol. 7, no. 20, pp. 12208–12216, 2017.
- [215] D. Kersting, S. Fasbender, R. Pilch, J. Kurth, A. Franken, M. Ludescher, J. Naskou, A. Hallenberger, C. von Gall, C. J. Mohr, *et al.*, “From in vitro to ex vivo: subcellular localization and uptake of graphene quantum dots into solid tumors,” *Nanotechnology*, vol. 30, no. 39, p. 395101, 2019.
- [216] X. Bao, Y. Yuan, J. Chen, B. Zhang, D. Li, D. Zhou, P. Jing, G. Xu, Y. Wang, K. Holá, *et al.*, “In vivo theranostics with near-infrared-emitting carbon dots—highly efficient photothermal therapy based on passive targeting after intravenous administration,” *Light: Science & Applications*, vol. 7, no. 1, p. 91, 2018.
- [217] S.-T. Yang, X. Wang, H. Wang, F. Lu, P. G. Luo, L. Cao, M. J. Meziani, J.-H. Liu, Y. Liu, M. Chen, *et al.*, “Carbon dots as nontoxic and high-performance fluorescence imaging agents,” *The Journal of Physical Chemistry C*, vol. 113, no. 42, pp. 18110–18114, 2009.
- [218] L. Jiang, H. Ding, M. Xu, X. Hu, S. Li, M. Zhang, Q. Zhang, Q. Wang, S. Lu, Y. Tian, *et al.*, “Uv–vis–nir full-range responsive carbon dots with large multiphoton absorption cross sections and deep-red fluorescence at nucleoli and in vivo,” *Small*, vol. 16, no. 19, p. 2000680, 2020.
- [219] W. Chen, J. Shen, Z. Wang, X. Liu, Y. Xu, H. Zhao, and D. Astruc, “Turning waste into wealth: facile and green synthesis of carbon nanodots from pollutants and applications to bioimaging,” *Chemical science*, vol. 12, no. 35, pp. 11722–11729, 2021.
- [220] Y.-F. Huang, X. Zhou, R. Zhou, H. Zhang, K.-B. Kang, M. Zhao, Y. Peng, Q. Wang, H.-L. Zhang, and W.-Y. Qiu, “One-pot synthesis of highly luminescent carbon quantum dots and their nontoxic ingestion by zebrafish for in vivo imaging,” *Chemistry—A European Journal*, vol. 20, no. 19, pp. 5640–5648, 2014.
- [221] A. Truskewycz, H. Yin, N. Halberg, D. T. Lai, A. S. Ball, V. K. Truong, A. M. Rybicka, and I. Cole, “Carbon dot therapeutic platforms: administration, distribution, metabolism, excretion, toxicity, and therapeutic potential,” *Small*, vol. 18, no. 16, p. 2106342, 2022.
- [222] M. Havrdova, K. Hla, J. Skopalik, K. Tomankova, M. Petr, K. Cepe, K. Polakova, J. Tucek, A. B. Bourlinos, and R. Zboril, “Toxicity of carbon dots—effect of surface functionalization on the cell viability, reactive oxygen species generation and cell cycle,” *Carbon*, vol. 99, pp. 238–248, 2016.
- [223] Y.-Y. Liu, N.-Y. Yu, W.-D. Fang, Q.-G. Tan, R. Ji, L.-Y. Yang, S. Wei, X.-W. Zhang, and A.-J. Miao, “Photodegradation of carbon dots cause cytotoxicity,” *Nature Communications*, vol. 12, no. 1, p. 812, 2021.
- [224] M. Herb, A. Gluschko, and M. Schramm, “Reactive oxygen species: not omnipresent but important in many locations,” *Frontiers in cell and developmental biology*, vol. 9, p. 716406, 2021.
-

-
- [225] R. Scherz-Shouval and Z. Elazar, “Ros, mitochondria and the regulation of autophagy,” *Trends in cell biology*, vol. 17, no. 9, pp. 422–427, 2007.
- [226] H. Kang, S. Rho, W. R. Stiles, S. Hu, Y. Baek, D. W. Hwang, S. Kashiwagi, M. S. Kim, and H. S. Choi, “Size-dependent epr effect of polymeric nanoparticles on tumor targeting,” *Advanced healthcare materials*, vol. 9, no. 1, p. 1901223, 2020.
- [227] Y. Nakamura, A. Mochida, P. L. Choyke, and H. Kobayashi, “Nanodrug delivery: is the enhanced permeability and retention effect sufficient for curing cancer?,” *Bioconjugate chemistry*, vol. 27, no. 10, pp. 2225–2238, 2016.
- [228] M. A. Subhan, S. S. K. Yalamarty, N. Filipczak, F. Parveen, and V. P. Torchilin, “Recent advances in tumor targeting via epr effect for cancer treatment,” *Journal of personalized medicine*, vol. 11, no. 6, p. 571, 2021.
- [229] S. Li, W. Su, H. Wu, T. Yuan, C. Yuan, J. Liu, G. Deng, X. Gao, Z. Chen, Y. Bao, *et al.*, “Targeted tumour theranostics in mice via carbon quantum dots structurally mimicking large amino acids,” *Nature biomedical engineering*, vol. 4, no. 7, pp. 704–716, 2020.
- [230] H. Liu, J. Guo, A. A. Aryee, L. Hua, Y. Sun, Z. Li, J. Liu, and W. Tang, “Lighting up individual organelles with fluorescent carbon dots,” *Frontiers in Chemistry*, vol. 9, p. 784851, 2021.
- [231] H. Liu, J. Yang, Z. Li, L. Xiao, A. A. Aryee, Y. Sun, R. Yang, H. Meng, L. Qu, Y. Lin, *et al.*, “Hydrogen-bond-induced emission of carbon dots for wash-free nucleus imaging,” *Analytical chemistry*, vol. 91, no. 14, pp. 9259–9265, 2019.
- [232] Z. Zhu, Q. Li, P. Li, X. Xun, L. Zheng, D. Ning, and M. Su, “Surface charge controlled nucleoli selective staining with nanoscale carbon dots,” *PloS one*, vol. 14, no. 5, p. e0216230, 2019.
- [233] H. Wu, L.-F. Pang, N. Wei, X.-F. Guo, and H. Wang, “Nucleus-targeted n-doped carbon dots via dna-binding for imaging of hypochlorous in cells and zebrafish,” *Sensors and Actuators B: Chemical*, vol. 333, p. 129626, 2021.
- [234] X.-W. Hua, Y.-W. Bao, Z. Chen, and F.-G. Wu, “Carbon quantum dots with intrinsic mitochondrial targeting ability for mitochondria-based theranostics,” *Nanoscale*, vol. 9, no. 30, pp. 10948–10960, 2017.
- [235] R. S. Li, P. F. Gao, H. Z. Zhang, L. L. Zheng, C. M. Li, J. Wang, Y. F. Li, F. Liu, N. Li, and C. Z. Huang, “Chiral nanoprobe for targeting and long-term imaging of the golgi apparatus,” *Chemical science*, vol. 8, no. 10, pp. 6829–6835, 2017.
- [236] D. Mohr, S. Frey, T. Fischer, T. Güttler, and D. Görlich, “Characterisation of the passive permeability barrier of nuclear pore complexes,” *The EMBO journal*, vol. 28, no. 17, pp. 2541–2553, 2009.
- [237] A. Ghavami, E. Van Der Giessen, and P. R. Onck, “Energetics of transport through the nuclear pore complex,” *PLoS One*, vol. 11, no. 2, p. e0148876, 2016.
- [238] I. W. Mattaj and L. Englmeier, “Nucleocytoplasmic transport: the soluble phase,” *Annual review of biochemistry*, vol. 67, no. 1, pp. 265–306, 1998.
-

-
- [239] L. Pan, J. Liu, and J. Shi, "Cancer cell nucleus-targeting nanocomposites for advanced tumor therapeutics," *Chemical society reviews*, vol. 47, no. 18, pp. 6930–6946, 2018.
- [240] X. Wang, Y. Wang, H. He, X. Chen, X. Sun, Y. Sun, G. Zhou, H. Xu, and F. Huang, "Steering graphene quantum dots in living cells: lighting up the nucleolus," *Journal of Materials Chemistry B*, vol. 4, no. 4, pp. 779–784, 2016.
- [241] X. Chen, X. Zhang, L.-Y. Xia, H.-Y. Wang, Z. Chen, and F.-G. Wu, "One-step synthesis of ultrasmall and ultrabright organosilica nanodots with 100% photoluminescence quantum yield: long-term lysosome imaging in living, fixed, and permeabilized cells," *Nano Letters*, vol. 18, no. 2, pp. 1159–1167, 2018.
- [242] A. Rocznik-Ferguson, C. S. Petit, F. Froehlich, S. Qian, J. Ky, B. Angarola, T. C. Walther, and S. M. Ferguson, "The transcription factor TFEB links mTORC1 signaling to transcriptional control of lysosome homeostasis," *Science signaling*, vol. 5, no. 228, pp. ra42–ra42, 2012.
- [243] L. Li, T. Wan, M. Wan, B. Liu, R. Cheng, and R. Zhang, "The effect of the size of fluorescent dextran on its endocytic pathway," *Cell biology international*, vol. 39, no. 5, pp. 531–539, 2015.
- [244] M. Stark, T. F. Silva, G. Levin, M. Machuqueiro, and Y. G. Assaraf, "The lysosomotropic activity of hydrophobic weak base drugs is mediated via their intercalation into the lysosomal membrane," *Cells*, vol. 9, no. 5, p. 1082, 2020.
- [245] L. Wu, X. Li, Y. Ling, C. Huang, and N. Jia, "Morpholine derivative-functionalized carbon dots-based fluorescent probe for highly selective lysosomal imaging in living cells," *ACS Applied Materials & Interfaces*, vol. 9, no. 34, pp. 28222–28232, 2017.
- [246] H. Liu, Y. Sun, Z. Li, J. Yang, A. A. Aryee, L. Qu, D. Du, and Y. Lin, "Lysosome-targeted carbon dots for ratiometric imaging of formaldehyde in living cells," *Nanoscale*, vol. 11, no. 17, pp. 8458–8463, 2019.
- [247] J.-P. Behr, "The proton sponge: a trick to enter cells the viruses did not exploit," *Chimia*, vol. 51, no. 1-2, pp. 34–34, 1997.
- [248] L. M. Vermeulen, S. C. De Smedt, K. Remaut, and K. Braeckmans, "The proton sponge hypothesis: Fable or fact?," *European Journal of Pharmaceutics and Biopharmaceutics*, vol. 129, pp. 184–190, 2018.
- [249] J. Nguyen and F. C. Szoka, "Nucleic acid delivery: the missing pieces of the puzzle?," *Accounts of chemical research*, vol. 45, no. 7, pp. 1153–1162, 2012.
- [250] C. K. Choudhury, A. Kumar, and S. Roy, "Characterization of conformation and interaction of gene delivery vector polyethylenimine with phospholipid bilayer at different protonation state," *Biomacromolecules*, vol. 14, no. 10, pp. 3759–3768, 2013.
- [251] M. Wojnilowicz, A. Glab, A. Bertucci, F. Caruso, and F. Cavalieri, "Super-resolution imaging of proton sponge-triggered rupture of endosomes and cytosolic release of small interfering rna," *ACS nano*, vol. 13, no. 1, pp. 187–202, 2018.
- [252] F. Du, X. Zhao, W. Lu, Z. Guo, S. Shuang, and C. Dong, "Dual-ligand functional-
-

- ized carbon nanodots as green fluorescent nanosensors for cellular dual receptor-mediated targeted imaging,” *Analyst*, vol. 144, no. 22, pp. 6729–6735, 2019.
- [253] T. Kashkoulinejad-Kouhi, S. Sawalha, S. Safarian, and B. Arnaiz, “A carbon-based nanocarrier for efficient gene delivery,” *Therapeutic Delivery*, vol. 12, no. 4, pp. 311–323, 2021.
- [254] L. Rueda-Gensini, J. Cifuentes, M. C. Castellanos, P. R. Puentes, J. A. Serna, C. Muñoz-Camargo, and J. C. Cruz, “Tailoring iron oxide nanoparticles for efficient cellular internalization and endosomal escape,” *Nanomaterials*, vol. 10, no. 9, p. 1816, 2020.
- [255] M. Lan, S. Zhao, Z. Zhang, L. Yan, L. Guo, G. Niu, J. Zhang, J. Zhao, H. Zhang, P. Wang, *et al.*, “Two-photon-excited near-infrared emissive carbon dots as multifunctional agents for fluorescence imaging and photothermal therapy,” *Nano research*, vol. 10, pp. 3113–3123, 2017.
- [256] F. Fiori, H. Moukham, F. Olia, D. Piras, S. Ledda, A. Salis, L. Stagi, L. Malfatti, and P. Innocenzi, “Highly photostable carbon dots from citric acid for bioimaging,” *Materials*, vol. 15, no. 7, p. 2395, 2022.
- [257] Q. Wang, Z. Feng, H. He, X. Hu, J. Mao, X. Chen, L. Liu, X. Wei, D. Liu, S. Bi, *et al.*, “Nonblinking carbon dots for imaging and tracking receptors on a live cell membrane,” *Chemical Communications*, vol. 57, no. 45, pp. 5554–5557, 2021.
- [258] A. C. Doughty, A. R. Hoover, E. Layton, C. K. Murray, E. W. Howard, and W. R. Chen, “Nanomaterial applications in photothermal therapy for cancer,” *Materials*, vol. 12, no. 5, p. 779, 2019.
- [259] A. M. Smith, M. C. Mancini, and S. Nie, “Second window for in vivo imaging,” *Nature nanotechnology*, vol. 4, no. 11, pp. 710–711, 2009.
- [260] K. W. Dunn, M. M. Kamocka, and J. H. McDonald, “A practical guide to evaluating colocalization in biological microscopy,” *American Journal of Physiology-Cell Physiology*, 2011.
- [261] S. Bolte and F. P. Cordelières, “A guided tour into subcellular colocalization analysis in light microscopy,” *Journal of microscopy*, vol. 224, no. 3, pp. 213–232, 2006.
- [262] E. Manders, J. Stap, G. Brakenhoff, R. Van Driel, and J. Aten, “Dynamics of three-dimensional replication patterns during the S-phase, analysed by double labelling of DNA and confocal microscopy,” *Journal of cell science*, vol. 103, no. 3, pp. 857–862, 1992.
- [263] F. P. Cordelieres and S. Bolte, “Experimenters’ guide to colocalization studies: finding a way through indicators and quantifiers, in practice,” *Methods in cell biology*, vol. 123, pp. 395–408, 2014.
- [264] E. Manders, F. Verbeek, and J. Aten, “Measurement of co-localization of objects in dual-colour confocal images,” *Journal of microscopy*, vol. 169, no. 3, pp. 375–382, 1993.
- [265] E. Lachmanovich, D. Shvartsman, Y. Malka, C. Botvin, Y. Henis, and A. Weiss, “Co-localization analysis of complex formation among membrane proteins by
-

- computerized fluorescence microscopy: application to immunofluorescence co-patching studies,” *Journal of microscopy*, vol. 212, no. 2, pp. 122–131, 2003.
- [266] F. Levet, G. Julien, R. Galland, C. Butler, A. Beghin, A. Chazeau, P. Hoess, J. Ries, G. Giannone, and J.-B. Sibarita, “A tessellation-based colocalization analysis approach for single-molecule localization microscopy,” *Nature communications*, vol. 10, no. 1, p. 2379, 2019.
- [267] L. Andronov, I. Orlov, Y. Lutz, J.-L. Vonesch, and B. P. Klaholz, “ClusterViSu, a method for clustering of protein complexes by Voronoi tessellation in super-resolution microscopy,” *Scientific reports*, vol. 6, no. 1, pp. 1–9, 2016.
- [268] A. Baddeley, E. Rubak, and R. Turner, *Spatial point patterns: methodology and applications with R*. CRC press, 2015.
- [269] J. Møller and R. P. Waagepetersen, “Modern statistics for spatial point processes,” *Scandinavian Journal of Statistics*, vol. 34, no. 4, pp. 643–684, 2007.
- [270] B. D. Ripley, “Modelling spatial patterns,” *Journal of the Royal Statistical Society: Series B (Methodological)*, vol. 39, no. 2, pp. 172–192, 1977.
- [271] T. Lagache, A. Grassart, S. Dallongeville, O. Faklaris, N. Sauvonnet, A. Dufour, L. Danglot, and J.-C. Olivo-Marin, “Mapping molecular assemblies with fluorescence microscopy and object-based spatial statistics,” *Nature communications*, vol. 9, no. 1, pp. 1–15, 2018.
- [272] T. Lagache, N. Sauvonnet, L. Danglot, and J.-C. Olivo-Marin, “Statistical analysis of molecule colocalization in bioimaging,” *Cytometry Part A*, vol. 87, no. 6, pp. 568–579, 2015.
- [273] J. A. Helmuth, G. Paul, and I. F. Sbalzarini, “Beyond co-localization: inferring spatial interactions between sub-cellular structures from microscopy images,” *BMC bioinformatics*, vol. 11, no. 1, pp. 1–12, 2010.
- [274] K. L. Fastabend, “Subzelluläre verteilung von funktionalisierten kohlenstoff-nanoteilchen,” Master’s thesis, 2022.
- [275] S. Fasbender, *The interaction of graphene quantum dots with human cells*. PhD thesis, 2020.
- [276] G. Rajender and P. Giri, “Formation mechanism of graphene quantum dots and their edge state conversion probed by photoluminescence and raman spectroscopy,” *Journal of Materials Chemistry C*, vol. 4, no. 46, pp. 10852–10865, 2016.
- [277] A. T. R. Williams, S. A. Winfield, and J. N. Miller, “Relative fluorescence quantum yields using a computer-controlled luminescence spectrometer,” *Analyst*, vol. 108, no. 1290, pp. 1067–1071, 1983.
- [278] S. Chen, J.-W. Liu, M.-L. Chen, X.-W. Chen, and J.-H. Wang, “Unusual emission transformation of graphene quantum dots induced by self-assembled aggregation,” *Chemical Communications*, vol. 48, no. 61, pp. 7637–7639, 2012.
- [279] M. Minsky, “Confocal scanning microscope,” *Rapport technique, Patent*, vol. 3, p. 14, 1955.
-

-
- [280] M. Minsky, "Memoir on inventing the confocal scanning microscope," *Scanning*, vol. 10, no. 4, pp. 128–138, 1988.
- [281] M. Muller, *Introduction to confocal fluorescence microscopy*, vol. 69. SPIE press, 2006.
- [282] K. Weisshart, "The basic principle of airyscanning," *Zeiss Technology Note*, vol. 22, 2014.
- [283] J. Huff, "The fast mode for ZEISS LSM 880 with Airyscan: high-speed confocal imaging with super-resolution and improved signal-to-noise ratio," 2016.
- [284] J. Huff, A. Bergter, J. Birkenbeil, I. Kleppe, R. Engelmann, and U. Krzic, "The new 2d superresolution mode for ZEISS Airyscan," 2017.
- [285] K. Korobchevskaya, B. C. Lagerholm, H. Colin-York, and M. Fritzsche, "Exploring the potential of airyscan microscopy for live cell imaging," in *Photonics*, vol. 4, p. 41, MDPI, 2017.
- [286] P. Dey, *Diagnostic flow cytometry in cytology*. Springer Singapore, 2021.
- [287] J. P. Golden, G. A. Justin, M. Nasir, and F. S. Ligler, "Hydrodynamic focusing—a versatile tool," *Analytical and bioanalytical chemistry*, vol. 402, no. 1, pp. 325–335, 2012.
- [288] A. L. Givan, *Flow cytometry: first principles*. John Wiley & Sons, 2013.
- [289] S. P. Perfetto, P. K. Chattopadhyay, and M. Roederer, "Seventeen-colour flow cytometry: unravelling the immune system," *Nature Reviews Immunology*, vol. 4, no. 8, pp. 648–655, 2004.
- [290] Y. Saeys, S. Van Gassen, and B. N. Lambrecht, "Computational flow cytometry: helping to make sense of high-dimensional immunology data," *Nature Reviews Immunology*, vol. 16, no. 7, pp. 449–462, 2016.
- [291] F. Mair, F. J. Hartmann, D. Mrdjen, V. Tosevski, C. Krieg, and B. Becher, "The end of gating? an introduction to automated analysis of high dimensional cytometry data," *European journal of immunology*, vol. 46, no. 1, pp. 34–43, 2016.
- [292] P. Qiu, E. F. Simonds, S. C. Bendall, K. D. Gibbs, R. V. Bruggner, M. D. Linderman, K. Sachs, G. P. Nolan, and S. K. Plevritis, "Extracting a cellular hierarchy from high-dimensional cytometry data with SPADE," *Nature biotechnology*, vol. 29, no. 10, pp. 886–891, 2011.
- [293] S. Van Gassen, B. Callebaut, M. J. Van Helden, B. N. Lambrecht, P. Demeester, T. Dhaene, and Y. Saeys, "FlowSOM: Using self-organizing maps for visualization and interpretation of cytometry data," *Cytometry Part A*, vol. 87, no. 7, pp. 636–645, 2015.
- [294] L. v. d. Maaten and G. Hinton, "Visualizing data using t-SNE," *Journal of machine learning research*, vol. 9, no. Nov, pp. 2579–2605, 2008.
- [295] E.-a. D. Amir, K. L. Davis, M. D. Tadmor, E. F. Simonds, J. H. Levine, S. C. Bendall, D. K. Shenfeld, S. Krishnaswamy, G. P. Nolan, and D. Pe'er, "viSNE enables visualization of high dimensional single-cell data and reveals phenotypic
-

heterogeneity of leukemia,” *Nature biotechnology*, vol. 31, no. 6, pp. 545–552, 2013.

Abbreviations

AFM	Atomic Force Microscopy
AML	Acute Myeloid Leukemia
CEE	Crosslinking Enhanced Emission
CND	Carbon Nanodot
CNT	Carbon Nanotube
CSR	Complete Spatial Randomness
DETA	Diethylenetriamine
EDC	1-Ethyl-3-(3-dimethylaminopropyl)carbodiimide
EPR	Enhanced Permeability and Retention
FDA	Food and Drug Administration (USA)
FSC	Forward Scatter
GFP	Green Fluorescent Protein
GNR	Graphene Nanoribbon
GREE	Giant Red Edge Effect
GQD	Graphene Quantum Dot
LAT1	Large Neutral Amino Acid Transporter 1
mRNA	Messenger Ribonucleic Acid
NHS	N-hydroxysuccinimide
NLS	Nuclear Localization Sequence
NMR	Nuclear Magnetic Resonance
NPC	Nuclear Pore Complex
PEG	Polyethylene Glycol
PEI	Polyethylenimine
PSF	Point Spread Function
RFP	Red Fluorescent Protein
ROS	Reactive Oxygen Species
SNR	Signal-to-Noise Ratio

SSC	Side Scatter
STED	Stimulated Emission Depletion
TEM	Transmission Electron Microscopy
tSNE	<i>t</i> -distributed Stochastic Neighbor Embedding
XPS	X-ray Photoelectron Spectroscopy

Danksagung

Ich danke ...

... meinem Doktorvater Prof. Dr. Thomas Heinzel dafür, dass er immer eine offene Tür und ein offenes Ohr für meine Anliegen hatte und dafür, dass er mir den Freiraum und das Vertrauen geboten hat meine wissenschaftliche Kreativität zu entfalten.

... der Jürgen-Manchot-Stiftung für die großzügige finanzielle Förderung und das entgegengebrachte Vertrauen. Ohne diese Mittel wären die Experimente im Rahmen dieser Arbeit in dieser Form nicht möglich gewesen.

... Prof. Dr. Cornelia Monzel für die Übernahme der Mentorenschaft und des Korreferats dieser Dissertation sowie für die fruchtbare Zusammenarbeit. Weiterhin möchte mich dafür bedanken, dass sie mich als Gast für einige Experimente aufgenommen hat, die in unseren Biolaboren nicht durchführbar waren.

... unseren Kooperationspartnern Prof. Dr. Laura Hartmann, Dr. Stephen Hill und Serap Üçlü aus der Arbeitsgruppe für Makromolekulare Chemie für die gemeinsame Arbeit an den Zucker-funktionalisierten Nanopartikeln. Insbesondere möchte ich hier Serap für die zahlreichen Stunden im Labor und die angenehme Zusammenarbeit danken.

... Prof. Dr. Rainer Haas aus der Hämatologie, dessen medizinische Expertise mir in zahlreichen Diskussionen neue Perspektiven eröffnet hat und dessen vielseitige Interessen immer ein Garant für eine gute Zusammenarbeit waren.

... Dr. Ron-Patrick Cadeddu und dem freundlichen Team aus dem hämatologischen Speziallabor dafür, dass sie meine Kollegen und mich gerne für Durchflusszytometrie-Experimente aufgenommen und uns bei Fragen und Problemen mit großer Expertise unterstützt haben.

... der Arbeitsgruppe für Molekulare Physikalische Chemie unter der Leitung von Prof. Dr. Claus Seidel die mich schon während meiner Masterarbeit für einige Experimente aufgenommen hat. Insbesondere spreche ich Dr. Ralf Kühnemuth meinen Dank aus, der mich mit viel Geduld in die experimentelle Arbeit an den recht komplexen Aufbauten herangeführt hat.

... Dr. Dieter Niederacher und Prof. Dr. Hans Neubauer aus der Arbeitsgruppe für Translationale Gynäkoonkologie dafür, dass sie mir die Arbeit in ihren Laboren in der frühen Phase meiner Arbeit ermöglicht haben und für den wissenschaftlichen Austausch zu KI in der Medizin.

... dem Team des Center of Advanced Imaging (CAi) der HHU für die Bereitstellung der Mikroskope für unsere Experimente und die Einführungen in diese Geräte.

... Dr. Stefan Fasbender, der mich während meiner Bachelor und Masterarbeit betreut hat, für seine Vorarbeiten zu dem Thema auf denen ich mit dieser Arbeit aufbauen durfte.

... Julienne, Oliver, Lennard, Cathrin, Saskia, Noah, Faranak, Daniela, Rika, Karin und Maxime mit denen ich während ihrer Bachelor und/oder Masterarbeit über GQDs, CNDs oder die Verarbeitung biomedizinischer Daten zusammenarbeiten durfte.

... Bianka für die Hilfe bei vielen organisatorischen Aufgaben, die in den letzten Jahren angefallen sind.

... meinen Doktoranden- und Postdoc-Kollegen vom Lehrstuhl für Festkörperphysik Jakob, Stefan, Carla, Cathrin, Laurin-kun, Svenja, Beate, Lukas und Mihai für den Kuchen, den sozialen Austausch am Institut und auch viele gemeinsame Stunden fernab von der Arbeit. Für die tolle Arbeitsatmosphäre und den Kuchen möchte ich auch den nicht-wissenschaftlichen Kollegen und den ehemaligen Bachelor- und Masteranden danken. Weiterhin möchte ich Carla, Laurin-sensei, Cathrin und Stefan für ihre hilfreichen Anmerkungen und das Korrekturlesen dieser Arbeit meinen Dank aussprechen.

... meiner Partnerin Veronica und meinen Eltern dafür, dass sie mich während dieser Zeit, so wie auch sonst, immer unterstützt haben und ich mich in allen Lebenslagen auf sie verlassen kann.
